Quantum Chaos in Atom Optics

Michael Brendan d'Arcy

A thesis submitted in partial fulfilment of
the requirements for the degree of
Doctor of Philosophy at the University of Oxford

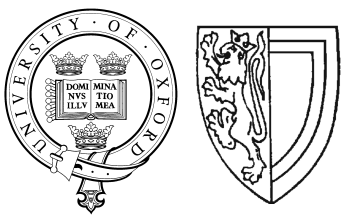

Balliol College
University of Oxford
Hilary Term 2002

Abstract

Quantum Chaos in Atom Optics

Michael Brendan d'Arcy, Balliol College, University of Oxford
DPhil Thesis, Hilary Term 2002

This thesis presents an account of experimental and numerical investigations of two quantum systems whose respective classical analogues are chaotic. These are the δ-kicked rotor, a paradigm in classical chaos theory, and the novel δ-kicked accelerator, created by application of a constant external acceleration or torque to the rotor. The experimental realisation of these systems has been achieved by the exposure of laser-cooled caesium atoms to approximate δ-kicks from a pulsed, high-intensity, vertical standing wave of laser light. Gravity's effect on the atoms can be controlled by appropriate shifting of the profile of the standing wave. Numerical simulations of the systems are based on a diffractive model of the potential's effect.

Each system's dynamics are characterised by the final form of the momentum distribution and the dependence of the atoms' mean kinetic energy on the number and time period of the δ-kicks. The phenomena of dynamical localisation and quantum resonances in the δ-kicked rotor, which have no counterparts in the system's classical analogue, are observed and investigated. Similar experiments on the δ-kicked accelerator reveal the striking phenomenon of the quantum accelerator mode, in which a large momentum is transferred to a substantial fraction of the atomic ensemble. This feature, absent in the system's classical analogue, is characterised and an analytic explanation is presented.

The effect on each quantum system of decoherence, introduced through spontaneous emission in the atoms, is examined and comparison is made with the results of classical simulations. While having little effect on the classical systems, the level of decoherence used is found to degrade quantum signatures of behaviour. Classical-like behaviour is, to some extent, restored, although significant quantum features remain. Possible applications of the quantum accelerator mode are discussed. These include use as a tool in atom optics and interferometry, a technique for measuring gravity, and a method of preparing atoms in a particular region of phase space. This may allow measurement of quantum phase space stability, and hence investigation of quantum chaos and quantum-classical correspondence.

Acknowledgements

> ... I have written my work, not as an essay which is to win the applause of the moment, but as a possession for all time.
>
> Thucydides, *The History of the Peloponnesian War* (I.xxii.4).

Such must be the feeling of every doctoral student as he completes his thesis. However, failure to win the applause of the moment seems a slightly more attainable target (and likely outcome) than the production of an everlasting masterpiece! Be that as it may, this thesis records the research in which I have been engaged over the last three years, and this would only have been possible with the help and friendship of my colleagues in the Clarendon Laboratory.

First of all, I would like to thank my supervisor Dr. Gil Summy. He has always been available to give cheerful advice and optimistic suggestions, and has managed to rescue the experiment from apparent afunctionality on a number of occasions, with the minimum of fuss. He has made a great difference to my approach to physics, and quite a few other things besides, and has been my most appreciative interlocutor on the subject of Clarendon lookalikes. Though we miss him now that he has moved to Oklahoma, no doubt he'll do very well. I would also like to thank Professor Keith Burnett, who has been my auxiliary supervisor and Head of Department. Keith has always been a voice of encouragement and understanding, as well as great physical insight, and he, along with Professor Colin Webb, made it possible for me to transfer to the Clarendon to study for this DPhil. Thanks also to Dr. Christopher Foot, who has helped to run the harmonious basement ship, for being a source of friendly advice and for inviting me to become a colleague in St. Peter's College.

My experimental co-workers have made my time here stimulating and enjoyable. Rachel Godun has been practically the ideal partner: organised, knowledgeable, pleasant and considerate. Markus Oberthaler gave me my first introduction to high-intensity experimentation, combined with physical intuition. Our visiting students Guillaume Hénin and Sophie Schlunk have made learning look quick and easy, as well as being good company. Our technicians Graham Quelch and George Matthews have enabled us to have reliable, stable and even aesthetically pleasing experimental apparatus. I must also thank the other basement folk for so many good times. Jan Arlt, Matthias Büchner, Donatella Cassettari, Gerald Hechenblaikner (an expert on everything from European history to Berlin nightclubs), Eleanor Hodby, Stephen Hopkins, Zhaoyuan Ma, Onofrio Maragò, Giuseppe Smirne, Nathan Smith and Angharad Thomas, plus David Lucas, Charles Donald and other members of the ion-trapping group, have all formed

a dynamic, talented and lively ensemble of which it has been a privilege to be part. Two more of this group, Simon Cornish and Stephen Webster, have, as fellow supporters of Liverpool FC, been valued tea-time conversationalists and kindred spirits in the midst of the ladies' indifference and Gil's disdain. Upstairs, Stephen Choi, Matthew Davis, Jacob Dunningham and the other members of Keith Burnett's theory group have been good friends, rugby enthusiasts and a theoretical physics treasury.

On a wider level, I would like to thank my tutors in Balliol College, Dr. Jonathon Hodby, Dr. Ian Kogan and Professor David Wark, for their help, guidance and encouragement since I arrived in Oxford. The heads of the Oxford ZEUS group with whom I worked during my brief time as a particle physics DPhil student, Professor Robin Devenish and Dr. Roman Walczak, showed great understanding and gave sympathetic advice as I made the transition to the atomic scale. Professor Giulio Casati and Professor Italo Guarneri made me most welcome when I visited the University of Insubria at Como in June 2000, and I am grateful for their scientific insight. Similarly, Dr. Simon Gardiner was my host when I visited the University of Potsdam in March 2001; I am looking forward to further collaboration with him when he comes to work in Oxford. My extra-physics friends from Balliol College and the Oxford University Catholic Society, especially Martyn O'Donnell, Luke O'Sullivan and Fr. Terence Crotty OP, have given me welcome relief from mathematical problems and experimental difficulties, and helped keep everything in perspective. They have my gratitude.

I must acknowledge those who have kept me alive and experimenting over the past three years. The money for this research was provided by the EPSRC, the Paul Instrument Fund of The Royal Society, the European Science Foundation through the 'BEC 2000+' fund and the TMR Network of the European Union. I have been the recipient of a Jowett Senior Exhibition from Balliol College and, latterly, a Research Fellowship from the Royal Commission for the Exhibition of 1851. My thanks to all these funding bodies.

Finally, I must thank my family. My brothers, Louis and Brian, have shown me appropriate disrespect and friendship throughout our time working and playing together at home, in school, in university, and more recently. My sister, Eleanor, has always been a delight to be around, and since I came to university has always been a cheerful voice on the end of the phone with her thoughts, anecdotes and Irish rugby-related questions. Mom and Dad have supported and inspired me all through the years, and their unconditional love has never failed to be a '*statio bene fida carinis*'. They have done more for me than I can ever thank them for, and this thesis is dedicated to them.

Contents

Chapter 1

Introduction

1.1 Dynamics and chaos

The study of dynamics is as old as science itself. The motion of the celestial bodies, for example, has been an object of wonder since ancient times [1, 2]. The publication of Newton's *Principia* in 1687 [3], in which were contained Newton's Laws of motion and gravitation, rendered many dynamical systems mathematically tractable. They were able to explain the motion of the moon and the observed terrestrial effects of gravity, as well as countless other physical phenomena. The bulk of the work over the subsequent 200 years centred on the development and solution of differential equations describing, almost exclusively, linear dynamics; treatment of nonlinear dynamics proved to be much more difficult. In 1890 the King of Sweden offered a prize for the solution to the equations describing the motion of an arbitrary system of point masses that attract each other according to Newton's Laws. Being a nonlinear, many-body system, this is very complex and has never been solved analytically. However, the contest did lead Poincaré to develop a completely new approach to problems of nonlinear dynamics [4, 5]. By analysing the evolution of the system in terms of trajectories in phase space, he was able to establish the nature of the possible types of behaviour open to the system. Such an approach yields great insight into the system's dynamics. As a consequence of his investigations, he realised that the structure of phase space could result in behaviour that was much more complex than had previously been appreciated. This was the first recognition of what is now called *chaos*.

Study of such complex dynamics was not widely pursued until the 1960s, when interest was renewed by improvements in computing power and consequent discoveries. In 1963, Lorenz [6], using a primitive computer, discovered that simple differential equations applied iteratively could yield the chaos observed by Poincaré. The meteorological models that they described exhibited sensitive dependence on initial conditions, meaning that long-range weather forecasting was all but impossible. This extreme dependence of a system's evolution on its initial state, and the

lack of predictability in this evolution, are essential attributes of chaotic systems. A working definition of chaos is as follows [7]:

> Chaos is aperiodic long-term behaviour in a deterministic system that exhibits sensitive dependence on initial conditions.

A phase space portrait is obtained by recording a particle's position in phase space at equal time intervals, or after successive iterations of a mapping. The sequence of these positions defines a particle's 'orbit'. An aperiodic orbit does not make periodic returns to its starting point in phase space, or points very close to this. Trajectories in which these types of behaviour did occur would constitute periodic and quasiperiodic orbits, respectively. In a chaotic system, initially neighbouring points in phase space have trajectories that diverge exponentially with time. Prior to the appreciation of the sensitivity of such systems to their initial conditions, it had been believed that the state of a classical system at any time in the future could be predicted by knowing its initial state. This was because Newton's Laws are deterministic. However, lack of infinitely precise knowledge, which must be the physically realistic situation, can render the future unpredictable. Any slight inaccuracy, either in the known value of the initial state or in the calculation process, can greatly affect the calculated outcome. This defines a 'time horizon' beyond which the ability to predict the state of a system within a certain tolerance breaks down.

Just as in Pascal's statement in the 17th Century that, 'Had Cleopatra's nose been shorter, the whole aspect of the world would have been different,' [8] a tiny modification to a chaotic system's initial state can have colossal ramifications. Scientifically, this has been a source of great interest over the past 30 years. An oft-expressed meteorological manifestation of such sensitivity is the case where the beat of a butterfly's wings in Oxford could, three months later, lead to a hurricane in the Gulf of Mexico. The study of the field of chaos has been greatly facilitated in recent times by the advent of high-speed computers. Without these, many of the structures in phase space that determine the behaviour of the systems of interest could not be observed. Much of the work described in this thesis has been reliant on the availability of this level of computing power. Controllable experiments into chaos have also been performed. Classical chaos can be observed in, for example, electrical circuits, chemical reactions and hydrodynamic systems (see Ref. [9] for further discussion of such systems). Chaos can also be observed in uncontrollable circumstances, from meteorological systems [10], to financial markets [11], to patterns of disease outbreak [12]. The incentives for developing a greater understanding of the behaviour of such systems are great, and will be of practical use as well as intrinsic value.

Chaos is intimately related to integrability. Integrable systems have as many constants of the motion as they have degrees of freedom, and can never exhibit chaotic behaviour. For an integrable classical system with N degrees of freedom, a given trajectory lies on an N-dimensional surface. Depending on its initial state, a particle in such a system will execute a periodic or quasiperiodic orbit, or else remain at the same point (a 'fixed point') for all time. A system is non-integrable

when the number of constants of the motion is less than the number of degrees of freedom. A necessary condition for this is that the system should be nonlinear. A classical system fulfilling the condition of non-integrability may exhibit chaotic behaviour of the sort identified by Lorenz. The phase space of such systems generally contains a mixture of periodic, quasiperiodic and aperiodic (chaotic) orbits, plus fixed points. When the initial conditions lie in a chaotic region then the future development of the system can only be determined in a probabilistic sense because of the extreme sensitivity to initial conditions. Due to the plethora of nonlinear systems in nature, non-integrability is very common and chaotic behaviour is by no means exceptional. The frequency of its occurrence makes the attainment of a deeper understanding all the more important.

1.2 Quantum mechanics

In the discussion thus far, chaos has been described in terms of classical mechanics. However, physics since the turn of the 20th Century has been revolutionised by the realisation that the behaviour of matter must be described by quantum mechanics. The classical behaviour observed in macroscopic systems is some kind of limit of the more fundamental wave-like behaviour exhibited at smaller energy and length scales. Prior to the formulation of quantum mechanics, it was believed that light was a wave and matter a corpuscle. The observation of the photoelectric effect [13] and Compton scattering [14, 15] demonstrated that light also had a particle nature. The first prediction that matter, by analogy with light, must also have a wave nature was made by de Broglie in 1923 [16, 17, 18]. Experimental verification that matter could, indeed, exhibit wave-like behaviour came in the form of diffraction of electrons. Davisson and Germer [19] observed the reflection of electrons from a crystal lattice of nickel, while Thomson [20] observed the transmission of electrons by a polycrystalline foil of different types of metal. Observation of diffraction in the scattering of H_2 and He from a cleaved LiF surface by Estermann and Stern [21] subsequently demonstrated that entire atoms could also behave in this way. The appropriate method of describing physical systems embodying this wave-particle duality was *quantum mechanics*. Two different forms of expression for this framework were developed: matrix mechanics, originated by Heisenberg [22], and wave mechanics, due to Schrödinger [23, 24, 25, 26]. That these are equivalent descriptions was shown by Schrödinger [27], and quantum mechanics was subsequently formulated in general terms by Dirac [28].

There were many consequences of this new description of the world, foremost among them being the probabilistic description of a system's development, which analysed the time-evolution of the probability amplitude ψ for the system to be in a certain state, and the Uncertainty Principle. This stated that conjugate quantities, such as position and momentum, could not simultaneously be known to arbitrary accuracy; there was an intrinsic lower limit on the product of the uncertainties in the knowledge of each. It is immediately clear that this could cause difficulties as regards the definition of chaotic behaviour. If there is some

uncertainty as to the values of a particle's position and momentum, there is some uncertainty as to its position in phase space. A particle may be described as a wavepacket of probability waves, but this occupies a region of phase space, not an infinitesimal point. A single quantum state occupies a region of phase space that has a volume of order h^N, where h is Planck's constant and N is the number of degrees of freedom. Therefore one cannot identify individual orbits in quantum phase space. How can there be extreme sensitivity to initial conditions if those initial conditions are not well defined? Does the probabilistic nature of quantum mechanics imply an uncertainty in the time-evolution of a chaotic system over and above that due to the classical sensitivity of the system to imperfections in knowledge of the initial state? The evolution of wavefunctions is unitary, so the overlap between two states is constant in time. How can this be reconciled with the divergent trajectories that are essential to classical chaos? Where do these difficulties leave the correspondence principle? Such are the questions that are addressed in the field of 'quantum chaos'.

1.3 Quantum chaos?

The first major attempt to bring together the fields of chaos and quantum mechanics was at the 1977 Volta Memorial Conference, entitled, 'Stochastic Behavior in Classical and Quantum Hamiltonian Systems' [29]. The corpus of literature describing the theoretical investigations that have been undertaken since this conference is very extensive. These investigations have focused on the quantum mechanical analogues of classically chaotic systems, in which a quantal manifestation of chaos might be expected. Due to the common occurrence of nonlinearity in classical systems, quantum mechanical systems whose classical analogue exhibits chaotic behaviour are actually more typical than integrable ones. The consensus of the investigations into such systems has been that the characteristics of the quantum and classical forms of behaviour are quite different [30, 31, 32, 33]. Above all, the extreme dependence of the evolution of a system on its initial state is not found in quantum mechanics. Studies to develop methods for quantising classically chaotic systems [30] and to establish quantum signatures of chaos [33] have been carried out, with some success. However, these theoretical analyses are quite different in nature from the more empirical approach adopted in the experimental and numerical investigations described in this thesis, and will not be discussed further. Future theoretical investigations may interpret the observations reported in subsequent chapters of this thesis in the context of these formal approaches to chaotic behaviour in quantum systems [30, 31, 33].

More similar to the thrust of the work described in this thesis have been the investigations in which quantum systems were examined in terms of the evolution with time of dynamical quantities. These include energy, momentum, angular momentum and ionisation probability. The behaviour of these quantities has been found to be quite different from that in the corresponding classical system. For example, the mean kinetic energy of a classically chaotic system has been found

to be, in general, quasiperiodic (and therefore not chaotic) in the quantum analogue. A very important phenomenon that is commonly observed in the quantum analogue of a classically chaotic, periodically driven system is dynamical localisation. An example of such a system is the δ-kicked rotor, which will be discussed in greater depth in Ch. 3. Due to its conceptual simplicity, coupled with its ability to exhibit important characteristic features of nonlinearity and chaos, this has long been a paradigm in classical chaos theory [34]. A particle is subjected to periodic δ-function-like kicks from a potential and these modify the value of the action variable. The change in the action variable due to a particular kick depends sinusoidally on the value of the angle variable at that instant. The generic classical behaviour is that the action variable displays diffusive behaviour; its rms value, for an ensemble of systems with a distribution of initial values, increases as the square root of the number of kicks applied to the system. The quantum system is quite different. For a short time it, too, exhibits diffusive behaviour in the action variable, but beyond a certain time, known as the quantum break time, the rate of increase in the rms value is suppressed relative to the classical system. This rms value subsequently exhibits quasiperiodic behaviour. The distribution of values of the action variable taken by an ensemble of systems is localised, meaning that it essentially fails to broaden with any further kicks. Furthermore, it is exponential in form and symmetrically dispersed around zero (assuming that the initial distribution of values was centred on zero). This is the phenomenon of dynamical localisation, first reported at the Volta conference (see Ref. [29], p. 334) after being discovered in numerical simulations of the quantum δ-kicked rotor. It was subsequently explained by analogy with the phenomenon of Anderson localisation of electronic states in random lattices [35, 36]. As will be discussed in the following sections, the effects of dynamical localisation were first observed experimentally in microwave ionisation of excited hydrogen atoms [37, 38, 39] and thereafter in the field of atom optics [40]. Experimental [41, 42] and theoretical [43] investigations in which these types of quantum system were subjected to noise and decoherence were also carried out in order to observe the modification to the dynamics. Decoherence resulting from interaction with the environment is an essential part of the macroscopic world, in which classical behaviour is generally found. Hence the resulting behaviour of the quantum systems thus perturbed might be expected to be more classical in appearance. This expectation was fulfilled only to a limited extent, and the link made by decoherence between quantum and classically chaotic dynamics is still a subject of debate. This will be discussed further in Ch. 5.

The question of quantum signatures of chaos is still far from resolved, despite the progress over the last 25 years. There is a need for further study of the similarities and differences in behaviour between a quantum system and its chaotic classical analogue. By identifying these, a greater understanding of the characteristics of 'quantum chaos', and of quantum mechanics itself, could be gained. Furthermore, the bulk of the investigation thus far has been theoretical, and so there is a need for experimental investigations of theoretically familiar quantum systems in order to examine the impact of real-life deviations from the idealisations assumed in the theory. Since classical behaviour arises in the real world, exper-

iments on real quantum systems might help to clarify the way in which classical behaviour has its origins in quantum mechanics, and the correspondence between the two descriptions of nature.

1.4 Quantum chaos in excited hydrogen atoms

Perhaps the earliest experimental investigation of a quantum system whose classical analogue has been analysed in terms of chaos was reported in 1974 by Bayfield and Koch [44]. The motivation for the experiment was an investigation of multiphoton ionisation, rather than chaos *per se*. Highly excited hydrogen atoms were subjected to microwave fields of different strengths to observe the multiphoton ionisation probability. At that time the connection between this system and chaos, through the chaotic nature of the classical trajectories of electrons experiencing electric fields of both nuclei and microwaves, had not yet been made. From the early 1980s onwards, however, experiments to investigate quantum systems with chaotic classical analogues were being proposed (see the paper by Ott *et al.* [43] and references therein). The explicit goal was the deepening of the understanding of chaos. Nonlinearity is common in nature, but is often accompanied by complexity that would render the system beyond mathematical modelling and simulation, and hence make the behaviour difficult to interpret physically. To be useful, therefore, the experimental systems being studied needed to be conceptually as simple as possible. The proposals centred on systems that involved the excitation of atomic electrons by oscillating electromagnetic fields. The first scenario was that in which the ionisation of atoms by microwaves, as carried out in Ref. [44], would be studied. The second was that in which the electromagnetic field would be applied to weakly-bound surface state electrons in liquid helium. In each case, it was feasible to model and analyse a system in which an electron moves under the combined influence of a Coulomb field plus an externally applied monochromatic oscillating electric field. In the second of the two scenarios, the problem was 1-dimensional, permitting a reasonably straightforward analysis. In the first, the problem could be made effectively 1-dimensional by preparation of the atoms, prior to interaction with the oscillating field, in an electronic state with a charge cloud that was very extended along the direction of the field. It was shown, however, that the behaviour was essentially unaltered in a more realistic 2-dimensional model [45], so that experiments could still permit a useful comparison with theory.

Since an experimental system in which excited atoms were subjected to microwaves had already been realised [44], it was by this method, rather than that involving liquid helium, that experimental characterisation of this type of quantum system was carried out. A further motivation for effort in this area was that the development and application of the so-called 'Kepler map' [45] made it possible to find a connection between the behaviour of the hydrogen atom in an oscillating electric field and the δ-kicked rotor model, the paradigm in chaos theory that was discussed above and in which dynamical localisation was first identified. A schematic diagram of the experimental procedure used in early investigations of

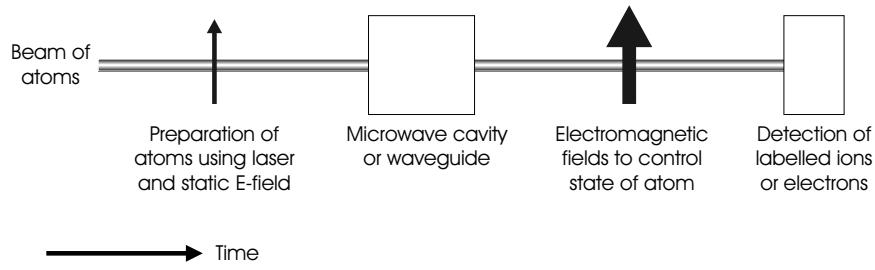

Figure 1.1: Schematic diagram of the method used to investigate the behaviour of excited atoms subjected to an oscillating electromagnetic field.

quantum chaos [37, 38, 39] is shown in Fig. 1.1. The methods in each of these experiments differed slightly in the details, but the essence was that hydrogen atoms in a beam were prepared in a highly excited state. The excitation was carried out by state-selective laser transitions in the presence of a static electric field. This allowed the atoms to be placed in a state for which the principal quantum number n had a value in the range 45 to 98. The excited atoms then passed through a waveguide or cavity in which a microwave field of controllable strength (and, in Refs. [37, 39], frequency) was present. An atom's interaction with the microwave field could alter the value of n, or even ionise it altogether. The beam of atoms then left the microwave chamber. Subsequent state-selective static field or microwave ionisation, followed by detection of the free electrons or ions thus produced, allowed the distribution of the atoms' values of n following the interaction in the cavity/waveguide to be established.

In the δ-kicked rotor, quantum behaviour is characterised by suppression of the classical diffusion in the action variable. In the case of excited hydrogen atoms exposed to an oscillating electromagnetic field, the action variable is $\hbar n$. Since the Kepler map allowed a formal connection to be made between these two systems, the expectation was that the quantum mechanical hydrogen atoms should exhibit a reduced spreading in the values of n after interaction with the field. The quantity that determined the character of the dynamics of the system, and whether quantum suppression should be important, was the scaled excitation frequency ω_0. This was the microwave frequency ω divided by the bound electron's classical orbit frequency, the so-called Kepler frequency $\omega_{\rm K}$. When the principal quantum number was n, this frequency was given by $\omega_{\rm K} = m_{\rm e}e^4/[(4\pi\epsilon_0)^2(n\hbar)^3]$, where $m_{\rm e}$ is the mass of an electron. The value of ω_0 could be varied by changing either ω or the initial value of an atom's principal quantum number, n_0. Theoretical investigation [45] indicated that the behaviour of the quantum system should be markedly different from that of the classical for $\omega_0 > 1$. The effect of the field on the atoms could be observed by measuring the distribution of the final values of n for a class of atoms that had a certain value of n_0. Dynamical localisation would be indicated by a distribution that was exponential in form and did not broaden as the duration of the exposure to the microwave field increased beyond the quantum break time. Another measure of the atoms' response was the strength of the field required to

ionise a certain fraction of the atoms, say 10%. In the event of quantum suppression of classical diffusion in n, ionisation should become more difficult and hence the field strength for 10% ionisation should rise above the classical value.

The results of the investigations in Refs. [37, 38, 39] indicated that the diffusion in the action variable was indeed suppressed in the experimental, quantum system relative to that in the classical system. In Ref. [37], with $n_0 = 72$ and several different values of ω_0 between 0.7 and 1.1, the distributions of the atoms' values of n after interaction with the microwaves were found to be exponential. The widths of the distributions were found to be consistent with those which would be expected, based on numerical simulation, when dynamical localisation had occurred. However, since the microwave pulses were not long enough to allow evolution of the system significantly beyond the expected value of the quantum break time, and since the distributions expected for both quantum and classical behaviour were exponential in form, it was not possible to be sure that cessation in diffusion of the action variable had occurred. A longer microwave pulse duration would be required to allow dynamical localisation to be conclusively demonstrated. Alternatively, experiments with a larger value of ω_0, therefore further in the distinctively quantum regime that exhibits different behaviour from the classical system, could provide conclusive proof of quantum suppression of diffusion. In Ref. [38], larger values of ω_0 up to 2.8 were used, and the microwave electric fields required to ionise 10% of the atoms were measured. The value of ω_0 was changed by introducing atoms with a different value of n_0 into the microwave cavity; the microwave frequency was kept constant. 3-dimensional numerical simulations of the classical analogue of the experimental system were also performed and the results compared with those measured experimentally. For $\omega_0 < 1$, the results of the experiment agreed well with those of the simulation, but this agreement was poorer in the regime $1 < \omega_0 < 2$. For $\omega_0 > 2$, the experimental and simulation results were incompatible: the experimental values of the electric field strength required to produce 10% ionisation were systematically higher than those of the classical system. This was evidence of quantum suppression of diffusion in the action variable. However, this experiment was not able to distinguish between two possible explanations for this suppression of diffusion. The first is dynamical localisation; the second is the existence of structures in phase space (cantori) that hinder quantum diffusion when the classical phase space area that leaks through them in each microwave period is less than $\hbar$ [46]. Each explanation was consistent with the behaviour observed in Ref. [38]. In Ref. [39], values of ω_0 up to 2.5 were applied to the atoms. In this experiment, ω_0 was varied by changing the values of both n_0 and ω. As in Ref. [38], the electric field required to ionise 10% of the atoms was measured, and compared with numerical simulations of both the classical and quantum systems. The experimental results were consistent with those of Ref. [38] in that they disagreed with the classical model for $\omega_0 > 2$. The two explanations of the quantum suppression of diffusion gave predictions for the variation with ω_0 of this 10% electric field that could be distinguished. The experimental results showed that for $\omega_0 > 2$ this field strength rose linearly with ω_0, and the rise was consistent with that expected when dynamical localisation occurs, and inconsistent with that expected when cantori

inhibit the quantum diffusion. Thus dynamical localisation was shown to be the explanation for quantum suppression of diffusion in the action variable, the first time that this had been experimentally verified.

These experiments, and their predecessors, in which microwave pulses were applied to excited hydrogen atoms constituted the first systematic experimental investigation of the behaviour of a quantum system whose classical analogue is chaotic. The system was sufficiently simple to permit comparison with theoretical predictions and the results of numerical simulation. The dynamics of the system could be connected by the Kepler map to those of the paradigmatic δ-kicked rotor, increasing the generality of the results, which proved that the classical diffusion in the action variable is suppressed in a quantum system. However, it would be desirable to find an experimental system that were more obviously a realisation of the δ-kicked rotor, preferably in 1-dimension. This would allow detailed comparison with the extensive body of theory, and the low dimensionality would yield considerable simplification of the analysis and simulation. The advances in the field of *atom optics* over the last 20 years, which have led to new techniques for the trapping, cooling and manipulation of atoms with lasers, have allowed just such a realisation to be achieved. Some of the important experimental techniques in this field, and the way in which they permitted the observation of dynamical localisation [40] and a realisation of the δ-kicked rotor [47], will be discussed in the following sections.

1.5 Atom optics

The fact that atoms are neutral means that they are much more difficult to manipulate than charged entities, such as electron and ions. A uniform electric field does not apply a force to an atom, and so more complicated schemes that make use of an atom's internal structure must be used for this purpose. Due to their size and charged structure, atoms readily scatter in a material. This means that the crystal diffraction techniques often used to manipulate neutron beams [48] are not easily applicable to atoms. Atoms do, however, have certain advantages over the other types of particle just mentioned because of their neutrality and internal structure. The insensitivity to local fields, and particularly to local field inhomogeneities, means that atoms' de Broglie waves are less susceptible to random phase shifts than those of charged particles, thus facilitating interferometry. The internal structure of atoms means that they can be stimulated to undergo transitions in the presence of an electromagnetic field, accompanied by the absorption and emission of photons. When an atom absorbs a photon, that photon's momentum is imparted to the atom. Similarly, when the atom emits a photon it recoils with a momentum equal and opposite to that of the photon. The multitude of allowed atomic transitions means that readily available, intense laser sources of visible or near-infrared light can be used to impart momentum to atoms and hence to trap, cool and precisely manipulate them.

Some important advances in the field of atom optics will now be reviewed.

These will encompass techniques of atom trapping and cooling, guiding, focusing, reflection and beam-splitting. The focus of this summary will be on techniques involving light, since that is the type of technique used for the experiments in this thesis. There are additional techniques, not discussed here, using static electric and magnetic fields (sometimes in tandem with light) or nanofabricated material structures to control the trajectory of atoms. A comprehensive guide to the whole field of atom optics is contained in Ref. [49].

The deflection of an atomic beam by light was first observed by Frisch in 1933 [50]. However, since the intensity of light from a thermal source is so low, it was not until the laser was invented that sufficient momentum could be imparted to atoms by light to allow them to be usefully manipulated. In 1985, Chu *et al.* [51] used a configuration in which sodium atoms were irradiated with counter-propagating beams of laser light, red-detuned from an allowed atomic transition, to lower the temperature of the atoms to around 240μK. This was the first experimental demonstration of the technique of Doppler cooling, in which an atom absorbs a photon from the beam against whose propagation direction it is moving (and whose light, therefore, is Doppler shifted closer to resonance) and re-radiates in a random direction. When averaged over many such events, the effect on the atomic momentum is dissipative, yielding a net reduction in the atomic momentum in the direction against the beam. Use of 6 mutually perpendicular beams reduces all components of the atoms' velocity and therefore results in cooling. Atoms cooled in this way were named 'optical molasses' [51]. Effects of the polarisation-gradient in the light field were found, fortuitously, to allow cooling below the limit that was predicted on the basis of competition between the cooling effect of the beams and the heating effect due to random scattering of the atoms from spontaneous emission. These effects allowed atomic temperatures in the region of 10μK to be achieved, and are discussed in a review of laser manipulation of atoms and particles written by Chu in 1991 [52].

Building on this principle, imposition of a magnetic field gradient in the region of the atoms allowed them to be trapped by the light force. The field gradient resulted in a position-dependent Zeeman shift in the atoms, and the use of circularly polarised light in the counter-propagating beams meant that the probability of light absorption varied with atomic position as well as velocity. By judicious choice of laser frequency, an atom that moved away from the zero of magnetic field, which coincided with the intersection point of the 6 laser beams, could be shifted closer to resonance with the light beam(s) propagating in the direction opposite to its displacement. Thus a restoring force would return the atom to the zero-field point, allowing it to be confined as well as cooled. This was the basis of the magneto-optic trap (MOT), first achieved by Raab *et al.* in 1987 [53]. Sodium atoms were cooled to around 600μK and confined to a region less than 0.5mm in diameter. An ensemble of trapped and cooled atoms constitutes a convenient source that allows further experiments to be performed using the atoms. A review of techniques of atom trapping and cooling is contained in Ref. [54], and an excellent pedagogical text covering this field has now been written [55].

When an atom lies in an electromagnetic field, the field polarises the atom

and so there is an interaction between the induced electric dipole moment and the local electric field. An atom in a light field therefore undergoes an energy shift, the 'light shift', discussed further in Appendix A and Ref. [56]. Spatial variation in the intensity of a light field causes an atom to experience a potential gradient and therefore a force, the 'dipole force', whose direction is determined by the sign of the light's detuning from an allowed transition of the atom. For red-detuning, an atom seeks the strongest light field, whereas atoms in blue-detuned light are weak field-seeking. The forces arising from non-uniform light fields have been used to manipulate atoms. A red-detuned laser beam with a Gaussian intensity distribution applies an approximately parabolic potential to atoms. As this results in focusing of a co-propagating atomic beam, such a laser can be used as a lens. This focusing was first demonstrated with a beam of sodium atoms in 1978 by Bjorkholm *et al.* [57]. The potential well in the centre of a red-detuned Gaussian beam also facilitates the trapping of atoms. Trapping of molasses-cooled sodium atoms in a cylinder 210μm long and 2.5μm in diameter by use of the dipole force in a single, focused, red-detuned laser beam was first performed in 1986 by Chu *et al.* [58]. This procedure offers an alternative to the magnetic field gradient trapping technique described above. Since an atom incident on a blue-detuned evanescent light field would experience a progressively stronger repulsive force the deeper it penetrated into the field, this could be used as an atomic mirror. Provided the incident atomic velocity was not too large, the atom's velocity would eventually be reversed by the light field. Reflection of sodium atoms in this way was achieved experimentally in 1988 by Balykin *et al.* [59], with a reflection coefficient of nearly 100%. The sinusoidally varying intensity in a standing wave of laser light is experienced as a spatially periodic potential by atoms. This means that it can cause diffraction or focusing of the atoms' de Broglie waves, and therefore constitutes another technique of atomic manipulation. A standing light wave was used to diffract a beam of sodium atoms by Gould *et al.* in 1986, and applied to the focusing of a beam of helium atoms in 1992 by Sleator *et al.* [60]. The experiments described in this thesis involved the exposure of caesium atoms to a standing wave of laser light, and its diffractive effect is central to the observed phenomena that will be discussed in subsequent chapters.

Atom optics has permitted great advances throughout the 1990s in the field of atom interferometry, which relies on the precise manipulation of atoms in order to coherently split and recombine atom waves. This has led to progress in the measurement of gravity, rotations, atomic properties such as polarisability and time, by atomic clocks. For a review of atom interferometry and an assessment of its future prospects, see Refs. [61, 62, 63]. One area of current technological research is into the construction of a robust apparatus that could be used for guiding atoms, whether thermal (as in a MOT) or Bose-condensed (see below). This could lead to miniaturisation and increased portability of the apparatus for atom interferometry. This type of improvement will be essential if the precision that atom interferometry promises is to become available for practical applications such as geophysical surveying, navigation and space-based clocks. It may also find use in manipulation of the output of an atom laser [64] for lithography or

other applications as yet unforeseen. This guiding can be achieved by the force that results from application of magnetic field gradients to the atoms. Fibres with current-carrying wires embedded in their walls [65] and microfabricated current-carrying wires on the surface of chips [66] have been experimentally shown to allow magnetic guidance of atoms, or even an atomic beam splitter [67]. Purely optical techniques can also be used for guiding atoms. In Ref. [68], blue-detuned laser light was injected into the glass walls of an optical fibre. This yielded an evanescent light field in the core, to which rubidium atoms were subjected. As in the case of the atomic mirror described above [59], this repelled atoms from the walls of the fibre, thus allowing them to be guided along a 6cm stretch of fibre with a flux of over 400 atoms per second. The relative ease with which atoms can be guided in this way may prove to be a useful tool for the interferometric applications previously indicated.

A field of great interest in which rapid and important progress has been made over the past decade is in the application of atom optics to the creation of a Bose-Einstein condensate (BEC) of alkali atoms. This is an exceptional state of matter in which there is phase coherence across an ensemble of bosons, all of which are in a single quantum state. The ensemble is described by a single wavefunction, and hence its spread in position and momentum are related by Fourier transformation. The interactions between the atoms are such that the ensemble behaves as a superfluid, thus making the system also interesting from a condensed matter viewpoint. The extremely narrow momentum distribution, and the coherence properties of the condensate, make it eminently suitable for use in interferometry and studies of phase and entanglement. Its superfluid nature has allowed extensive investigation of rotational behaviour and vortices. BEC in alkali atoms was first created in 1995 by the group at JILA, Colorado, using ultra-cold rubidium atoms [69]. This was shortly followed by the achievement of a BEC of sodium atoms by the group at the Massachusetts Institute of Technology [70]. The low atomic temperatures and high densities made attainable by atom optical techniques and evaporative cooling were of critical importance to the success of these and subsequent experiments. Unfortunately, any assessment of the state of the art in studies of BEC becomes immediately out of date, such is the dynamism of the field. However, a review of the techniques and advances that led to the attainment of BEC in alkali atoms, and of the research into its properties that quickly followed, is contained in Ref. [71]. Slightly more recent proceedings of a summer school and workshop on Bose-Einstein condensates, atom lasers, atom optics, and atom interferometry held in 2000 [72] do provide a comprehensive and detailed guide to the physical principles, theoretical work and experiments in progress in this field. An in-depth survey of the different aspects of current research into ultracold matter was published in an 'Insight' section of *Nature* in March 2002 [73].

The outline of atom optical techniques above encompasses elements that can act as a source, a lens, a mirror and a beam-splitter for atomic de Broglie waves. Other procedures that can be used to divide the amplitude of atom waves, thus acting as beam-splitters, also exist. These allow precisely controlled momentum

impulses to be imparted, with varying levels of efficiency, to laser-cooled atoms and are summarised in Sec. 6.1.1. They are all believed to be coherent techniques, maintaining the phase information in an atomic state, though this essential attribute for interferometric applications has yet to be demonstrated experimentally in some cases. Lenses, mirrors and beam-splitters are familiar elements in the manipulation of light, so the description 'atom optics' for all the techniques described above is appropriate. Essentially, the traditional roles of light and matter have been reversed, so that instead of light being manipulated by optical elements composed of matter, now matter waves are being controlled by analogues of these elements, created using light.

The importance of the discoveries made in these fields has been recognized twice by the Nobel Committee in recent years. The 1997 prize was awarded to S. Chu, C. Cohen-Tannoudji, and W.D. Phillips 'for development of methods to cool and trap atoms with laser light', without which much of the subsequent work in atom interferometry and Bose-Einstein condensation would have been impossible. The significance of the creation of a BEC of laser-cooled atoms, and the experimental investigations that followed, was underlined when the 2001 prize was awarded to E.A. Cornell, W. Ketterle, and C.E. Wieman 'for the achievement of Bose-Einstein condensation in dilute gases of alkali atoms, and for early fundamental studies of the properties of the condensates'. The proximity of two such awards to workers in the same field emphasises what an exciting time this is in atomic physics.

1.6 Investigations of quantum chaos using atom optics

The techniques of atom optics allowed the observation of dynamical localisation in a conceptually simpler system than that involving microwaves and excited hydrogen atoms, described in Sec. 1.4. This was achieved [40] by the group led by M.G. Raizen, based in Austin, Texas. The experimental arrangement will not be described in great detail because it was broadly similar to that used for the experiments in this thesis, which is extensively discussed in Ch. 2, but it is shown schematically in Fig. 1.2(a). The quantum system under test was an ensemble of laser-cooled sodium atoms. Following release from a MOT, these atoms were subjected to a spatially periodic potential realised by the application of a standing wave of laser light. To create the standing wave, the output of a dye laser was split and the two resulting beams were aligned so as to counter-propagate. It should be noted that this standing wave was horizontally oriented, unlike the vertical beams used for the experiments described in the chapters to follow. The fact that the atoms had been trapped and cooled in a MOT allowed them to be acted upon for a relatively long time by the standing wave, and in a much more convenient configuration than would be required if the atoms were in a supersonic beam. As shown in Fig. 1.2(a), one of the counter-propagating beams passed through an electro-optic modulator that could vary its phase and, therefore, the position of the spatial profile of the standing wave. The voltage to the EOM was varied sinusoidally with

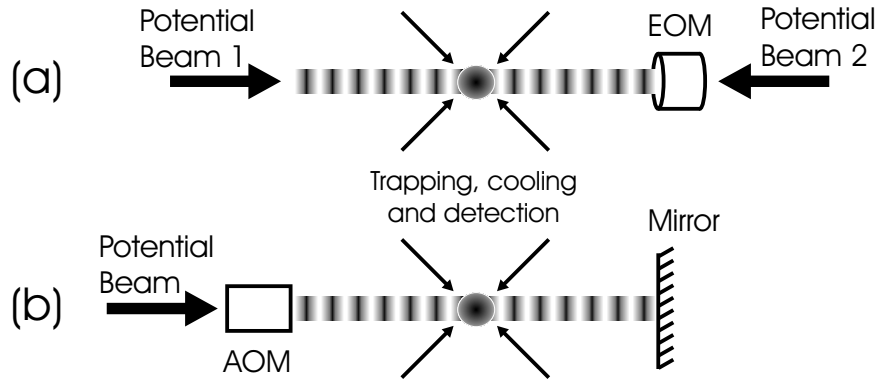

Figure 1.2: Schematic diagrams of (a) the experimental arrangement used to observe dynamical localisation in Ref. [40] and (b) the arrangement used to achieve an experimental realisation of the quantum δ-kicked rotor in Ref. [47]. In (a), the EOM was used to vary the relative phase between the counter-propagating potential beams, derived from the same laser output, therefore varying the position of the spatial profile of the standing wave. In (b), the AOM was used to control the intensity of light in the standing wave, thus allowing it to be pulsed.

time so that the atoms experienced a potential whose position oscillated with a controllable amplitude. Following application of the standing wave, free expansion of the atoms occurred. Molasses cooling light was then re-applied to the atoms to allow their spatial distribution to be measured by using a CCD camera to monitor their fluorescence. Knowing the time of free expansion allowed the atoms' momentum distribution immediately following the application of the standing wave to be calculated. It had been shown theoretically [74] that the dynamics of a system subjected to a time-varying potential of this type could, in certain dynamical regimes, approximate that of the δ-kicked rotor. Therefore dynamical localisation of the diffusion in the action variable, which in this case was atomic momentum, would be expected. This was indeed observed; the initial Gaussian distribution of atomic momenta became exponential in form. The variation in the width of this exponential distribution with the amplitude of modulation of the potential's position was found to match closely that predicted by theory [74]. Thus dynamical localisation was observed for the first time in cold atoms.

Although the system shown in Fig. 1.2(a) allowed the observation of dynamical localisation, it did not constitute a realisation of the δ-kicked rotor. The effect on the atoms of the modulation in the position of the potential could only approximate that of a pulsed potential delivering δ-function-like kicks. The next step was to realise a closer approximation to the ideal δ-kicked rotor by applying a pulsed, spatially periodic potential to the atoms. This was also achieved by the Austin group, using a system very similar to that used in their observation of dynamical localisation. This is shown schematically in Fig. 1.2(b). Following release from the MOT, the cold sodium atoms were subjected to a single beam of laser light that was retroreflected by a mirror so as to create a standing light wave. The intensity

in this beam was controlled by an acousto-optic modulator (AOM) that allowed the beam to be pulsed on. The potential experienced by the atoms had, therefore, a time-dependence similar to a series of δ-functions, and thus an experimental version of the δ-kicked rotor was realised. Of course, this was not an ideal δ-kicked rotor, the most important difference being that the pulses had a finite duration. The temporal full width at half maximum (FWHM) light intensity was 100ns, and the rise and fall time was 25ns. Nevertheless, the system did constitute an excellent approximation to the δ-kicked rotor, and allowed further observation of dynamical localisation. The atoms had a momentum distribution that was Gaussian after cooling, but after 8 pulses this had become exponential and showed no further significant change as up to 42 further pulses were applied. A plot of the variation of the mean kinetic energy of the atoms with the number of pulses applied showed a sub-linear growth, whose rate decreased as the number of pulses increased. Classical diffusive behaviour of the action variable would yield a linear growth in this mean kinetic energy with pulse number, and hence the experimentally observed behaviour demonstrated again the quantum suppression of classical diffusion.

The achievement of an atom optical realisation of the quantum δ-kicked rotor opened up a new vista of opportunities for experimental investigation of this paradigmatic system. The similarities and differences in the behaviour of this quantum system as compared with that of its chaotic classical counterpart, and the fact that this behaviour is experimentally observed rather than numerically modelled, can yield information regarding the properties of quantum mechanics and the ways in which quantum-classical correspondence may arise. It becomes possible to test theoretical predictions and thus verify the current understanding of quantum mechanics. Experiments also provide an opportunity to examine the possible role of decoherence, an unavoidable aspect of any real-life system, in this correspondence, and the sensitivity of quantum behaviour to its effects. The culmination of these efforts will be to attach a clear meaning to 'quantum chaos', and to understand how the complex classical phenomena associated with chaos have their origin in quantum systems. Atom optical experiments in this context have been performed since 1995 in Austin, and, using a similar experimental arrangement, in Auckland [42]. The work of both groups is important and will be referred to in subsequent chapters.

1.7 Outline of thesis

In the experiments discussed in this thesis, the vertical orientation of the standing wave allowed gravity to play an important role in the system's dynamics. The investigations therefore encompassed studies of both the standard δ-kicked rotor and the so-called δ-kicked accelerator, in which the rotor evolves under the influence of gravity. In Ch. 2, the apparatus with which the experiments were performed is described. In Ch. 3 the behaviour of the quantum δ-kicked rotor, as observed both experimentally and through numerical simulation, is discussed and comparison is

made with that of its classical analogue. In Ch. 4, the quantum δ-kicked accelerator is characterised by experimental and numerical investigation. Comparison is made with the behaviour of its classical analogue, and the striking phenomenon of the quantum accelerator mode is discussed and analysed. In Ch. 5, the way in which decoherence affects the evolution of the quantum δ-kicked systems is examined and the extent to which this disruption to the evolution of the wavefunction may be said to make the system more classical is considered. In Ch. 6, possible applications of the phenomenon of quantum accelerator modes to manipulation of atoms, measurement and investigation of quantum chaos are examined and evaluated. Ch. 7 concludes the thesis with a brief summary of the results and some comments on the direction of future investigations.

Chapter 2

Experimental setup

The experiments described in this thesis were carried out using a system of laser-cooled caesium atoms. The atoms, initially present as a low pressure vapour in an ultra-high vacuum system, were trapped and cooled by off-resonant laser light in a magneto-optic trap (MOT). Following molasses cooling, the laser light was removed and the atoms fell freely under gravity. They then experienced the spatially-varying potential of a vertical standing wave of high-intensity laser light that was applied as a series of pulses. If desired, the atoms could be placed in a superposition of hyperfine states by the application of a $\pi/2$-pulse of microwaves prior to, or in the middle of, the pulses of the standing wave. A further $\pi/2$-pulse of microwaves, with a variable phase relative to the first, could be applied following the standing wave pulse train. The position of the standing wave profile relative to the atoms could be controlled by a crystal phase modulator through which the standing wave passed. Finally, the momentum distribution of the atoms was measured by a time-of-flight (TOF) technique. This chapter describes the experimental arrangement, and the method of detection of the atoms.

2.1 Vacuum system

The vacuum system consisted of three distinct chambers, as shown in Fig. 2.1, that were coupled together by flanges that enclosed copper gasket seals. The upper section was a quartz cell of square cross-section, whose outer dimensions were 17 mm by 17 mm by 55 mm and whose walls were 1.5 mm thick. This allowed optical access to the system so that the MOT could be created and the vertical standing wave of light applied. The middle chamber was a custom-made ten-way cross, also made from 314 grade stainless steel. The presence of this section was a relic of previous experiments performed with the same system, and so its geometrical characteristics were not in any way optimised for the experiments described in this thesis. If anything, they made them more difficult as the greater volume of the system and complexity of the shape limited the vacuum that could be attained. The

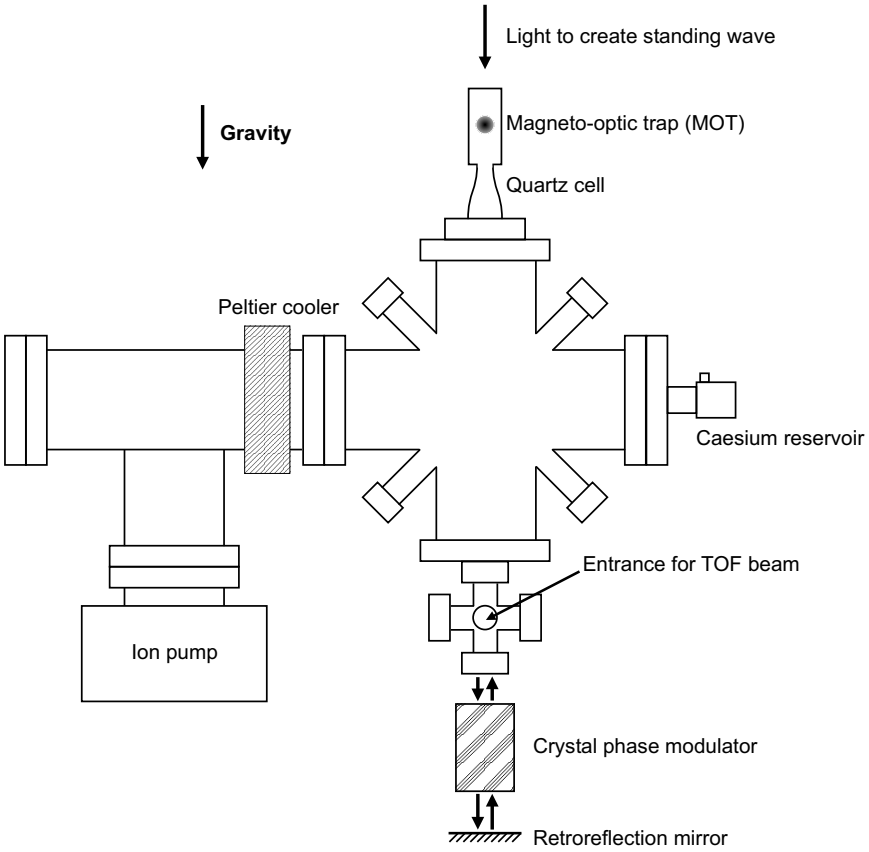

Figure 2.1: Vacuum system

lower chamber was a standard six-way cross made from 314 grade (A2) stainless steel by Vacuum Generators. It contained standard viewports (Vacuum Generators ZVPZ64) that allowed laser light to be passed through. The viewport at the base of the system allowed the vertical beam to pass out of the system before being retroreflected to create the standing wave. The viewports at the sides of the lower chamber allowed a sheet of laser light to be shone through and used for the time-of-flight (TOF) measurement system for the atomic momenta. A reservoir containing 1g of 99.98% pure caesium (bought from Alfa Aesar) was attached to the middle chamber of the system and was separated from the vacuum region by a valve. The caesium had been placed in the reservoir by a procedure in which an ampoule containing caesium was broken and the liquid caesium poured into the reservoir. This was carried out in a glove box containing an argon atmosphere to prevent oxidation of the caesium.

The ultra-high vacuum needed for the experiments was achieved using the standard procedure of a 'bake out'. The system was exposed to a steady, high temperature for an extended period of time while a turbo pump was used to achieve the best possible vacuum. After removal of the external heaters, further pumping with the turbo pump and an ion pump was carried out. The valve between the caesium reservoir and the vacuum system was kept closed during the bakeout

process. In the initial bakeout, radiators surrounded the vacuum system, and a heating wire was coiled around it. The baking procedure lasted four days, over which time the temperature was ramped up to $\sim 140^{\circ}$C over a period of about 30 hours, held at that temperature for about 24 hours then left to cool down overnight after the removal of the heaters. An additional bakeout then took place in which the temperature was gradually increased up to $\sim 150^{\circ}$C over about 20 hours and held there overnight. After the current to the heaters had been reduced so that the system cooled to $\sim 30^{\circ}$C, the pressure in the system, as measured by an ion gauge in the central chamber, was 7×10^{-9} mbar. The ion pump was then switched on, and the turbo pump continued to run. The ion pump was a Varian Diode VacIon Plus 25 that could pump at a rate of 25ℓ/s and was controlled by a Varian MiniVac controller. After three days of pumping with both the turbo and ion pumps, the pressure had fallen to 4×10^{-9} mbar. The caesium reservoir was then opened to allow caesium vapour to diffuse throughout the system. This caused a rise in pressure, and over the two weeks for which the caesium was allowed to diffuse the turbo pump was kept running in addition to the ion pump. The turbo pump was then removed, while the ion pump was kept running constantly. Between the ion pump and the main body of the system was a Peltier cooler that was used to cool this region of the system down to a temperature of around 0°C. Thus any caesium vapour in the vicinity would condense and adhere to the inner sides of the vacuum system, rather than coming into contact with the ion pump itself. This was to avoid the coating of the electrodes in the ion pump by caesium, an effect which could lead to the short-circuiting of the pump and hence malfunction. For all the experiments described in this thesis, the pressure in the system was of the order of 10^{-8} mbar.

2.2 Magneto-Optic Trap (MOT)

The caesium atoms were trapped and cooled using a six-beam magneto-optic trap (MOT) configuration [53, 75]. A cross-section of this part of the system is shown in Fig. 2.2. Note the definition of the axes, as this convention will be used throughout this thesis. Trapping occurred at the point where the overlap of the six beams of laser light coincided with the zero of the magnetic field produced by the trapping field coils. To achieve further cooling of trapped atoms, the trapping magnetic field was removed, the intensity of laser light was reduced and the red-detuning of the light from an allowed transition of the caesium atom was increased. Atoms were released from the trap by removing the light altogether. The various elements of the MOT will now be discussed in detail.

2.2.1 Magnetic fields

Two parallel coils, whose currents flowed in opposite directions, created a spatially-varying magnetic field in the region of the vacuum system enclosed by the quartz cell. Each coil carried a current of 1.5 A, consisted of 100 turns and had a radius of

2.3 cm. The separation in the y-direction between the coils was 4 cm. These coils created a magnetic field whose gradient at the mid-way point between the coils had a theoretical value of 23 G/cm. Measurements made using a Hall probe, though imprecise due to the size of the probe itself, were consistent with this value. Positioned around the quartz cell were three pairs of large Helmholtz coils (not shown in Fig. 2.2), each of rectangular cross-section and consisting of 20 turns, whose function was to counteract the Earth's magnetic field. The x-axis coils carried a current of 9 mA, measured 170 mm by 175 mm and were separated by 170 mm. The y-axis coils carried a current of 24 mA, measured 200 mm by 205 mm and were separated by 175 mm. The z-axis coils carried a current of 348 mA, measured 300 mm by 305 mm and were separated by 200 mm. The initial minimisation of the magnetic field at the position of the trapped atoms was achieved by adjusting the currents in the Helmholtz coils so as to minimise the temperature (*i.e.* the momentum width) of the atomic cloud. Subsequently, the currents were adjusted until a phenomenon that is adversely affected by a non-zero value of this field, such as a quantum accelerator mode (see Ch. 4) was best observed. The magnetic field experienced by the atoms after the trapping coils were switched off was measured using microwaves, as described in Sec. 2.7, and was found to be 10 mG. This should be compared with the local value in Oxford of the Earth's gravitational field, which is (484.3 ± 0.5) mG with a magnetic inclination of 66.73° [76].

2.2.2 Light

The MOT was realised using three intersecting retroreflected beams of circularly polarised laser light as shown in Fig. 2.2. Two of the beams were in the xz-plane, with an acute angle of intersection that was approximately 60°. The third beam was directed along the y-axis. Each beam was directed towards the quartz cell and, after passing though it, traversed a $\lambda/4$ plate. The beam was then retroreflected, passing again through the $\lambda/4$ plate before re-entering the system. Thus an arrangement consisting of three pairs of counter-propagating, circularly polarised beams of light was achieved. The intensity of the beams in the xz-plane was 5.0 mW/cm^2, while that of the y-beam was 3.6 mW/cm^2; the diameter of each beam was approximately 1.5 cm. The measurement of laser powers in the experiment was performed using a Coherent LaserMate-Q power meter (accurate to 3.5%). For powers of more than 50 mW (*e.g.* the light creating the standing wave, see Sec. 2.3), a 1000:1 attenuator was placed in front of the sensor of the power meter.

The light used for trapping the atoms was 15 MHz red-detuned from the ($F = 4 \rightarrow F'' = 5$) cycling D2 transition ($6^2S_{1/2} \rightarrow 6^2P_{3/2}$), which is shown in Fig. 2.3. To prevent the atoms from being optically pumped into the $F = 3$ level and then lost from the trap, repumper laser light, which was resonant with the ($F = 3 \rightarrow F'' = 4$) D2 transition, was co-propagating with the light in one of the xz-beams. Its intensity was 0.7 mW/cm^2. In the presence of the trapping magnetic field gradient of 23 G/cm, the trapping light yielded a MOT which had a spatial distribution that was approximately Gaussian, with a full width at half-maximum

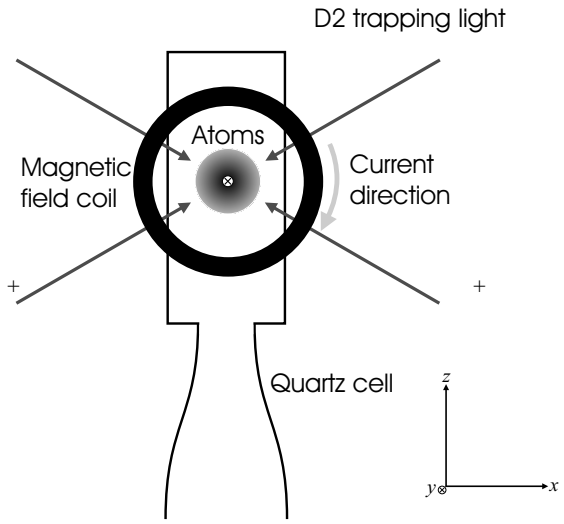

Figure 2.2: Magneto-optic trap

(FWHM) of ~ 1 mm. To cool the atoms to the optical molasses state, *i.e.* to reduce the momentum width of the distribution, the red-detuning of the light from the $(F = 4 \rightarrow F'' = 5)$ transition was increased to 75 MHz and the intensity of the light was reduced to 15% of the value used for trapping.

Both the trapping/cooling light and the repumping light were produced by laser diodes located on a separate optical table from that of the main vacuum system in which the atoms were trapped and the experiments performed. This was for greater experimental convenience as a considerable number of optical elements were needed to ensure the laser light was delivered to the system at the required frequency and with the correct timings. An optical table devoted to the lasers and the optical elements downstream afforded sufficient space for easy deployment of the optics. Polarisation-preserving optical fibres (Point Source, model FDS AP5K850,2,2) then guided the light from the laser table to the vacuum system table to create the MOT and perform experiments.

For the trapping and cooling, a master-slave laser arrangement was used so that sufficient optical power could be obtained. This is shown in Fig. 2.4. The injection of light from the frequency-locked master laser into the slave forced the slave output to be at the same frequency as that of the master output, *i.e.* the slave was 'injection-locked'. The master laser was an extended cavity grating laser (SDL5412) in which the diffraction grating served the purpose of stabilising the laser by selecting a single longitudinal mode. The laser was powered by a low-noise laser diode driver (model EW1034, built in-house) at a current of 76 mA and was thermally stabilised by two Peltier coolers, one on the laser chip itself, controlled by a Newport 325 diode temperature controller, the other between the brass and Dural bases supporting the laser. The latter Peltier cooler was controlled by an in-house-built controller (model EW1231). The power output of the master laser was 20 mW in a collimated beam. Coarse alteration of the frequency of the master light

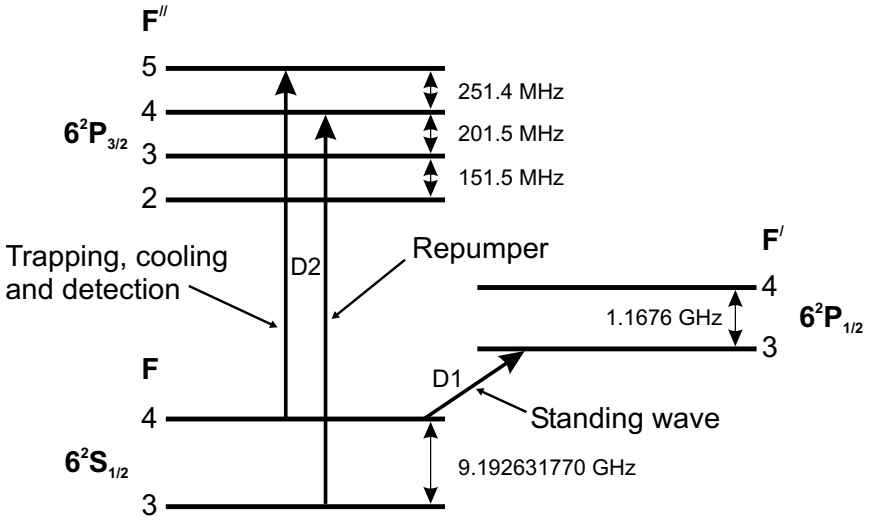

Figure 2.3: Energy levels of the caesium atom

could be accomplished by changing the voltage to the piezoelectric crystal (made from lead zirconate titanate, known as PZT) on which the grating was mounted, while fine variation was performed by altering the current supplied to the laser.

The master laser was locked to the ($F = 4 \rightarrow F'' = 5$) D2 transition by a saturated absorption technique [77]. In order to generate an error signal for locking, a signal generator was used to provide a 40 kHz modulation of the current to the laser diode and hence in the laser frequency. This modulation frequency was very low compared with the line width of the transition, 5.22 MHz. Following passage of master light through a caesium cell in a pump-probe arrangement, see Fig. 2.4, a photodiode was used to measure the time-variation of the absorption of the probe beam. The Doppler profile, on which the peaks in the absorption due to transitions in stationary atoms were superimposed, was subtracted by using the absorption signal of another probe for which there was no counter-propagating pump beam. The time variation of the photodiode signal was at 40 kHz, and this signal was mixed with a reference signal from the signal generator. The laser was locked by altering the laser current and the orientation of the grating so that the time-averaged output of the mixer, after passage through a low-pass filter and an integrator, was kept at zero. Fast feedback to the laser was achieved by altering the current, slow feedback by altering the voltage to the piezoelectric crystal. Once locked, the master laser would usually remain at the correct frequency for several hours (barring any sudden disturbances in the laboratory). From the fact that altering the detuning of the trapping light by 1 MHz had a discernible effect on the size of the trap and the temperature of the atoms within it, the linewidth of the locked laser was believed to be less than 1 MHz, though this was not explicitly measured. It was certainly narrow enough to cause no difficulties in carrying out the experiments described in this thesis.

The output of the master laser was used to provide light for both injection to

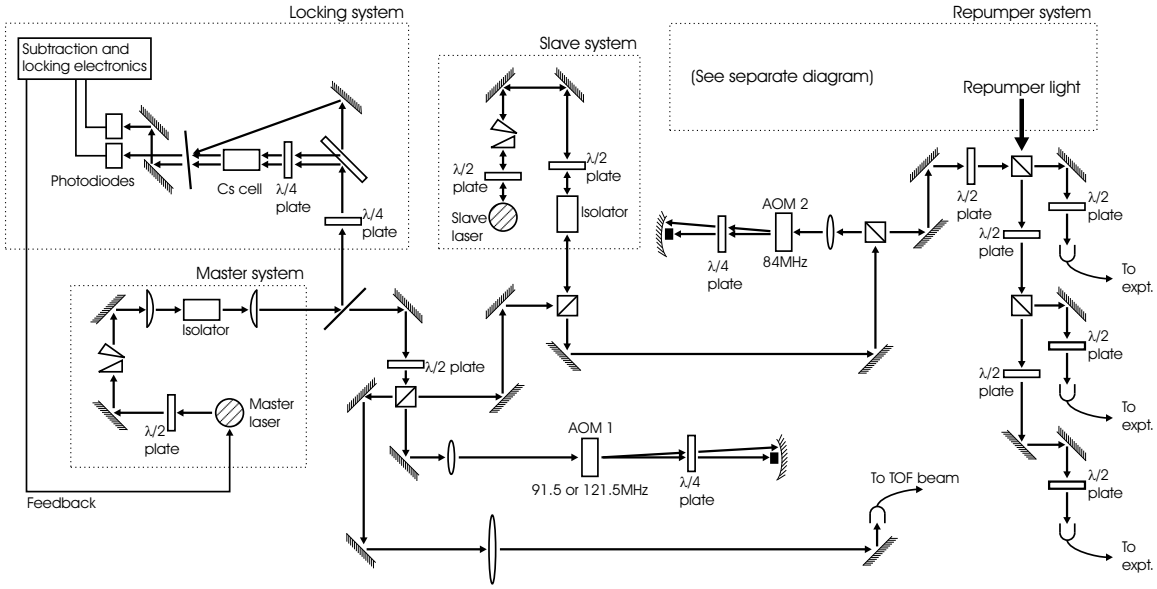

Figure 2.4: The optical table arrangement for the production of light of the correct power and frequency from the master and slave diode lasers.

the slave laser, and the time-of-flight (TOF) detection of the atoms (see Sec. 2.6). The TOF light was required to be resonant with the ($F = 4 \rightarrow F'' = 5$) D2 transition, while the light from the laser for trapping and cooling had to be red-detuned by either 15 MHz or 75 MHz. To satisfy these requirements, a small amount of light (~ 1 mW) was separated from the master output to be used for the TOF procedure. The rest was sent through a double-pass acousto-optic modulator (AOM) setup. This AOM (Crystal Technology, model 3080-122), labelled AOM1 in Fig. 2.4, was driven at either 91.5 MHz or 121.5 MHz, depending upon whether the light to be sent to the MOT was to be 15 MHz or 75 MHz detuned. The method used in our system for controlling the AOMs has been documented elsewhere [78, 79]. From each pass through the AOM, the first order in the negative frequency direction that it produced was kept while the other orders were blocked, so that the total frequency shift resulting from the double passage was either -183 MHz or -243 MHz. Following this procedure, the light was injected to the slave laser. The values of the total power injected in the cases of the 183 MHz or 243 MHz detuned light were 470μW and 210μW, respectively. The injection-locked slave (an SDL5422) gave out 135 mW in a collimated beam of linearly polarised light. It was powered by another low-noise laser current driver built in-house (model EW1250); the current supplied was 300 mA and the laser was thermally stabilised by a Peltier cooler attached to the diode chip. As in the case of the master, the cooler was controlled by a Newport 325 diode temperature controller.

The light from the slave was double-passed through another AOM (Gooch and Housego, model AOM001/2) that was driven at 84 MHz; this is labelled AOM2 in Fig. 2.4. The first order in the positive frequency direction from each of the passes

was used, so the double pass yielded an increase of 168 MHz in the frequency of the light. Hence the final frequency was either 15 MHz or 75 MHz red-detuned from the ($F = 4 \rightarrow F'' = 5$) D2 transition, as required. Following passage through this AOM, the light, still linearly polarised, was split into three approximately equal portions by two consecutive polarising beam-splitting cubes. The light was directed into polarisation-preserving optical fibres to be sent to the vacuum system for trapping and cooling. To take advantage of the polarisation-preserving nature of the fibres, the plane of polarisation of the linearly polarised light going into each fibre was adjusted to the correct orientation by means of a $\lambda/2$ plate. Approximately 75% of the light directed into the fibres was delivered to the MOT system, and with the correct orientation of the light's plane of polarisation in the fibre there was very little drift ($< 5\%$) with time or temperature of either the transmission fraction or the polarisation of the emergent light. On the other hand, there was a daily drift with laboratory temperature, despite the presence of air conditioning, of the power inserted into the fibres. This was because of the long optical path that was traversed by light from the slave laser prior to reaching the fibres. The drift was around 10%, and resulted in a commensurate variation in the number of trapped atoms. It did not, however, seriously impede the experiments because a specific level of trap fluorescence, indicating a certain trap size, was used in any given run of the experiment. After leaving the fibres, the light for each trapping beam was passed though a $\lambda/4$ waveplate to convert it to σ^+ or σ^- circularly polarised light, as appropriate, and then through a telescope to expand the beam diameter from ~ 2 mm to ~ 1.5 cm, ready to form the MOT. The light was then directed into the system as shown in Fig. 2.2.

The repumper laser was an SDL5702-H1 distributed Bragg reflector (DBR) diode laser. This was powered by a Melles Griot diode laser driver, and the current that was supplied to it was ~ 75 mA. This yielded a power output of 11.5 mW. The laser driver also controlled the temperature stabilisation of the diode by the attached Peltier cooler. The repumper laser was locked to the ($F = 3 \rightarrow F'' = 4$) D2 transition by a saturated absorption arrangement very similar to that used in the case of the master laser, and this is shown in Fig. 2.5. The current to the repumper was dithered at a frequency of 30 kHz by a signal generator. As the repumper laser did not have a grating plus PZT crystal setup, feedback to the laser to keep it locked to the correct transition frequency was provided by the current only. The repumper laser locking system worked very well, and the laser would generally remain locked to the correct frequency all day. The output of this laser was then combined with a fraction of the slave light as it was being directed into one of the fibres carrying light to the MOT, and thus was present in one of the xz-beams in the MOT assembly.

The intensity of the light in the trapping/cooling beams was controlled by the power in the first order produced by AOM2. This was determined by the amplitude of the 84 MHz signal supplied to AOM2. As stated, the intensity in the beams that trapped the atoms was 5.0 mW/cm^2 in the case of the xz-beams and 3.6 mW/cm^2 in the case of the y-beam. For cooling the atoms prior to performing a shot of the experiment, the current in the trapping magnetic field coils was turned off.

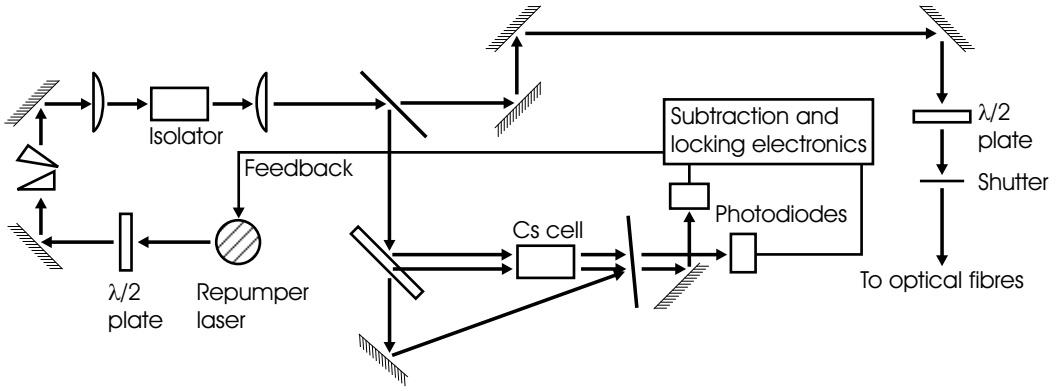

Figure 2.5: The optical table arrangement for the production of light of the correct power and frequency from the repumper diode laser.

The light in the trapping beams, whose intensity was reduced to 15% of its former value and whose detuning was increased to 75 MHz, was applied to the atoms for 12.4 ms. The repumping light, at the same intensity as when the atoms were being trapped, was also applied over this time. Finally, the intensity of cooling light was reduced to zero by changing the amplitude of the frequency being sent to AOM2 to zero. The intensity in the repumping beam was maintained at full strength for a further 3.8 ms so that all the trapped and cooled atoms would be left in the $F = 4$ ground state. The repumper light was then blocked using a shutter (a razor blade connected to a magnetic relay) that was operated by a shutter-driver built in-house. These timings, and how they relate to the rest of the experimental procedure, are shown in Fig. 2.9. Following removal of the light, the atoms began to fall freely under gravity.

Thus was obtained a sample of $\sim 10^7$ atoms at a temperature of 5μK, all in the $F = 4$ hyperfine state. The ensemble had a Gaussian momentum distribution with a FWHM of 12 photon recoils and a Gaussian spatial distribution that had a FWHM of around 1 mm.

2.3 Ti:sapphire laser and standing wave

The experiments described in this thesis relate to the effect of a spatially periodic potential applied as a series of δ-function-like pulses to a system of particles whose associated de Broglie waves have wavelengths comparable with that of the potential. This potential was realised by using a standing wave of off-resonant laser light, which was obtained from a titanium sapphire (Ti:sapph) laser. The Ti:sapph ($Ti:Al_2O_3$) laser, and its associated pump laser, were located on the same optical table as the diode lasers described in Sec. 2.2.2, so the light produced by the Ti:sapph had to be conducted to the main experimental system by a polarisation-preserving optical fibre. The arrangement of the apparatus used to produce the light from the Ti:sapph laser is shown in Fig. 2.6.

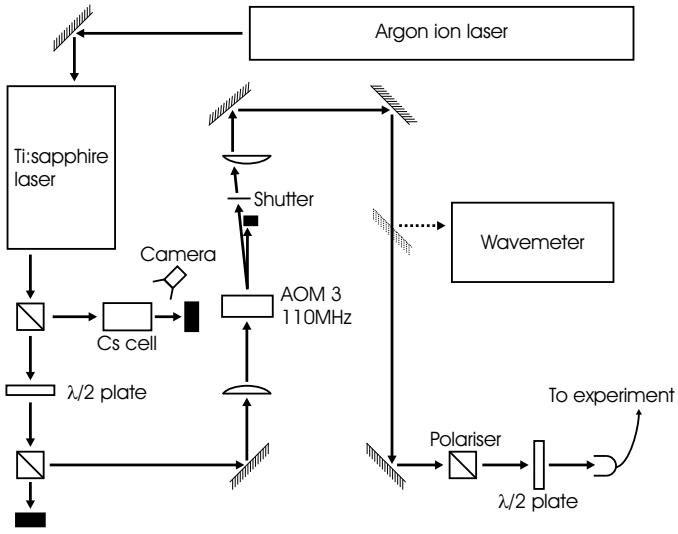

Figure 2.6: The optical table arrangement for the production of light using the Ti:sapphire laser. The wavemeter and the mirror directing the light into it were only present for the initial setup of the Ti:sapphire laser to allow the correct wavelength of light to be obtained. This mirror and the associated light beam are therefore depicted using dashed lines.

The laser used was a Microlase (now Coherent) MBR E-110 bow-tie ring laser that was set up to run at a single frequency with a wavelength in the vicinity of 894 nm. The laser was pumped by approximately 11.5 W of light from a Coherent Innova 200 argon ion laser running in 'multi-line visible' mode, giving light at wavelengths in the green part of the visible spectrum. This pump light was injected into the cavity of the Ti:sapph laser via a periscope. The output power of the Ti:sapph depended very sensitively on achieving the correct orientation of the pump beam, and on a good day it was possible to obtain 1.25 W of light at 894 nm, with power fluctuations of around 1%. When first setting up the laser, the light that it produced could be of a wavelength up to 1 nm different from that which was desired. In order to find the correct wavelength, a fraction of the light from the laser was injected into a Burleigh wavemeter and the birefringent filter of the Ti:sapph laser was adjusted until the correct wavelength (894.347 nm) was obtained. Following this adjustment, the wavemeter was removed from the system and only used again if a substantial laser realignment caused the wavelength of output light to change considerably.

The MBR E-110 contained as part of its setup a high finesse reference cavity, and a small fraction of the light produced by the laser was directed into this cavity. The laser was locked to one of the fringes of this cavity and hence a line width of less than 100 kHz could be achieved. It was possible to scan the frequency of the laser while in lock, or out of lock, by altering the length of the reference cavity using an electronically controlled long extension piezo ceramic. For the experiments described in this thesis, light that was red-detuned by around 30 GHz from the

($6^2S_{1/2} \rightarrow 6^2P_{1/2}$) ($F = 4 \rightarrow F' = 3$) D1 transition was required. To obtain this detuning, a very small fraction ($< 1\%$) of the output of the Ti:sapph was directed through a caesium cell that was monitored by a camera. When fluorescence was observed, it could be deduced that the frequency of the light was resonant with the ($F = 4 \rightarrow F' = 3$) D1 transition. The 'Scan Offset' of the Ti:sapph laser was then changed to a setting corresponding to the required red-detuning. This altered the length of the reference cavity and hence the frequency of the laser output.

The locking achieved using the reference cavity was not as robust as that obtained when using the saturated absorption technique in the case of the diode lasers, as described in Sec. 2.2. The frequency of the light would vary on a time scale of 1 second by values of the order of 100 MHz. This was observed by measuring with a fast photodiode the beat frequency of the light from the locked Ti:sapph laser and light from a laser diode that had been locked by the saturated absorption technique to the ($F = 4 \rightarrow F' = 3$) D1 transition. However, this level of frequency variation was small in comparison with the detuning of the light from the ($F = 4 \rightarrow F' = 3$) D1 transition. As the corresponding variation in the potential experienced by the atoms in the standing wave of this light was less than 1%, it did not adversely affect the experiments. The stability of the Ti:sapph laser was generally good. One of the advantages of this particular model was that the laser cavity was monolithic, having being machined from a single block of aluminium. This yielded a high level of inherent stability and a correspondingly small linewidth. In our experimental arrangement, the laser was placed underneath an air blower that applied a laminar air flow to the laser to minimise any settling of dust within the laser cavity. Thus the laser could usually be run for a period of several months without the need for any cleaning or realignment of the internal mirrors. It would generally remain locked to the correct frequency for an hour or so before falling out of lock and having to be readjusted and relocked to the required frequency.

The light emerging from the laser was passed through an AOM (Crystal Technology, model 3110-140) that, when active, was driven at 110 MHz. This is labelled AOM3 in Fig. 2.6. To ensure maximum power throughput through the AOM, the light passed through a converging lens before entering it. Another converging lens after the AOM restored the collimation. The purpose of AOM3 was to allow the D1 light intensity being sent to the MOT to be controlled and switched on and off rapidly. All orders produced by the active AOM were blocked except the first (in the negative frequency shift direction, though the sign of the frequency shift was of no consequence since the magnitude of the frequency shift itself was negligible in comparison with the detuning of the light from the ($F = 4 \rightarrow F' = 3$) D1 transition). Approximately 70% of the light entering AOM3 was to be found leaving in this order. Following the AOM, the light was passed through a polarising cube to ensure that only linearly polarised light entered the optical fibre that would guide the light to the main experimental setup. Immediately before entry to the fibre, the light passed through a $\lambda/2$ plate to rotate its plane of polarisation to match the optimum transmission axis of the fibre so that polarisation would be preserved and thermal drifts in transmitted power or polarisation would be minimised. The

transmission fraction of this fibre was around 65%, and 575 mW emerged from the fibre when the power produced by the Ti:sapph laser was 1.25 W. Typically there were fluctuations of up to 5% on an time scale of 1 second in the value of the emergent power.

Since the light that was delivered to the optical fibre came from the first order output of the AOM, and since all other emergent orders were blocked, the control of the intensity of the D1 light forming the standing wave was straightforward: when the AOM was active, light would be input to the fibre; when the AOM was not active, no light would be delivered to the fibre and so there would be no standing wave. By varying the amplitude of the 110 MHz signal, the power in the first order output of the AOM, and hence the intensity of the light forming the standing wave, was varied. Thus the strength of the potential experienced by the atoms in the standing wave could be controlled. The amplitude of the 110 MHz signal supplied to AOM3 was controlled by the output of a programmable arbitrary waveform synthesizer (Hewlett-Packard, model HP 8770A). This had a time resolution in the region of 10ns, so could provide the very fast switching that was required to define the pulses of light leaving the AOM. To produce a sequence of pulses, its output consisted of a series of square pulses of 500ns duration and variable separation. The form of the required pulse sequence was supplied to the arbitrary waveform generator by the control computer via a GPIB interface.

AOM3 was capable of sufficiently fast switching that the time variation of the intensity of the pulses of light supplied to the main system was approximately square in form and had a duration of 500ns. However, such a short pulse duration (necessary for the experiments performed) meant that the throughput of light could not reach its steady state value before the AOM was switched off. Consequently the mean power in the first order of the AOM over the duration of the pulse, as measured by a fast photodiode, was $\sim 2/3$ the steady state power. Hence the power emerging from the fibre when a light pulse was being applied to the system was ~ 380 mW. For the experiments described in this thesis, a train of such pulses was applied to the system. Apart from these pulses, it was desired that no D1 light should enter the system and so a shutter was placed after the AOM (operated by another shutter-driver that had been built in-house). This was only open for a time of the order of 10 ms, over which the pulses could be applied to the system. Ideally, this shutter would not be necessary since extinction of the light in the first order emerging from the AOM when the amplitude of the 110 MHz signal was reduced to zero would result in no power being delivered to the fibre. However, RF noise in the AOM caused some population of the first order even when the amplitude of the 110 MHz signal was zero. Additionally, there was a small amount of light in the zeroth order from AOM3 which reached the fibre because the orders at the point of blocking were not sufficiently spatially separated to allow complete obstruction of the zeroth order, and none of the first, to be achieved. The unwanted power entering the system when the shutter was open was very small ($\sim 10\mu$W) but the closure of the shutter reduced it to zero so as to eliminate any adverse effect on the experiments that even such a low power of far-detuned light could have.

The light emerging horizontally, still linearly polarised, from the optical fibre

was reflected from two 45° mirrors in order to direct it vertically downwards into the vacuum system. Prior to each of these mirrors the plane of polarisation of the light was rotated by a $\lambda/2$ waveplate to an orientation that allowed the light to be reflected with the minimum degradation in the linearity of its polarisation. Additionally, the light was passed through a polarising cube after the first mirror, before the second $\lambda/2$ plate, in order to ensure that light was linearly polarised before being reflected downwards into the vacuum system. Passage through these components resulted in some loss of power, so that the power of a pulse of light in the downward-propagating beam was $\sim 250\,\mathrm{mW}$. The light then entered the quartz cell, passed through the cold caesium atoms, and left the vacuum system, passing through a crystal phase modulator (see Sec. 2.4) before being retroreflected from a mirror sited below the vacuum system. In this way, a standing wave of light that was far-detuned from the ($F = 4 \rightarrow F' = 3$) D1 transition was realised. The counterpropagating beams forming the standing wave had a Gaussian intensity profile. The intensity profile was measured by progressively blocking the beam with a micrometer and measuring the power after the blockage as a function of micrometer position. Immediately after the fibre, the FWHM of the Gaussian profile was 1.14 mm. Immediately below the base of the vacuum system, before entering the phase modulator, the FWHM was 1.47 mm and the total power in a pulse of the beam was $\sim 200\,\mathrm{mW}$. The beam that emerged after having passed though the polarising optics above the cell for the second time (because it had been retroreflected) was also Gaussian in profile with a FWHM of 1.05 mm. The power in a pulse of this beam was $\sim 65\,\mathrm{mW}$.

Assuming that this retroreflected beam lost the same fraction of its power in traversing the polarising optics as did the down-going beam, the power in the up-going beam after it left the cell was $\sim 100\,\mathrm{mW}$. Making the additional assumption that a fixed fraction of the power was lost when each air-quartz interface was traversed, the approximate power in the up-going beam experienced by the atoms was 120 mW and that in the down-going beam was 220 mW. Further, assuming that the FWHM of the up-going beam at the position of the atoms was 1 mm, for want of more information, it can be said that the atoms experienced a standing wave created by two counter-propagating beams each of power 120 mW and FWHM 1 mm, and superimposed on this a downwards-propagating travelling wave of power 100 mW. The energy of each atom was shifted by an amount determined, through the ac Stark shift (also known as the light shift), by the intensity and detuning of the light in which the atom found itself [56]. Therefore, since the intensity of light in the standing wave varied sinusoidally with position, it acted as a spatially periodic potential for the atoms. This is discussed in more detail in Ch. 3 and Appendix A. It is clear from the description above that the estimate of the intensity of light experienced by atoms in the standing wave was subject to a number of assumptions. Given the uncertainty in the exact power in the up-going beam at the position of the atoms, and the beam waist, a discrepancy between the true strength of the potential experienced by the atoms and that which would be deduced from the numbers above by a factor of 2 is not implausible. In fact, comparison of the results of numerical simulations, as described in Chs. 3 and 4, with those of the

experiment implies that the experimental potential experienced by the atoms was up to 1.5 times that which would be deduced from the intensity values above. This is quite within the limits of the experimental uncertainty.

The position of the potential relative to the atoms could be varied by changing the phase between the down-going light and the retroreflected light; this was the purpose of the crystal phase modulator. Since the potential associated with the travelling wave had no spatial dependence, it had no effect on the dynamics of the atoms and henceforth will be ignored.

2.4 Crystal phase modulator

The crystal phase modulator (Leysop, model EM 200K) was a low voltage transverse KD*P electro-optic modulator comprising two crystals joined end-to-end along the direction of light throughput. Application of a voltage across the two crystals changed the optical path length of these crystals as experienced by linearly polarised light with its plane of polarisation parallel to the specified axis of the crystal. Thus the phase of the light emerging from the crystals was altered. The light forming the standing wave passed twice through this phase modulator, before and after retroreflection. This allowed the phase modulator to shift the relative phase between the down-going and up-going beams and hence the vertical position of the profile of the standing wave. Precise control of the voltage supplied to the phase modulator, therefore, allowed precise control of the position of the standing wave profile relative to the atoms.

The transmission of the phase modulator was better than 90%, its windows were made from BK7, the length of each crystal was 40 mm and the aperture was 2.2 mm. The voltage to the phase modulator was supplied by a high voltage differential amplifier (Leysop, 5000V series). This was controlled by an analogue signal from a function generator (Stanford Research Systems, model DS345) and produced an output voltage that was 1000 times the input signal from the function generator. The phase shift produced by the modulator scaled linearly with the applied voltage. The modulator was calibrated by applying a sequence of standing wave pulses to the atoms and shifting the phase of the standing wave mid-way through this sequence. The resulting momentum distribution of the atoms was then compared with that which would be produced in the absence of any phase shift. Only when the phase shift produced in the up-going beam relative to the down-going beam was 2π would the atomic momentum distributions in the two cases be identical, and this allowed the voltage required by the phase modulator to produce this phase shift to be established. The clearest demonstration of the effect of shifting the profile of the standing wave occurred when the interval between consecutive pulses was such as to give rise to a quantum accelerator mode (see Ch. 4), which had a very asymmetric momentum distribution. In this case it was obvious when the shift in phase had made no difference to the final momentum distribution and this allowed an accurate measurement of the 2π phase shift voltage. This voltage was in the region of 500V for light of wavelength 894 nm, though it varied somewhat ($\pm 5\%$)

depending on the precise orientation of the modulator relative to the throughgoing light.

For certain experiments described in this thesis (those investigating the δ-kicked rotor, see Chs. 3 and 5) it was necessary to negate the effect of gravity on the evolution of the atomic wavefunction between kicks from the potential. This was achieved by shifting the position of the standing wave profile between consecutive kicks so that it was the same, relative to the atomic cloud (which fell freely under gravity), at the instant of the next kick as it would be if there were no local gravitational field present. The position of the profile at the moment of a kick varied quadratically with time, effectively 'accelerating' with the free-fall acceleration of gravity. Thus the phase of an atomic wavefunction relative to the periodic potential was always the same as that which would be found in the absence of gravity. In order to achieve this shifting of the potential, the voltage supplied to the phase modulator by the pre-programmed function generator had to be stepped so as to change quadratically with the pulse number. All voltages applied to the modulator were *modulo* the 2π phase shift voltage. The time between consecutive kicks could be anywhere between 5μs and 210μs, but since the slew rate of the high voltage amplifier was in the region of $800\text{V}/\mu\text{s}$, it was always possible to produce the requisite voltage shift in the time interval available.

For other experiments described in this thesis (some of those involving the δ-kicked accelerator, see Chs. 4 and 6) it was necessary to mimic the situation where the free-fall acceleration of gravity was non-zero but greater or less than its true value, or even in the opposite direction. The standard acceleration of gravity is given in the 1998 CODATA recommended values as $g_n = 9.80665\text{ms}^{-2}$ [80]. Making the correction for the latitude of Oxford (51.767°N) using the Geodetic Reference Formula of 1967 [81], though neglecting the effect of altitude or geological corrections, the local gravitational acceleration is $g_{\text{local}} = 9.8113\text{ms}^{-2}$. This modification of the effect of gravity was accomplished by a quadratic variation in the position of the standing wave profile, as in the case where gravity's effect was negated. However, the size of the phase jump between two potential kicks was greater or smaller than, or of a different sign to, that between the corresponding kicks in the gravity-removing case. For example, if it was necessary to diminish but not remove gravity's effect on the atoms' evolution, the standing wave would 'accelerate' downwards at a slower rate than the free-fall acceleration. To reverse gravity's effect, the standing wave would accelerate downwards at a higher value than g, so that to the freely-falling atoms it would appear that they were accelerating upwards relative to the periodic potential. To attain a higher effective downward gravitational acceleration on the atoms than g, the standing wave would 'accelerate' upwards. Hence it was possible to mimic experimentally a whole range of gravitational scenarios.

2.5 Microwaves

For certain experiments performed in this work it was necessary to place the caesium atoms in one or other of the hyperfine levels $F = 3$ and $F = 4$ within the $6^2S_{1/2}$ ground state, or in a superposition of both. This was achieved using pulses of microwaves that caused the atoms to execute the magnetic dipole transition between these two hyperfine levels. This is the clock transition, used in the definition of the second [82]. In the absence of any local magnetic fields, the frequency of the $(F = 3, m_F = 0 \rightarrow F = 4, m_F = 0)$ transition is 9.192631770 GHz, by definition. However, it was found experimentally that the frequency needed to apply $\pi/2$ microwave pulses to the atoms most accurately at both the times indicated in Fig. 2.9 was 9.192632085(5) GHz, where the bracketed number indicates the amount of experimental variability in the value of the last digit. Since the magnetic field in the vicinity of the cold atoms in the experiment was only 10 mG, the second-order Zeeman shift [82] cannot account for the discrepancy between this frequency and the ideal figure. It is believed to be due to two factors. Firstly, the atoms were in different positions, and therefore experienced different microwave powers, at the times of the two $\pi/2$-pulses. Secondly, the shape of each microwave pulse was not an ideal 'top hat' due to the finite switching time of the apparatus. The 0.2 mm distance fallen by the atoms over the 0.8 ms duration of each $\pi/2$-pulse would further distort the effective pulse shape. The frequency used differed from the ideal value because it had to compensate as well as possible for these experimental imperfections.

Microwaves of the required frequency were generated by mixing two signals. The first was a 9.18 GHz signal obtained by using a Ferranti phase locked cavity oscillator to multiply the 5 MHz signal from a temperature stabilised quartz crystal oscillator. The cavity oscillator produced the 1836th harmonic, which has a frequency of 9.18 GHz. These crystal and cavity oscillators were housed in a copper box to reduce pickup, and were always left switched on in order to maintain frequency stability. The second signal was a 12.632085 MHz signal from either one of two SRS DS345 function generators, each of which was connected via its 'timebase' port to the unmultiplied 5 MHz microwave signal from the quartz crystal oscillator. This acted as a reference signal and ensured phase locking between all three frequency supplies. A schematic diagram of the system used in the experiment to produce microwaves of the required frequency, phase and power is shown in Fig. 2.7.

Mixing of the 12.6 MHz and 9.18 GHz signals took place in a single sideband up-converter located in the copper box. The local oscillator frequency (L) was the 9.18 GHz signal, the intermediate frequency (I) was the 12.6 MHz signal and the output signal, the RF frequency (R), was 9.192632085 GHz. When the appropriate signals were applied to the L and I ports, the microwave power output of the up-converter was approximately 0 dBm. The microwaves were conducted by flexible cable from the up-converter to a manually adjustable attenuator that could produce a signal attenuation of anywhere between 0 dB and 50 dB. For the experiments described here, this was generally set to a value in the region of 23 dB, optimised

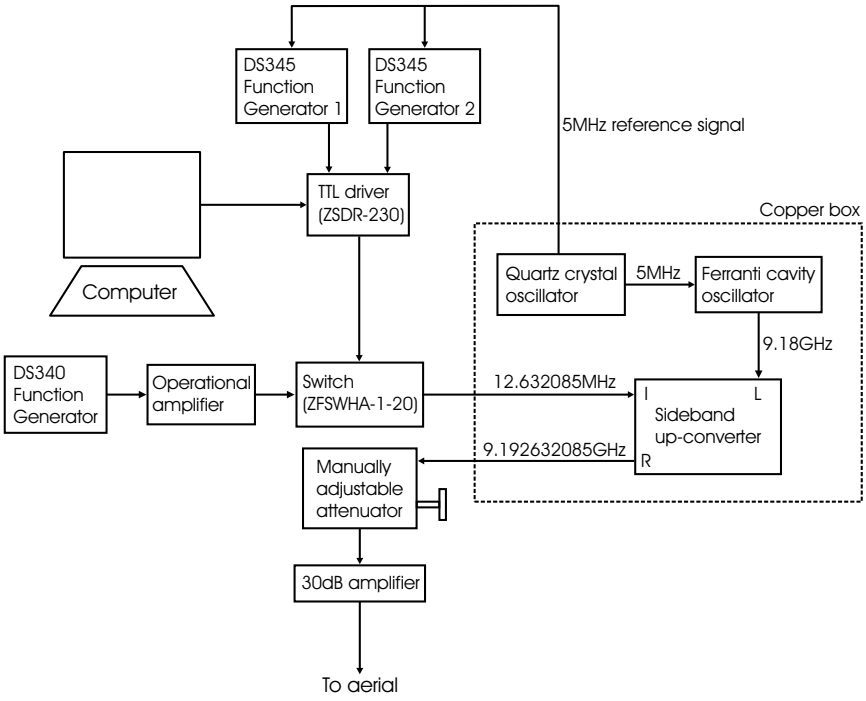

Figure 2.7: The system used to produce microwaves of the required frequency, phase and power.

so that a microwave pulse lasting 1.6 ms would most efficiently transfer atoms from the $F = 3, m_F = 0$ state to the $F = 4, m_F = 0$ state, thus acting as a π-pulse. The microwaves were then amplified by a 33 dB amplifier (Atlantic Microwave, model AS-2545) and conducted to the vacuum system via a semi-flexible co-axial copper cable that was 3 mm in diameter. This terminated in an aerial that was 2.0 cm long (*i.e.* 0.6 wavelengths), situated adjacent to the quartz cell and lying along the y-axis. This produced a dipole field which was then experienced by the caesium atoms.

To control the application of the microwaves, switches had to be used since, as stated, the microwave frequency stability demanded that the signal suppliers themselves should operate without interruption. When no signal was supplied to the I port of the up-convertor, no output was obtained from the R port and hence the output of microwaves could be controlled by application or removal of the 12.6 MHz signal. The DS345 function generator output was passed through a switch (Mini Circuits, model ZFSWHA-1-20) that had a turn-on time of less than 10ns. The output of this switch was determined by supplying to the control input either 0V (producing at least 60 dB attenuation to the input signal) or -5V (giving a signal attenuated by ~ 1 dB). The control voltage was produced by an SRS DS340 function generator connected to an inverting operational amplifier. When performing the experiments, the output of this function generator took the form of a series of square pulses whose durations determined the duration of the transmission of the 12.6 MHz signal by the switch. The finite switching time of the

up-converter in response to the application and removal of the 12.6 MHz signal led to the non-square microwave pulse shape referred to above.

For certain experiments, such as a type of Ramsey separated oscillatory fields experiment [83, 84] in which two $\pi/2$-pulses of microwaves with different phases were applied to atoms, it was necessary to be able to vary the phase of the microwave pulses. To accomplish this, both DS345 function generators were used. The control computer could instruct, via a GPIB interface, one of these function generators to vary its phase as required. The output of each function generator was connected to a TTL driver (Mini Circuits, model ZSDR-230) controlled by the computer. Depending on whether the TTL input to this driver was high or low, the driver's output was the signal from one or the other DS345 function generator. This was then supplied to the up-converter for mixing with the 9.18 GHz signal. Since the phase of the up-converter output was determined by the phase of the incoming 12.6 MHz signal, by switching the TTL driver between microwave pulses it was possible for consecutive $\pi/2$-pulses to have phases that differed by any desired amount.

2.6 Detection system

The momentum distribution of the atoms was measured by a time-of-flight (TOF) technique. After the atoms had been acted upon by pulses of the standing light wave and/or microwaves, they fell freely under gravity through a sheet of light that propagated along the y-direction in the lower part of the vacuum system. This TOF beam was created by taking light directly from the master laser without passage through any AOMs. Hence the light was resonant with the ($6^2S_{1/2} \rightarrow 6^2P_{3/2}$, $F = 4 \rightarrow F'' = 5$) D2 transition. The light was conducted towards the experiment by an optical fibre and then passed through a cylindrical telescope so that the beam took the form of a sheet that measured 10 mm in the x-direction and 1.5 mm in the z-direction. The power in the TOF beam was 250μW and the beam was retroreflected so that it passed twice though the vacuum system. When the atoms in the cloud fell though the beam, they absorbed light from the beam, re-emitting it in all directions through spontaneous emission. Hence the power in the beam after passage through the vacuum system was reduced, and the amount of absorption of light was increased due to the beam's double passage. Single passage would have resulted in less than half the absorption signal as the light would then have exerted a net force on the atoms causing them to be accelerated. The velocity thus acquired would mean that the atoms would experience a different frequency of light in the beam because of the Doppler shift and hence would no longer resonantly absorb light. A plan view (looking along the z-axis) of the TOF system is shown in Fig. 2.8.

In order to measure the momentum distribution of the atoms, the power in the TOF beam following passage though the vacuum system was measured as a function of time using a photodiode system. The variation of the absorption with time allowed the spatial distribution of atoms at the z-position of the TOF beam

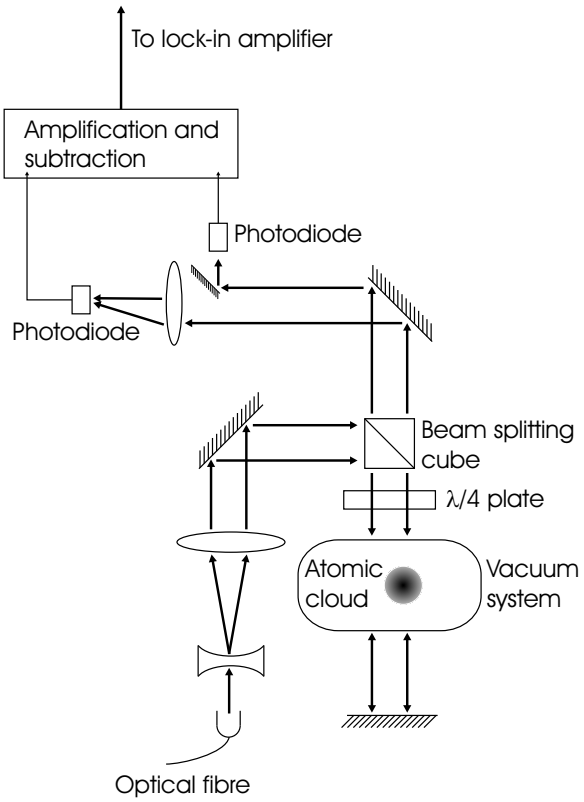

Figure 2.8: Plan view of the time-of-flight measurement system. Note that the position of the atomic cloud did not coincide with the centre of the sheet of light in the TOF beam, thus allowing the part of this beam in which there was negligible absorption from atoms to be directed into one photodiode. The output signal of this photodiode was subtracted from that of the other in order to reduce noise in the TOF signal (see text).

to be deduced. The vertical distance between the position of the MOT and the TOF beam was 53 cm, meaning that, after release from the MOT, the atoms took 0.33s to reach the TOF beam due to gravitational free fall. Since the FWHM of the atoms' momentum distribution following molasses cooling was 12 photon recoils, corresponding to a velocity width of $4.2\,\mathrm{cm\,s^{-1}}$, the spatial extent of the atoms by the time they reached the TOF beam was 1.4 cm (and more than this if the momentum distribution had been broadened by the application of standing wave pulses). Hence the initial spatial distribution of atoms in the trap, about 1 mm, constituted $\sim 7\%$ of the total spatial distribution at the time of passage through the TOF beam. Thus the spatial distribution after free flight was almost entirely determined by the momentum distribution of the atoms following their interaction with the laser standing wave and microwaves. Hence the measurement of this spatial distribution permitted the momentum distribution of the atoms to be deduced. The TOF beam had a finite thickness of 1.5 mm in the z-direction, which is approximately 11% of the spatial extent at the time of measurement of atoms with an initial momentum width of 12 photon recoils. This meant that the TOF measurement technique could not resolve momenta to better than one photon recoil. However, this resolution was sufficient for the investigations described in this thesis.

The photodiode system used to measure the absorption was as follows. The width of the TOF beam was such that it could be aligned so that its edge would almost entirely miss the falling cloud of atoms. There was very little absorption of this part of the beam, which was directed into one photodiode after the double passage through the vacuum system. The bulk of the beam, through which the atoms fell and from which there was substantial absorption, was focused and directed into another photodiode. The outputs of the two photodiodes were then amplified and balanced so that when one was subtracted from the other the net signal was zero in the absence of a falling atomic cloud. This subtraction technique allowed common sources of background to the desired signal (*e.g.* from absorption due to the caesium vapour in the vacuum system, or from noise in the intensity or frequency of light in the TOF beam) to be eliminated. When the cloud of atoms passed through the TOF beam, there was a substantial change in the output of the subtracted signal, which was then supplied to a lock-in amplifier (EG & G, model 5210). To allow the lock-in amplification, the current to the master laser was dithered at a frequency of 40 kHz, as in the locking technique described in Sec. 2.2.2. When the TOF detection was about to commence, the amplitude of this dither was increased by a factor of four. This modulation of the laser current led to a 40 kHz variation in the frequency of the light in the TOF beam. The lock-in amplifier worked by amplifying the magnitude of the signal in the subtraction output that oscillated at 80 kHz, twice the dither frequency. This signal resulted from oscillations of the laser frequency around the resonant value. One current oscillation corresponded to two coincidences of the laser frequency with the resonant value. Amplification of the absorption signal at this frequency greatly increased the signal-noise ratio of the TOF absorption measurement to about 200:1. For some early experiments, noise in the current supply to the master laser caused frequency noise in the TOF

light that reduced the signal-noise ratio of the TOF measurements. In this case the experimental data had to be averaged over several repetitions in order to improve the ratio. Due to the finite bandwidth of the lock-in amplifier, which was effectively acting as an 80 kHz filter, there was some distortion of narrow measured distributions, leading to an apparent asymmetry and a consequent increased width of the distributions. For example, a distribution whose true width was 12 photon recoils had an apparent width due to the lock-in amplifier of 12.5 photon recoils, and the high-momentum half-width exceeded the low-momentum half-width by $\sim 8\%$. The asymmetry and width increase were less pronounced for wider distributions (*i.e.* those with smaller high-frequency components), and in no case was this effect a serious problem.

2.7 Timing

It is evident from the descriptions above that the precise timing of all the components of the experimental apparatus was crucial to its successful operation. This timing was achieved through a combination of the outputs of the control computer, running a program (written in 'C') that was specifically designed for the operation of this experiment, and those of a commercially supplied programmable delay/pulse generator (Stanford Research Systems, model DG535) that was triggered by the computer near the beginning of each shot of the experiment. The computer communicated with the experimental apparatus by two methods: the first was via two National Instruments 12-bit analogue output and digital I/O boards (model AT-AO-10), plus a 12-bit data acquisition board (model AT-MIO-16) that was also capable of both analogue and digital I/O functionality. The second method was via the GPIB interface, which allowed the computer to program certain components to generate the required voltage pulse sequences. Specifically, the computer used GPIB to program the following devices:

- the DG535 delay generator, so that this could trigger the DS340 and DS345 function generators and the HP 8770A arbitrary waveform synthesizer at the appropriate times
- one of the DS345 function generators used for production of microwaves of the correct frequency. The program set the precise frequency (in the region of 12.6 MHz) that it was to supply, and the phase of its waveform relative to that of the other DS345 used for the microwaves (which was not connected to the GPIB interface)
- the HP 8770A arbitrary waveform synthesizer, so that this would supply the required sequence of pulses to activate the AOM controlling the application of the standing wave of light
- the DS345 that was used to control the voltage to the crystal phase modulator, so that phase jumps of the correct size occurred at the correct times relative to the pulses of the standing wave

- the DS340 that controlled the duration of the microwave pulses applied to the atoms.

All these instructions were loaded to the relevant pieces of equipment at the beginning of each experiment and, if the parameters were to be varied mid-experiment, re-loading took place between individual shots. With the exception of the DS345 that supplied the 12.632085 MHz signal to produce the correct microwave frequency, all of the GPIB-programmable components required an external trigger before yielding an output. These triggers were supplied by the DG535 delay generator after it had received its trigger from the computer. This system of triggering allowed precise control of the timings in the experiment, because the delay generator had a time resolution of 5ps in the pulse edge and an rms jitter of 50ps. Both of these levels of performance were more than sufficient for the needs of the experiments described in this thesis.

In addition to triggering the delay generator, and programming via GPIB, the computer was responsible for using analogue and digital signals, sent at the appropriate times by the National Instruments boards, to control the current to the trapping coils, the dither in the current to the master laser diode, the position of the shutters, the frequency and power sent to the AOMs used to manipulate the light from the master and slave lasers, and the source of the 12.6 MHz signal used to define the microwave frequency. The clock that determined the timings of these analogue and digital output pulses was located on the data acquisition board. The timing of the pulses produced by the computer was not as accurate as that of the GPIB-programmable components of the apparatus. Thus the experimental timings controlled by the computer were more prone to jitter than those from the function generators (accurate to less than 1μs) or arbitrary waveform synthesizer (accurate to $\sim$ 10ns), and could vary from shot to shot by times in the region of 100μs, although the typical amount of variation was around 5μs. However, the precision of the timings controlled by the computer was less crucial than that of the pulses from the function generators and arbitrary waveform synthesizer, so this jitter was not a serious shortcoming. The interval between successive pulses of the standing wave was the time interval in which precision was most important, and the performance of the arbitrary waveform synthesizer met the needs of the experiment.

A given shot of the experiment began with the trapping of the atoms. This would continue until the trap reached a certain specified size (measured by using a lens plus photodiode to detect the fluorescence light from the trapped atoms). The atoms would then be cooled and released from the trap, and, following this, the trigger pulse to the DG535 delay generator would be sent by the computer. The relative timings of all the pulses of light and microwaves used are shown in Fig. 2.9. After the release of the atoms, a π-pulse of microwaves (the '$F = 3$ pump pulse') could, if required, be applied to the atoms to place a certain fraction of them in the $F = 3, m_F = 0$ state. If applied, this would then be followed by a pulse of trapping light (the 'blow-away pulse') which would push away any atoms remaining in the $F = 4$ hyperfine level. Following this, a second π-pulse of

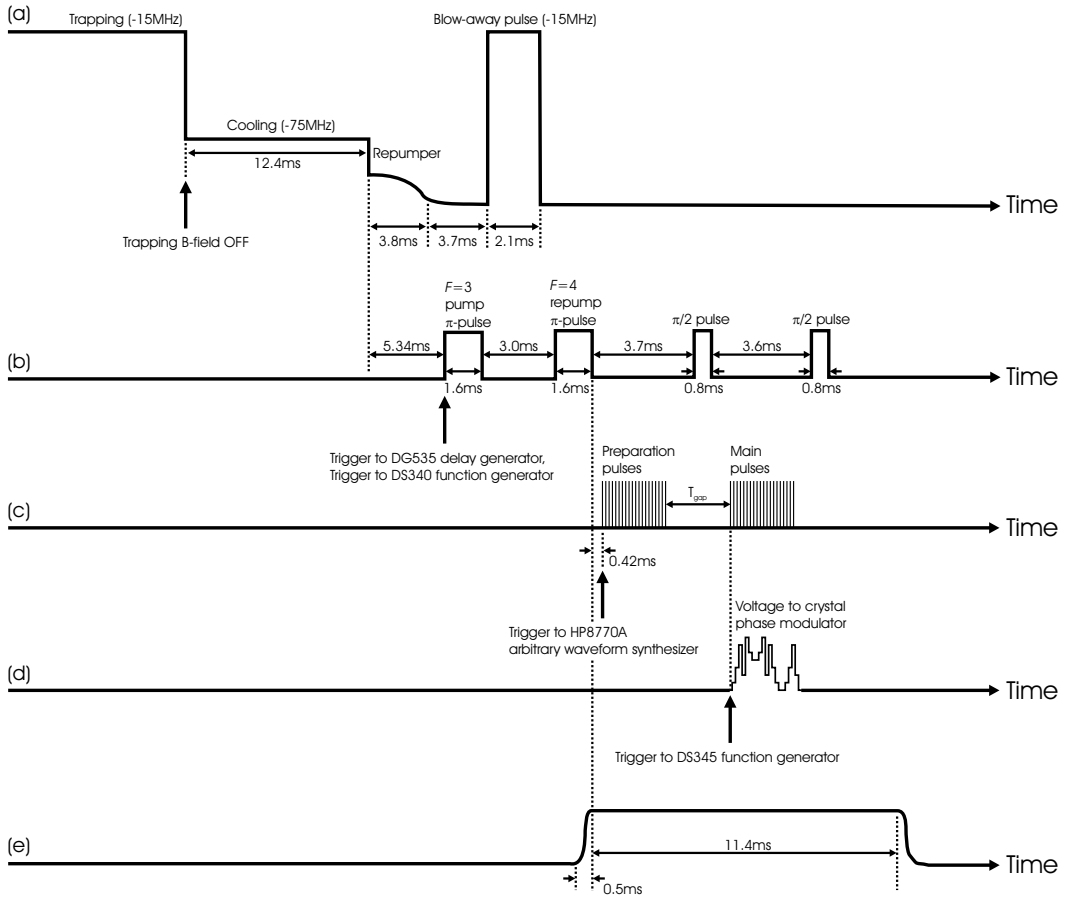

Figure 2.9: The timings of the various pulses that might be applied in a shot of the experiment (see text): (a) diode laser light, (b) microwaves, (c) standing wave pulses, (d) the voltage steps to the crystal phase modulator to shift the standing wave profile to vary gravity's effect, (e) the opening and closing of the shutter permitting standing wave light pulses to be applied. Different microwave and standing wave pulse sequences were used in different experiments, and the blow-away pulse of trapping light was also an optional tool. The voltage to the crystal phase modulator was sometimes held at zero, in order to leave gravity's effect unaltered.

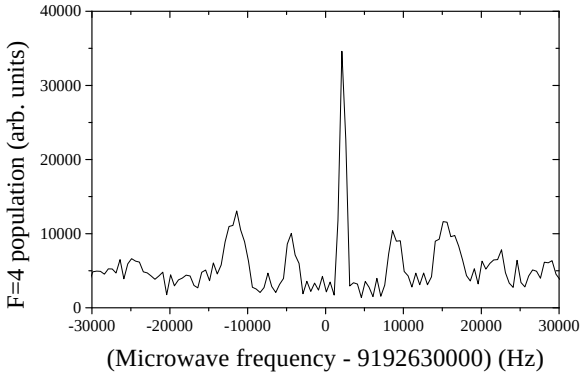

Figure 2.10: The population of atoms in the upper hyperfine level ($F = 4$) of the $6^2S_{1/2}$ ground state after application of a single microwave pulse lasting 0.8 ms, and having the frequency shown, to an ensemble of atoms in the $F = 3$ hyperfine state.

microwaves (the '$F = 4$ repump pulse') could be applied to place all the remaining atoms in the $F = 4, m_F = 0$ state. This sequence of pulses would be used if a well-defined magnetic substate were required prior to application of standing wave pulses and subsequent microwave pulses. The standing wave pulses could be applied in two sequences, the 'preparation pulses' and the 'main pulses', separated by a variable time T_{gap}. These terms will be explained in their experimental context in subsequent chapters. While the main pulses were being applied, the voltage to the crystal phase modulator could be varied so as to remove gravity's effect on the evolution of the atomic wavefunctions. $\pi/2$-pulses of microwaves could be applied before and after the main pulse sequence to examine the interference between atom waves that had been exposed to the periodic potential of the standing wave. These microwave pulses could also be applied in the absence of any pulses of standing wave light to allow experiments of a Ramsey separated oscillatory fields type [83, 84]. After the application of these light and microwave pulses, the computer would increase the level of current dither in the supply to the master laser in order to allow the TOF measurement of the momentum distribution. The output of the lock-in amplifier was sent to the data acquisition board of the control computer where it was processed by an analogue-to-digital converter before being written to disc.

As an example of the operation of the system, and to justify the statement that the magnetic field experienced by the atoms once the Earth's field had been cancelled was 10 mG, there follows a description of the procedure followed to measure this quantity. For this measurement, during the cooling process the repumper light was switched off before the cooling light (in contrast to the usual practice) so that atoms would be optically pumped into the $F = 3$ hyperfine level of the ground state. All m_F magnetic substates were occupied, assumed equally. Following release of the atoms, a microwave pulse of 0.8 ms duration was applied to the atoms and the population of atoms in the $F = 4$ level, in any magnetic substate, was measured by the TOF beam and lock-in amplifier. This was repeated for a

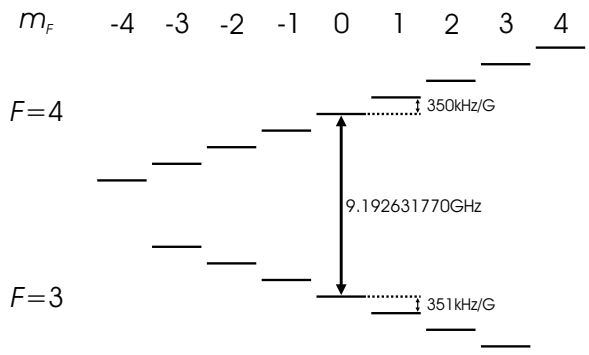

Figure 2.11: The magnetic substates of the $F = 3$ and $F = 4$ hyperfine levels of the $6^2S_{1/2}$ ground state of caesium, and their frequency shifts with applied magnetic field. The shift in the frequency of the $(F = 3, m_F = 0 \rightarrow F = 4, m_F = 0)$ transition due to the second order Zeeman shift is not shown. It is given by $\Delta\nu = 427.45\,\mathrm{Hz/G^2}$ [82], so is negligible for the 10 mG residual magnetic field that was present in the region of the MOT after cancellation of the Earth's field.

range of microwave frequencies from 9.192582062 GHz to 9.192682062 GHz. The results are shown in Fig. 2.10. As can be seen from this figure, there are five distinct peaks in the frequency range from 9.192610000 GHz to 9.192650000 GHz. The mean frequency separation of these peaks is therefore 6.625 kHz. A given magnetic sublevel of the $F = 4$ hyperfine level of the $6^2S_{1/2}$ ground state is shifted upwards in energy in the presence of an external field by an amount corresponding to a frequency shift of $m_F \times 350\,\mathrm{kHz/G}$, as shown in Fig 2.11. Similarly, a given magnetic sublevel of the $F = 3$ hyperfine level is shifted downwards in energy by an amount corresponding to a frequency shift of $m_F \times 351\,\mathrm{kHz/G}$. The number of peaks present in this frequency range indicates that only $\Delta m_F = 0$ transitions occurred, and so the frequency difference between adjacent peaks should be $B \times (350 + 351)\,\mathrm{kHz}$, where B was the local magnetic flux density in gauss. Since this frequency difference was 6.625 kHz, it was deduced that the local magnetic flux density was 10 mG, to 1 significant figure. Additionally, since only $\Delta m_F = 0$ magnetic dipole transitions occurred in this experiment, the atoms experienced the microwaves as having σ-polarisation [85]. The microwaves applied to the atoms were linearly polarised along the y-axis, since this was the orientation of the aerial, so the orientation of the magnetic dipole moment of the atoms must have been in the xz-plane. This means that the residual magnetic field that they experienced due to imperfect cancellation of the Earth's magnetic field must also have been in the xz-plane. As described in Sec. 2.2.1 the pair of Helmholtz coils used to compensate the Earth's magnetic field in which the largest current flowed was that which eliminated the z-component. Since this is the largest component of the Earth's field (the magnetic inclination of the field in Oxford is 66.73°), it would be expected that any residual field due to imperfect compensation would be in this direction, and the results shown here are consistent with this.

Chapter 3

Phenomenology of the δ-kicked rotor

One-dimensional integrable systems perturbed by a periodic train of position-dependent kicks have been the subject of extensive theoretical study in order to investigate chaotic dynamics, both in the classical and quantum mechanical regimes [31, 86]. This has been due to the ease of integrating the equations of motion of such nonlinear systems. For many years the δ-kicked rotor has been such a paradigm in classical chaos theory [34]. This is due to the system's simplicity, coupled with the range of regular and chaotic types of behaviour that it can exhibit. These characteristics made it a natural subject of investigation in the study of the behaviour of a quantum system whose classical analogue can display chaotic motion. This became an area of experimental physics once the field of atom optics allowed realisations of excellent approximations to the idealised quantum δ-kicked rotor [42, 47, 87]. Such studies are important because they cast light on the way in which classical chaotic phenomena have their origins in the quantum domain, and allow investigation of quantum-classical correspondence. The behaviour of the quantum δ-kicked rotor is markedly different from that of the classical version, as will be seen shortly.

This chapter describes some of the essential characteristics of the behaviour of the classical δ-kicked rotor, both in the regular and chaotic regimes. The quantum δ-kicked rotor is then considered, and experimental and theoretical investigations (involving computer simulations) into its behaviour are described.

3.1 Classical δ-kicked rotor

The δ-kicked rotor is a very simple one-dimensional physical system that experiences a time-periodic perturbation. The original model of this name consists of a pendulum of length a and mass m (or, equivalently, a rotator with moment of inertia $J = ma^2$) that is kicked with a momentum impulse X at equal time intervals T. As shown in Fig. 3.1, the angular velocity is constant between kicks.

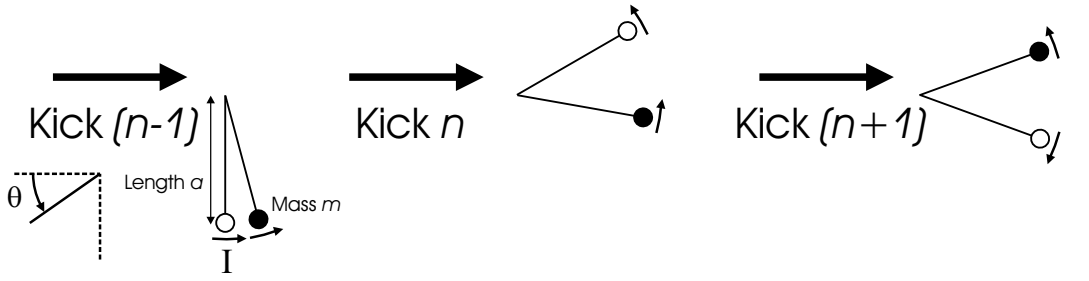

Figure 3.1: An example of the time evolution of the circular kicked rotor. The angular position, θ, and scaled angular momentum, I, of two particles at initially neighbouring points in phase space are shown immediately before the application of each kick.

If θ is the angular position at the instant of a kick, the change in the angular momentum L is $Xa\sin\theta$. We can introduce the scaled angular momentum I, defined by $I = LT/J$, and the scaled kicking strength $K = XaT/J$. K is called the *stochasticity parameter*, since the characteristics of the behaviour in the system, *i.e.* whether the motion is predominantly regular or chaotic, are determined entirely by its value. The time-evolution of the dimensionless action-angle co-ordinates (I and θ respectively, in standard notation) may then be expressed by the *standard mapping* equations [86]

$$I_{n+1} = I_n + K\sin(\theta_n), \tag{3.1}$$
$$\theta_{n+1} = \theta_n + I_{n+1}. \tag{3.2}$$

where I_n and θ_n are the angular momentum and position just before the $(n+1)$th kick.

A formally equivalent system is one in which a particle receives δ-function kicks from a spatially periodic potential, see Fig. 3.2. This is important because a system of this type provides additional possibilities for experimental realisation. The momentum impulse received by the particle at the instant of each kick is sinusoidally dependent on the position of the particle at the instant of that kick. If the maximum impulse which the potential can impart is $X_{\max}$, the mapping equations for this system can be written as

$$p_{n+1} = p_n + X_{\max}\sin(Gz_n), \tag{3.3}$$
$$z_{n+1} = z_n + p_{n+1}\frac{T}{m}. \tag{3.4}$$

where p_n and z_n are the momentum and position respectively of the particle just before the $(n+1)$th kick, m is the mass of the particle and T is the time interval between successive kicks. $G = 2\pi/\lambda_{\text{spat}}$, where λ_{spat} is the spatial period of the potential. Once again, dimensionless action-angle variables (the momentum and position of the particle, in this case) may be obtained by appropriate scaling. In this case, the relations $\chi = Gz$ and $\rho = GTp/m$ are used so as to achieve the

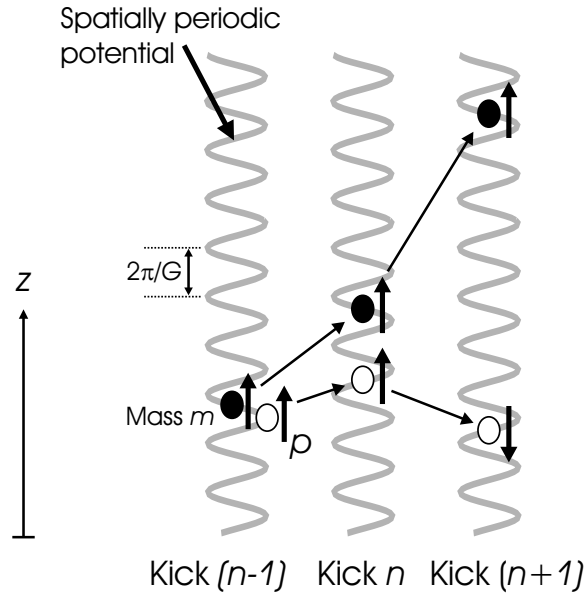

Figure 3.2: An example of the time evolution of the linear kicked rotor. The position, z, and momentum, p, of particles at initially neighbouring points in phase space are shown immediately before the application of each kick.

following mapping equations:

$$\rho_{n+1} = \rho_n + K\sin(\chi_n), \tag{3.5}$$
$$\chi_{n+1} = \chi_n + \rho_{n+1}. \tag{3.6}$$

As in the rotational case, there is only one free parameter, $K = X_{\max}GT/m$. If we introduce a scaled time, $t' = t/T$, the potential acting on the particles has the form

$$V = K[1+\cos(\chi)]\sum_n \delta(t'-n), \tag{3.7}$$

and is clearly periodic in both space and time. The dynamics of the system can be usefully exhibited by stroboscopic plots of particles' trajectories in phase space. The phase space portraits thus obtained have several axes of symmetry and the periodicity of the portraits (2π in both χ and ρ), coupled with these symmetries, means that all information about the dynamics of the system can be obtained by studying the intervals $0 \le \chi < 2\pi$ and, $0 \le \rho < \pi$. However, in this thesis the practice has been adopted of showing phase plots in which, although the values of χ are calculated *modulo* 2π and plotted over the interval $0 \le \chi < 2\pi$, the values of ρ are plotted over the interval $-\infty \le \rho < \infty$. This makes the degree of spreading of the system's momentum distribution clearer, hence allowing the gross characteristics of the system's dynamics to be quickly ascertained.

Figure 3.3 shows the phase space portraits obtained by evolving a set of 400 particles whose initial positions and momenta formed a grid of values of χ and ρ. One hundred iterations of the standard mapping were applied with different values

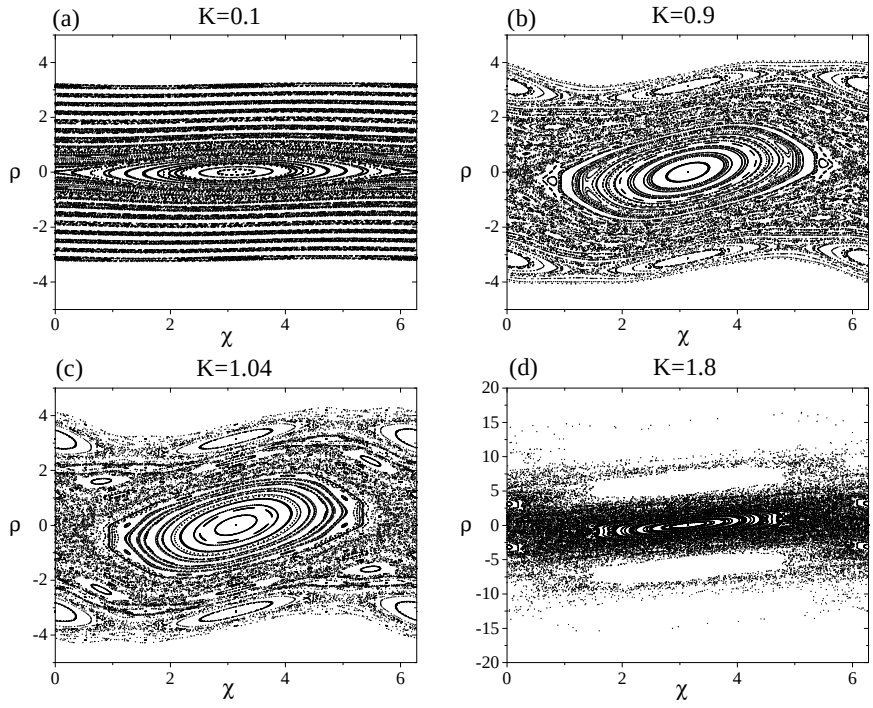

Figure 3.3: Phase space portraits for the kicked rotor produced by 100 iterations of the standard mapping, with (a) $K = 0.1$, (b) $K = 0.9$, (c) $K = 1.04$ and (d) $K = 1.8$.

of K and the values of χ and ρ for each particle after each pulse were plotted. The grid of initial points used consisted of values of χ from 0 to 2π in steps of 0.1π and values of ρ from $-\pi$ to π in steps of 0.1π. When $K = 0.1$ it is clear that very little spreading of the momentum distribution has occurred and that the phase space consists mainly of regions of regular behaviour that enclose regions of stochasticity. Diffusion in momentum space of the particles in the system is prevented by the existence of so-called Kolmogorov-Arnol'd-Moser (KAM) tori [88, 89, 90]. These surfaces in phase space form barriers through which particle trajectories may not pass [86], and, as a result, diffusion to arbitrarily high momenta may not occur. Put another way, to a particle that begins with certain values of χ and ρ, some parts of phase space are inaccessible. As the value of K increases, the KAM tori break down and momentum diffusion can occur to a greater degree. The stochastic regions increase in extent at the expense of the regular regions; that is why K is called the stochasticity parameter. This behaviour is evident in Fig. 3.3(b). As discussed in Ref. [86], the last KAM boundary breaks when $K = 0.9716354$, and for larger values of K diffusion to arbitrarily large momenta may occur. Hence the extent of the momentum diffusion in Fig. 3.3(c) is larger than that for Fig. 3.3(b). Once a KAM torus breaks, its influence does not disappear immediately, for a cantorus (a perforated KAM torus) remains and inhibits, though does not completely prevent, momentum diffusion across the boundary [91]. That is why the spreading of the momentum diffusion after 100 kicks (*i.e.* 100 iterations of the standard mapping)

for $K = 1.04$ is not much greater than that for $K = 0.9$. As is clear from Fig. 3.3(d), for the significantly larger value of $K = 1.8$, the degree of momentum diffusion is considerably greater, though the influence of cantori in inhibiting diffusion is still obvious from the oval-shaped unpopulated regions of phase space.

The particles in the stochastic regions of phase space execute random walks in momentum space; that is why the broadening of the momentum distribution is diffusive in form. The width of the distribution of such particles increases as the square root of the kick number. This type of behaviour is known as *normal diffusion*. If the kick number is n, and the width of the momentum distribution increases as $n^{1/2}$, then the mean kinetic energy of these particles increases linearly with n. However, not all the particles in the system are to be found in stochastic regions of phase space, and those particles in the stable regions modify the characteristics of the behaviour of the ensemble as a whole. Some particles can have values of χ and ρ prior to a kick such that, for certain K, the particle receives the maximum impulse from a kick and also receives this maximum impulse from all subsequent kicks. Thus the momentum of the particle increases linearly with n and its energy increases quadratically. Such particles are said to be in an *accelerator mode* [86]. When a system contains such particles, the mean kinetic energy of the ensemble increases as n^α, where $\alpha > 1$. Thus the increase in energy is superdiffusive. This type of behaviour is called *anomalous diffusion*. In other circumstances, *i.e.* for different values of K, some particles may be in regions of stability in phase space such that successive kicks tend to counteract one another's effect. Thus there is very little increase in the momentum of such particles and the mean kinetic energy of the ensemble increases as n^α, where $\alpha < 1$. This, too, is anomalous diffusion, though in this case the energy increase is subdiffusive. At small values of K, the inhibition of momentum diffusion by KAM boundaries would also yield subdiffusive energy growth.

As stated above, there is one free parameter in this system, K, that determines the characteristics of phase space and the behaviour of the mean kinetic energy of the system. This assertion relies on the initial distribution of positions and momenta of particles being sufficiently fine-grained, and covering all of phase space, because the precise behaviour of an individual particle will depend on its initial values of position and momentum, as well as on K. Since the momentum increase is generally diffusive, it can be characterised by a diffusion parameter $D(K)$, so that the mean kinetic energy is given by

$$\bar{E}(n) = D(K)n^\alpha \tag{3.8}$$

where $\alpha = 1$ for normal diffusion and $\alpha \neq 1$ for anomalous diffusion. The energy here is expressed in scaled units, in which the kinetic energy of an individual particle is $E = \rho^2$. An expression for $D(K)$ can be derived using the method of Fourier paths [86] and the result is

$$D(K) = \frac{K^2}{2}\left[\frac{1}{2} - J_2(K) - J_1^2(K) + J_2^2(K) + J_3^2(K)\right], \tag{3.9}$$

where the series in brackets is truncated at order K^{-1}, and $J_m(K)$ is the mth order

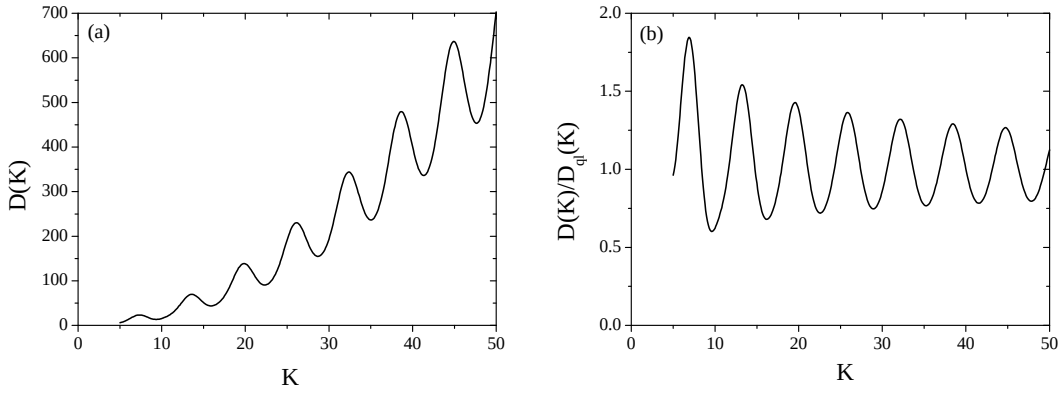

Figure 3.4: (a) The diffusion parameter $D(K)$. (b) The ratio of the diffusion parameter to the quasilinear result, $D_{\rm ql}(K)$.

Bessel function of the first kind. In the Fourier path method, this result is achieved by taking into account kick-to-kick correlations; truncation at order K^{-1} means that only low-order correlations are considered. If the correlations are ignored, so we assume that at every kick the positions of the particles are randomly and uniformly distributed between 0 and 2π, we obtain the so-called quasilinear result $D_{\rm ql}(K) = K^2/4$. The diffusion parameter is plotted in Fig. 3.4(a), and its ratio to the quasilinear result is shown in Fig. 3.4(b). Values of the diffusion parameter for $K < 4.5$ as calculated by the expression in Eq. (3.9) are inaccurate because the effect of KAM tori and their remnant cantori in limiting momentum diffusion is significant. Furthermore, $D(K)$ does not fully express the extent of the momentum diffusion in the case where this is anomalous. It always assumes linear diffusion and does not fully incorporate the effect of highly correlated motion in the regions of stability in phase space. To remedy these inaccuracies, additional Fourier paths would have to be calculated to yield quantitative agreement with numerical results. This is a long and tedious process and additional physical insight can more usefully be attained by numerical iteration of the standard mapping.

For large values of K (say $K > 4$) where most of phase space is chaotic, a particle may move throughout the chaotic region of phase space and 'stick' to a region of stability for some time before leaving it to continue its momentum diffusion. Such a particle will, therefore, contribute to the phenomenon of anomalous diffusion, either enhancing or reducing the momentum diffusion in the cases where the stable region leads to ballistic momentum increase or negligible momentum increase, respectively. A general particle will undergo periods of random walk in momentum space, interspersed by periods of ballistic momentum increase and periods of very little momentum increase. Such a particle will, therefore, execute a Lévy flight trajectory in momentum space [92]. The extent to which the various types of motion in momentum space can occur depends on K and is evident in the variation of $D(K)$ though, as stated, this does not fully take the influence of stable trajectories into account. From Fig. 3.4(b), it is clear where momentum diffusion is maximal or minimal in relation to the quasilinear result. Figure 3.5 shows the

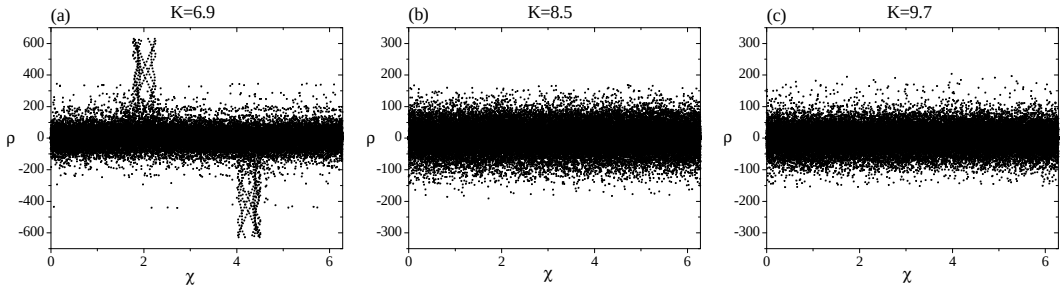

Figure 3.5: Phase space portraits for the kicked rotor produced by 100 iterations of the standard mapping, with (a) $K = 6.9$, (b) $K = 8.5$, and (c) $K = 9.7$. Note the accelerator modes in (a), and the subdiffusive growth of the width of the momentum distribution in (c).

phase space portraits in the cases (i) $K = 6.9$, where the ratio $D(K)/D_{\rm ql}(K)$ is a maximum, (ii) $K = 8.5$, where $D(K)/D_{\rm ql}(K) \simeq 1$ and (iii) $K = 9.7$, where $D(K)/D_{\rm ql}(K)$ is a minimum. As in the case of Fig. 3.3, these portraits were generated by 100 iterations of the standard mapping. For $K = 6.9$ and $K = 9.7$, the system displays anomalous diffusion. The behaviour of the system in the two cases is superdiffusive and subdiffusive, respectively, and the trajectories of particles in accelerator modes are particularly clear in Fig. 3.5(a). For $K = 8.5$ the system exhibits normal diffusion and the momentum distribution in Fig. 3.5(b) is markedly broader than that in Fig. 3.5(c).

In the system with which the experiments in this thesis were performed, the application of pulses of the periodic potential constituted by the standing wave would result in the system behaving as a quantum δ-kicked rotor. Therefore it was useful to simulate the analogous classical δ-kicked rotor system in order to see the differences and similarities in behaviour. This was achieved by performing an iteration of the standard mapping to calculate the trajectories of 10^5 particles with a range of initial values of χ and ρ. The distribution of these initial positions and momenta took into account that in the experiment itself. The atoms in the MOT had an initial momentum distribution (after trapping and cooling) that was Gaussian, centred around zero, with a FWHM of 12 photon recoils (see Ch. 2). This corresponded to a temperature of 5μK. Their spatial distribution was effectively uniform over any given period of the potential. The output of this simulation gave the momentum distribution of the particle ensemble after a specified number of kicks had been applied to the system.

The behaviour of the δ-kicked rotor is usually analysed in terms of the evolution of the momentum distribution. In the absence of any asymmetric perturbation to the system, such as a unidirectional external force like gravity, the momentum distribution is always symmetric. Another frequently used measure of its behaviour is the mean kinetic energy (henceforth referred to as the 'mean energy') of the particles in the system. The variation of the mean energy with kick number or K is a clear indicator of the characteristics of the system's behaviour, and the

calculation of its value using a momentum distribution obtained from numerical simulation or experiment is straightforward. Therefore this quantity is extensively employed in this thesis. The momentum distributions shown are expressed in units of the momentum of a photon, $\hbar k_1$, in the light composing the standing wave (red-detuned from the caesium D1 transition). The mean energies are also been presented in experimental units. The unit of energy is the recoil energy of an atom when it absorbs one photon from the standing wave, *i.e.* $E_{\rm rec} = \hbar^2 k_1^2/2m$. The data have been presented in experimental units rather than the customary theoretical scaled units χ and ρ because they allow a ready feel for the magnitude of the dynamical processes at play. The quantities that were varied systematically in the experiment were the time period T of a standing wave pulse sequence, and the number n of pulses applied. These quantities could be very precisely controlled, whereas there was less control over the strength of the optical potential experienced by the atoms, and therefore the value of K, due to fluctuations in the intensity and detuning of light in the standing wave, some uncertainty in the calibration of AOM3 that controlled this intensity (see Sec. 2.3), and the range of light intensities experienced by the atoms. The mean energies have been plotted as a function of the quantities, T and n, that were known with precision.

Figure 3.6 shows four examples of momentum distributions, plotted on a logarithmic scale, that have been calculated by the simulation of the classical δ-kicked rotor. For the experimental system under discussion, $G = 1.4051 \times 10^7\,{\rm m}^{-1}$ because the spatial period $\lambda_{\rm spat}$ of the pulsed potential is half the wavelength of the light, which is 894.347 nm for the D1 transition in caesium. The mass of a caesium atom is $m = 2.209 \times 10^{-25}\,{\rm kg}$. To generate these pseudoexperimental momenta, the value $T = 60.5\mu{\rm s}$ for the kicking interval was used. This is the value that was used in many of the experiments described in this thesis. The characteristics of the momentum distributions in Fig. 3.6 are noteworthy. Figure 3.6(a) shows the initial Gaussian distribution that has a FWHM of $12\hbar k_1$. Figure 3.6(b) shows the result of evolving this distribution over 50 iterations of the standard mapping, with $K = 6.9$. As described above, anomalous diffusion is evident for this value of K, and the accelerator modes are very clear in the momentum distribution. It should also be noted that the central bulk of the distribution is not Gaussian in form. Figure 3.6(c) shows the result of the same evolution of the initial distribution but with $K = 8.5$. For this value of K, normal diffusion is apparent ($D(K)/D_{\rm ql}(K) \simeq 1$) and the momentum distribution remains Gaussian, though it has broadened significantly compared with its initial state. Figure 3.6(d) shows the outcome of the application of 50 iterations of the standard mapping with $K = 9.7$. Again, the distribution has remained Gaussian but is noticeably narrower than that shown in Fig. 3.6(c). Anomalous diffusion is evident in Fig. 3.6(d) but has suppressed rather than enhanced the spreading of the momentum diffusion relative to the quasilinear case.

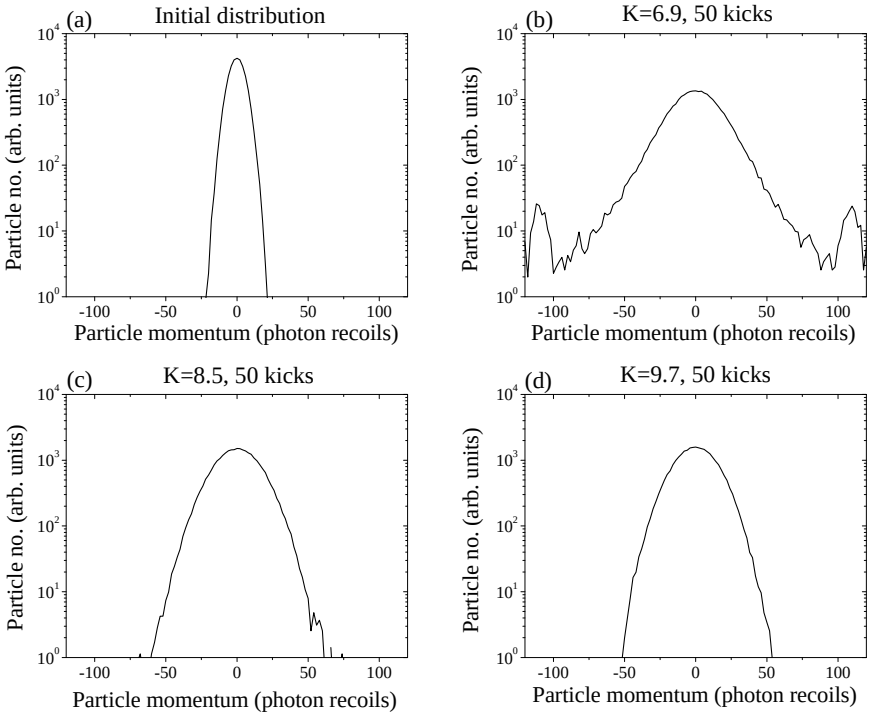

Figure 3.6: The momentum distribution of particles in the classical δ-kicked rotor system as generated by simulation. Note that the distributions have been plotted on a logarithmic scale. (a) The initial distribution, corresponding to a temperature of 5μK, (b) distribution after 50 kicks with $K = 6.9$, (c) distribution after 50 kicks with $K = 8.5$, and (d) distribution after 50 kicks with $K = 9.7$. Note the accelerator modes in (b), and the fact that the momentum distribution in (d) is narrower than in either (b) or (c).

3.2 Quantum δ-kicked rotor

The quantum δ-kicked rotor (see the seminal paper by Casati *et al.* on p. 334 of Ref. [29]) is the quantum mechanical analogue of the classical δ-kicked rotor discussed in Sec. 3.1. A spatially periodic potential is applied to a quantum system as a series of δ-function pulses. The Hamiltonian of this system is

$$\hat{H} = \frac{\hat{p}^2}{2m} + \frac{X_{\max}}{G}[1 + \cos(G\hat{z})] \sum_n \delta(t - nT), \tag{3.10}$$

where $\hat{p}$ is the momentum operator and $\hat{z}$ the position operator. The other quantities are as defined in Sec. 3.1, *i.e.* m is the particle mass, $X_{\max}$ is the magnitude of the maximum possible impulse received by a classical point particle, t is the time, T is the time interval between applications of the potential (the 'pulse period'), n is the kick number and $G = 2\pi/\lambda_{\text{spat}}$, where λ_{spat} is the spatial period of the potential. The caret $\hat{}$ is used to denote operator quantities, so that, for example, $\hat{z}$ is the operator corresponding to the classical position z. As in Eqs. (3.5) and (3.6), scaling to obtain the dimensionless parameters χ and ρ may be used, and the Hamiltonian may be expressed in terms of their corresponding operators $\hat{\chi}$ and $\hat{\rho}$, as well as the stochasticity parameter K. Whereas the development of the classical δ-kicked rotor was described by the standard mapping, the evolution of the quantum system is determined by successive applications of the *Floquet operator*, $\hat{U}$ [31]. This operator is obtained by integrating the Schrödinger equation from the instant just before one kick to the instant just before the next. It expresses the effect on the system of one application of the potential, plus the subsequent free evolution that takes place for a time T. Thus

$$\hat{U} = \hat{U}_{\text{free}}\hat{U}_{\text{int}} \tag{3.11}$$

where $\hat{U}_{\text{int}}$ is the operator describing the effect of the potential and $\hat{U}_{\text{free}}$ describes the subsequent free evolution. Hence if $|\psi_n\rangle$ is the wavefunction of the system just before the application of the $(n+1)$th kick, we can write $|\psi_{n+1}\rangle = \hat{U}|\psi_n\rangle$. The Floquet operator for the δ-kicked rotor is given by

$$\hat{U} = \exp\left(-i\frac{\hat{p}^2}{2m\hbar}T\right)\exp\left(-i\frac{X_{\max}}{\hbar G}[1 + \cos(G\hat{z})]\right) \tag{3.12}$$

$$= \exp\left(-i\frac{\hat{\rho}^2}{2\hbar}\right)\exp\left(-i\frac{K}{\hbar}[1 + \cos(\hat{\chi})]\right). \tag{3.13}$$

where the last expression is in terms of dimensionless quantities. Note that, in addition to K, there is a quantum parameter, $\hbar$, present in the Floquet operator. This is defined by $\hbar = \hbar G^2 T/m = -i[\hat{\chi}, \hat{\rho}]$. Since $\hbar$ is equal to the commutator of $\hat{\chi}$ and $\hat{\rho}$, it is effectively a scaled Planck constant and as such it plays a role in determining the character of the system's evolution. If the action of the system (*i.e.* the momentum attained as a result of the kicking process) is large compared with the value of $\hbar$, the system may be expected to behave in a more classical

manner since Planck's constant is effectively smaller. Thus the quantum mechanical evolution of the system is determined by two independently variable quantities, K and $\bar{k}$, whereas the evolution of the classical system depends on only one parameter, K. When $\bar{k}$ is a rational multiple of 4π, *i.e.* $\bar{k} = 4\pi a/b$, where a and b are mutually prime integers, the system is said to exhibit a *quantum resonance* [31, 93, 94] of order b. The characteristics of this phenomenon will be discussed in Sec. 3.3. The terminology 'quantum resonance' should not be confused with the 'nonlinear resonances' that exist in classically chaotic systems and whose overlap leads to unbounded momentum diffusion in the classical δ-kicked rotor. It has been argued (see, for example, p. 412 of Ref. [31]) that the term 'quantum resonance' should not be used for the phenomena occurring when $\bar{k} = 4\pi a/b$, in order to avoid precisely this confusion. However, as the use of the term 'quantum resonance' to describe these phenomena has become standard, this thesis conforms to the established convention.

At the instant of the application of each δ-function pulse of the potential, the de Broglie wave of a particle experiences a position-dependent phase shift $K[1+\cos(\chi)]/\bar{k}$. The amplitude of the variation with position of this phase shift is $\phi_d = K/\bar{k}$. Thus the effect of the potential may be viewed as being equivalent to that of a phase diffraction grating. Since the spatial period of this grating is $\lambda_{\text{spat}} = 2\pi/G$, the grating may impart momenta to the incident matter wave in units of $\hbar G$. The quantity ϕ_d is the maximum classical impulse that can be received by a particle, expressed in units of momentum recoil from the phase grating, *i.e.* $\phi_d = X_{\max}/\hbar G$. It determines the probability of different momenta (integer multiples of $\hbar G$) being imparted by the grating to portions of the incident de Broglie wave, *i.e.* the probability of populating different diffraction orders. This may be seen more clearly by rewriting the part of the Floquet operator that expresses the effect of the kick, namely $\exp(-iK[1+\cos(\hat{\chi})]/\bar{k})$, with the use of the relation $\phi_d = K/\bar{k}$, and the identity $\exp(-i\epsilon\cos x) \equiv \sum_{r=-\infty}^{\infty}(-i)^r J_r(\epsilon)\exp(-irx)$ [95] to give

$$\exp\left(-i\frac{K}{\bar{k}}[1+\cos(\hat{\chi})]\right) \equiv \exp(-i\phi_d)\exp(-i\phi_d\cos(\hat{\chi})) \tag{3.14}$$

$$\equiv \exp(-i\phi_d)\sum_{r=-\infty}^{\infty}(-i)^r J_r(\phi_d)\exp(-ir\hat{\chi}) \tag{3.15}$$

$$\equiv \exp(-i\phi_d)\sum_{s=-\infty}^{\infty} i^s J_s(\phi_d)\exp(is\hat{\chi}) \tag{3.16}$$

where the last equivalence can be made since the sum is over all possible s. Thus the effect of a kick can be decomposed into an infinite sum of momentum displacement operators, $\exp(is\hat{\chi})$, weighted by sth order Bessel functions of the first kind, $J_s(\phi_d)$. The global phase, ϕ_d, that is imparted to the de Broglie wave by each application of the potential has no effect on the dynamics of the system and may be ignored. We can examine the application of the nth kick of the potential to an incident plane wave $\psi(\chi) \propto \exp(i\kappa\chi)$. A plane wave in this form with scaled wavenumber κ (not necessarily an integer) corresponds to a momentum eigenstate with eigenvalue $\kappa\hbar G$ (in experimental units). Suppose this momentum state were populated by

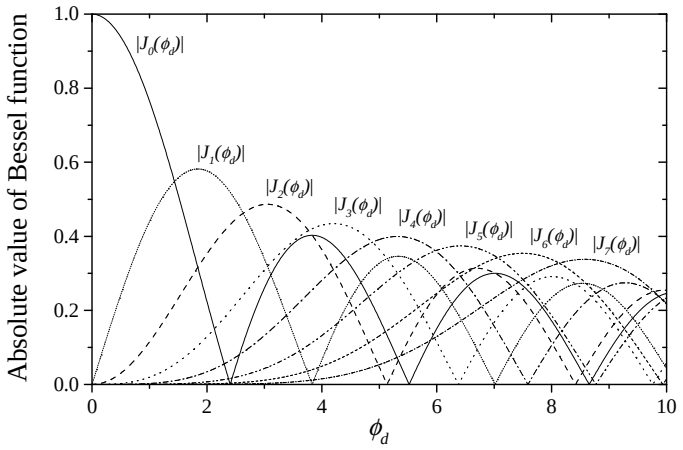

Figure 3.7: The absolute values of the Bessel functions $J_n(\phi_d)$ for integer values of n from 0 to 7.

diffraction from an initial plane wave incident on the periodic potential, and which had a momentum ρ_i in the direction of the potential. If it were populated due to the transfer of u units of momentum by the $(n-1)$ previous applications of the potential then $\kappa = \rho_i/k + u$ and its dimensionless momentum would be $\rho_{u,n-1} = \rho_i + uk$. The operator $\hat{U}_u^{\rm int}$ representing the effect of the nth kick of the potential on this plane wave state $|u\rangle$ can be written as a sum of matrix elements, $\hat{U}_{vu}^{\rm int}$, each of which has the form [31]

$$\hat{U}_{vu}^{\rm int} = i^{v-u} J_{v-u}(\phi_d)|v\rangle\langle u| \tag{3.17}$$

The states $|v\rangle$, with dimensionless momenta $\rho_{v,n} = \rho_i + vk$, are the possible final momentum states populated by diffraction from the potential. It can be seen that the probability of being diffracted from the uth state to the vth state is dependent on $J_{v-u}(\phi_d)$ and hence on the value of ϕ_d. The Bessel function $J_s(\phi_d)$ has its maximum value when $\phi_d \sim (s+1)$. This can be seen in Fig. 3.7, which shows the absolute values of eight Bessel functions of the first kind as a function of ϕ_d. Hence the preferentially imparted momentum transfer resulting from a kick increases as ϕ_d increases. It is also clear from Fig. 3.7 that as ϕ_d increases, the number of different values of s for which $|J_s(\phi_d)|$ is significantly different from zero, say greater than 0.15, rises. Therefore as ϕ_d increases so does the range of momenta imparted by a kick. Both the most probable value of $(v-u)$, and the range of values of v that are significantly populated by diffraction from the state $|u\rangle$, increase as ϕ_d increases. The effect of the potential on a wavefunction in which a range of states $|u\rangle$ is occupied can be represented by $\hat{U}_{\rm int}$, which is equal to a sum over the operators $\hat{U}_u^{\rm int}$ for all the individual values of u. Hence

$$\hat{U}_{\rm int} = \sum_{u=-\infty}^{\infty} \sum_{v=-\infty}^{\infty} i^{v-u} J_{v-u}(\phi_d)|v\rangle\langle u| \tag{3.18}$$

Following the application of the nth kick, free evolution of all the different populated momentum states $|v\rangle$ occurs and results in further accumulation of phase, but

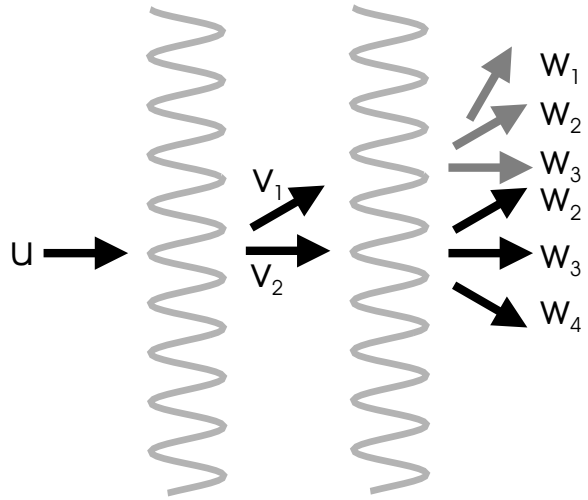

Figure 3.8: The diffractive effect of two pulses of the standing wave applied to an initial plane wave in the momentum state $|u\rangle$ (see text). Upon diffraction, this plane wave populates the states $|v_1\rangle$ and $|v_2\rangle$, which then evolve freely. Each of these then populates further states $|w_1\rangle$ to $|w_4\rangle$; the grey states are those created from diffraction of $|v_1\rangle$, while the black states are those created from diffraction of $|v_2\rangle$. The contributions to $|w_2\rangle$, for example, from each v-state may reinforce if the phases accumulated by the v-states between the two diffractions differ by an integer multiple of 2π.

no change in the population of the different diffraction orders. The operator $\hat{U}_{\text{free}}$ representing this free evolution can be written as another sum of matrix elements

$$\hat{U}_{\text{free}} = \sum_{v=-\infty}^{\infty} \hat{U}^{\text{free}}_{v_f v} = \sum_{v=-\infty}^{\infty} \exp(-i\phi_v)\delta_{v_f v}|v_f\rangle\langle v| \tag{3.19}$$

where $|v\rangle$ and $|v_f\rangle$ are the occupied states at the beginning and end of the free evolution period, respectively, and ϕ_v is the phase accumulated by $|v\rangle$ over the interval between the nth and $(n+1)$th kicks. This is given by

$$\phi_v = \frac{1}{2\hbar k}[\rho_i^2 + (v\hbar k)^2 + 2v\hbar k\rho_i] \tag{3.20}$$

The response of the initially plane wave to subsequent applications of the Floquet operator is determined by the differences in the phases accumulated over the periods of free evolution by the momentum states $|v\rangle$. Why is this? After having evolved freely, any one of these states will respond to the diffractive effect of the next application of the potential by populating numerous neighbouring momentum states $|w\rangle$. The probability amplitude of populating each of the states $|w\rangle$ is determined by $\hat{U}_{\text{int}}$. An example of this process is shown in Fig. 3.8. Different momentum states, $|v_i\rangle$, populated by the first diffraction can contribute to the population in a certain momentum state, $|w_i\rangle$, following the second diffraction. The relative phases of the contributions to $|w_i\rangle$ from the different momentum states $|v_i\rangle$ will determine the population of $|w_i\rangle$. Taking the example shown in Fig. 3.8,

if the phases ϕ_v evolved by $|v_1\rangle$ and $|v_2\rangle$ between the successive applications of the potential differ by an integer multiple of 2π, the contributions from each state to, say, $|w_2\rangle$ will reinforce. The states $|v_1\rangle$ and $|v_2\rangle$ are said to 'rephase'. For two different momentum states $|v\rangle$ and $|v'\rangle$ created by diffraction from the plane wave $|u\rangle$, the difference in the values of ϕ_v is

$$F_{v,v',\rho_i} = \phi_v - \phi_{v'} = \frac{1}{2}[(v^2 - v'^2)k + 2\rho_i(v - v')] \tag{3.21}$$

If two different initial plane waves with momenta $\rho_{i,1}$ and $\rho_{i,2}$ give values of F that differ by an integer multiple of 2π, the response to the potential of these plane waves will be identical. The relative phases accumulated between kicks by the diffraction orders produced from each wave will be identical *modulo* 2π. This will be true if $(\rho_{i,1} - \rho_{i,2})(v - v') = 2Z\pi$, where Z is an integer. Since v and v' are integers, this condition will be fulfilled for all v and v' if $(\rho_{i,1} - \rho_{i,2}) = \text{integer} \times 2\pi$. Thus initial momenta that differ by an integer multiple of 2π are identical in their response to the application of the potential. The response of a plane wave of any momentum is, therefore, equivalent to that of a plane wave whose momentum lies in the range $-\pi < \rho \leq \pi$. These momenta will be called *reduced momenta* and they demonstrate all the different types of dynamical behaviour that are possible in the system. The similarity with the periodicity of the classical phase space should be noted. This equivalence, in both the classical and quantum systems, of momenta that differ by integer multiples of 2π is due to the spatial periodicity of the system. This phenomenon is similar to the solid state physics result in which any Bloch state is equivalent to one whose wavevector differs from that of the first by an integer number of reciprocal lattice vectors and lies in the first Brillouin zone [96, 97]. However, in that case the potential is time-independent and the equivalence is between momenta separated by integer multiples of k, in the scaled units used here, and the first Brillouin zone encompasses the range $-k/2 < \rho \leq k/2$. The momenta in this range are known as *quasimomenta*. The quasimomentum is a conserved quantity in the diffractive process that results from the pulsed application of the potential in the δ-kicked rotor, since this imparts momenta in integer multiples of k. The reduced momentum is not conserved.

When k is an integer multiple of 4π, so that the system fulfils the condition for a first-order quantum resonance, the interval T between successive applications of the δ-function pulses of the potential is of special significance. Over this time, the phase ϕ_v evolved by every diffraction order produced from an incident wave with no initial momentum component in the direction of the potential (*i.e.* $\rho_i = 0$) is an integer multiple of 2π. Consequently, the wave at the end of the period of free evolution is an exact re-image of the form it had at the beginning of it, that is, immediately after the previous application of the potential. The condition $k = 4\pi$ leads to an expression for the smallest free evolution time for which this effect occurs

$$T_{\mathrm{T}} = \frac{4\pi m}{\hbar G^2} \tag{3.22}$$

This re-imaging is an effect already known in optics, called the Talbot effect [98], and this time T_{T} is known as the Talbot time. Due to this re-imaging, the free

evolution of the wave between applications of the potential can be neglected when the pulse period is an integer multiple of T_{T}. The effect of the potential is then equivalent to a single δ-function pulse whose effective value of ϕ_d increases by a fixed amount, equal to the true single-pulse value of ϕ_d, with each successive application. When the pulse period is an odd half-integer multiple of T_{T}, *i.e.* an odd integer multiple of the half-Talbot time $T_{1/2}$, the wave at the end of the free evolution period is π radians out of phase with its form at the beginning of this period, so the phase distribution of the re-image is displaced laterally by $\lambda_{\mathrm{spat}}/2$. Such a pulse period corresponds to a second-order quantum resonance of the system. For higher-order quantum resonances, given by pulse periods for which $T = T_{\mathrm{T}}a/b$, where a and b are mutually prime integers and $b > 2$, the fractional Talbot effect occurs in which a modified re-image of the wave, with a spatial period different from λ_{spat}, is produced. The case just discussed of $b = 2$, $T = aT_{1/2}$, where a is an odd integer, constitutes a special case of the fractional Talbot effect.

The Talbot effect for evolution times equal to integer multiples of $T_{1/2}$ was first observed in atom optics by passing a beam of sodium atoms through two identical material gratings (therefore *amplitude* gratings) separated along the beam path by a certain distance [99]. The contrast of the Moiré fringes produced by movement of the second grating in the direction perpendicular to the beam was a measure of the extent to which re-imaging occurred. The separation distance between the gratings was varied and the corresponding variation of the Moiré contrast was measured. The maxima in contrast occurred when the transit time of the beam between the gratings was an integer multiple of $T_{1/2}$, so that re-imaging occurred. This investigation was of the Talbot effect in the spatial domain, as diffraction was effected by the static gratings acting on a moving beam. Use of the static grating meant that the magnitude of the momentum of a diffracted atom, and hence its kinetic energy, remained constant and only its direction was altered. For this reason it was necessary to be in the regime of the paraxial approximation in order to observe the re-imaging. If this approximation had not been applicable then the variation of wavefront phase across an observation plane perpendicular to the beam path would have prevented the re-imaging. Due to the short de Broglie wavelength λ_{dB} of the atoms in the beam, the paraxial approximation $\lambda_{\mathrm{dB}} \ll \lambda_{\mathrm{spat}}$, where λ_{spat} is the spatial period of the grating, was applicable and re-imaging was observed.

The Talbot effect can also be observed in atom optics in the time domain. In this case, the gratings are applied as pulses of a standing wave of light, as in the experiments discussed in this thesis, and are *phase* gratings. Due to the short duration of the pulses, there is a range of photon momenta present in the light so diffraction into several orders, separated in momentum by $\hbar G$, is possible (this will be discussed below in the context of the Kapitza-Dirac effect [100]). The change to the atomic momenta means that the kinetic energy of the atoms is modified, so different diffraction orders accumulate different phases ϕ_v, as described above, over the subsequent free evolution. When this free evolution occurs for a time T_{T}, a wave that initially had no momentum in the direction of the grating, $\rho_i = 0$, is re-imaged.

This means that the spatial dependence of the wave's phase after the free evolution is exactly the same as that immediately following the application of the standing wave. There is no paraxial approximation involved. This effect was observed by applying pulses of a standing wave of light to a Bose-Einstein condensate of sodium atoms [101]. The first pulse populated a number of diffraction orders, which then evolved freely until the second pulse was applied. When the free evolution time was T_{T}, the application of the second pulse resulted in further diffraction, and the distribution of population in the diffraction orders was the same as that which would be observed due to a single pulse of twice the potential strength. This meant that re-imaging of the wavefunction must have occurred, so that, after evolving freely for a time T_{T}, the wavefunction must have replicated the form that it had immediately after the first pulse. When the interval between the pulses was $T_{1/2}$, the application of the second pulse resulted in a reversal of the diffractive effect of the first and the final momentum distribution of the atoms was identical to that before the application of the first pulse. This was an experimental confirmation that if free evolution occurs for a time $T_{1/2}$ then the re-image of the wavefunction is π radians out of phase with the form it had immediately after the first application of the potential. The quantum resonance phenomena that will be discussed in Sec. 3.3 are further manifestations of phenomena related to the Talbot effect.

The investigations of the quantum δ-kicked rotor that are detailed in this thesis were performed using the experimental apparatus described in Ch. 2, and using numerical simulations. For the experimental work, as explained in Ch. 2, approximately 10^7 caesium atoms were trapped and cooled in a MOT to a temperature of 5μK. They were then released and pulses of a standing wave of light that was red-detuned by 20 to 30 GHz from the ($F = 4 \rightarrow F' = 3$) D1 transition were applied. The energy of an atomic state in an applied light field is altered by the *light shift* (or *ac Stark shift*) [102], the magnitude of which is proportional to the intensity of the light field. Therefore the standing wave produced an energy shift in the occupied ground states of the atoms ($F = 3$ or $F = 4$ or both, depending on which experiment was being performed) that was sinusoidally dependent on z. Thus the standing wave constituted a spatially periodic potential for the atoms. As described in Sec. 2.3, these pulses were 500 ns in duration and approximately square as a function of time. This meant that they were not exact δ-functions, as the theory assumes. However, this distinction was unimportant so long as the atoms fulfilled the conditions for the Raman-Nath approximation, in which case the optical potential constituted a thin diffraction grating. In this approximation, the kinetic energy of the atom is neglected over the time t_p for which a pulse of light is applied, and is valid provided that the distance moved by an atom over the duration of a pulse is much less than the period of the potential. When the duration of the potential is sufficiently long that the distance moved by the atom is no longer small compared with the spatial period of the potential, the atom begins to average over the potential and this approximation breaks down. The averaging results in a reduction in the modulation depth of the potential applied to the atomic de Broglie waves. This effect occurs to some degree as soon as there is any movement of the atoms while the potential is applied, but can be neglected

for low atomic velocities. If the effect were neglected when the 'in-potential' distance travelled by an atom was less than $\lambda_{\rm spat}/10$, say, then it could be neglected for all atomic momenta whose magnitude was less than $27\hbar k_1$. In practice, however, reduction of the potential's effect due to a failure of the system to fulfil the Raman-Nath condition was only significant for much higher momenta than this, such as in the wings of the momentum distribution at a quantum resonance (see Sec. 3.3) or when quantum accelerator modes were created in the quantum δ-kicked accelerator (see Ch. 4).

As stated, the spatially periodic potential experienced by the atoms in the experiments discussed in this thesis was produced by the light shift, of which there is an extensive discussion in Appendix A. If the atom is considered as a two-level system then, subject to fulfilment of the condition for applicability of the Raman-Nath approximation, the Hamiltonian of the atoms in the standing wave may be written (from Eqs. (A.39) and (A.41)) as

$$\hat{H} = \frac{\hat{p}^2}{2m} - \frac{X_{\rm max}}{G}[1 + \cos(G\hat{z})] \sum_{n=0}^{\infty} \delta(t - nT) \tag{3.23}$$

where

$$X_{\rm max} = \frac{1}{2}\left(\frac{\hbar\Omega_{1,\rm max}^2}{4\delta_L}\right) t_p G \tag{3.24}$$

In Eq. (3.24), $\Omega_{1,\rm max}$ is the Rabi frequency experienced by an atom at a maximum of intensity in the standing wave. The transition frequency of the two-level system is ω_0 and the frequency of the light in the standing wave is ω_L, so $\delta_L = \omega_0 - \omega_L$ is the detuning of the light from the transition frequency. Experimentally, the light was red-detuned so $\delta_L > 0$. Equation (3.23) is valid provided that the light is sufficiently far-detuned from the frequency of the transition that there is a negligible probability of excitation to the upper state of the two-level system. This is satisfied if the condition $\delta_L t_p \gg 1$ is fulfilled, so that the temporal envelope of the pulse does not have strong frequency components near the laser detuning. As described in Appendix A, $\delta_L t_p$ was of the order of 10^5, so the neglect of the upper state is justified. It is ironic that the non-ideal nature of the experiment, in which the pulses were of finite duration, resulted in considerable simplification of the atomic dynamics. If the pulses had truly been δ-functions, the condition $\delta_L t_p \gg 1$ could not have been fulfilled and occupation of the excited state would have had to have been taken into account. When the caesium atoms used were in the $F = 4$ ground state, both the $F' = 3$ and $F' = 4$ excited states contributed with comparable strength to the light shift in the $F = 4$ state, as though there were two two-level systems acting in parallel. This has been taken into account in the analysis of Appendix A and the result of the analysis is that the maximum value of ϕ_d experienced by the atoms in the experiment was 2.3 (which will be expressed as 0.7π, as it parametrises the phase imprint of each application of the potential to a de Broglie wave). As mentioned in Sec. 2.3, however, there is some uncertainty as to the strength of the experimental potential and, in reality, the maximum value of ϕ_d was almost certainly larger than 0.7π.

Comparison of Eqs. (3.10) and (3.23) shows that the experimental energy shift of the atoms in the potential was negative, whereas the theoretical analysis above was performed for a positive potential. This distinction is of no consequence, since one potential can be obtained from the other by a shift in the (arbitrarily chosen) zero of energy and origin of position. To express this in another way, the potentials as written differ in their action on the atomic de Broglie waves only by a physically unobservable phase. The important properties of the potential are its spatial period and its modulation depth. Since the effect of the potential on a superposition of plane waves with wavefronts of infinite extent is considered, the resulting behaviour of the de Broglie waves will not depend on the sign of the potential, nor on its absolute position. The relative position of the spatial profile of the potential from pulse to pulse is, however, of crucial importance in determining the response of the matter waves, as will be clear from the discussion of the δ-kicked accelerator in Ch. 4. This position was controlled in the experiments by use of the crystal phase modulator as described in Sec. 2.4. Once released from the optical molasses, the atomic cloud fell downwards under the influence of gravity. For these investigations of the δ-kicked rotor it was necessary to remove the effect of gravity on the response of the atoms to the potential. This was achieved by using the phase modulator to shift the spatial profile of the potential at each pulse so that at the instant of the pulse the position of the profile of the standing wave relative to the atomic cloud was the same as it would have been if there were no gravitational field present.

Following release of the atoms from the MOT, the required number of pulses of the standing wave was applied. The separation between consecutive pulses had a user-determined value, t_d, so that the pulse period of the system was $T = t_d + t_p$. After application of the pulses, the atoms fell until they passed through the time-of-flight beam and their momentum distribution was measured and recorded. There was a certain amount of noise in the potential applied to the atoms due to the fluctuations of around 5% in the power of the laser light forming the standing wave. This varied on a time scale of about 1 second, as described in Sec. 2.3. For a given pulse train the power was virtually constant because the duration of the train (up to 6.3 ms) was always much less than the time scale of the power fluctuations. However, since the depth of the potential experienced by the atoms could vary from experiment to experiment by up to $\sim 5\%$, the momentum distribution that resulted from averaging over several repetitions of a given experiment could differ from that which a single run would yield. Noise due to spontaneous emission following excitation of the atom to an excited state by the standing wave light was completely negligible because the detuning of the light from any allowed transitions was so large. Using the optical Bloch equations for a two-level system [56], the steady-state spontaneous emission rate R of atoms in a far-detuned light field is given by $R = \Omega_1^2\Gamma/4\delta_L^2$, where Ω_1 is the Rabi frequency and Γ is the linewidth of the transition from which the detuning of the applied light is δ_L. This expression is valid provided that $\delta_L \gg \Omega_1, \Gamma$. This condition was comfortably fulfilled by the experimental system under discussion since δ_L was around $2 \times 10^{11}\,\mathrm{rad\,s^{-1}}$, the maximum value of Ω_1 was about $5 \times 10^9\,\mathrm{rad\,s^{-1}}$, and $\Gamma = 2.86 \times 10^7\,\mathrm{rad\,s^{-1}}$. This

result means that the mean number of spontaneous emissions undergone by each atom due to a 500 ns pulse of red-detuned D1 light in these experiments was less than 2×10^{-3}. Another potential source of noise was presented by vibrations of the apparatus, and particularly of the retroreflecting mirror. These would alter the spatial position of the potential relative to the atoms, and it would only require a vibration amplitude comparable to λ_{spat} to prevent the potential from having any effect. The results in the thesis indicate that this was not a serious problem, but it may help to account for quantitative differences between the results of the experiments and the corresponding numerical simulations. Since pulse trains only lasted up to 6.3 ms, any vibrations would have had to have a frequency greater than about 160 Hz in order to be harmful. That their effect was small can be attributed to the massive optical table on which the apparatus was located.

It should be noted that in the regime of its behaviour as a thin phase diffraction grating, the action of the potential on the atomic de Broglie waves was a manifestation of the Kapitza-Dirac effect [100, 103, 104, 105]. The Kapitza-Dirac effect as originally elucidated [100] referred to the diffraction of free electrons by a standing wave of light (also described as stimulated Compton scattering); this has recently been observed for the first time [106]. As stated above, the important properties of this type of potential are its spatial period and its modulation depth. In the non-ideal case of a real potential, the length of its finite duration is also crucial in determining the character of the behaviour that its application produces in the atoms. The potential can be approximated around each of its minima (the antinodes of the light intensity) as having a quadratic dependence on position, *i.e.* as a harmonic potential. Using this harmonic approximation, a classical oscillation frequency ω_{osc}, determined by the modulation depth and spatial period of the potential, can be defined. The duration t_p of a pulse relative to the time period of a classical oscillation is an essential factor in determining the character of the interaction of the atomic de Broglie waves with the potential. The other essential factor is the uncertainty in the energy transferred by the application of a pulse; this is also determined by the pulse duration, t_p. The uncertainty in the energy transferred by the interaction is $\tilde{E} = \hbar/2t_p$. If this is much larger than the photon recoil energy E_{rec} then a pulse of the potential can populate numerous different momentum states separated by $\hbar G$, subject to the modulation depth of the potential being sufficiently strong to supply the necessary energy. This will result in the Kapitza-Dirac effect provided that $\omega_{\mathrm{osc}} t_p \ll 1$. In the case of longer pulse durations for which this condition is not fulfilled, the de Broglie waves undergo significant evolution in the presence of the potential and the Raman-Nath approximation is no longer valid. This leads to channelling of the de Broglie waves into the potential wells [107], resulting in focusing of the atoms, and gives rise to applications in lithography [108]. For even longer pulse durations, $\tilde{E} < E_{\mathrm{rec}}$ and Bragg scattering of special incident atomic momenta occurs [109], in which the atomic kinetic energy is conserved. This is the regime in which the phenomenon of Pendellösung, when the evolution of the de Broglie waves in the light field causes the probability amplitude to oscillate back and forth between two different momentum states, is exhibited [109, 110].

To quantify the parameters of the experimental system under discussion, the pulse duration, t_p, was 500 ns, meaning that the uncertainty in the energy imparted by a pulse was $\tilde{E} = 1.1 \times 10^{-28}$J, or $85E_{\rm rec}$. Hence diffraction into many orders was possible. If the maximum depth of the potential is given by $V_{\rm max} = 2X_{\rm max}/t_pG$ then the classical oscillation frequency can be expressed as $\omega_{\rm osc} = (V_{\rm max}G^2/2m)^{1/2}$. The values of Ω_1 and δ_L given above mean that the maximum light shift that was experienced by an atom was 9.6×10^{-28}J, which is $770E_{\rm rec}$, and that $\omega_{\rm osc}t_p \simeq \pi/10$. Therefore the evolution of the atoms over the period of time for which the potential was applied could be neglected, the Raman-Nath condition was fulfilled and the potential resulted in Kapitza-Dirac behaviour. As will be discussed in Sec. 3.3.3, the strength of the potential experienced by the atoms may have been up to 1.5 times that assumed here but this does not affect any of the above conclusions. However, in the case of the large momenta that the atoms acquired in certain experiments involving quantum resonances in the δ-kicked rotor (see 3.3) or quantum accelerator modes in the δ-kicked accelerator (see Ch. 4) the movement of the atoms within the standing wave over the time for which it was applied meant that the Raman-Nath approximation was no longer valid and direct identification of the behaviour with the Kapitza-Dirac effect would not be possible.

The numerical techniques used to perform simulations of this quantum system modelled an idealised version of the system in which the kicks were true δ-functions. This was a valid description of the experimental system in the Raman-Nath regime. Even when the Raman-Nath approximation was no longer entirely valid, the results of a simulation of an ideal system were of value in trying to interpret the observed phenomena. Only for the highest momenta attained by the atoms in the δ-kicked accelerator did the Raman-Nath approximation yield results markedly different from the experimental observations, as will be discussed in Ch. 4. The simulations were performed by repeated application of the Floquet operator $\hat{U} = \hat{U}_{\rm free}\hat{U}_{\rm int}$ to an initial state that consisted of an incoherent superposition of plane waves (the simplifying assumption that there were no phase relationships between the different initial momenta present was made). The distribution of the momenta of the plane waves in this initial state reflected the distribution of atomic momenta after molasses cooling and hence was Gaussian, centred around zero with a FWHM of $12\hbar k_1$ ($6\bar{k}$ in scaled units). The simulations operated in a momentum basis with the evolution of each plane wave considered separately. The final states generated by all the initial plane waves were then added incoherently to obtain the momentum distribution of the atomic ensemble. A schematic diagram of this procedure is shown in Fig. 3.9.

The momenta ρ_i of the initial plane waves ran from $-7\bar{k}$ to $+7\bar{k}$ in steps of $0.025\bar{k}$. Although the response to the potential of any momentum greater than π or less than $-\pi$ was identical to that of a reduced momentum in the range $-\pi < \rho \leq \pi$, the entire range $-7\bar{k}$ to $+7\bar{k}$ had to be used to allow meaningful comparison with the experimental results because there was a Gaussian, rather than a uniform, distribution over the momenta. This meant that different reduced momenta were present in the initial distribution in different proportions, and simply evolving initial momenta uniformly distributed over the range $-\pi$ to π would not have

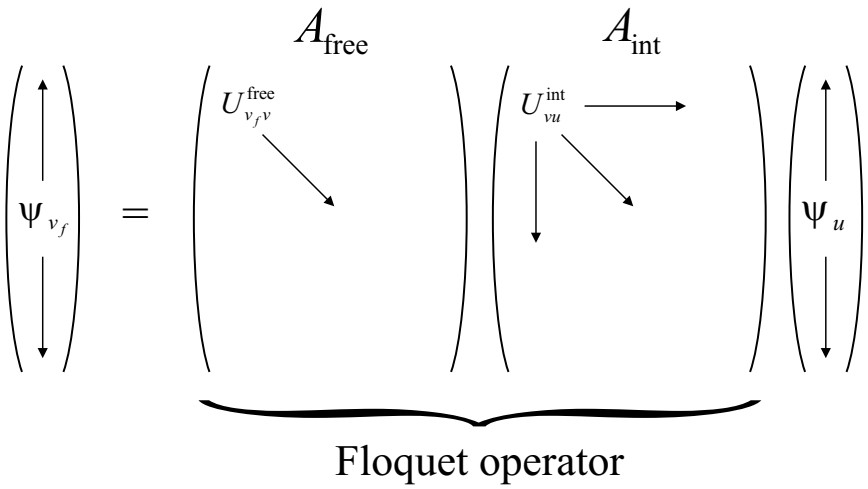

Figure 3.9: The procedure used to perform numerical simulations of the quantum δ-kicked rotor. The values ψ_u and ψ_{v_f} gave the amplitudes for occupation of diffracted momentum states from an initial plane wave of scaled momentum ρ_i. The Floquet operator could be applied repeatedly to simulate the effect of a pulse train. The laboratory momentum distribution was calculated from the resulting vector of occupation amplitudes, and the distributions from different values of ρ_i were added incoherently (see text). The matrix elements U^{int}_{vu} and $U^{\text{free}}_{v_f v}$ are defined by Eqs. (3.17) and (3.19), respectively.

been equivalent to the evolution of the experimental distribution. A given plane wave, with an initial momentum ρ_i, was written as a column vector of 121 elements, ψ_u, whose index u ran from -60 to $+60$. Each element represented the amplitude of occupation of the uth diffracted momentum state, *i.e.* the probability amplitude of the wave to have received u units of momentum ($u\hbar G$ in experimental units) from the phase diffraction grating constituted by the potential. Thus in the initial column vector for each plane wave, every element was zero apart from the $u = 0$ element, whose value was 1. To this column vector was then applied a 121×121 interaction matrix A_{int} that expressed the operator $\hat{U}_{\text{int}}$, as defined in Eq. (3.18). This resulted in a redistribution of the (complex) amplitude over the different momentum states, and represented the diffractive effect of the periodic potential on the atomic de Broglie waves. Each interaction was then followed by the application of a diagonal 121×121 free evolution matrix A_{free} that expressed the operator $\hat{U}_{\text{free}}$, as defined in Eq. (3.19). This simply added a phase ϕ_v to the phase of each complex amplitude and represented the phase accumulated by each momentum state in the wave due to the free evolution over a time T, as expressed in Eq. (3.20). The Floquet operator, $\hat{U}$, was applied as many times as required and this process was performed in parallel for each of the initial plane waves. The state of the system after each iteration was stored, as well as the final state. For each individual plane wave, the result gave the probability amplitude for occupation of each possible momentum state up to $\pm 60\hbar k$. The initial momentum of each plane wave was used to calculate the laboratory momentum of each of the populated diffraction orders,

$\rho_{\mathrm{lab},v} = \rho_i + v\hbar k$. The populations (rather than probability amplitudes) of different momenta were then binned in a histogram and the results generated by different initial plane waves were added together incoherently. This yielded the momentum distribution of the atomic ensemble, as would be measured by a TOF system. The momentum bins were generally of $\hbar k$ width ($2\hbar k_1$ in experimental units, which will be used in presentation of the results), although when high resolution was required the bin width was set to $0.1\hbar k$. These momentum distributions could be viewed as generated or used to calculate the mean energy of the atomic ensemble.

3.3 Characterisation of the δ-kicked rotor

Two aspects of the behaviour of the δ-kicked rotor, as realised using an ensemble of laser-cooled atoms, are particularly suitable for experimental investigation and characterisation, both of a qualitative and quantitative nature. These are the momentum distribution of the atoms and their mean energy. The variation of these properties with certain experimental and theoretical parameters distinguishes different regimes of the system's behaviour and thus manifests the underlying physics. It will now be discussed for the experimental system under study and the corresponding numerical simulations.

3.3.1 Momentum distributions

After trapping and cooling, the momentum distribution of the atoms in the experiment was Gaussian, with a FWHM of $12\hbar k_1$. The initial investigation was of the effect on the atoms of applying pulses of the potential with a pulse period T chosen such that this effect was fairly generic. Therefore T could not be an integer multiple of $T_{1/2}$, in which case it would correspond to a low-order quantum resonance and lead to atypical behaviour of the system, as will be discussed below. For the system under study, $T_{\mathrm{T}} = 133.3\mu$s and $T_{1/2} = 66.7\mu$s. Therefore a pulse period $T = 60.5\mu$s was used, and 30 pulses of the standing wave, with a detuning from the $(F = 4 \rightarrow F' = 3)$ transition of 30 GHz, were applied to the atoms. The resulting momentum distribution was measured, and the outcome of the experiment was averaged over three shots in order to improve the signal-noise ratio; a value in the region of 200:1 was attained. The initial and final distributions, as measured experimentally, are shown in Fig. 3.10(a), while those generated by the corresponding classical simulation, with $\phi_d = 0.8\pi$, are shown in Fig. 3.10(b). As will be discussed in Sec. 3.3.3, this is the value of ϕ_d that gave the best qualitative agreement between the variation with T of the mean energy of the system as deduced from the quantum numerical simulation and that calculated from the experimental results. It was, therefore, also the most appropriate value to use in the classical simulations.

Certain characteristics of the momentum distributions in Fig. 3.10 are immediately clear; note that the scale is logarithmic. In each case, the initial Gaussian momentum distribution has been broadened by the kicks from the potential, but

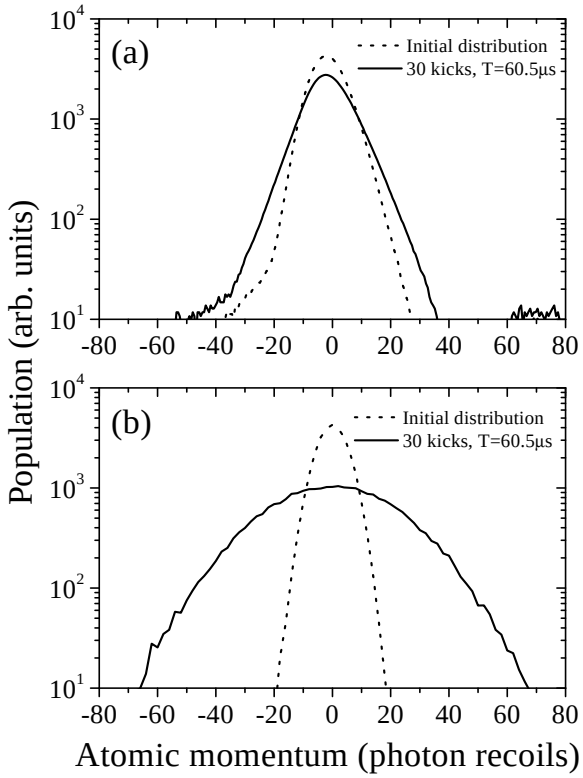

Figure 3.10: (a) Experimentally measured momentum distributions for the δ-kicked rotor system in the case where dynamical localisation is evident. The dotted line is the distribution after cooling, prior to application of any pulses of the standing wave. The continuous line is the distribution after 30 pulses, for a pulse period of 60.5μs. The light forming the standing wave was 30 GHz red-detuned from the ($F = 4 \rightarrow F' = 3$) D1 transition. Note that the distributions are plotted on a logarithmic scale, so the linear form of the plot after 30 pulses indicates an exponential distribution. (b) Momentum distributions produced by the numerical simulation of the classical δ-kicked rotor system. The dotted line is the initial distribution, prior to application of any kicks. The continuous line is the distribution after 30 kicks, for a pulse period $T = 60.5\mu$s, and $\phi_d = 0.8\pi$ ($\Rightarrow K = 14.3, \bar{k} = 1.81\pi$).

the final momentum distributions in the experimental and ideal classical cases differ in two crucial respects. Firstly, in the experimental, quantum system the final distribution is exponential, and therefore appears linear on the logarithmic scale of Fig. 3.10(a). In the classical system the momentum distribution has remained Gaussian, and therefore appears parabolic in Fig. 3.10(b). Secondly, the FWHM of the experimental distribution is $17\hbar k_1$, whereas that of the classical distribution is $52\hbar k_1$. The fact that the quantum system has a final distribution that is much narrower than the classical, and quite different in form, is a manifestation of the phenomenon of *dynamical localisation* [29, 35, 36]. This is the quantum mechanical suppression of the classical momentum diffusion, so that the spreading of the momentum distribution ceases after a certain number of kicks. Before this effect sets in, the momentum diffusion is classical in form, so that the FWHM increases as $n^{1/2}$. The value of n beyond which no further increase in the width of the momentum distribution occurs is called the *quantum break time*, n_{break}, and its value depends on both K and $\bar{k}$. The momentum distribution has become exponential in form by the time that n_{break} kicks have been applied to the system, and shows no modification to its form with further kicks. The momentum distribution is now an eigenstate of the Floquet operator; such eigenstates are exponential in form [36]. The width in scaled units of the exponentially localised momentum distribution is characterised by the *localisation length*, ξ, which is proportional to $n_{\text{break}}\bar{k}$ [111]. The form of the distribution in scaled units is given by $N(\rho) \propto \exp(-2|\rho|/\xi)$, where $N(\rho)$ is the population of atoms with momentum ρ [112, 113]. Shepelyansky has shown how the magnitude of ξ can be related to the classical diffusion parameter, $D(K)$ [112, 113]. Rather than using the classical stochasticity parameter K as the argument of the expression for $D(K)$ in Eq. (3.9), a quantum stochasticity parameter K_q is used, where K_q is defined by

$$K_q = 2\phi_d \sin\left(\frac{\bar{k}}{2}\right) \tag{3.25}$$

Using this quantity and the results in Refs. [112, 113], the localisation length can be written as

$$\xi = \bar{k}\frac{D(K_q)}{2} \tag{3.26}$$

Thus the localisation length in unscaled units can be written as

$$\zeta = \hbar G\frac{D(K_q)}{2} \tag{3.27}$$

$$= \hbar k_1 D(K_q) \tag{3.28}$$

The quantitative agreement of this expression with the results of the experiment and the quantum simulation is poor, as this expression consistently underestimates the width of the exponential momentum distribution. However, the work described in Refs. [112, 113] indicates that full quantitative agreement is not to be expected. On the other hand, the qualitative behaviour of the magnitude of ζ is in agreement with the experimental and numerical observations of the momentum width. This

is most clear when the variation of the mean energy of the system with the pulse period T is studied, and is discussed in Sec. 3.3.3. Furthermore, the behaviour of $D(K_q)$ also gives an indication of the number of kicks for which classical-like momentum diffusion occurs in a system prior to the onset of dynamical localisation because $n_{\text{break}} \propto \zeta$. Again, the value of n_{break} yielded by this formula is much less than that which is observed, but as a measure of whether the quantum break time is relatively large or small the formula is useful.

In the experimental and numerical investigations conducted, changes in the value of T for the pulse sequence applied to the atoms resulted in a variation of the width of the atomic momentum distribution after 30 pulses, and of the corresponding quantum break time. However, provided that T did not yield a value of $\hbar$ that corresponded to a quantum resonance, the resulting distribution was always exponential in form. In the case of the broad atomic distributions, for T in the region of 30μs, n_{break} was sufficiently large that the spreading of the atomic distribution had not ceased by the stage that 30 pulses had been applied to the system, although the exponential nature of the distribution was already apparent. Hence it can be concluded that the atomic momentum distribution quickly becomes exponential upon application of non-resonant pulses, though dynamical localisation takes longer to bring momentum diffusion to a halt. This is consistent with behaviour observed by the Austin group and described in Ref. [114]. Using caesium atoms and applying pulses with a period of 20μs, thus operating well in the regime of broad momentum distributions, the distribution was found to be exponential in form after only 17 kicks. The rate of broadening decreased as pulse number increased, but was still substantial after 70 pulses.

The qualitatively different case of a quantum resonance is now examined. As stated, this occurs for values of T that are rational multiples of the Talbot time, $T_{\text{T}} = 133.3\mu$s. Therefore, an investigation was made of the effect of applying 30 pulses of the standing wave to the atoms with the pulse period equal to $T_{1/2}$. The resulting momentum distribution is shown in Fig. 3.11(a), while Fig. 3.11(b) shows that produced by the numerical simulation of the effect on the corresponding classical system of 30 kicks, with $\phi_d = 0.8\pi$. It is immediately clear that the experimental distribution after 30 pulses is quite different from that shown in Fig. 3.10(a). It is non-exponential in form and there is significant population of the high-momentum states in the wings of the distribution. This is a manifestation of a quantum resonance. This data is consistent with that presented in the investigation of ballistic peaks at quantum resonances in Ref. [115], though the signal-noise ratio in Fig. 3.11(a) is higher and hence the resonant behaviour is more clear-cut. In a quantum resonance, certain initial momentum classes undergo ballistic increase in their momentum with each pulse of the potential, and these lead to the population of high-momentum states. As argued in Sec. 3.2, the response of a momentum ρ_i to pulses of the potential is determined by the differences in the inter-pulse phases accumulated by the momentum states thus populated. These phase differences are given by F_{v,v',ρ_i}, defined in Eq. (3.21). In the case of adjacent states, so that

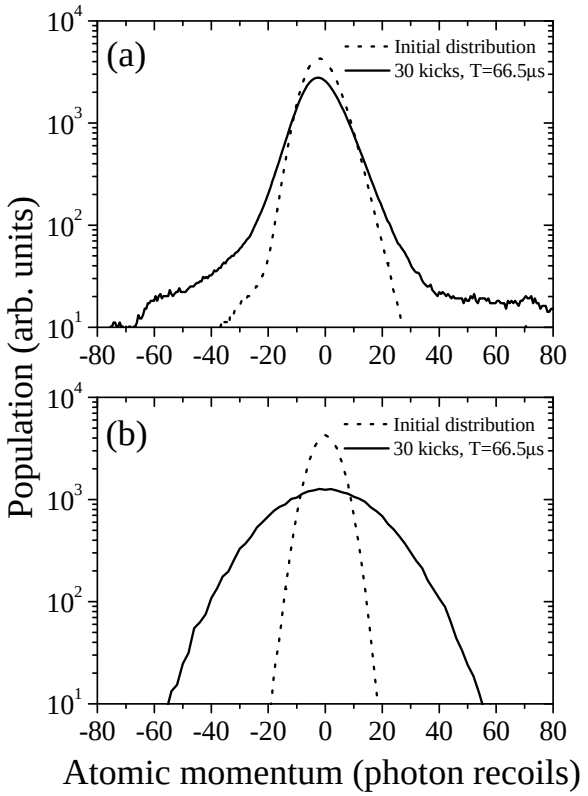

Figure 3.11: (a) Experimentally measured momentum distributions for the δ-kicked rotor system at the lowest second-order quantum resonance. The dotted line is the distribution after cooling, prior to application of any pulses of the standing wave. The continuous line is the distribution after 30 pulses, for a pulse period of 66.5μs, which is close to the half-Talbot time. The light forming the standing wave was 30 GHz red-detuned from the ($F = 4 \rightarrow F' = 3$) D1 transition. (b) Momentum distributions produced by the numerical simulation of the classical δ-kicked rotor system. The dotted line is the initial distribution, prior to application of any kicks. The continuous line is the distribution after 30 kicks, for a pulse period $T = 66.5\mu$s, and $\phi_d = 0.8\pi$ ($\Rightarrow K = 15.8, \bar{k} \simeq 2\pi$). Note that in both (a) and (b) the distributions are plotted on a logarithmic scale.

$(v - v') = 1$, the expression for F can be written

$$F_{v,v-1,\rho_i} = (2v - 1)\frac{\bar{k}}{2} + \rho_i \tag{3.29}$$

When the pulse period is $T_{1/2}$, $\bar{k} = 2\pi$, and since v is always an integer, F is then equal to $(\alpha\pi + \rho_i)$, where α is an odd integer. Thus if $\rho_i = 0$, the free phase difference evolved between adjacent states is an odd integer multiple of π, and the wave as a whole prior to the next kick is π out of phase with its state immediately after the previous kick. Two successive kicks will cancel out each other's effect and thus there will be no steady momentum diffusion; the width of the momentum distribution will oscillate from kick to kick. This is exactly the situation described in the investigation of the Talbot effect in the spatial domain using a Bose-Einstein condensate of sodium atoms [101]. On the other hand, if the value of ρ_i is such that F is an integer multiple of 2π then, as described previously, successive kicks will be cumulative in their diffractive effect on the initial plane wave. Thus a ballistic increase in the extent of the momentum states populated from this plane wave will occur, and this is the signature of a quantum resonance. For $\bar{k} = 2\pi$, this occurs for $\rho_i = ..., -3\pi, -\pi, +\pi, +3\pi, ...$ (*i.e.* for a reduced momentum, which at this value of $\bar{k}$ is equal to the quasimomentum, of π). Therefore the population in the wings of the experimental momentum distribution in Fig. 3.11(a) is due to the diffraction of the initial momentum $\hbar G/2$, as well as all other momenta that differ from this by integer multiples of $\hbar G$.

The results of the numerical simulation of the corresponding classical system, shown in Fig. 3.11(b), demonstrate that the classical behaviour is quite unlike that of the quantum system, and not dissimilar to that observed in the case $T = 60.5\mu$s, as shown in Fig. 3.10(b). Once again, the distribution has been broadened by the application of the kicks, but has remained Gaussian in form. In the case of $T = 66.5\mu$s, the distribution after 30 kicks is somewhat narrower, with a FWHM of $42\hbar k_1$, than in the case of $T = 60.5\mu$s, for which the FWHM is $52\hbar k_1$. For these values of T, K takes the values 15.8 and 14.3, respectively, and so this variation in momentum width is expected from the corresponding values of the classical diffusion parameter $D(K)$, as shown in Fig. 3.4. There is no qualitative difference between the behaviour observed in the classical system when $T = 66.5\mu$s and that observed when $T = 60.5\mu$s, and in neither case is there any deviation from the behaviour that would be expected when normal diffusion occurs. Thus it is quite clear that the forms of the momentum distributions in the experimental system, either when dynamical localisation or quantum resonant behaviour is occurring, are distinctively quantum mechanical features.

3.3.2 Variation in mean energy with pulse number

The mean energy of the particles in the δ-kicked rotor system is a quantity that is most useful in characterising the behaviour of the system. It is, of course, determined by the momentum distribution of the particles and the study of its variation with changes in certain experimental parameters affords the opportunity

of straightforward quantitative assessment of the response of the system to these changes. In the experiments performed, the quantities varied were, firstly, the number of pulses n of the potential applied to the system for a fixed value of the pulse period T, and, secondly, the value of T for a fixed value of n. The resulting behaviour of the system in the two cases is discussed here and in Sec. 3.3.3, respectively.

The variation of the mean energy of the atomic ensemble with n demonstrates the type of momentum diffusion that is taking place and hence allows the nature of the system's behaviour (dynamical localisation, quantum resonance, classical-like, or not) to be determined. As in the study of the momentum distributions, the first experimental investigation was of the behaviour of the system in the case where dynamical localisation occurred. The value of T was set to 60.5μs, and the number of pulses applied to the system was scanned from 1 to 50. The detuning of the light in the standing wave from the $(F = 4 \rightarrow F' = 3)$ transition was 30 GHz. For each individual value of n, the experiment was repeated 3 times and the average of the resultant momentum distributions was found. This average was then used to calculate the mean energy of the system. A momentum boundary at $\pm 80\hbar k_1$ was imposed in order to reduce the inaccuracy in the calculated values of the mean energy due to noise in the wings of the TOF measurement; only the momentum distribution within the range $-80\hbar k_1 \leq p \leq +80\hbar k_1$ was used for the energy calculation. As can be seen from Fig. 3.10, the signal was so much smaller beyond this boundary than in the centre that any reduction of the calculated mean energy of the atoms below its true value was negligible. Numerical simulations of both the quantum system and the corresponding classical system were also performed, with $T = 60.5\mu$s and $\phi_d = 0.8\pi$, and the momentum distributions thus produced were used to calculate the variation with n of the mean energy of the ensemble. Figure 3.12 shows the variation with pulse number n of the mean energies thus calculated, in the cases of (a) the experimental data and the results of the quantum simulation, and (b) the results of the classical simulation.

The behaviour of the quantum δ-kicked rotor as shown in Fig. 3.12 is an example of dynamical localisation. This has two signatures: the first, the exponential form of the momentum distribution, was shown in Fig. 3.10 and discussed in Sec. 3.3.1, while the second is the cessation of momentum diffusion after the quantum break time, n_{break}, that is particularly evident when the variation of the mean energy with pulse number is examined. In Fig. 3.12(a), the experimental values of the mean energy show that there is a relatively rapid increase in the mean energy of the system with the first three pulses that are applied, but that the rate of increase is reduced beyond the third pulse. This is expected; for pulse numbers $n < n_{\text{break}}$, the momentum diffusion is classical-like and the growth in the mean energy of the system with n is linear. The experimental data show the quantum suppression of momentum diffusion beyond n_{break}. This is more obvious in the results of the quantum simulation, as also shown in Fig. 3.12(a). In this case, too, the rate of increase in the mean energy is reduced beyond the third pulse but, in contrast to the experimental results, there is negligible increase in the mean energy beyond n_{break}. Instead there are small-amplitude quasiperiodic oscillations.

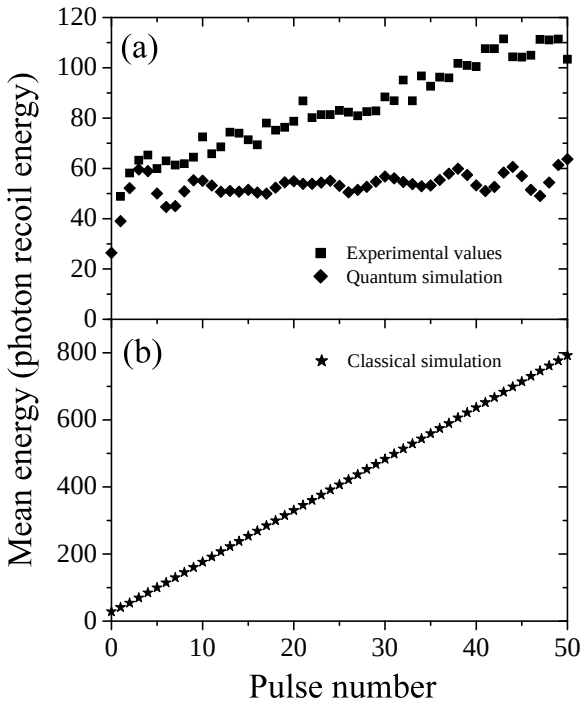

Figure 3.12: (a) Variation in the mean energy of the atomic ensemble with pulse number as calculated from the experimentally measured momentum distributions and those produced by the quantum simulation. The pulse period in each case was $T = 60.5\mu$s; the red-detuning from the ($F = 4 \rightarrow F' = 3$) D1 transition of the light forming the potential was 30 GHz, while the value of ϕ_d used in the simulation was 0.8π. (b) Variation in the mean energy of the atomic ensemble with pulse number as calculated from the momentum distributions generated by the classical simulation. The pulse period was $T = 60.5\mu$s and the value of ϕ_d used was 0.8π. Note the difference between (a) and (b) in the scales along the energy axis.

The differences between the results from the experiment and those of the numerical simulation can be accounted for by the fact that there were sources of noise present in the experimental system that are absent in the idealised system modelled in the simulation. Gravity's effect was removed through the use of the crystal phase modulator to shift the profile of the standing wave. However, there was some experimental uncertainty as to the precise value of the shift applied to the laser light in attempting to achieve this, and it was not possible to be sure that gravity's effect had been completely removed. As will be discussed in Ch. 4, gravity has a major effect on the dynamics of the system, and greatly enhances the rate of increase in the mean energy with n for a pulse period of $T = 60.5\mu$s. Therefore any residual affect that it might have would raise the rate of increase in the mean energy of the system relative to the ideal case of zero gravity. Furthermore, inaccuracy in the pulse-to-pulse positioning of the standing wave profile could be similar in its effect to vibrations, by randomising the relative position of the profile in consecutive kicks. True vibrations were also present in the system at some level, and the resultant variation in the position of the atoms relative to the potential would be expected to degrade dynamical localisation, thus leading to increased momentum diffusion after the quantum break time. It may also be that some variation in the intensity of light in the standing wave occurred during a pulse train, though, as discussed in Sec. 3.2, the measured time scale of such variation (1 second) indicates that this was not a major effect. It is known that amplitude noise can degrade localisation and so lead to an increase in the broadening of the momentum distribution, and a non-zero increase in the mean energy, beyond n_{break} [116, 117]. Additionally, the experimental noise in the wings of the momentum distribution as measured by the TOF system led to a small mean energy offset on which the true mean energy of the atoms was superimposed. This also contributes to the lack of quantitative agreement between the results of the simulation and the experiment, as does the range of values of ϕ_d experienced by the atoms in the experiment. This is in contrast to the unique value of ϕ_d used in the numerical simulations.

Use of the quantum simulation can show how individual plane waves, with different values of ρ_i, respond differently to the application of the potential. Figure 3.13 shows how the mean energy varies with n for six different initial plane waves with initial momenta ranging from 0 to $\hbar k_1$, using data generated by the quantum simulation. In each case, the variation is quasiperiodic, though the amplitudes and periods of this variation differ considerably for different values of the initial momentum. Non-resonant quasiperiodic oscillations of this type have been observed previously in numerical simulations of the quantum δ-kicked rotor [36, 118, 119, 120]. The type of quasiperiodic variation that is evident in the results of the quantum simulation shown in Fig. 3.12(a) is the result of summing over the behaviour of many initial plane waves. The experimental situation depicted in the same figure is further complicated because the atoms experience a range of values of ϕ_d due to the Gaussian profile of the intensity in the laser beams. The observed variation in the mean energy with n is a superposition of that due to atoms experiencing all the different values of ϕ_d. Since the period of the oscillations

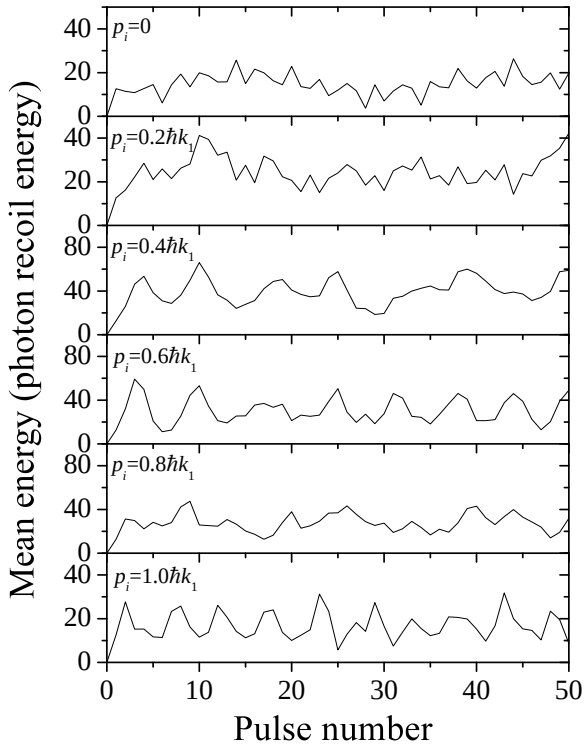

Figure 3.13: Variation in the mean energy with pulse number of different initial plane waves, as calculated from the momentum distributions generated by the quantum simulation. The pulse period was $T = 60.5\mu$s and the value of ϕ_d used was 0.8π. The plane waves had initial momenta p_i equal to 0, $0.2\hbar k_1$, $0.4\hbar k_1$, $0.6\hbar k_1$, $0.8\hbar k_1$ and $1.0\hbar k_1$, as labelled on the figure.

decreases as the value of ϕ_d increases, this results in a washing-out of oscillations of the atomic ensemble. Furthermore, the level of noise in the experimental data hampers identification of the oscillations which, even in the ideal case described by the simulation, are small in amplitude.

Despite the lack of quantitative agreement between the results from the experiment and the quantum simulation, there is, nevertheless, good qualitative agreement in certain important respects. Firstly, the classical-like momentum diffusion and its suppression beyond n_{break} in the subsequent dynamical localisation is evident in both sets of data. Secondly, the existence of quasiperiodic oscillations is clear in the results generated by the simulation and is not incompatible with the results from the experiment. This is characteristic of the behaviour of the system when $k \neq 4\pi a/b$, so that we do not have a quantum resonance. The value of n_{break} varies as T varies, and for certain values of T (*e.g.* $T = 30.5\mu$s) can be well over 100, but these essential characteristics of momentum diffusion, namely dynamical localisation and quasiperiodic oscillation, are always present. The behaviour exhibited by the results of the classical simulation, as shown in Fig. 3.12(b), demonstrates that these characteristics are peculiar to the quantum δ-kicked rotor. For this value of T, the classical δ-kicked rotor shows normal momentum diffusion, resulting in a linear variation of the mean energy with n and a constant value of the diffusion parameter $D(K)$. Signatures of dynamical localisation are completely absent, and this is true of the classical system no matter what the value of T. Therefore, the momentum diffusion of the quantum δ-kicked rotor in a regime in which dynamical localisation occurs can be seen to be quite distinct from that of its classical analogue.

A further aspect of the behaviour of the system that can be examined following the application of a pulse to a plane wave is the evolution with time of the spatial distribution of the wave. The spatial distribution resulting from diffraction of an initial plane wave is obtained by taking the Fourier transform of the momentum distribution. For a continuous momentum, and hence wavevector, variable the spatial and momentum distributions would be related by

$$\psi(z) = \frac{1}{2\pi} \int_{-\infty}^{\infty} \bar{\psi}(k) e^{-ikz} dk \tag{3.30}$$

where k is the wavevector, $\psi(z)$ is the probability amplitude distribution in position space and $\bar{\psi}(k)$ in the distribution in wavevector space. In the numerical simulation of the effect of the potential on a single plane wave, the momentum states that can be occupied are discrete, with adjacent states being separated by $\hbar G$. Therefore

$$\psi(z) = \frac{1}{2\pi} \sum_{u=-60}^{60} \bar{\psi}(k_u) e^{-ik_u z} \Delta k \tag{3.31}$$

where Δk is the wavenumber separation, G, of adjacent momentum states and $\bar{\psi}(k_u)$ is the amplitude of occupation of the momentum state $|u\rangle$. The wavevector of this state is given by $k_u = k_i + uG$, where $p_i = \hbar k_i$ is the initial momentum of the plane wave in the z-direction. Figure 3.14 shows the evolution with time

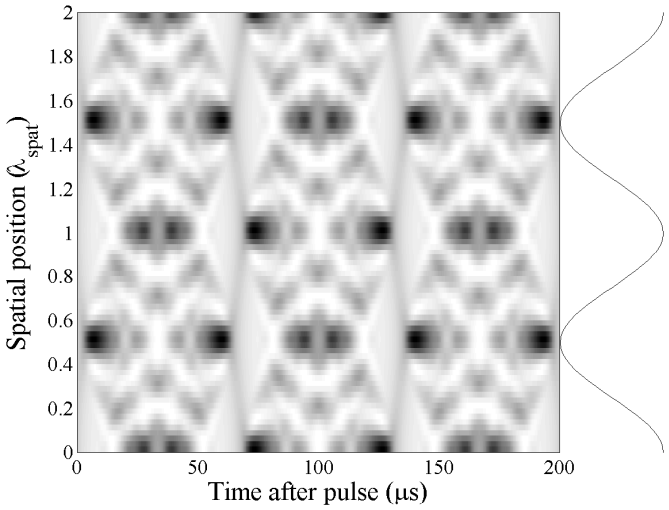

Figure 3.14: Evolution with time of the spatial distribution of an initially plane de Broglie wave, with initial momentum $p_i = 0$, after a pulse of the potential, with $\phi_d = 0.8\pi$. The darkness of the shading is proportional to the value of $|\psi(z)|^2$. The z-profile of the potential is shown on the right, to the same scale.

of the spatial distribution of a wave, $|\psi(z)|^2$, following a single application of a pulse with $\phi_d = 0.8\pi$. The darkness of the shading is proportional to the value of $|\psi(z)|^2$. This distribution was generated by use of Eq. (3.31) to transform the results of a numerical simulation of the quantum δ-kicked rotor system for a plane wave with $p_i = 0$. The spatial profile of the periodic potential is also shown. After the wave has evolved freely for 60.5μs the spatial distribution is non-uniform and the wave is periodically localised at regions of zero potential gradient. For a plane wave with $p_i \neq 0$, the spatial distribution at a time t after the pulse is the same as that shown in Fig. 3.14, apart from being offset by $(p_i/m)t$ in the z-direction. This is obvious from consideration of the behaviour of the de Broglie wave as viewed in the frame moving with velocity p_i/m relative to the laboratory frame. In the moving frame, a plane wave whose initial laboratory momentum $p_i \neq 0$ will seem to evolve with time like a wave with $p_i = 0$, as shown in Fig. 3.14. This means that at a time t the spatial distribution of the wave with $p_i \neq 0$ must be offset in the laboratory frame by $(p_i/m)t$ from that shown in Fig. 3.14. Therefore, after the system has evolved freely for 60.5μs following a pulse, all initial plane waves give rise to distributions that are periodically localised in space. When additional pulses are applied at intervals of 60.5μs, the inter-pulse free evolution is such that the wave is well-localised just before the application of each pulse. The fact that each wave is localised in a region of a particular potential gradient means that the periodic variation of the potential, which is responsible for diffraction, is less evident to the de Broglie wave. A low rate of momentum spreading through diffraction is, therefore, not a surprising consequence, though the existence of dynamical localisation does not seem an obvious corollary.

Experimental investigations of the behaviour of the system close to the lowest

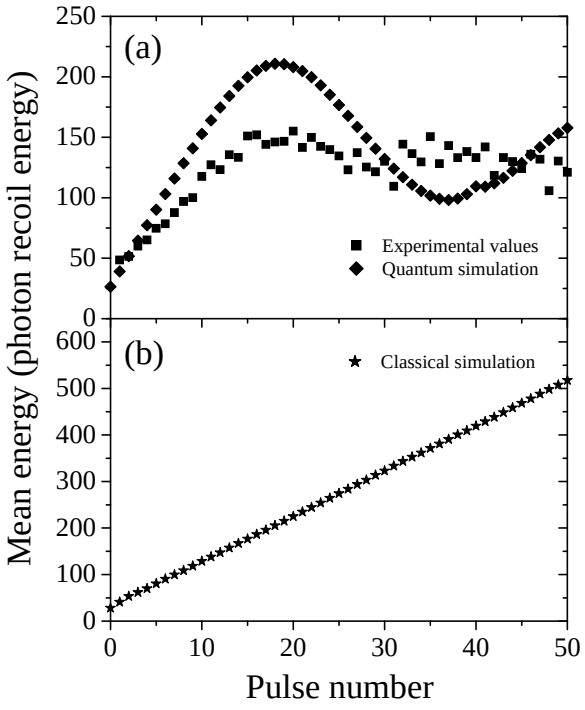

Figure 3.15: (a) Variation in the mean energy of the atomic ensemble with pulse number as calculated from the experimentally measured momentum distributions and those produced by the quantum simulation. The pulse period in each case was $T = 66.5\mu$s, corresponding to $\bar{k} \simeq 2\pi$, the lowest second-order quantum resonance; the red-detuning from the ($F = 4 \rightarrow F' = 3$) D1 transition of the light forming the potential was 30 GHz, while the value of ϕ_d used in the simulation was 0.8π. (b) Variation in the mean energy of the atomic ensemble with pulse number as calculated from the momentum distributions generated by the classical simulation. The pulse period was $T = 66.5\mu$s and the value of ϕ_d used was 0.8π. Note the difference in the scales along the energy axis between (a) and (b), and also between this figure and Fig. 3.12.

second-order quantum resonance, the half-Talbot time $T_{1/2}$, were undertaken. As when investigating the $T = 60.5\mu$s case, the number of pulses applied to the system was varied from 1 to 50 and the effect of gravity was removed through the use of the crystal phase modulator. Apart from the different value of the pulse period used, $T = 66.5\mu$s, the experimental procedure used was identical to that in the case of $T = 60.5\mu$s and, likewise, simulations of idealised quantum and classical systems were performed. The variation in the mean energy with pulse number as calculated from the experimental data at $T = 66.5\mu$s is shown in Fig. 3.15(a), along with that calculated from the results of the quantum simulation. The results from the classical simulation are shown in Fig. 3.15(b).

The behaviour of the quantum system that is observable in Fig. 3.15(a) is quite different from that when $T = 60.5\mu$s, as shown in Fig. 3.12(a). Rather then a short phase of classical-like diffusion followed by dynamical localisation after the quantum break time, Fig. 3.15(a) shows an initial phase of energy growth that is linear,

as in the classical system, but with a steeper gradient than at $T = 60.5\mu$s, and which persists for a much larger number of pulses. This does not end at a quantum break time, beyond which there is almost no diffusion, but instead there are large-amplitude oscillations in the mean energy. This characterises the behaviour of the experimental system, with its continuous spread of atomic momenta, at a first- or second-order quantum resonance, and the results from the experiment and simulation are qualitatively in agreement. The period of the oscillation is different in the two cases, and there are two reasons for this. The first is that, as at $T = 60.5\mu$s, the period of the oscillations depends on ϕ_d, and a range of values of ϕ_d was experienced by the atoms in the experiment. Thus the observed behaviour is a superposition of oscillations with different periods. The second reason is that the experimental pulse period may have been slightly different ($\pm 0.1\mu$s) from 66.5μs, and the response of the system to the potential in the vicinity of a quantum resonance depends very sensitively on the exact value of T, as will be discussed below. Indeed, this experimental uncertainty in the value of T made exact fulfilment of the condition $k = 2\pi$ nigh-on impossible (for which the precise value $T = 66.7\mu$s would be needed). Even if the timing differences were not an issue, complete quantitative agreement between the simulation and the experiment would not be expected because the noise present in the depth and position of the experimental potential applied to the atoms would hamper the resonant transfer of momentum to the atoms, thus reducing the amplitude of the oscillations in the mean energy. The range of values of ϕ_d present in the experiment not only affected the periods of oscillation but also the energy transferred to atoms, thus impairing agreement with the simulation, where a unique value was used. Additionally, the noise in the wings of the TOF signal that yielded the momentum distribution constituted a background upon which the features due to variation of the momentum width would be superimposed. Nevertheless, the qualitative agreement between the results of simulation and experiment is good.

The rapid growth in the mean energy is due to those momentum classes that best allow fulfilment of the condition $F = 2Z\pi$, where Z is an integer, as discussed in Sec. 3.3.1, and F is defined by Eq. (3.29). As stated, the momenta that fulfil this condition when $k = 2\pi$ are $\rho_i = \pi, 3\pi$, etc., so that $p_i = \hbar k_1, 3\hbar k_1$, etc. in experimental units. To demonstrate this more clearly, Fig. 3.16 shows the variation with pulse number of the mean energy, as calculated from the results of numerical simulation, of a quantum system whose initial state consists of a single plane wave with a certain momentum p_i in the direction of the standing wave. The value of this momentum ranges from 0 to $\hbar k_1$, as stated on the individual graphs. Two values of T were used: the first was 66.5μs, equal to that in the experimental realisation, and the second was 66.7μs, which fulfilled exactly the $T = T_{1/2}$ resonance condition. It can be seen from Fig. 3.16 that such a small change in the value of T noticeably alters the dynamics of the system. Figure 3.16 shows that the response to the potential of each momentum class when $T = 66.5\mu$s, in solid lines, is oscillatory in nature, but in each case the amplitude of oscillation decreases with increasing pulse number. This decrease occurs because the value of T does not quite fulfil the $k = 2\pi$ resonance condition.

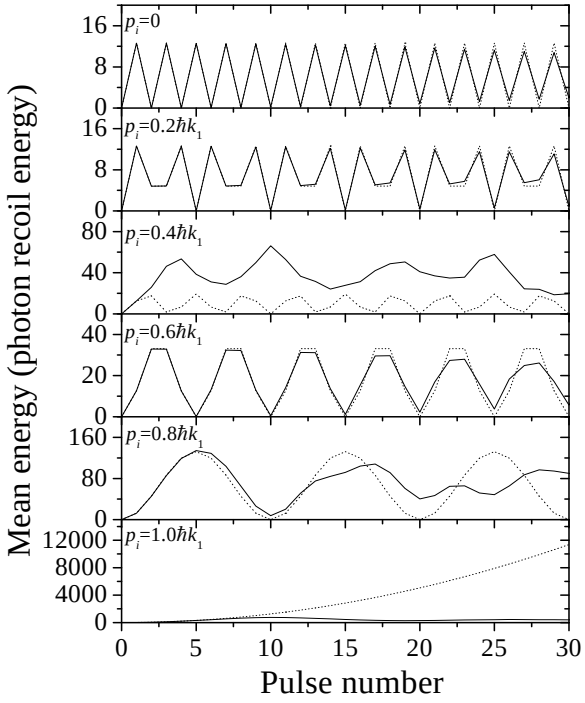

Figure 3.16: Variation in the mean energy with pulse number of different initial plane waves, as calculated from the momentum distributions generated by the quantum simulation. The solid line shows the variation when the pulse period was the experimentally used value of $T = 66.5\mu$s; the dotted line shows the result when $T = T_{1/2} = 66.7\mu$s. The value of ϕ_d used in each case was 0.8π. The plane waves had initial momenta p_i equal to 0, $0.2\hbar k_1$, $0.4\hbar k_1$, $0.6\hbar k_1$, $0.8\hbar k_1$ and $1.0\hbar k_1$, as labelled on the figure.

When $T = T_{1/2}$, so that $\bar{k} = 2\pi$, there are no oscillations in the $p_i = \hbar k_1$ case. Since $F = 2\pi$ for this momentum, the ballistic momentum increase characteristic of a quantum resonance occurs. For the other values of p_i, oscillations do occur and their amplitude and period are constant as the pulse number increases. When p_i is far from any value that fulfils the condition for $F = 2\pi$, the amplitude of oscillation is very small; the $p_i = 0, 0.2\hbar k_1$ cases are examples of this. On the other hand, when p_i is closer (*e.g.* $0.8\hbar k_1$) to a value necessary for resonant growth, the initial growth in mean energy persists for a larger number of pulses and the mean energy attained is much larger, as are the period and amplitude of the oscillations. In the case of $p_i = \hbar k_1$, the growth of the mean energy is quadratic with n, continues indefinitely, and attains a very large value after 30 pulses. This value is so large that a modified version of the simulation, in which momentum states up $\pm 100\hbar G$ were considered, proved necessary in order to obtain a reliable form for the momentum distribution after 30 pulses. When $T = 66.5\mu$s, the initial growth of mean energy with n in the $p_i = \hbar k_1$ case is close to quadratic, and continues until the 10th pulse. Beyond this pulse, however, oscillatory behaviour is evident. This case of the behaviour of an initial plane wave in a quantum δ-kicked rotor system in which there is inexact fulfilment of the resonance condition on T (and therefore $\bar{k}$), but exact fulfilment of the condition on p_i, has been studied [119]. The mean energy of the system was found to increase quadratically for a certain number of kicks before oscillatory behaviour took over. The closer $\bar{k}$ was to the ideal value, the larger the number of kicks for which the quadratic growth would occur, and this is in agreement with the behaviour shown in Fig. 3.16. In the experimental system, there was a continuous spread of momenta present. Therefore in Fig. 3.15(a), the oscillatory variation of the experimental mean energy with pulse number at $T = 66.5\mu$s is due to the superposition of the oscillations of the individual plane waves, like those shown in Fig. 3.16. Despite the imperfect fulfilment of the resonance condition by the experimental value of T, the behaviour observed is qualitatively different from that in the case of dynamical localisation. The momentum energy growth is greatly enhanced and so the system bears a signature of the quantum resonance.

Can the oscillations at non-resonant values of p_i when $T = T_{1/2}$ be understood? Figure 3.14 shows that after an initially plane wave with momentum $p_i = 0$ has evolved freely for a time $T_{1/2} = 66.7\mu$s following a pulse, there is no amplitude modulation of the wave. The modulation of the wave is exclusively in phase, and is shifted by π radians from that modulation which existed immediately after the pulse. This is so because each momentum state $\hbar k_u$ populated by the diffraction has evolved a free phase $u^2\pi$, which is an even multiple of π for even diffraction orders and an odd multiple when u is odd. This is equivalent to an offset of $\lambda_{\mathrm{spat}}/2$ in the spatial distribution as deduced from Eq. (3.31). From the argument above regarding the viewing of initial plane waves with $p_i \neq 0$ in a frame moving with velocity p_i/m relative to the laboratory frame, it is clear that for all values of p_i there will be no amplitude modulation of the wave after it has evolved freely for $T_{1/2}$. The spatial dependence of the phase modulation will be offset by $(p_i/m)T_{1/2}$ from that of the $p_i = 0$ case. Therefore the total effect of n applications of the potential on a plane wave of initial momentum p_i, with a pulse period $T_{1/2}$, can be

expressed thus

$$V(z)_{\text{total}} = \frac{X_{\max}}{G} \sum_{j=0}^{n-1} (-1)^j [1 + \cos(G(z - j(p_i/m)T_{1/2}))] \tag{3.32}$$

Depending on the value of p_i, this sum will equal a constant after some number of pulses, n_0. This means that n_0 pulses will have no net diffractive effect on the plane wave, and the mean energy of the system will be the same as initially. Therefore the mean energy of an initial plane wave oscillates, and the period of oscillation is n_0. If the pulse period were the Talbot time T_{T}, so that the free phase evolved by every diffraction order from a plane wave with $p_i = 0$ were an integer multiple of 2π, the effect of the n pulses of the potential on a plane wave with initial momentum p_i could be written

$$V(z)_{\text{total}} = \frac{X_{\max}}{G} \sum_{j=0}^{n-1} [1 + \cos(G(z - j(p_i/m)T_{\text{T}}))] \tag{3.33}$$

In this case, too, the mean energy of an initial plane wave that did not fulfil the condition for resonant growth would oscillate with a pulse number period given by that value of n for which V_{total} is independent of z. Therefore the behaviour of non-resonant momenta at the first- and second-order quantum resonance values of T is qualitatively similar.

The plots in Fig. 3.15(a) showing the growth of the mean energy of the atomic ensemble with pulse number, and in Fig. 3.16 showing the way in which the individual momenta respond to the potential, demonstrate how the system behaves on its way to attaining the momentum distribution shown in Fig. 3.11. The population in the wings of this distribution, which is responsible for the large value of the mean energy of the system, is due to the large momentum growth of initial momenta around the special values $p_i = \hbar k_1, 3\hbar k_1$, etc. The behaviour of the δ-kicked rotor as manifested by the variation in the mean energy with pulse number is normally considered in the 'long-time limit', *i.e.* for a large number of pulses. This is because many kinds of transient behaviour occur in the early stages of kicking the system, which then die away. That long-time limit was not reached in the experiments under discussion here as only a maximum of 50 pulses was applied. Experimental limitations (specifically, the maximum waveform duration that could be stored by a DS345 function generator) precluded the application of further pulses, but the number applied was sufficient to ascertain the salient characteristics of the quantum behaviour. At the quantum resonance the long-time growth in the mean energy of a system with a continuous range of initial momenta, as in the experimental system under discussion, should be linear [121, 122]. This is because only a fraction of the atomic ensemble participates in the quadratic growth of mean energy, and this fraction decreases with increasing pulse number. The decrease is because the greater the number of pulses applied, the more accurately an initial momentum has to approximate the special $F = 2\pi$ value in order to continue to exhibit quadratic growth of energy with n. If it fails to do so, it enters the regime of mean energy oscillations. Thus the increase in mean energy of the ensemble

is constantly tempered by the falling number of atoms participating in quadratic growth, resulting in a net linear growth in the mean energy. Clearly, this still leads to a much greater level of energy growth than at non-resonant values of $\bar{k}$, for which dynamical localisation occurs at n_{break}, and there is no subsequent growth in the mean energy.

The variation with n in the mean energy of the classical system for $T = 66.5\mu$s, as calculated from the results of the classical simulation, is shown in Fig. 3.15(b). It is quite different from that of the quantum system, shown in Fig. 3.15(a), and not dissimilar to that evident in Fig. 3.12(b), for which $T = 60.5\mu$s. The growth in the mean energy at $T = 66.5\mu$s is constant, and linear, thus demonstrating the presence of normal momentum diffusion. The rate is somewhat smaller than at $T = 60.5\mu$s, but this is expected due to the different values of $D(K)$ for the different pulse periods. The behaviour of the classical system is completely different from that of the quantum system, showing that the large increases in mean energy and subsequent oscillations are distinctively quantum mechanical features.

3.3.3 Variation in mean energy with pulse period

As stated in Sec. 3.1, the experimental parameters which could be controlled the most precisely and which, therefore, were the quantities that were varied in order to examine the behaviour of the system were the number of pulses of the potential, n, applied to the atomic ensemble, and the period, T, of application of these pulses. Varying the value of T while keeping other quantities the same was equivalent to varying the value of $\bar{k}$ and therefore fundamentally altered the dynamics of the quantum system. By measuring the mean energy attained by the atomic ensemble after a fixed number of pulses for the different values of T, it was possible to examine the different types of behaviour in the different regimes defined by $\bar{k}$ and contrast the effect on the quantum system of varying T, and therefore $\bar{k}$, with that on the classical system.

For the experimental investigation of the effect of varying T, a fixed number of pulses of the standing wave (in this case, 30) was applied to the atoms. The value of T was varied from 6.5μs to 210.5μs in steps of 1.0μs, and in each case the experiment was repeated three times and the average of the resulting momentum distributions was found. The phase modulator was used to remove gravity's effect at all the different values of T. As in the case of the experiments described in the sections above, the detuning of the light in the standing wave from the ($F = 4 \rightarrow F' = 3$) transition was 30 GHz. The averaged momentum distribution was used to calculate the mean energy of the system, after a momentum boundary at $\pm 120\hbar k_1$ had been imposed in order to reduce the inaccuracy in the calculated values of the mean energy due to noise in the wings of the TOF measurement. The signal beyond this boundary was much smaller than that at the centre of the momentum distribution so the imposition of this momentum cut resulted in negligible ($< 5\%$) reduction in the calculated mean energy of the atoms below its true value. In addition, numerical simulations of both the quantum system and the corresponding classical system were performed, with 30 pulses applied, T varied

from 6.5μs to 210.5μs, and $\phi_d = 0.8\pi$. The momentum distributions thus produced were used to calculate the variation with T of the mean energy of the ensemble. Figure 3.17(a) shows the variation with T of the mean energies calculated from the experimental data and the results of the quantum simulation. Figure 3.17(b) shows the variation of the initial rate of increase of the mean energy, as deduced from the use of the quantum stochasticity parameter K_q in the expression for the classical diffusion parameter in Eq. (3.9) (see Eqs. (3.25) and (3.34) and the discussion below), while Fig. 3.17(c) shows the mean energy as calculated from the results of the classical simulation. Figure 3.17(c) also shows the mean energies predicted by using Eq. (3.35) given below, plus the expression for the classical diffusion parameter in Eq. (3.9).

Note that the value of ϕ_d used in the numerical simulations, 0.8π, was larger than that deduced from the measured values of the experimental parameters, 0.7π, as given in Sec. 3.2. However, 0.8π was used because it was found to give a variation in mean energy $\bar{E}$ with T that, qualitatively, was the most similar to that obtained from the experimental data. It also yielded good qualitative agreement with the experimental investigations of the δ-kicked accelerator, as discussed in Ch. 4. As regards the variation with T of $\bar{E}$ in the δ-kicked rotor, the use in the numerical simulations of a value of ϕ_d that was too small, *e.g.* 0.5π, meant that the broad peaks in $\bar{E}$ visible in Fig. 3.17(a) at $T \sim 30, 100, 160\mu$s were not present. On the other hand, use of a value of ϕ_d that was too large, *e.g.* 1.4π, yielded a periodic variation in $\bar{E}$ with T that was too rapid. The broad $\bar{E}$ peaks in Fig. 3.17(a) were replaced by a double peak structure, with local minima at $T \sim 30, 100, 160\mu$s. Clearly, this does not resemble the experimental results. It is worth remarking, however, that even in this case the structures at the quantum resonances ($T_{1/2}$,$T_{\rm T}$,$3T_{1/2}$) were present and qualitatively the same as in Fig. 3.17(a). They were largely unaffected by the change in the value of ϕ_d since the existence of a quantum resonance depends only on the value of $\bar{k}$, not ϕ_d. There was a degree of uncertainty in the value of certain experimental parameters that determine the value of ϕ_d, such as the waist of the beam forming the standing wave, its intensity at the position of the atoms, and its exact detuning from the $(F = 4 \rightarrow F' = 3)$ transition. This uncertainty meant that a peak value of ϕ_d anywhere in the region of π was quite possible, and so the value $\phi_d = 0.8\pi$ was a reasonable and justifiable one to use as a type of ensemble average in the numerical simulations.

Figure 3.17 shows that the variation of the mean energy of the system with T is very different in the classical and quantum mechanical cases. The qualitative agreement between the results from the experiment and the quantum simulation, as shown in Fig. 3.17(a), is good and the form of the variation in the mean energy in the two cases exhibits the same essential features of maxima, minima and sharp spikes. These will be discussed further below. The quantitative agreement is less good, the mean energies as calculated from the experimental data being approximately twice as large as those calculated from the output of the simulations. The previously described reasons for quantitative disagreement explain this discrepancy, namely the noise in the wings of the TOF distribution (which provides a small energy offset on which the true mean energy of the atomic ensemble is super-

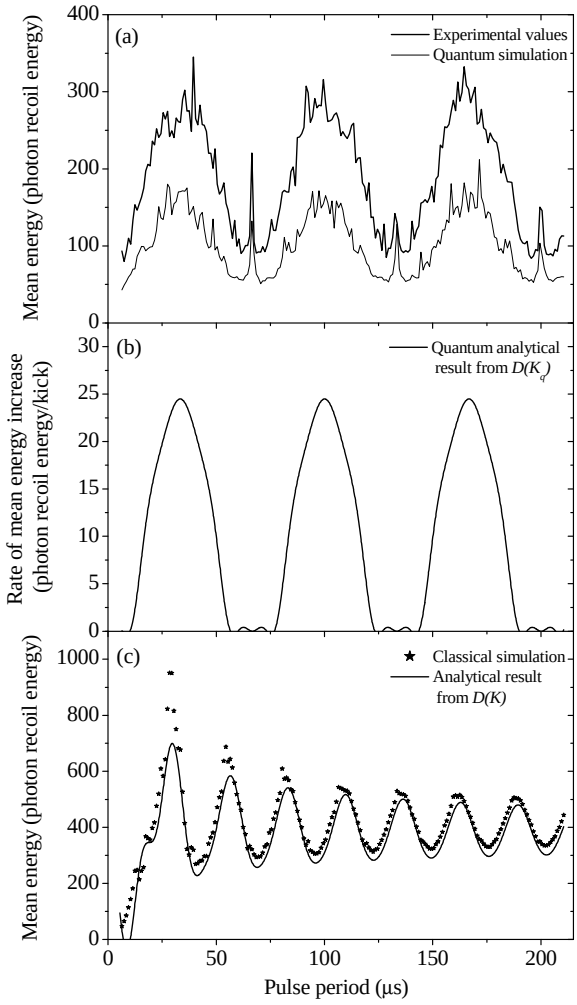

Figure 3.17: (a) Variation with pulse period of the mean energy of the atomic ensemble after 30 potential pulses, as calculated from the experimentally measured momentum distributions (thick line) and those produced by the quantum simulation (thin line). The pulse period ranged from $T = 6.5\mu$s to 210.5μs, in steps of 1.0μs; the red-detuning from the $(F = 4 \rightarrow F' = 3)$ D1 transition of the light forming the potential was 30 GHz, while the value of ϕ_d used in the simulation was 0.8π. (b) Initial rate of increase in mean energy with pulse number as deduced from use of the quantum stochasticity parameter K_q in the analytical expression for $D(K)$ (see Eqs. (3.9) and (3.34)). The qualitative agreement with the maxima and minima in mean energy in (a) is good. (c) Variation in the mean energy of the atomic ensemble after 30 kicks with pulse period as calculated from the momentum distributions generated by the classical simulation. The value of ϕ_d used was 0.8π. In addition, the mean energy that the system is predicted to attain after 30 kicks using Eq. (3.35) and the analytical expression for $D(K)$ in Eq. (3.9) is superimposed, and shows good agreement with the numerically calculated values, except where anomalous diffusion is evident at the peaks and troughs of the mean energy (see text).

imposed), the range of values of ϕ_d experienced by the atoms in the experimental system (which makes quantitative agreement with a simulation that uses a unique value of ϕ_d unlikely), and the noise in the depth and position of the potential applied to the atoms (which modifies the rate of momentum diffusion, and degrades dynamical localisation). An additional contributing factor to this disagreement is the fact that atoms in the wings of the distribution, at large momenta, violate the Raman-Nath condition. At the quantum resonances (which correspond to the observed spikes) the population at such momenta is non-negligible, and its experimental value would be lower than in an ideal δ-kicked system, as modelled in the simulations. This effect is less important for the distributions away from the resonances, at which the population at large momenta is very small.

The mean energy attained after a fixed number of pulses in the quantum mechanical system appears to vary periodically with T, and the period is $T_{1/2}$. Periodic variation is consistent with the idea that $\bar{k}$ determines the nature of the dynamics of the system, and that two values of $\bar{k}$ that differ by 4π are physically indistinguishable [119]. This is equivalent to saying that pulses applied with a period of T have the same effect on the system as those applied with a period of $T + T_{\mathrm{T}}$. As described in Sec. 3.3.1, the response of a plane wave with initial scaled momentum ρ_i to the application of the potential is determined by the phase evolved between adjacent diffracted states over the inter-kick free evolution. This phase is $F_{v,v-1,\rho_i}$, given by Eq. (3.29). From the form of Eq. (3.29), it can be seen that an increase in the value of $\bar{k}$ by 4π, corresponding to an increase by T_{T} in the pulse period, leads to an increase in the value of $F_{v,v-1,\rho_i}$ by $2\pi\alpha$, where α is an odd integer. Therefore, the evolution of the system for the two different values of $\bar{k}$ should be physically indistinguishable and a T_{T} periodicity of the response of the system to pulses is expected. However, Fig. 3.17(a) appears to indicate that the period is actually $T_{1/2}$. This is due to the fact that the system consists of an ensemble of momenta spread over the whole range of reduced momentum values. Although the behaviour of each value of ρ_i varies periodically with T and the period is T_{T}, the period of the variation in the mean energy of the ensemble as a whole is half this value. It is worth pointing out that this periodic nature of the response of the system to the potential as T is varied means that two different values of the classical stochasticity parameter K $(= \phi_d\bar{k})$ can yield identical dynamics. This occurs if they are produced by the same value of ϕ_d and two values of $\bar{k}$ that are separated by an integer multiple of 2π. Classically, any change in K leads to a change in the character of the system's behaviour, as described by the modification to the value of $D(K)$, and this is an important respect in which the quantum system differs from the classical.

A number of characteristics, in addition to the periodicity, of the variation with T of the response of the quantum system deserve comment. There are two distinct features that are apparent in the plots of Fig. 3.17(a). The first is the sharp spikes in the mean energy, referred to above, that occur at $T_{1/2}$, T_{T} and $3T_{1/2}$ (66.7μs, 133.3μs and 200.0μs, respectively). These are due to the existence of the quantum resonances, and the values of k that correspond to these pulse periods are 2π, 4π and 6π, respectively. As stated previously, $T_{1/2}$ corresponds to the lowest

second-order ($b = 2$ in the expression $k = 4\pi a/b$) quantum resonance, and T_{T} is the lowest first-order resonance. According to theory, the higher the order of the resonance, the narrower in T-space is the resonance and thus the more accurately the condition on T must be fulfilled in order to observe the ballistic momentum increase [119, 121, 123]. The third- and higher-order quantum resonances are so narrow as to be practically unobservable experimentally, especially when the $\sim 0.1\mu$s uncertainty in the value of T is taken into account, so only the first- and second-order quantum resonances are clearly visible in the data. In the results of the quantum simulation, the heights of the three spikes are approximately equal, whereas in the results from the experiment the spike at $T_{1/2}$ is considerably higher than the others. This is an experimental artefact; as the pulse period increases, the inaccuracy in the pulse-to-pulse phase shift produced by the phase modulator to remove gravity's effect has a greater effect. Thus at larger values of T the higher momentum states in a quantum resonance are less efficiently populated. Figure 3.17(a) shows that the width of the second-order resonances, as observed both numerically and experimentally, is the same as that of the first-order. In view of the theoretical received wisdom given above, this is surprising, but it is a consequence of the fact that the initial momentum distribution of the ensemble covers the entire range of reduced momenta, some of which give rise to resonant growth at $T_{1/2}$ and $3T_{1/2}$, and some of which yield this growth at T_{T}. Consideration of the behaviour of the spatial distribution of the atoms' de Broglie waves allows this observation to be understood in another way. In Fig. 3.14 the evolution of the spatial distribution following the application of a pulse to a plane wave with $\rho_i = 0$ is shown. The distribution after evolution for a time $T_{1/2} + \delta T$, where δT may be positive or negative and has a magnitude of less than 10μs, is qualitatively similar to that found when the evolution time is $T_{\mathrm{T}} + \delta T$ or $3T_{1/2} + \delta T$. For a range of ρ_i, the spatial distribution produced by each will, as discussed in Sec. 3.3.2, be the same in form as that shown in Fig. 3.14 but offset by an amount $(p_i/m)t$ after a time t. Since the spatial distribution of the de Broglie waves of the ensemble as a whole will be similar close to each of these resonant times, the response of the system to a subsequent pulse might also be expected to be similar. Hence the range of values of T, around each of the resonant values, for which a pulse train causes resonant broadening in an ensemble with a range of momenta would be comparable, yielding spikes of equal width, as observed.

The second distinct feature of the variation of the mean energy of the quantum system with T is the rise and fall of this quantity for values of T between those corresponding to the first- and second-order quantum resonances. This behaviour reflects the variation of the values of localisation length ζ and the quantum break time n_{break} with T. For pulse periods in the region of 30μs, 100μs and 160μs, the mean energy attained after 30 pulses is much larger than for those values of T close to, but not at, the quantum resonances. The momentum distribution of the atomic ensemble in these regions of high mean energy is exponential after the 30 pulses, suggesting that dynamical localisation is having an effect, but a graph of mean energy versus pulse number shows that the rate of growth with n is still large after 30 pulses, and n_{break} has not yet been reached. These results indicate that both

ζ and n_{break} are much larger in these regions than close to the first and second-order quantum resonances. As discussed in Sec. 3.3.1, a qualitative description of the variation in ζ and n_{break} is given by the use of the quantum stochasticity parameter K_q, defined in Eq. (3.25), in the expression for the classical diffusion parameter $D(K)$, as given in Eq. (3.9). The use of $D(K_q)$ also predicts the periodic response in T of the system to the pulses of the potential. Using the results in Refs. [112, 113], the initial rate of mean energy growth with pulses of the potential can be written

$$\frac{d\bar{E}}{dn} = \frac{(\hbar G)^2}{2m} D(K_q) \tag{3.34}$$

This quantity is plotted in Fig. 3.17(b). As is clear from the graph, the maxima and minima of the initial rate of mean energy growth match those of the mean energy attained after a fixed number of pulses, which have been observed both experimentally and using the quantum mechanical simulations. The mean energy growth shows the same periodic behaviour, with apparent period $T_{1/2}$, that is evident in Fig. 3.17(a). It is not appropriate simply to multiply this growth rate by the number of pulses applied to the system in order to evaluate the expected mean energy after 30 pulses because the mean energy does not grow at a constant, linear rate. The growth rate decreases as the number of pulses increases, due to dynamical localisation, and this occurs more quickly in some regions (close to the first- and second-order quantum resonances, where $n_{\text{break}} < 5$) than in others (*e.g.* $T = 30\mu$s, where $n_{\text{break}} > 100$). The variation of $D(K_q)$ is, however, useful as an indicator of the extent of mean energy growth that occurs in the different regimes of k as T is varied. It is noteworthy that $D(K_q)$ does *not* predict the existence of the spikes in the mean energy due to the first- and second-order quantum resonances. As stated earlier, the expression for the classical stochasticity parameter $D(K)$ in Eq. (3.9) only takes low-order correlations into account. The energy growth at a quantum resonance is due to the fulfilment of certain conditions on the phase accumulated by diffracted orders over the free evolution between consecutive pulses. The resulting behaviour of the system has a high kick-to-kick correlation, and could be described as 'correlated diffraction'. Hence it might be expected that the use of $D(K_q)$ would not fully take this behaviour into account, and so the spikes in the mean energy due to quantum resonances would be absent.

To emphasise that the behaviour of the quantum system is quite different from that of the classical, the behaviour of the classical system subjected to 30 kicks, with a range of pulse periods and $\phi_d = 0.8\pi$, was modelled by numerical simulation. The resulting values of the mean energy are shown in Fig. 3.17(c). Superimposed on this are the values of the mean energy predicted by using $D(K)$ to obtain an expression that yields the mean energy of a classical system, in experimental units, after n kicks. This is

$$\bar{E} = n \frac{m}{(GT)^2} D(K) \tag{3.35}$$

The classical variation in the mean energy with T is very different from the that of the quantum mechanical system and does not take a periodic form with a period determined by the first- and second-order quantum resonances. It does, however,

exhibit a type of periodic variation, though its amplitude decreases with increasing T. This behaviour is also clear in the analytical prediction given by Eq. (3.35) and, indeed, the quantitative agreement between the results from the numerical simulation and this analytical expression is very good for $T > 19\mu$s (this corresponds to $K > 4.5$; as discussed in Sec. 3.1, $D(K)$ is only reliable for $K > 4.5$ due to the influence of KAM tori and cantori in restricting momentum diffusion at smaller values of K). An additional point of interest is that the use of a larger value of ϕ_d would yield a more rapid variation with T of the mean energy attained by the classical system after a fixed number of kicks. This has some similarity to the more rapid variation, for values of T between those of the first- and second-order quantum resonances, observed in the quantum system as ϕ_d is increased from, say, 0.8π to 1.5π. Nevertheless, the general form of the quantum variation is still quite different from that in the classical. In the classical system the quantum resonance values of T have no special significance, and the behaviour of the system at these values does not remain fixed as ϕ_d is varied.

The discrepancies between the numerical and analytical results for the classical variation with T of $\bar{E}$, such as they are, merit comment. The most significant discrepancy is the fact that the mean energies of the system given by the numerical results at the local maxima are much higher than the corresponding analytical results. This is due to the fact that anomalous diffusion is important at these values of T, and particles fulfil the conditions for entering long-lived classical accelerator modes. The motion of such particles is highly correlated from kick-to-kick, and this degree of correlation is not taken into account in the truncated expression for $D(K)$ in Eq. (3.9), in which only low-order correlations are considered. Thus the large degree of energy growth is not fully expressed. The other, less pronounced, discrepancy is that the numerical simulation yields higher mean energies than the analytical result at the local minima. Here, too, correlated motion is important as momentum growth is subdiffusive, and so exact quantitative agreement with the prediction of $D(K)$ could not be expected. Additionally, the system modelled by the numerical simulation has an initial momentum distribution that is Gaussian, as in the experiment, whereas the analytical expression assumes an initially uniform momentum distribution (in each case the initial position distribution is uniform). This difference could be expected to modify slightly the numerical result relative to the analytical prediction, though it must be noted that even if an initially uniform momentum distribution is used for numerical simulation then, in spite of generally excellent qualitative agreement, quantitative agreement is not perfect [86].

3.4 Summary

This chapter has focused on several different characteristics of the behaviour of the quantum δ-kicked rotor as realised in an atom-optical system: the form of the momentum distributions, the growth in mean energy with pulse number and the dependence of the extent of energy growth on the pulse period. The quantum phenomena of dynamical localisation and the quantum resonance have been

discussed and the contrast made with the behaviour of the ideal classical system described by the standard mapping. The experimental behaviour has been found to be radically different from that of the classical system, and in good qualitative agreement with the results of a numerical simulation of the quantum system based on a diffractive model of the effect of the potential. This experimental system is an important means of characterising a real, as opposed to idealised, quantum system and pinpointing the differences that quantum mechanics makes to the behaviour of a system whose classical analogue is chaotic.

Chapter 4

The δ-kicked accelerator and quantum accelerator modes

The δ-kicked rotor is a paradigm in classical chaos theory, and the experimental system described in this thesis was set up so as to investigate its quantum mechanical counterpart. Over the course of the investigations, however, it quickly became apparent that the acceleration, due to gravity, of the atoms in the direction of the kicking laser beams was having a significant effect on the dynamics of the system. This acceleration caused the phases accumulated by the diffracted de Broglie waves between the light pulses to be modified relative to the zero-acceleration situation of the δ-kicked rotor. Since the kicked atoms were accelerated between pulses, the system was dubbed the 'δ-kicked accelerator'. The rotational equivalent would be the application of a constant torque to the system shown in Fig. 3.1. This chapter will describe the behaviour that has been observed in this system, and will focus in particular on the startling phenomenon of the quantum accelerator mode.

4.1 The δ-kicked accelerator

4.1.1 The classical system

Classically, the delta-kicked accelerator is a system in which an ensemble of particles is subjected to a series of regularly-spaced kicks. The magnitude and direction of the kick experienced by an individual particle depends sinusoidally on the position of the particle at the instant of the kick, as in the case of the δ-kicked rotor. The system differs from the δ-kicked rotor in that there is an additional, constant, unidirectional force that also acts on the particles. Thus the displacement of a particle between kicks depends not only on its momentum after the previous kick but also on the force that is causing uniform acceleration of the particle during the interval between consecutive kicks. Due to the discrete nature of the time evolution of the system, in which the interval T between consecutive δ-function

kicks defines the period of the cycle of processes occurring, the momentum and position of a particle obey mapping equations. These are analogous to those of the standard mapping in Eqs. (3.3) and (3.4), which describe the δ-kicked rotor. If the uniform acceleration produced by the external force is a, then the mapping equations in the case of the δ-kicked accelerator are given by

$$p_{n+1} = p_n + X_{\max}\sin(Gz_n) + maT, \tag{4.1}$$

$$z_{n+1} = z_n + p_{n+1}\frac{T}{m} - \frac{1}{2}aT^2. \tag{4.2}$$

where, as in the case of the standard mapping, p_n and z_n are the momentum and position of the particle just before the $(n+1)$th kick and m is the mass of the particle. $G = 2\pi/\lambda_{\text{spat}}$, where λ_{spat} is the spatial period of the sinusoidally varying potential that applies the kicks to the particles. For the system under discussion in this thesis, the uniform external acceleration was due to the force of gravity acting downwards so, bearing in mind the sign convention defined in Fig. 3.2, $a = -g$. Again as in the standard mapping, scaling can be performed in order to obtain dimensionless equations. The scaling relations are $\chi = Gz$, $\rho = GTp/m$, $K = X_{\max}GT/m$ (K is the stochasticity parameter) and $\gamma = gGT^2$. Therefore the dimensionless equations for the kick-to-kick mapping of the δ-kicked accelerator are

$$\rho_{n+1} = \rho_n + K\sin(\chi_n) - \gamma, \tag{4.3}$$

$$\chi_{n+1} = \chi_n + \rho_{n+1} + \frac{\gamma}{2}. \tag{4.4}$$

Note that in contrast to the δ-kicked rotor, there are two independent parameters, K and γ, on which the macroscopic behaviour of the system depends. The experimental system under discussion afforded the possibility of varying the value of γ by use of the crystal phase modulator, while K was varied by adjusting the value of the pulse period T; in this case the value of γ was simultaneously varied. There will be further discussion of the effect on the dynamics of the system of the variation of T in Sec. 4.2.

Certain characteristics of the behaviour of the system can be established by examining the phase space portraits generated from the results of a numerical evolution of an ensemble of classical particles with a range of initial momenta and positions under the mapping of Eqs. (4.3) and (4.4). Figure 4.1 shows the phase portraits obtained by evolving a set of 400 particles through 100 iterations of this mapping. The initial positions and momenta formed a grid of values of χ and ρ, where χ varied from 0 to 2π in steps of 0.1π and ρ varied from $-\pi$ to π in steps of 0.1π. In order to specify a value for γ, a particular value of T had to be assumed. The value used was $T = 60.5\mu$s because many of the investigations into the quantum δ-kicked accelerator, and particularly into quantum accelerator modes, were conducted using this value. This meant that $\gamma = 0.504$. Figure 4.2 shows the same data as Fig. 4.1 but plotted only within a restricted range of ρ, to match that shown in Fig. 3.3. Thus the effect of the presence of gravity on the

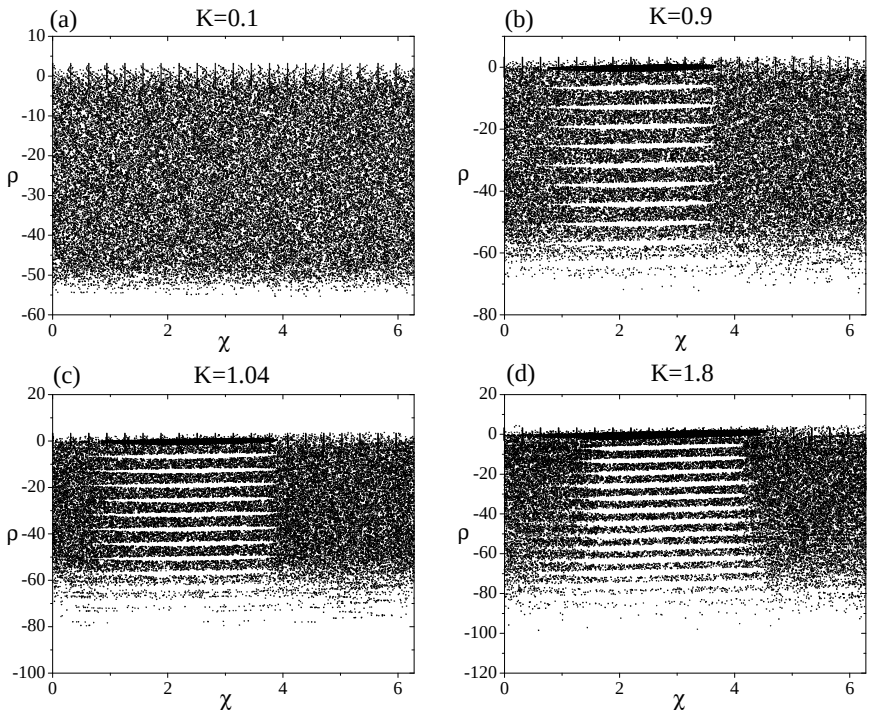

Figure 4.1: Phase space portraits for the kicked accelerator produced by 100 iterations of the mapping equations (4.3) and (4.4), with (a) $K = 0.1$, (b) $K = 0.9$, (c) $K = 1.04$ and (d) $K = 1.8$. In each case, $\gamma = 0.504$, corresponding to a pulse period of 60.5μs in the Earth's gravitational field.

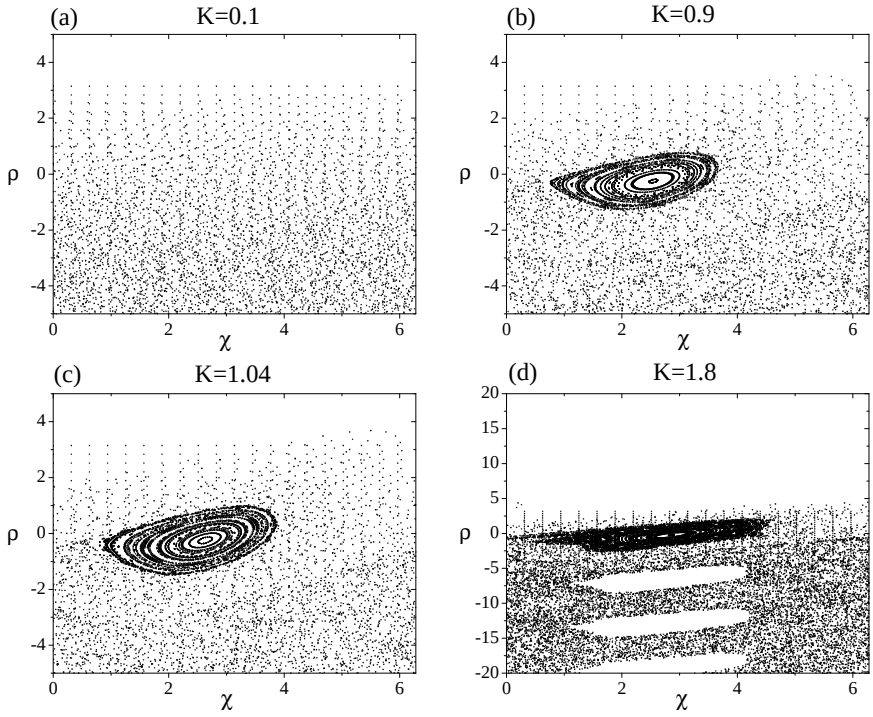

Figure 4.2: Phase space portraits of the data shown in Fig. 4.1 but with the range of the graphs restricted to the same as that in Fig. 3.3. (a) $K = 0.1$, (b) $K = 0.9$, (c) $K = 1.04$ and (d) $K = 1.8$. $\gamma = 0.504$ in each case.

'fine structure' of the phase space, *i.e.* the regions of stability that are evident in Fig. 3.3, can be shown.

Figures 4.1(a) and 4.2(a) show the phase space portraits obtained when $K = 0.1$. These show that when K is small, and the effect of gravity is present, there is no region of stability in phase space, in contrast to the regime of small K in the δ-kicked rotor, as shown in Fig 3.3(a). The reason for this is that the effect of the uniform acceleration, parametrised by γ, is much greater than that of the δ-kicks, parametrised by K, and so the momentum change of particles between pulses is dominated by the effect of gravity. This prevents them from remaining in stable orbits in phase space, while the presence of the kicks prevents the particles' motion from being simply that of uniformly accelerated projectiles. Hence the phase space has the appearance of a chaotic sea. The asymmetric form of the behaviour in phase space is also very clear from Fig. 4.1(a), the momentum diffusion being almost exclusively in the negative direction. For a larger value of K, the strength of the kicks received by the particles is greater relative to the effect of gravity. Figures 4.1(b) and 4.2(b) show that when $K = 0.9$ there is a stable region of phase space that is considerably smaller than that in the case of the δ-kicked rotor, as shown in Fig. 3.3(b). Since gravity has broken the symmetry of the system, the stable region has become warped and has a 'teardrop' shape. It is also clear from Fig. 4.1(b) that the momentum diffusion of the system is predominantly in the negative direction, and is somewhat larger than in the case of $K = 0.1$. This also demonstrates the increased importance of the kicks in the dynamics of the system. The behaviour in Figs. 4.1(c) and 4.2(c) (for which $K = 1.04$), and in Figs. 4.1(d) and 4.2(d) (for which $K = 1.8$) is qualitatively similar to that in Figs. 4.1(b) and 4.2(b) but, as expected, the increased kicking strength enhances the degree of momentum diffusion in both the positive and negative directions. The general asymmetric form of the momentum diffusion due to gravity's effect remains, as do the warped stable regions. One clear feature of Figs. 4.1(b), 4.1(c) and 4.1(d) is the unpopulated regions of phase space for values of ρ in the negative direction from the initially populated region. These, as in the case of the δ-kicked rotor, are due to the influence on the system's dynamics of cantori, which inhibit momentum diffusion into certain regions of phase space. From the figures, the shape of these excluded regions appears to change, for given values of K and γ, with the value of ρ. For example, in Fig. 4.1(d) these excluded regions cover a wider range of χ values as the value of ρ becomes more negative. However, in reality the shape of the cantori and hence the excluded regions does not vary with ρ. The appearance of variation is due to the fact that the system has only been evolved for a finite number of kicks. Consequently, at large, negative values of ρ there are fewer data points present to define the extent of the unpopulated regions. All the unpopulated regions must have the same extent, because the 2π periodicity of phase space still holds, even when the value of γ is non-zero. A plot generated from 200 evolutions of the mapping equations can demonstrate that the extent of each of these excluded regions is, indeed, the same and the periodicity of phase space is maintained.

The extent of the momentum diffusion of the classical δ-kicked rotor system is quantified by the diffusion parameter $D(K)$, given in Eq. (3.9). As stated in

Sec. 3.1, this can be derived using the method of Fourier paths, as shown in Ref. [86]. This technique can also be applied to the case of the δ-kicked accelerator, and an outline of the derivation is given in Appendix B. The result of this derivation yields the following expression for the diffusion parameter, $\tilde{D}(K,\gamma)$, of the δ-kicked accelerator, correct to order K^{-1}:

$$\tilde{D}(K,\gamma) = \frac{K^2}{2}\left[\frac{1}{2} - J_2(K)\cos(\gamma) - J_1^2(K)\cos(2\gamma) + J_2^2(K) + J_3^2(K)\right] - \gamma\bar{\rho}_i + \frac{n\gamma^2}{2}, \tag{4.5}$$

where $\bar{\rho}_i$ is the mean initial scaled momentum, $J_m(K)$ is the mth order Bessel function of the first kind and n is the number of steps in the path. As expected, this diffusion parameter depends on the scaled value of the gravitational acceleration, γ, as well as on K. Just as in the expression for $D(K)$, the fact that the series of Bessel functions is truncated means that only low-order kick-to-kick correlations are taken into account. The initial momentum distribution of the experimental ensemble of atoms is symmetric around $\rho = 0$, so $\bar{\rho}_i = 0$. The last term on the RHS, $n\gamma^2/2$, expresses the effect of the free-fall acceleration of the ensemble of particles. This provides a negative offset to the momentum distribution, as is clear from Fig. 4.1, but this effect is not of interest and so this term will be neglected. What is of interest is the effect that gravity has in modifying the dynamics of the particles in the falling centre-of-mass frame of the ensemble. In the experiment, the TOF detection system measures the momenta of the atoms *relative* to that momentum which the atoms would possess due to free-fall under gravity. These relative momenta, due to the action of the kicking potential, are the quantities of interest. Hence the diffusion parameter that quantifies the effect of the kicking potential in the presence of an external unidirectional force has the form

$$D(K,\gamma) = \frac{K^2}{2}\left[\frac{1}{2} - J_2(K)\cos(\gamma) - J_1^2(K)\cos(2\gamma) + J_2^2(K) + J_3^2(K)\right]. \tag{4.6}$$

The variation of this diffusion parameter with K is plotted in Fig. 4.3(a) for $\gamma = 0.504$, which corresponds to the usual value of gravity, $g = 9.81\,\mathrm{m\,s^{-2}}$, with $T = 60.5\mu$s. For comparison, the $\gamma = 0$, zero-gravity case (the δ-kicked rotor) is included. The ratio of $D(K,\gamma)$ to the quasilinear result, $D_{\mathrm{ql}} = K^2/4$, in the two scenarios is shown in Fig. 4.3(b). Fig. 4.3 shows that the difference made by the value $\gamma = 0.504$ to the extent of the momentum diffusion caused by the δ-kicks, in comparison to the zero-gravity case, is not large. Physically, the pulse period is sufficiently small that the modification by gravity to the kick-to-kick change in the values of the position and momentum cannot markedly alter the dynamics of the system and hence the extent of momentum diffusion. For a larger value of T, and hence γ, gravity would have more time between kicks in which to act and could sufficiently alter the particles' positions and momenta as to modify significantly the extent of momentum diffusion. This would depend on the value of γ, however, as $D(K,\gamma)$ varies periodically with γ. For some values of γ, the presence of gravity would leave the energy transfer to the system in the falling frame unaltered.

Figure 4.4 shows the momentum distributions, as generated by numerical simulation, of the classical ensemble of particles in the δ-kicked accelerator system after

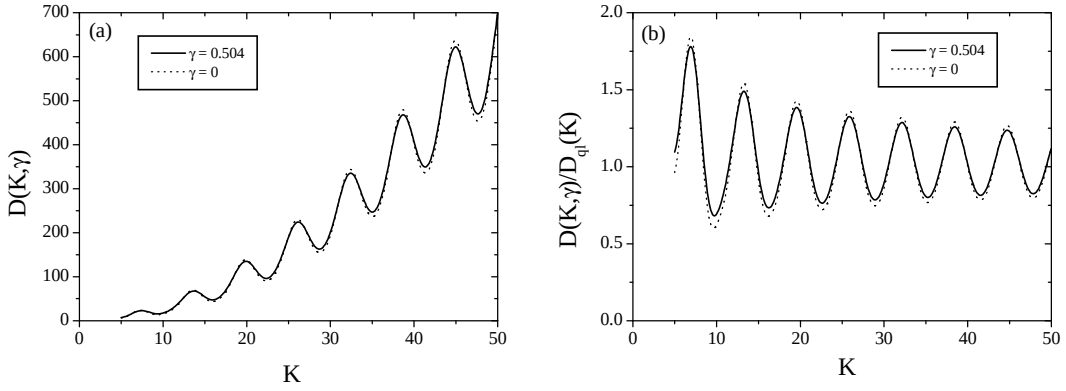

Figure 4.3: (a) The diffusion parameter of the δ-kicked accelerator, $D(K,\gamma)$ for two different values of γ. Note that the $\gamma = 0$ case corresponds to the δ-kicked rotor. (b) The ratio of the diffusion parameter to the quasilinear result, $D_{\rm ql}(K)$.

50 kicks, for various different values of K. These momentum distributions are in the freely-falling frame (as are all the momentum distributions for the δ-kicked accelerator shown in this thesis). In each case the value of γ was equal to 0.504, and the results are plotted on a logarithmic scale. The values of K used were the same as those in Fig. 3.6, namely (i) $K = 6.9$, where $D(K,\gamma)/D_{\rm ql}(K)$ is a maximum, (ii) $K = 8.5$, where $D(K,\gamma)/D_{\rm ql}(K) \simeq 1$, and (iii) $K = 9.7$, where $D(K,\gamma)/D_{\rm ql}(K)$ is a minimum. Comparison with the results shown in Fig. 3.6 indicates that the most obvious effect of the presence of gravity has been to make the distributions asymmetric. This is to be expected; gravity has broken the symmetry of the system, and it is natural that this is manifested by the momentum distribution. Figure 4.4(b) shows an example of anomalous diffusion in the δ-kicked accelerator. As in the δ-kicked rotor, accelerator modes are evident, but the populations of the modes in the positive and negative momentum directions are not equal, nor are the magnitudes of their momenta. Figure 4.4(c) shows an example of normal diffusion in the δ-kicked accelerator, where $D(K,\gamma)/D_{\rm ql}(K) \simeq 1$. The momentum distribution is asymmetric and has the form of a warped Gaussian; the FWHM is also somewhat larger ($\sim 40\hbar k_1$) than the corresponding case in the δ-kicked rotor, as shown in Fig. 3.6(c), for which the FWHM is $\sim 36\hbar k_1$. Figure 4.4(d) shows an example of anomalous diffusion where $D(K,\gamma)/D_{\rm ql}(K) < 1$. Here, too, the momentum distribution has the form of a slightly warped Gaussian, and is narrower (FWHM $\sim 36\hbar k_1$) than the $K = 8.5$ case. It too is broader than its corresponding δ-kicked rotor system, as shown in Fig. 3.6(d), for which the FWHM is $\sim 34\hbar k_1$. Thus it can be concluded that the presence of gravity has caused some modification to the dynamics of the system in terms of its symmetry-breaking effect, but the general character of the system's response to the δ-kicks is not very different from that of the δ-kicked rotor.

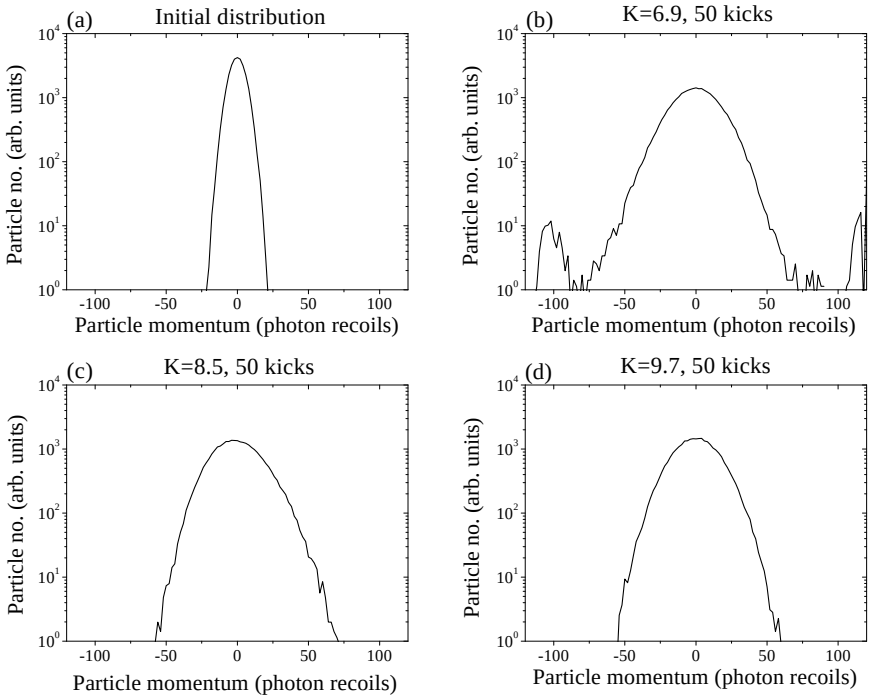

Figure 4.4: The momentum distribution of particles in the classical δ-kicked accelerator system as generated by simulation, with $\gamma = 0.504$. Note that the distributions have been plotted on a logarithmic scale. (a) The initial distribution, corresponding to a temperature of 5μK, (b) distribution after 50 kicks with $K = 6.9$, (c) distribution after 50 kicks with $K = 8.5$, and (d) distribution after 50 kicks with $K = 9.7$. The forms of the distributions after 50 kicks are quite different from those of the δ-kicked rotor, as shown in Fig. 3.6, in that for each value of K the distribution is asymmetric. The populations of the accelerator modes in (b) are unequal, and the momentum distributions in (c) and (d) are warped Gaussians. As in the case of the δ-kicked rotor, the distribution in (d) is narrower than in either (b) or (c). These momentum distributions are in the freely-falling frame, as are all subsequent momentum distributions shown for the δ-kicked accelerator.

4.1.2 The quantum system

In the quantum δ-kicked accelerator a spatially periodic potential is applied in a series of δ-function pulses to a wavefunction or wavepacket, and an additional linear potential, which corresponds to a unidirectional external force, acts on the system. For the experimental arrangement described in this thesis, in which the unidirectional force is that of gravity, the Hamiltonian of the system has the form

$$\hat{H} = \frac{\hat{p}^2}{2m} + mg\hat{z} + \frac{X_{\max}}{G}[1 + \cos(G\hat{z})] \sum_n \delta(t - nT), \tag{4.7}$$

where g is the free-fall acceleration due to gravity and the other quantities used have the same meanings as in Eq. (3.10). As in the case of the quantum δ-kicked rotor, the evolution of the system is determined by successive applications of the Floquet operator, $\hat{U}$, which expresses the effect on the system of one application of the potential, followed by the subsequent free evolution. Thus, again as in the case of the δ-kicked rotor, $\hat{U}$ is the product of two operators, the first, $\hat{U}_{\rm int}$, representing the effect of the spatially periodic potential on the de Broglie wave and the second, $\hat{U}_{\rm free}$, representing the free evolution that occurs for a time T following an application of the potential. Since in the ideal δ-kicked accelerator the periodic potential acts for an infinitesimal time, the presence of gravity has no bearing on its effect and so the interaction operator can be written

$$\begin{aligned}
\hat{U}_{\rm int} &= \exp\left(-i\frac{X_{\max}}{\hbar G}[1 + \cos(G\hat{z})]\right) && (4.8)\\
&= \exp\left(-i\frac{K}{k}[1 + \cos(\hat{\chi})]\right) && (4.9)\\
&\equiv \exp(-i\phi_d) \sum_{s=-\infty}^{\infty} i^s J_s(\phi_d) \exp(is\hat{\chi}) && (4.10)
\end{aligned}$$

The absence of any gravity-dependent term in the operator that represents the effect of the periodic potential is a valid approximation in the description of the experimental system provided that the conditions for being in the Raman-Nath regime, as described in Ch. 3, are fulfilled. As in the case of the δ-kicked rotor, the $\exp(-i\phi_d)$ in the expression for $\hat{U}_{\rm int}$ in Eq. (4.10) represents the global phase ϕ_d that is imparted to the de Broglie wave by each application of the potential. As this has no effect on the dynamics, it will henceforth be ignored.

For the free-evolution operator, on the other hand, the presence of gravity modifies the phase evolved by the different diffracted orders from the potential because it causes a linear shift with time of the momenta of those orders. The operator can be written

$$\begin{aligned}
\hat{U}_{\rm free} &= \exp\left(-\frac{i}{\hbar}\left[\frac{\hat{p}^2}{2m} + mg\hat{z}\right]T\right) && (4.11)\\
&= \exp\left(-\frac{i}{k}\left[\frac{\hat{\rho}^2}{2} + \gamma\hat{\chi}\right]\right) && (4.12)
\end{aligned}$$

The $\hat{\rho}$ and $\hat{\chi}$-dependent parts of this operator can be factorised (see Appendix C) to yield the equivalence relation

$$\exp\left(-\frac{i}{\hbar}\left[\frac{\hat{\rho}^2}{2}+\gamma\hat{\chi}\right]\right) \equiv \exp\left(-\frac{i}{2\hbar}[\hat{\rho}^2+\gamma\hat{\rho}]\right)\exp\left(-\frac{i}{\hbar}\gamma\hat{\chi}\right)\exp\left(-\frac{i}{4\hbar}\gamma^2\right) \quad (4.13)$$

Consideration of the effect of this operator on an incident plane wave $\psi(\chi) = \exp(i\kappa\chi)$ shows that the term $\exp(-i\gamma\hat{\chi}/\hbar)$ is a momentum displacement operator, because it changes the value of κ to $(\kappa - \gamma/\hbar)$, and describes the free-fall due to gravitational acceleration between pulses of the potential. The term $\exp(-i\gamma^2/4\hbar)$ represents a global phase applied to the system as a whole and so has no effect on its dynamics; from now on it will be ignored. When applied to a momentum eigenstate, such as the plane wave currently under discussion, the term $\exp(-i[\hat{\rho}^2+\gamma\hat{\rho}]/2\hbar)$ results in a phase shift. The relative values of this phase shift for adjacent momentum states populated by diffraction from the potential will determine how the system develops with time. As was made clear in the discussion of the classical system, the effect of gravity in modifying the momentum distribution of atoms in a freely-falling frame (which was the distribution measured by the TOF system in the experiment) is the process of interest. Gravity has this effect because it modifies the phases accumulated during the inter-kick free evolution by different momentum states.

From Eqs. (4.10) and (4.13), it is clear that the Floquet operator, which expresses both the interaction with the potential and the free evolution between kicks, can be decomposed into a combination of momentum displacement operators and terms involving the momentum operator $\hat{\rho}$. This means that the most obvious choice of basis for a numerical analysis of the system is one of momentum eigenstates. Since the free-fall of the atomic ensemble was not of interest, the momentum basis used in numerical simulations of the quantum δ-kicked accelerator was offset by $-\gamma/\hbar$ between successive iterations. This is how the effect of the term $\exp(-i\gamma\hat{\chi}/\hbar)$ in the Floquet operator was incorporated. Hence after $(n-1)$ applications of the (kick+free evolution) cycle, $|u\rangle$ was defined as the basis state whose scaled laboratory momentum immediately prior to the nth pulse of the potential was given by

$$\rho_{u,n-1} = \rho_i + u\hbar - (n-1)\gamma \quad (4.14)$$

where ρ_i is the initial scaled momentum of the plane wave in the z-direction. This is a state that has received u units of momentum from diffractive pulses of the periodic potential, and its momentum in the falling frame is $\rho'_u = \rho_i + u\hbar$. As in the case of the δ-kicked rotor, the operator describing the interaction of the periodic potential with a distribution over such states can be written as a sum of matrix elements:

$$\hat{U}_{\rm int} = \sum_{u=-\infty}^{\infty}\sum_{v=-\infty}^{\infty}\hat{U}^{\rm int}_{vu} = \sum_{u=-\infty}^{\infty}\sum_{v=-\infty}^{\infty} i^{v-u}J_{v-u}(\phi_d)|v\rangle\langle u| \quad (4.15)$$

where $|v\rangle$ and $|u\rangle$ are the final and initial momentum states, respectively. The evolution following the nth kick, in which no change in the relative populations of

the different momentum states occurs but phase is accumulated, is also represented by a sum of matrix elements:

$$\hat{U}_{\rm free} = \sum_{v=-\infty}^{\infty} \hat{U}_{v_f v}^{\rm free} = \sum_{v=-\infty}^{\infty} \exp(-i\phi_v)\delta_{v_f v}|v_f\rangle\langle v| \tag{4.16}$$

where $|v\rangle$ and $|v_f\rangle$ are the occupied states at the beginning and end of the free evolution period, respectively, and ϕ_v is the phase accumulated by $|v\rangle$ over the interval between the nth and $(n+1)$th kicks. The presence of gravity modifies the value of ϕ_v relative to that which applies in the case of the δ-kicked rotor, as given by Eq. (3.20). For the δ-kicked accelerator, ϕ_v is given by

$$\phi_v = \frac{1}{2\hbar k}[\rho_i^2 + (v\hbar k)^2 + n(n-1)\gamma^2 - \gamma(2n-1)(\rho_i + v\hbar k) + 2v\hbar k\rho_i] \tag{4.17}$$

As shown in Appendix C, this result was obtained by using the expression for $\rho_{u,n-1}$ in Eq. (4.14) to evaluate the formula $\phi_v = [\rho_{v,n}^2 + \gamma\rho_{v,n}]/2\hbar k$, deduced from the $\hat{\rho}$-dependent term in the Floquet operator. This term takes into account the fact that the momentum changes continuously due to gravitational acceleration over the interval between consecutive pulses. Note that the laboratory momentum at the end of the free evolution period, $\rho_{v,n}$, not the momentum ρ'_v in the falling frame, had to be used to calculate correctly the value of ϕ_v.

As discussed in Sec. 3.2, the response of an incoming wave to applications of the Floquet operator is determined by the differences in the values of ϕ_v accumulated by adjacent momentum states. For two different momentum states $|v\rangle$ and $|v'\rangle$, the difference in the phases accumulated over the free evolution between the nth and $(n+1)$th kicks is given by (*c.f.* Eq. (3.21))

$$F_{v,v',\rho_i} = \phi_v - \phi_{v'} \tag{4.18}$$

$$= \frac{1}{2}[(v^2 - v'^2)\hbar k - \gamma(2n-1)(v-v') + 2\rho_i(v-v')] \tag{4.19}$$

Just as in the case of the δ-kicked rotor, two different initial plane waves with initial momenta $\rho_{i,1}$ and $\rho_{i,2}$ will respond identically to the application of the periodic potential if the relative phases accumulated between consecutive kicks by the different diffraction orders produced from each wave are the same *modulo* 2π. This requirement is satisfied if the two plane waves yield values of F that differ by an integer multiple of 2π, and this is true for all v and v' if $(\rho_{i,1} - \rho_{i,2}) =$ integer $\times\, 2\pi$. Thus the concept of reduced momenta is also applicable to the δ-kicked accelerator, and the behaviour of initial momenta separated by an integer multiple of 2π is identical. For a given value of T, the momenta which behave identically are separated by $\hbar G T_{1/2}/T$, in experimental units, which is exactly the same as in the case of the δ-kicked rotor.

The quantum δ-kicked accelerator was investigated using the experimental apparatus described in Ch. 2 and the method of numerical simulation discussed in Ch. 3. For the experimental investigations, pulses of the standing wave of light were applied to the atoms after they had been cooled in optical molasses and

released. The light in the standing wave was red-detuned from the caesium D1 transition and, as discussed in Ch. 3, it applied a spatially-varying potential to the atoms. The difference from the investigation of the δ-kicked rotor was that the crystal phase modulator was, in general, not active. This left gravity's effect unmodified so that there was a relative acceleration between the falling atoms and the profile of the standing wave. The phase modulator could, however, be used to vary the effective value of gravity and hence investigate its effect in the δ-kicked accelerator system. Following the application of the light pulses, the momentum distribution of the atoms was measured by the TOF method.

The numerical simulation was very similar to that used in the modelling of the δ-kicked rotor, though adapted so as to incorporate the effect of gravity. It assumed that the Raman-Nath condition was always fulfilled, so that the interaction with the spatially periodic potential was instantaneous, and that all the atoms experienced the same value of ϕ_d. The range of z-momenta of the initial plane waves considered ran from $-7\hbar k$ to $+7\hbar k$ in steps of $0.025\hbar k$, and their distribution was Gaussian, centred around zero with a FWHM of $6\hbar k$. The same column vector formalism as in the case of the δ-kicked rotor was used to express the state of an initial plane wave after a given number of interactions. A given initial plane wave was written as a column vector of 121 elements, ψ_u, whose index ran from -60 to $+60$. These were the basis states in the falling frame, the value of ψ_u representing the probability amplitude of occupying the state with scaled momentum ρ'_u. The same interaction matrix as for the δ-kicked rotor, A_{int}, was used to express the operator $\hat{U}_{\text{int}}$, as defined in Eq. (4.15), and the same form of free evolution matrix, A_{free}, was used to express the operator $\hat{U}_{\text{free}}$, as defined in Eq. (4.16). The value of ϕ_v used in this matrix was, however, that defined in Eq. (4.17) rather than that in Eq. (3.20). The application of the Floquet operator was performed in parallel on all the initial plane waves over as many iterations as required, and the results were added incoherently. The momentum distributions obtained from the numerical simulation were histograms of the populations of the basis momentum states with falling-frame momenta ρ'_u; as stated above, the laboratory momentum basis (*i.e.* the values of ρ_u) was offset by $-\gamma/\hbar k$ between successive iterations. The bins in the histogram generally had a width of $\hbar k$, although for high resolution a bin width of $0.1\hbar k$ was used. The momentum distributions thus produced could then be examined in their own right, or used to calculate the mean energy of the system.

4.2 Characterisation of the δ-kicked accelerator

As in the study of the δ-kicked rotor, the behaviour of the δ-kicked accelerator can most usefully be characterised by examining the form of the momentum distribution of the ensemble and the variation of the mean energy of the particles in that ensemble with pulse number n or pulse period T. There are obvious qualitative differences in the behaviour of each of these facets of the system between the quantum δ-kicked accelerator and its classical counterpart, and, indeed, between the quantum δ-kicked accelerator and the quantum δ-kicked rotor, as will be made

clear in this section.

4.2.1 Momentum distributions

As described in Sec. 3.3, the application of pulses of a periodic potential to a quantum system in the absence of any symmetry-breaking external force, *i.e.* in a realisation of the δ-kicked rotor, generally results in the phenomenon of dynamical localisation. The momentum distribution initially broadens but ceases to do so after the quantum break time n_{break}, by which stage the form of the distribution is exponential and remains so upon application of further pulses. The momentum distribution of the corresponding classical system in the usual regime of normal diffusion broadens with increasing pulse number. This broadening occurs indefinitely and the width of the distribution varies as $n^{1/2}$. Furthermore, an initially Gaussian distribution remains Gaussian in form for all n. The momentum diffusion process was investigated experimentally for the δ-kicked rotor for a value of $T = 60.5\mu$s, as reported in Sec. 3.3.1, and so it was natural to examine the behaviour of the δ-kicked accelerator for the same value of T and number of pulses applied. Therefore 30 pulses of the standing wave at a detuning of 30 GHz from the $(F = 4 \rightarrow F' = 3)$ transition were applied to the atomic ensemble with the crystal phase modulator inactive, and the resulting momentum distribution was measured by the TOF system. This procedure was averaged over three shots in order to improve the signal-noise ratio so that a value of around 200:1 was achieved. To allow comparison with the classical analogue, a numerical simulation of the application of 30 kicks to a classical δ-kicked accelerator system, with $T = 60.5\mu$s, $\phi_d = 0.8\pi$ and $g = 9.80665\,\text{m}\,\text{s}^{-2}$, was performed. This value of g is the 1998 CODATA recommended value [80]. Figure 4.5(a) shows the experimentally measured initial and final momentum distributions, while Fig. 4.5(b) shows the corresponding distributions generated by the numerical simulation of the classical system. As in Ch. 3, all the results in this chapter will be presented in experimental units: $\hbar k_1$ for momenta and E_{rec} for energies.

In Fig. 4.5(a) the experimental system exhibits a very clear feature in which a part of the momentum distribution has been displaced by the action of the optical potential to a more negative value, leaving the distribution highly asymmetric. The existence of this group in momentum space of accelerated atoms is called a *quantum accelerator mode*. Comparison with Fig. 4.5(b) shows that the asymmetry is quite different from the mild asymmetry that is usual in the classical system (as described in Sec. 4.1.2). The classical momentum distribution after the application of 30 kicks has broadened considerably but, though asymmetric (being more extended in the direction of positive momenta), still reflects its initially Gaussian form. The accelerator mode in the experimental system is an effect peculiar to the quantum mechanical system, and is quite different from the classical accelerator modes that are present in Figs. 3.6(b) and 4.4(b). Indeed, these classical modes have no need of gravity in order to be present, whereas the effect of the additional unidirectional force is critical in the production of this quantum phenomenon.

The behaviour of a quantum accelerator mode can be demonstrated by a plot of

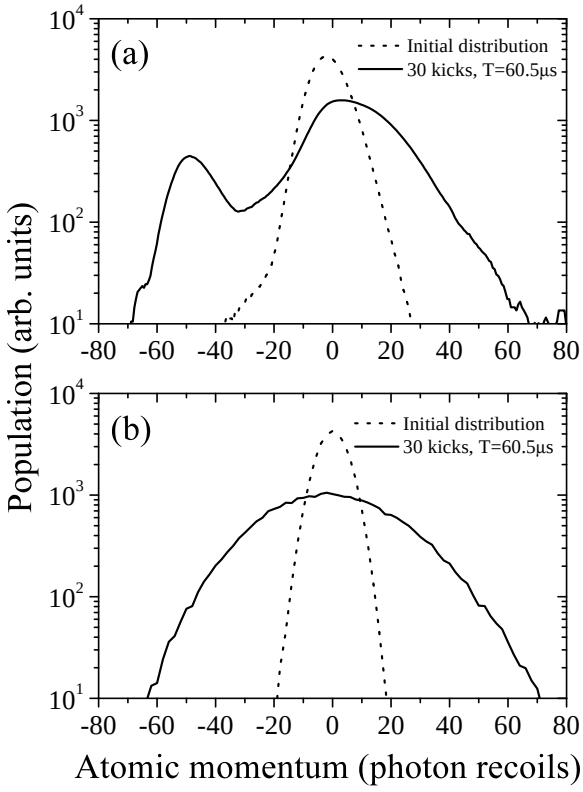

Figure 4.5: (a) Experimentally measured momentum distributions for the δ-accelerator system in the case where a quantum accelerator mode has been produced. The dotted line is the distribution after cooling, prior to application of any pulses of the standing wave. The continuous line is the distribution after 30 pulses, for a pulse period of 60.5μs. The light forming the standing wave was 30 GHz red-detuned from the ($F = 4 \rightarrow F' = 3$) D1 transition. (b) Momentum distributions produced by the numerical simulation of the classical δ-kicked accelerator system. The dotted line is the initial distribution, prior to application of any kicks. The continuous line is the distribution after 30 kicks, for a pulse period $T = 60.5\mu$s, and $\phi_d = 0.8\pi$ ($\Rightarrow K = 14.3, \bar{k} = 1.81\pi$). Note that the distributions in (a) and (b) are plotted on a logarithmic scale.

the variation of the momentum distribution of the atomic ensemble as the number of pulses applied to the system is increased. Figure 4.6 shows the momentum distributions that were measured in the experimental δ-kicked accelerator system as the number of light pulses applied to the atoms was increased from 1 to 100. The scale on which the population for any given measurement is plotted is linear. It is clear that from an initially Gaussian momentum distribution a portion of the atomic ensemble moves out linearly in momentum space as the number of pulses applied increases. After 30 pulses approximately 14% of the atoms are in the accelerator mode. This fraction depends on the value of ϕ_d experienced by the atoms in the system; if this value is increased (by, for example, reducing the detuning of the light in the standing wave) then the population of the accelerator mode increases due to the greater efficiency of populating its momentum states by the diffractive process. The FWHM in momentum of the group of accelerated atoms after 30 pulses is $15\hbar k_1$, and this width is dominated by that of the initial atomic ensemble ($12\hbar k_1$) from which it was created. It is interesting to note that this momentum width is the same after 50 pulses as after 30 pulses.

Several other aspects of the behaviour shown in Fig. 4.6 merit comment. The first is that the pulse-to-pulse efficiency of populating an accelerator mode is high. The experimental population of atoms in the accelerator mode falls linearly with increasing pulse number, following the approximate equation (for n ranging from 30 to 50)

$$f(n) = c - mn \tag{4.20}$$

where $f(n)$ is the fraction of the atomic population in the accelerator mode after n pulses, $c = 0.201 \pm 0.004$ and $m = 0.00215 \pm 0.00009$. Thus the population in the accelerator mode after 50 pulses is 68% of that after 30 pulses. Once atoms have entered an accelerator mode, there is a large probability that they will remain there. The experimental variation of the fraction of the atomic ensemble in the accelerator mode is shown in Fig. 4.7(a). From Fig. 4.6 it is evident that after around 80 pulses the population of the accelerator mode is small. The momentum that the periodic potential has imparted to the atoms by this stage is in excess of 100 photon recoils (corresponding to a velocity of $0.34\,\mathrm{m\,s^{-1}}$). The laboratory velocity of these atoms was larger than this because the acceleration due to the optical potential was in the same direction as the gravitational acceleration. Prior to the application of the pulses the atoms fell freely under gravity for 5.20 ms, and gravity also acted during the 4.84 ms over which the 80 pulses with a period of 60.5μs were applied. Thus the total velocity imparted by gravity to the atoms was $0.099\,\mathrm{m\,s^{-1}}$, and the final velocity of atoms to which 80 pulses had been applied was over $0.45\,\mathrm{m\,s^{-1}}$. This means that during a pulse of 500 ns, the distance moved by the atoms was 0.5 periods of the standing wave of light, resulting in considerable averaging over the potential and an effective reduction in potential height. The Raman-Nath condition was compromised, and the progressive increase in the degree of this averaging as the number of pulses and hence atomic momentum increased is the major reason for the reduction in the population of the accelerator mode with increasing pulse number.

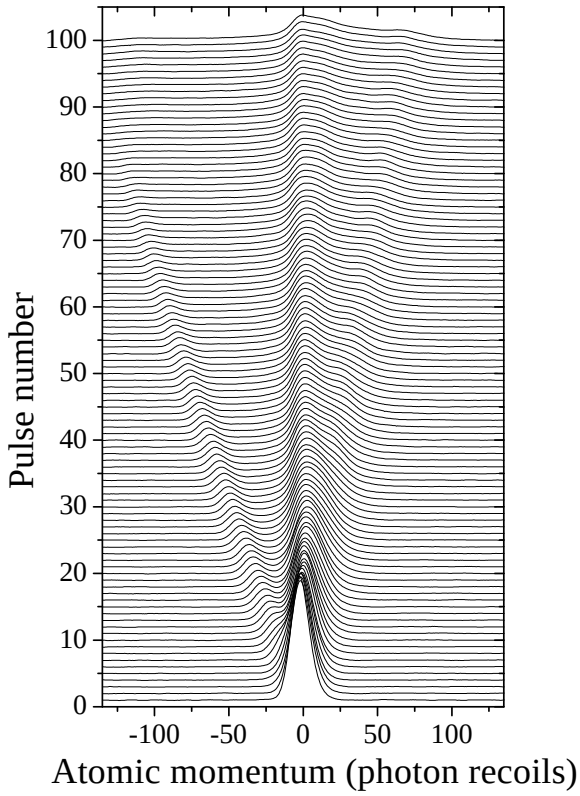

Figure 4.6: Experimentally measured momentum distributions for the δ-kicked accelerator system as an increasing number of pulses of the periodic potential was applied to the system. The pulse period was $T = 60.5\mu$s and the red-detuning of the standing wave light from the ($F = 4 \rightarrow F' = 3$) D1 transition was 30 GHz. The linear dependence of the momentum attained by the quantum accelerator mode on the number of pulses applied is clearly visible. The distributions are plotted on a linear scale, in contrast to Fig. 4.5.

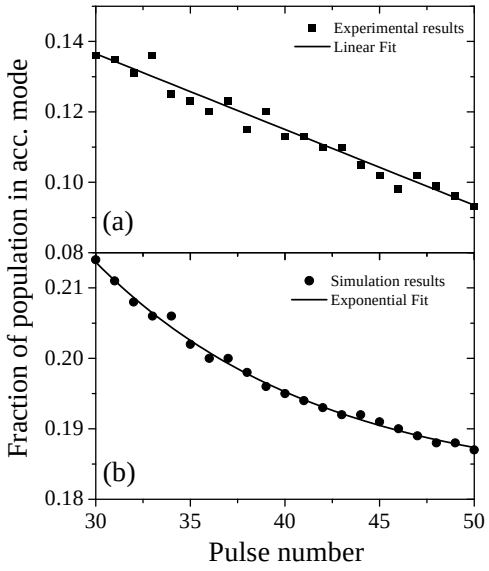

Figure 4.7: Variation of the fraction of the atomic ensemble found in the accelerator mode for pulse numbers between 30 and 50, with $T = 60.5\mu$s, in (a) the experimental data, as shown in Fig. 4.6 and (b) the data from the quantum simulation, as shown in Fig. 4.8.

The pulse-to-pulse efficiency of populating an accelerator mode is even higher in the numerical simulations of the quantum system than in the experiment. This is expected, since the Raman-Nath condition is never violated. The momentum distributions generated by the numerical simulation for pulse numbers up to 100 are shown in Fig. 4.8. The range of momenta that can be considered by the simulation, $-120\hbar k_1$ to $+120\hbar k_1$, is slightly more restricted than that of the experimental TOF measurement, $-138\hbar k_1$ to $+157\hbar k_1$, so for the highest pulse numbers the accelerator mode has gone beyond the boundary of the momentum range. Nevertheless, the agreement between the experimental and numerical results is excellent. The significantly higher efficiency of populating the accelerator mode in the numerical results is because the simulation assumes that the diffractive pulses are infinitesimal in length so that the Raman-Nath condition is always perfectly fulfilled. It is also likely that the value of ϕ_d experienced by many of the atoms in the experiment was less than that used in the simulation, 0.8π. This would contribute to a lower experimental efficiency in creating and maintaining an accelerator mode.

To quantify this difference in efficiency, the fraction of the atomic ensemble found in the accelerator mode after 30 pulses in the simulation is 0.21, which is approximately 1.5 times that which is found in the experiment. In the numerical simulation the fraction of atoms in the accelerator mode after 50 pulses is 0.19, compared with 0.093 in the experiment. However, a notable difference in the behaviour is that the experimental fraction of atoms in the accelerator mode declines linearly with pulse number, as shown in Fig. 4.7(a) and given in Eq. (4.20), whereas the population in the numerical simulation falls exponentially, as shown

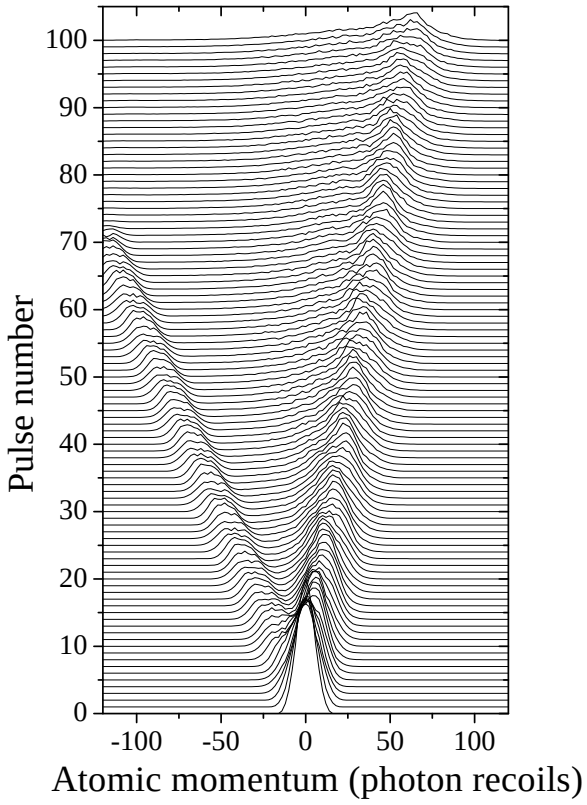

Figure 4.8: Momentum distributions generated by the numerical simulation of the quantum δ-kicked accelerator system as an increasing number of pulses of the periodic potential was applied. The pulse period is $T = 60.5\mu$s, and $\phi_d = 0.8\pi$. The general behaviour is in close agreement with that shown in Fig. 4.6. As in Fig. 4.6, the distributions are plotted on a linear scale.

in Fig. 4.7(b). The fraction of atoms $f(n)$ found in the accelerator mode of the numerical simulation after n pulses, for values of n between 30 and 50, is given by

$$f(n) = A + B\exp(-n/d) \tag{4.21}$$

where $A = 0.1814 \pm 0.0012$, $B = 0.41 \pm 0.07$ and $d = 11.8 \pm 0.9$. Therefore the pulse-to-pulse efficiency of populating the accelerator mode is over 98% for pulse numbers in the range 30 to 50. The more rapid, linear decay in the experimental population of the accelerator mode can be accounted for by the fact that the decay is due not only to a failure of a certain fraction of the accelerator mode population to be diffracted into the next momentum state of the mode upon application of the potential (as in the simulation, and which leads to an exponential decay) but also to the violation of the Raman-Nath condition, as well as to experimental imperfections such as vibrations in the apparatus and noise in the strength of the potential.

The experimental fact that the atoms experienced a range of ϕ_d, which extended down to small values that were much less than π, also explains another difference between the results shown in Fig. 4.6 and Fig. 4.8. In the experimental data of Fig. 4.6, there is a certain class of atoms which stay close to the zero of momentum and seem almost unaffected by the application of the potential. This class of atoms is not present in the results of the simulation. These are the atoms in the periphery of the MOT which experienced a small light intensity from the standing wave and hence little diffraction. Their fairly constant momentum distribution is superimposed on the distribution due to the rest of the atoms which experienced larger light intensities and hence values of ϕ_d. The distributions of the latter atoms are qualitatively similar to those produced by the simulation.

Interestingly, both the experimental and numerical data show the main body of atoms, which do not enter the accelerator mode, 'recoiling' in the opposite direction in momentum space, as though a kind of conservation-of-momentum law were being obeyed. Figure 4.9 shows how the mean momentum of the atomic ensemble varies with pulse numbers between 0 and 50 for both the experimental data shown in Fig. 4.6 and the numerical results shown in Fig. 4.8. The data from the simulation shows that the mean momentum of the ensemble is rigorously conserved as an increasing number of pulses is applied, always remaining at zero. The data from the experiment shows that this mean momentum is always small (after 50 pulses the accelerator mode has reached a momentum of $\sim 80\hbar k_1$ yet the mean momentum of the atoms is $\sim 2\hbar k_1$) but not constant, exhibiting a slow rise with increasing pulse number. These positive values can be attributed to two distinct effects. Firstly, in the experimental system the atoms in the accelerator mode increasingly violate the Raman-Nath condition as more pulses are applied to the system so that they move to a state of more negative momentum (for $T = 60.5\mu$s). This, as discussed earlier, results in a reduction in the population of the accelerator mode. The population of atoms recoiling in the opposite, positive direction is not as significantly affected by this process because the momenta attained are much lower. Secondly, as discussed in Sec. 2.6, the lock-in amplifier introduces a 'stretching' of the measured momentum distribution in the positive direction. This

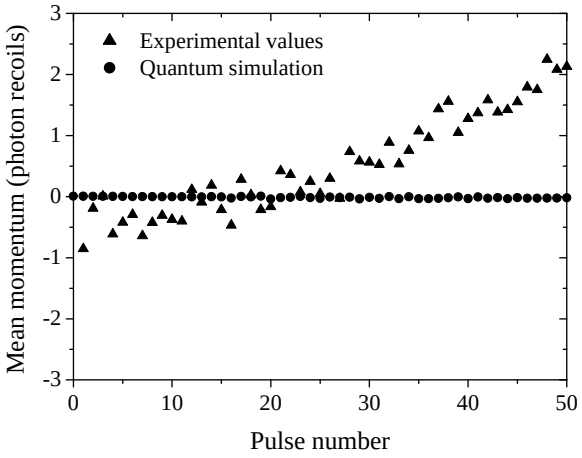

Figure 4.9: Variation with pulse number of the mean momentum of the atomic ensemble in the results from the experiment, as shown in Fig. 4.6, and the numerical simulation, as shown in Fig. 4.8. In each case, $T = 60.5\mu$s.

means that the experimentally measured mean momentum would be expected to show a positive offset relative to its true value. For these two reasons the mean momentum of the system departs from zero, and becomes more positive as the number of pulses increases and the population of atoms in the accelerator mode decreases. Since the simulation assumes that the Raman-Nath condition is always fulfilled, the fraction of atoms in the accelerator mode after a given number of pulses is higher than in the experiment (see Eq. (4.20) and Eq. (4.21)) and the mean momentum of the ensemble remains at zero.

It is also useful to examine how the momentum distribution of the δ-kicked accelerator system after a fixed number of pulses varies with the pulse period T. Experimentally, 30 pulses were applied to the system, with a light detuning of 30 GHz, and the pulse period was varied from 6.5μs to 210.5μs in steps of 1.0μs. The variation of the resultant momentum distribution with T is shown in Fig. 4.10. The quantum accelerator modes can clearly be distinguished as a separate group of atoms from the main bulk. Figure 4.10 shows, however, that accelerator modes can only exist for values of T in the vicinity of those corresponding to first or second-order quantum resonances in the δ-kicked rotor, namely $T_{1/2}$, T_{T} and $3T_{1/2}$ (66.7μs, 133.3μs and 200.0μs, respectively) for the range of values of T studied experimentally. Secondly, the momentum reached by the accelerator mode after a given number of pulses depends on the value of T. As the value of T approaches that of a quantum resonance, the magnitude of the momentum attained by the accelerator mode after 30 pulses increases and appears to diverge at the resonance itself. Furthermore, an accelerator mode can exist in either the positive or negative momentum directions (against or with the direction of gravitational acceleration, respectively). The direction of the acceleration for values of T just less than $T_{1/2}$ is opposite to that which is observed for values just greater than $T_{1/2}$. The same result is also found for the accelerator modes at values of T to either side of

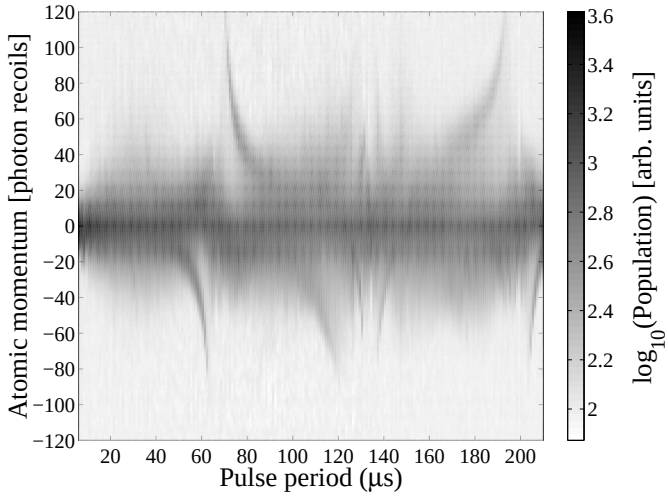

Figure 4.10: Experimentally measured momentum distributions following the application of 30 pulses of the standing wave to the ensemble of atoms for values of the pulse period ranging from 6.5μs to 210.5μs in steps of 1.0μs. The red-detuning of the light from the ($F = 4 \rightarrow F' = 3$) D1 transition was 30 GHz. In this figure, the density of shading is proportional to the logarithm of the population of atoms (in arbitrary units) at a certain momentum, for a certain pulse period. Hence each vertical slice in this figure is a momentum distribution analogous to that shown in Fig. 4.5(a).

$3T_{1/2}$, though the direction of the acceleration for values just below this quantum resonance is in the opposite direction to that for values just below $T_{1/2}$. The accelerator modes in the vicinity of T_{T} do not have the same population, nor attain the same magnitude of momentum, as those in the vicinity of $T_{1/2}$ or $3T_{1/2}$. The existence of accelerator modes and their characteristics will be discussed in detail in Sec. 4.3. Another noteworthy aspect of the results shown in Fig. 4.10 is that, for a large magnitude of momentum ($> 75\hbar k_1$), the population of an accelerator mode in the positive momentum direction is greater than that of a mode in the negative direction. This can be explained by the fact that the Raman-Nath condition plays the most significant role in determining the efficiency of acceleration up to such a large momentum. When atoms are accelerated by the pulses in the positive momentum direction, *i.e.* upwards, they are accelerated against the direction of gravity. This means that when the atoms have attained a certain momentum due to the effect of the potential, their velocity relative to the standing wave of light is lower in magnitude than it would be if the atoms were accelerated downwards by the same amount, thus augmenting gravity's effect. Therefore atoms accelerated in the negative momentum direction violate the Raman-Nath condition for a smaller momentum gained from the potential than do atoms accelerated in the positive direction. This explains the difference in the relative efficiencies of acceleration to high momenta in the two different directions.

The phenomenon of 'conservation of momentum' by the atomic ensemble can also be demonstrated when T is varied. Figure 4.11 shows the variation with T in

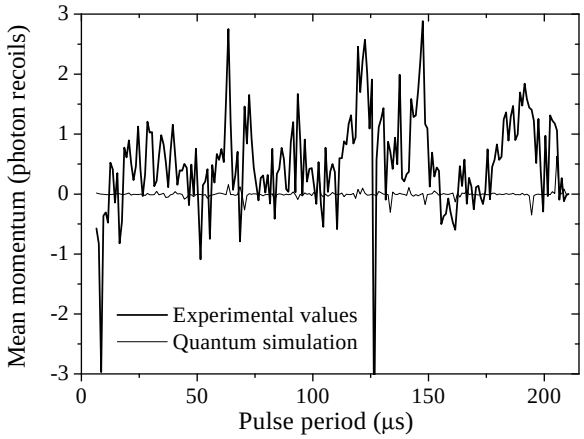

Figure 4.11: Variation with pulse period of the mean momentum of the atomic ensemble after 30 pulses in the results from the experiment, as shown in Fig. 4.10, and from the corresponding numerical simulation.

the mean momentum of the atomic ensemble after 30 pulses as deduced both from the experimental data shown in Fig. 4.10 and from the corresponding numerical simulation. It is clear that the experimental mean momentum always remains close to zero, but is not exactly constant. The most marked excursions from zero occur where accelerator modes are present, as can be seen from a comparison between Fig. 4.10 and Fig. 4.11. Even here, the amplitude of the deviation from zero is small, less than $4\hbar k_1$, in comparison with the magnitude of the momentum reached by the accelerator, which may exceed $100\hbar k_1$. As in the case of the variation in the mean momentum with pulse number, these non-zero values of the mean momentum can be explained by the fall-off in the population of the accelerator mode through violation of the Raman-Nath condition, and the distortion of the measured momentum distribution by the lock-in amplifier. The results from the numerical simulation of the quantum system show that the mean momentum is always very close to zero. The small deviations from the zero value occur because the momentum range of the simulation is limited to $\pm 120\hbar k_1$, and for certain values of T (close to $T_{1/2}$ and $3T_{1/2}$) the momentum of the accelerator mode after 30 pulses has exceeded this range. Thus some of the atomic distribution is lost and the mean momentum is skewed in the direction away from that of the accelerator mode. Nevertheless, the general result is that the mean momentum of the atomic ensemble in the asymmetric system constituted by the δ-kicked accelerator is conserved when pulses are applied to it, no matter what the value of T.

This conservation of mean momentum is an ensemble effect that results from having a spread of initial momenta that extends over the whole of phase space. Figure 4.12 shows the variation with pulse number, as calculated using numerical simulation, of the mean momentum of a quantum δ-kicked accelerator system whose initial state is a single plane wave, with pulse period equal to 60.5μs and $\phi_d = 0.8\pi$. Two different plane wave momenta are studied: the first, $\hbar k_1$, can give

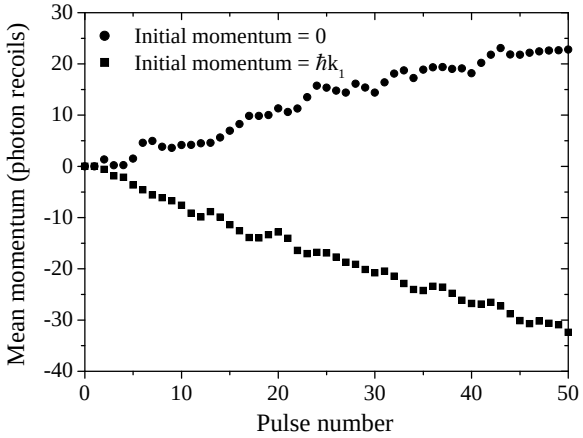

Figure 4.12: Variation with pulse number of the mean momentum in the quantum δ-kicked accelerator, as calculated from numerical simulations, when the initial state consists of a single plane wave. The pulse period was 60.5μs and the value of ϕ_d used in the simulation was 0.8π. The initial momenta of the plane wave considered were $\hbar k_1$, which can gave rise to an accelerator mode (and whose corresponding momentum distribution is shown in Fig. 4.17(a)) and 0, which cannot give rise to an accelerator mode.

rise to an accelerator mode, as is shown later in Fig. 4.17(a), while the second, 0, cannot. Figure 4.12 shows that in neither case does the mean momentum of the atomic system remain constant with pulse number. When the accelerator mode is present there is a large, linear and negative variation in its value with pulse number. When the accelerator mode is not present there is still a net transfer of momentum to the system, but it is smaller in magnitude and in the positive direction. The experimental ensemble of atoms averages over these different types of behaviour because its momentum spread covers the whole range of reduced momenta. Any initial plane wave has no spatial localisation, so the initial momentum distribution covers the whole of phase space. Classically, this would correspond to the particles in the system, distributed over all possible reduced momenta, experiencing all the different values of the potential gradient in the standing wave and so exploring all possible phase space trajectories. Averaging over all these trajectories means that the net momentum transfer to the system as a whole is zero (in the falling frame), though the transfer to individual plane waves (quantum mechanically) or particles (classically) can be substantial.

4.2.2 Variation in mean energy with pulse number

As in the case of the δ-kicked rotor, the variation with pulse number of the mean energy of the atomic ensemble in the quantum δ-kicked accelerator is a useful way in which to characterise the behaviour of the system and emphasise the qualitative differences with that of the corresponding classical system. Figure 4.13(a) shows the variation with pulse number of the mean energy of the quantum δ-kicked accelerator system, both as measured experimentally and as calculated from the results

of the numerical simulation. As usual, the experimental momentum distributions used to calculate these mean energies were an average over three repetitions of the experiment, and the light forming the periodic potential was detuned by 30 GHz from the ($F = 4 \rightarrow F' = 3$) transition. A momentum boundary of $\pm 120\hbar k_1$ was applied when calculating mean energies from these experimental momentum distributions. This reduced the effect of noise in the wings of the TOF measurement in artificially raising the calculated values of the mean energy. For comparison, the corresponding experimental and numerical results for the quantum δ-kicked rotor are included. It is immediately evident that the presence of the unidirectional acceleration of gravity has dramatically increased the mean energy attained by the δ-kicked accelerator compared to the δ-kicked rotor. This increase occurs in the δ-kicked accelerator because of the existence of an accelerator mode, as shown in Fig. 4.6 and Fig. 4.8, while in the δ-kicked rotor the energy growth is prevented by dynamical localisation. In contrast, gravity's effect on the classical δ-kicked accelerator is small. Figure 4.13(b) shows the variation with pulse number of the mean energy of the classical δ-kicked accelerator and δ-kicked rotor systems, as calculated from the results of numerical simulation. In both cases the momentum diffusion is normal, so that the mean energy of the system increases linearly with pulse number. The presence of gravity has resulted in a slight raising of the mean energy attained by the system after 50 pulses relative to the classical δ-kicked rotor, due to the modifications made by gravity to the kick-to-kick positions of the particles in the system. This effect is nugatory in comparison to that of gravity on the quantum system.

There is quantitative disagreement between the results of the experimental and numerical investigations of the quantum δ-kicked accelerator system, as shown in Fig. 4.13(a). The increase with pulse number in the mean energy of the system as modelled numerically is larger than that of the experimental system, yielding a mean energy after 50 pulses that is approximately twice the experimental value. There are two main reasons for this discrepancy. The first is that, as previously discussed, the numerical simulation assumes that all the atoms experience the same value of ϕ_d, and one that is large enough (0.8π) to ensure the existence of an accelerator mode with a substantial population, as shown in Fig. 4.8. Experimentally, this was not the case because of the Gaussian form of the intensity distribution in the laser beam forming the periodic potential and of the spatial distribution of atoms in the MOT. The atoms experienced a range of values of ϕ_d, so the fraction found in the accelerator mode after 30 pulses in the experiment was approximately 2/3 of that which is found there in the numerical simulation. Secondly, the finite duration of the experimental pulses means that the atoms were never truly in the Raman-Nath regime, whereas the numerical simulation assumes pulses of zero duration, by applying the operator $\hat{U}_{\text{int}}$ as given in Eq. (4.15), so that the Raman-Nath condition is always fulfilled. Therefore, as discussed in Sec. 4.2.1, the efficiency of attaining high momenta in the accelerator mode is much larger than in the experiment. The violation of the Raman-Nath condition also explains the fact that the rate of increase of the mean energy with pulse number in the experiment is closer to linear than in the simulation. In the experiment,

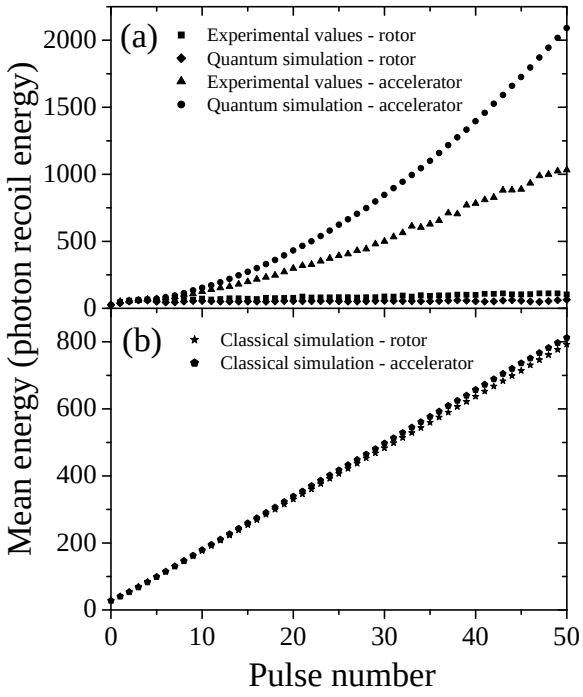

Figure 4.13: (a) Variation in the mean energy of the atomic ensemble with pulse number as calculated from the experimentally measured momentum distributions and those produced by the quantum simulation. The results from both the δ-kicked accelerator and the δ-kicked rotor are shown. The pulse period in each case was $T = 60.5\mu$s; the red-detuning from the ($F = 4 \rightarrow F' = 3$) D1 transition of the light forming the potential was 30 GHz, while the value of ϕ_d used in the simulation was 0.8π. (b) Variation in the mean energy of the atomic ensemble with pulse number as calculated from the momentum distributions generated by the classical simulations of the δ-kicked accelerator and the δ-kicked rotor. The pulse period was $T = 60.5\mu$s and the value of ϕ_d used was 0.8π. Note the difference between (a) and (b) in the scales along the energy axis.

the momentum of the accelerator mode and the group of atoms 'recoiling' in the opposite momentum direction increases linearly with pulse number. Violation of the Raman-Nath condition causes the population thus accelerated to decline with each additional pulse, so the rate of increase in the mean energy of the system as a whole is reduced. Another, less important, factor hampering quantitative agreement between the experiment and the numerical simulation is that there was some noise in the experimental system. This arose from variation in the intensity of the light forming the standing wave, and hence in the depth of the potential, and vibrations in the apparatus that caused a degree of noise in the position of the standing wave profile. Any such noise, which is entirely absent in the simulation, would upset the diffractive process that leads to the creation of an accelerator mode and hence reduce its population, thus impairing the agreement between experimental and numerical results.

Despite the quantitative discrepancies, both the experimental investigation and the numerical simulation of the quantum δ-kicked accelerator indicate that the variation of the mean energy of the system with pulse number is quite different from that of the δ-kicked rotor. Whereas the phenomenon of dynamical localisation is an example of the quantum mechanical *inhibition* of momentum transfer relative to that of the classical system, the quantum accelerator mode that occurs in the δ-kicked accelerator is an example of the quantum mechanical *enhancement* of momentum transfer. That this should exist as the counterpart to inhibition is, perhaps, not surprising, though the first observation of a quantum accelerator mode most certainly was.

4.2.3 Variation in mean energy with pulse period

The variation with T of the mean energy attained by the δ-kicked accelerator after a fixed number of pulses is an important means of exploring the types of dynamics that are accessible. This variation was calculated from the experimentally measured momentum distributions (shown in Fig. 4.10) obtained after 30 pulses of the standing wave, with the light forming the periodic potential detuned by 30 GHz from the $(F = 4 \rightarrow F' = 3)$ transition and values of T ranging from 6.5μs to 210.5μs in steps of 1.0μs. The mean energy was also calculated using the momentum distributions produced by the corresponding numerical simulations of the quantum system, with $\phi_d = 0.8\pi$. The results of these calculations are shown in Fig. 4.14(a). As in the case of the δ-kicked rotor, a momentum boundary of $\pm 120\hbar k_1$ was imposed on the experimental data to increase the signal-noise ratio.

Figure 4.14(b) shows the theoretical values of the initial rate of increase in the mean energy with pulse number, $d\bar{E}/dn$, over the same range of T. The use of K_q, defined in Eq. (3.25), as the argument of the classical diffusion parameter $D(K)$ to find $d\bar{E}/dn$ in the quantum δ-kicked rotor was discussed in Sec. 3.3.3. The maxima and minima of the initial energy growth rate, as predicted by the formula for $d\bar{E}/dn$ in Eq. (3.34), were found to match those of the mean energy attained by the δ-kicked rotor system after a fixed number of pulses, as determined from experiment and numerical simulation. Applying the same principle to the quantum δ-kicked

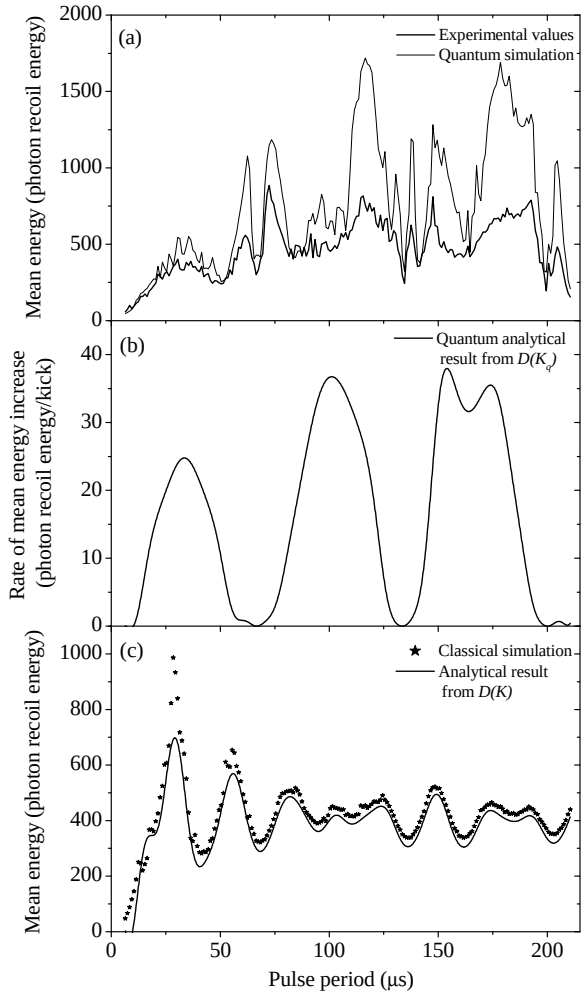

Figure 4.14: (a) Variation with pulse period of the mean energy of the atomic ensemble after 30 potential pulses, as calculated from the experimentally measured momentum distributions and those produced by the quantum simulation. The pulse period ranged from $T = 6.5\mu$s to 210.5μs in steps of 1.0μs; the red-detuning from the ($F = 4 \rightarrow F' = 3$) D1 transition of the light forming the potential was 30 GHz, while the value of ϕ_d used in the simulation was 0.8π. (b) Initial rate of increase in mean energy with pulse number as deduced from use of the quantum stochasticity parameter K_q in the analytical expression for $D(K)$ (see Eqs. (4.6) and (3.34)). There is some qualitative agreement with the maxima and minima in mean energy in (a), as deduced from the experiment and quantum simulation, away from the pulse intervals that give rise to quantum accelerator modes. (c) Variation with pulse period in the mean energy of the atomic ensemble after 30 kicks, as calculated from the momentum distributions generated by the classical simulation. The value of ϕ_d used was 0.8π. In addition, the mean energy that the system is predicted to attain after 30 kicks, using the analytical expressions for $\bar{E}$ in Eq. (3.35) and $D(K)$ in Eq. (4.6), is superimposed. It shows good agreement with the numerically calculated values, except where anomalous diffusion is evident at the peaks and troughs of the mean energy (see text).

accelerator, K_q was used as the argument of the classical diffusion parameter $D(K)$ for this system, given in Eq. (4.6). $D(K_q)$ was evaluated for values of T ranging from 6.5μs to 210.5μs in steps of 0.1μs (and hence values of γ from 0.006 to 6.10) and the analytical expression for $d\bar{E}/dn$ was used to find the initial rate of mean energy increase. Figure 4.14(c) shows the variation with T of the mean energy of the classical δ-kicked accelerator, calculated after 30 kicks. This figure also includes the mean energy predicted by the analytical expression in Eq. (3.35), where the classical diffusion parameter used was that of the δ-kicked accelerator, given in Eq. (4.6).

The results shown in Fig. 4.14(a) illustrate the huge enhancement in energy transfer to the system when a quantum accelerator mode exists. The quantum accelerator modes are manifested by peaks in the value of the mean energy in the region of those pulse periods corresponding to first- and second-order quantum resonances (66.7μs, 133.3μs and 200.0μs). These maxima match the quantum accelerator modes that are evident in the plot of momentum distribution versus T, shown in Fig. 4.10. Comparison of the values of the mean energy attained for these particular values of T with those in the corresponding graph for the δ-kicked rotor, in Fig. 3.17(a), shows that the mean energy attained after a fixed number of pulses is much higher when a quantum accelerator mode exists. Even the local maxima in mean energy of the kicked rotor, the quantum resonances, are much smaller than the energy attained through the existence of a quantum accelerator mode. The qualitative agreement between the experimental results and those of the quantum numerical simulation is good, and the same salient features are evident (peaks due to accelerator modes, local minima at the quantum resonance times and slow variation with T of the mean energy away from the quantum resonances and accelerator modes). The quantitative disagreement is due to the previously described factors: the experimental variation and uncertainty in the value of ϕ_d experienced by the atoms, the violation of the Raman-Nath condition and presence of noise in the depth and position of the potential.

The comparison between the experimentally and numerically obtained mean energies, shown in Fig. 4.14(a), and the values of the initial rate of mean energy growth as deduced from $D(K_q)$, shown in Fig. 4.14(b), sheds some additional light on the nature of the enhancement in momentum diffusion and hence energy growth in the quantum δ-kicked accelerator. The most noticeable feature is what is not present: the peaks due to accelerator modes, so clear in the results shown in Fig. 4.14(a), are not even hinted at in the behaviour of $D(K_q)$. Their absence is similar to the absence in Fig. 3.17(b) of the peaks in mean energy due to enhanced momentum diffusion at the quantum resonances. In each case, this absence can be understood by bearing in mind that the expressions for $D(K)$ given in Eqs. (3.9) and (4.6) are truncations of an infinite series, correct to order K^{-1}. As discussed in Sec. 3.3.3, the behaviour of the δ-kicked rotor at a quantum resonance can be described as 'correlated diffraction' due to the fulfilment of certain conditions on the phase accumulated by momentum states between successive kicks. The existence of the quantum accelerator mode in the δ-kicked accelerator depends on fulfilment of a similar rephasing condition (see Sec. 4.3) and the system's kick-

to-kick correlation is high. Use of K_q in the truncated expressions for $D(K)$, which do not take high-order correlations into account, would not be expected to express fully this behaviour. Hence the absence of peaks corresponding to quantum accelerator modes is not surprising. Away from the values of T that give rise to quantum accelerator modes, the variation in the theoretical initial rate of energy growth shows a reasonable level of agreement with that of the mean energy attained after a fixed number of pulses by the experimental system. Better agreement is obtained with the data generated by the numerical simulation. For small values of T, less than $T_{1/2}$, the variation is similar to that of the δ-kicked rotor. This is because γ, proportional to T^2, is small so the effect of gravity is rather limited. For larger values of T within the range shown, the increased value of γ raises the predicted initial value of the mean energy growth relative to that in the δ-kicked rotor. It should also be noted that this variation in the initial rate of energy growth is not strictly periodic with T, in contrast to the behaviour of the δ-kicked rotor shown in Fig. 3.17(b). The predicted rate of energy growth does fall to zero at values of T that are integer multiples of $T_{1/2}$ (and the experimental and numerical results for the quantum δ-kicked accelerator do show local minima in mean energy at these values of T, unlike the peaks that occur in the quantum δ-kicked rotor) but the maxima in the energy growth, which occur for values of T mid-way between the quantum resonance times, grow in height as T increases. The quadratically increasing value of γ as T rises is responsible for this disruption of periodicity. For values of T higher than those shown in Fig. 4.14(b), the rate of energy growth continues to show minima at integer multiples of $T_{1/2}$, but the maxima between these values of T vary in form and height; the height does not exhibit a steady increase with T. The dynamics of the system for two values of T separated by $T_{1/2}$ are, in general, inequivalent, unlike in the δ-kicked rotor.

The behaviour of the classical system shown in Fig. 4.14(c) is quite different from that of the quantum system, and also from that of the classical δ-kicked rotor, as shown in Fig. 3.17(c). The pronounced peaks due to quantum accelerator modes are absent, as expected, and, as in the case of the rotor, the mean energy varies more rapidly with T than does that of the quantum system. Pulse periods such as integer multiples of $T_{1/2}$ have no special significance and may correspond to local maxima or minima in mean energy, depending on the values of ϕ_d and g. Since $\gamma = gGT^2$, when T is small the effect of gravity in modifying the kick-to-kick positions of the particles is not large enough to modify the dynamics noticeably, because γ is also small. Hence the oscillatory variation of $\bar{E}$ with T is similar to that of the kicked rotor. On the other hand, as T increases, gravity's effect in modifying the dynamics is more significant and this alters the degree of momentum diffusion of the system for a given value of T. The dependence of $D(K)$ on $\gamma(T)$ means that close to certain higher values of T, such that $\cos(\gamma) = \cos(2\gamma) = 1$, the local variation in the mean energy with T would again appear similar to that of the δ-kicked rotor.

The agreement between the analytical results and those from the classical numerical simulation is generally excellent. As in the case of the kicked rotor, the agreement is poorer for those values of T where anomalous diffusion is evident

and, in particular, where classical accelerator modes exist. This is due to the failure of the truncated expression for $D(K)$ to take into account all the high-order kick-to-kick correlations that determine the dynamics in these cases. In any event, perfect agreement between the numerical and analytical results would not be expected since the system modelled numerically has a Gaussian initial distribution of momenta (to match the experimental system) but the analytical result assumes a uniform distribution. Although the variation with T of the momentum diffusion differs for the classical δ-kicked accelerator and rotor, the scale of the energy transfer to the system is not very different in the two cases. This is in contrast to their quantum analogues, in which the presence of gravity results in a much greater transfer of energy to the atomic ensemble. The marked difference between the variation with T of the mean energy attained after a fixed number of pulses by the classical δ-kicked accelerator and that of its quantum analogue confirms that the large enhancement of energy transfer due to quantum accelerator modes is a peculiarly quantum phenomenon.

4.3 Quantum accelerator modes

Why do quantum accelerator modes occur? The phenomenon of broadening of the momentum distribution at a quantum resonance in the δ-kicked rotor was explained in terms of the phase evolved between successive pulses by different momentum states (see Sec. 3.3.1). These momentum states were populated by the phase diffraction grating constituted by the periodic potential. When the momentum of the initial plane wave ρ_i and the pulse period T were such that the difference in the phase evolved over the free evolution between consecutive pulses by adjacent momentum states was an integer multiple of 2π, a broadening of the momentum distribution would occur because the diffractive effects of successive pulses would reinforce one another. This 'rephasing' is also responsible for the existence of a quantum accelerator mode.

Equation (4.17) gives the phase ϕ_v evolved between the nth and $(n+1)$th kicks by the momentum state $|v\rangle$, populated from an initially plane wave with a scaled momentum ρ_i. The scaled momentum (not in the falling frame) of $|v\rangle$ at the end of this free evolution period is $\rho_{v,n} = \rho_i + v\hbar k - n\gamma$. Equation (4.19) gives the difference F_{v,v',ρ_i} in the values of ϕ_v for two momentum states, $|v\rangle$ and $|v'\rangle$. When $|v\rangle$ and $|v'\rangle$ are adjacent states, so that $v' = (v-1)$, this phase difference can be written

$$F_{v,v',\rho_i} = \frac{1}{2}[(2v-1)\hbar k - \gamma(2n-1) + 2\rho_i] \tag{4.22}$$

$$= v\frac{\hbar G^2 T}{m} - ngGT^2 + \frac{GTp_i}{m} + \frac{gGT^2}{2} - \frac{\hbar G^2 T}{2m} \tag{4.23}$$

$$= Av - Bn + C \tag{4.24}$$

where p_i is the momentum of the initial plane wave in experimental units, $A = \hbar G^2 T/m$ $(= \hbar k)$, $B = gGT^2$ $(= \gamma)$ and $C = (2p_i + mgT - \hbar G)GT/2m$. There is a

'rephasing' between the states $|v\rangle$ and $|v-1\rangle$ when F is equal to an integer multiple of 2π. As described in Fig. 3.8 and the accompanying text, when the $(n+1)$th pulse is applied, the diffractive effect of the potential results in the population of a number of momentum states $|w\rangle$ from each incoming state $|v\rangle$. When two adjacent incoming states $|v\rangle$ and $|v'\rangle$, in phase just after the nth pulse, fulfil the rephasing condition it means that the states $|w\rangle$ that they subsequently populate can constructively interfere. There will be large occupation of $|w\rangle$ provided that the diffraction process has been able to impart sufficient momentum. This depends on the value of ϕ_d, which determines the values of the Bessel functions in Eq. (4.15) that give the amplitude for populating one momentum state by diffraction from another. Following application of the $(n+1)$th pulse, the state $|w\rangle$ will, in turn, accumulate phase relative to its neighbouring states until the application of the $(n+2)$th pulse. The same condition on the phase difference F_{w,w',ρ_i} evolved by adjacent states will determine states the $|w\rangle$ that can give rise to highly occupied states $|x\rangle$ following the $(n+2)$th pulse.

The value of v that allows the rephasing condition to be satisfied defines a region of momentum space that will be preferentially occupied through constructive interference. Therefore the variation of this value with n describes a momentum trajectory that will be followed by the atomic population. If a quantity $F' = F \bmod 2\pi$, where the mod is taken on the interval $[-\pi, \pi]$, is defined then the rephasing condition can be written $F' = 0$. This interval is chosen rather than the more usual $[0, 2\pi]$ so that F' is continuous around values of v that satisfy the rephasing condition. The difference between the δ-kicked accelerator and the δ-kicked rotor is that there is a term dependent on γ and n in the expression for F_{v,v',ρ_i}. In the δ-kicked rotor, F' does not depend on n and therefore the momentum states that fulfil the rephasing condition will do so after every pulse. As more pulses are applied, the momentum distribution will spread by diffraction in order to occupy all these available states and the momentum distribution will broaden symmetrically. This is what happens at a quantum resonance. In the δ-kicked accelerator, however, there is a linear change with n in the value of v that satisfies the condition $F' = 0$. The preferentially occupied momentum state, therefore, also varies linearly with n and a portion of the atomic ensemble moves out linearly in phase space as pulses are applied. This is a quantum accelerator mode. The linear trajectory in momentum space is clearly visible in the experimental data of Fig. 4.6 and the data from the numerical simulation in Fig. 4.8. For the strength of the potential applied in the experiments described in this thesis, and the value $\phi_d = 0.8\pi$ that was used in the simulations, the diffraction was such that the change per pulse in the momentum of the preferentially occupied state was less than or of the order of $3\hbar G$ (see Eq. (4.15) and Fig. 3.7). The potential was not strong enough to produce by diffraction a larger change in the momentum of the populated state, even if the fulfilment of the rephasing condition would permit this.

For fixed values of p_i, T and the other experimental parameters, F' is a function of two variables only, n and v. Physically, both these quantities are integers, since the number of pulses applied must be integral and the diffraction process can

only impart momenta in integer multiples of $\hbar G$. To establish the preferentially occupied momentum state after n pulses it is necessary to find the value of v for which the condition $F' = 0$ is satisfied. This condition cannot, in general, be satisfied for integer v and n so the momentum states that will be occupied after n pulses will be those whose value of v is close to the non-integer value deduced from the solution to $F' = 0$. For fixed n, F varies smoothly with v and hence F' varies periodically. This means that there will be an infinite number of different values of v that can satisfy the condition $F' = 0$ and thus allow rephasing. However, since the strength of the potential only allows the population by a diffractive pulse of momentum states that differ from the incoming pulse by up to $\sim 3\hbar G$, the preferentially populated value of v will, in fact, change by the smallest possible amount consistent with fulfilment of the rephasing condition. In practice, this means that the magnitude of the change in v from one pulse to the next must be less than the period of the variation in F' with v while n is kept constant.

From the form of Eq. (4.24), the period of F' as v is varied for constant n would appear to be $2\pi/A$. However, this would only be the case if v were a continuous variable, which is unphysical. The restriction on v to integer values means that F' is being sampled at unit intervals. The largest period of variation in F' consistent with the values taken by F' at the sampling points (and therefore the only physically significant one) is the largest possible value of $2\pi/|A - 2\pi\beta|$, where β is an integer. The largest value of this period is given by $2\pi/|A'|$, where $A' = A \bmod 2\pi$. This is analogous to the phenomenon of aliasing in signal processing [124]. In the same way, for constant v the value of F' is being sampled at integer values of n. Thus the maximum period of the variation in F' with n at constant v that would be deduced from the values at the sampling points is $2\pi/|B'|$, where $B' = B \bmod 2\pi$. For both A' and B' the mod is taken on the interval $[-\pi, \pi]$, as in the case of F'. Therefore, to find the variation of the preferentially populated value of v with n, and hence the trajectory of the accelerator mode in momentum space, it is necessary to satisfy the equation

$$F' = A'v - B'n + C' \tag{4.25}$$

$$= 0 \tag{4.26}$$

where $C' = C \bmod 2\pi$. It is C', rather than C, that is of physical significance because two different values of C separated by an integer multiple of 2π yield the same value of F', for given v and n. From Eq. (4.25) it is clear that the line in (n, v) space that satisfies Eq. (4.26) has a gradient of B'/A'. It is that value of v which fulfils the rephasing condition after n pulses that will populate higher momentum states after diffraction, which must then rephase, and so on. Hence it can be concluded that the trajectory of the accelerator mode is given by the values of v that satisfy the equation

$$v = \left(\frac{B'}{A'}\right) n \tag{4.27}$$

where $n \geq 1$. As discussed above, in general this specifies values of v that are non-integer. The populated values of v, and therefore those that compose the ac-

celerator mode, will be those integers that are closest to the theoretically preferred value given by this formula.

As an example of the operation of this formula, the much-studied case of $T = 60.5\mu$s is considered. For this value of T, $A = 5.702$ and $B = 0.504$. Therefore $A' = -0.581$ and $B' = 0.504$, so $B'/A' = -0.868$. This implies that the preferentially occupied momentum state after 50 pulses would be given by $v = -43.4$, corresponding to an accelerator mode momentum of $-86.8\hbar k_1$. The experimentally measured central momentum of an accelerator mode created by 50 pulses with $T = 60.5\mu$s is $(-77.6 \pm 0.5)\hbar k_1$, while that produced by the quantum simulation is $-(86 \pm 1)\hbar k_1$. The larger uncertainty in the result from the simulation is due to the irregular shape of the mode and hence the difficulty in assigning a central momentum value. Nevertheless, the agreement between the analytical prediction and the result of the numerical simulation is excellent. The agreement between the analytical result and that of the experiment is less good (the difference is around 10%). This discrepancy could be explained by the non-ideal nature of the experiment. Firstly, the experimental interval between consecutive pulses was 60μs, and the duration of each was 0.5μs, giving a pulse period of 60.5μs. This is not completely equivalent to a situation where the pulses are δ-functions and the interval, and hence pulse period, is 60.5μs. The free evolution of the wavefunction between pulses can only take place in the experiment over a time of 60μs, rather than 60.5μs as in the simulation. This may lead to a lower momentum transfer; for example, Eq. (4.27) indicates that if $T = 60.0\mu$s, the momentum attained after 50 pulses should be $-79.0\hbar k_1$. This effect of the non-δ-function nature of the pulses is likely to be the most important cause of the quantitative disagreement. Secondly, G could differ from the assumed value if the retroreflection of the beam of light to create the standing wave were imperfect. In this case, the effective spatial period of the standing wave would be longer and G smaller. The modification to the value of G only increases as the square of the misalignment angle of the retroreflected beam. This was certainly no more than 5 mrad, which would lead to a reduction in G by 0.1%. Eq. (4.27) predicts that this would result in an accelerator mode momentum after 50 pulses with $T = 60.5\mu$s of $-85.1\hbar k_1$, yielding a small reduction in momentum transfer. Thirdly, if the standing wave itself were not exactly parallel to the local gravitational acceleration then the effective value of g, and hence B', would be reduced. This means that the momentum transfer would be slightly smaller. For example, if the orientation of the standing wave differed from that of gravity by 90 mrad (5°), the analytical prediction for the momentum of the accelerator mode after 50 pulses, with $T = 60.5\mu$s, is $-86.5\hbar k_1$. The system is, therefore, quite insensitive to the precision of this orientation.

Despite the quantitative discrepancy, the general agreement of the experimental momentum of the accelerator mode with the predicted value is good. It is clear from Fig. 4.10 that the direction of the accelerator mode can vary with the value of T. This is also predicted by Eq. (4.27), from the signs of A' and B' as T is varied. Figure 4.15 shows the variation with T of the predicted momentum of an accelerator mode after 30 pulses, as deduced from Eq. (4.27). The similarity to the behaviour of the accelerator mode shown in Fig. 4.10 is obvious. Note that the

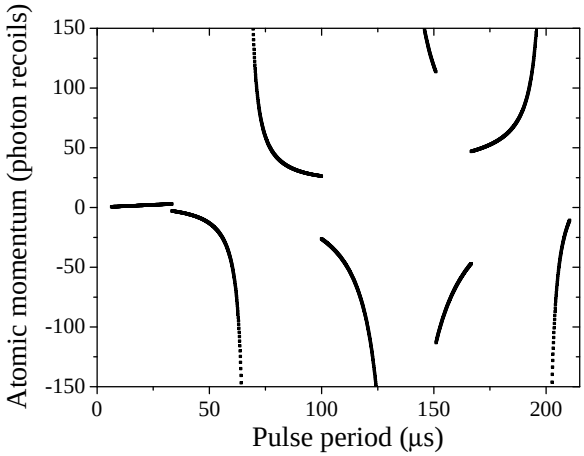

Figure 4.15: Variation with T of the momentum of a quantum accelerator mode after 30 pulses as predicted by Eq. (4.27). The agreement with Fig. 4.10 is excellent.

momenta of the accelerator modes diverge at those pulse periods that correspond to quantum resonances in the δ-kicked rotor. The existence of an accelerator mode obeying Eq. (4.27) depends upon fulfilment of the correct initial condition that will allow the relation $F' = 0$ to be satisfied for all n. Substitution of the expression in Eq. (4.27) into Eq. (4.25) yields the result that for the value of v that satisfies the rephasing condition when evolving between the nth and $(n+1)$ pulses:

$$F' = A'\left(\frac{B'}{A'}\right)n - B'n + C' \tag{4.28}$$

$$= C' \tag{4.29}$$

For atoms that are in the accelerator mode this must be equal to 0, so $C' = 0$. This means that $C = 2\pi q$, where q is an integer, and this relation constitutes a condition on the initial momentum of a plane wave that can give rise to a quantum accelerator mode.

$$C = 2\pi q \tag{4.30}$$

$$\Rightarrow \frac{GTp_i}{m} + \frac{gGT^2}{2} - \frac{\hbar G^2 T}{2m} = 2\pi q \tag{4.31}$$

$$\Rightarrow p_i = \left[q\frac{T_{1/2}}{T} + \frac{1}{2}\left(1 - \frac{mgT}{\hbar G}\right)\right]\hbar G \tag{4.32}$$

Therefore the initial plane waves that can give rise to a quantum accelerator mode are equally spaced in momentum and form a momentum comb with a spacing of $(T_{1/2}/T)\hbar G$. The accelerator mode created from any one of these suitable initial momenta populates several neighbouring values of v around the theoretical, non-integer value given by Eq. (4.27). Since the momentum separation of these states is $\hbar G$, this accelerator mode consists of a momentum comb whose spacing is $\hbar G$. The accelerator mode created from an initially *continuous* momentum distribution will

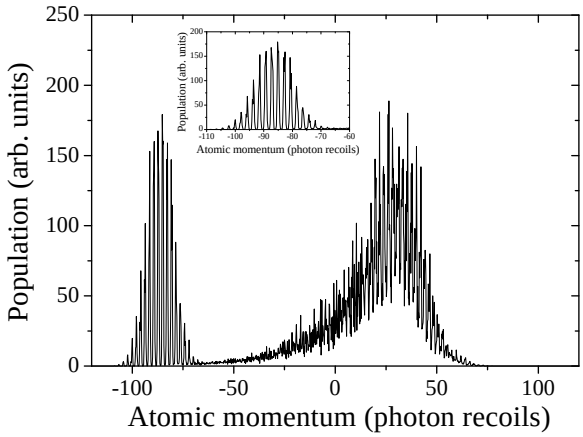

Figure 4.16: Momentum distribution of the quantum δ-kicked accelerator system after 50 pulses with a pulse period of 60.5μs, as produced by numerical simulation. This is a high-resolution momentum histogram; the bin size is $0.1\hbar G$. The comb structure of momentum in the accelerator mode is clear, particularly on the expanded scale shown inset. Note that the population scale is linear, not logarithmic.

also have a comb-like structure, determined by the superposition of the $\hbar G$-spaced combs from each plane wave that satisfies the $C' = 0$ condition. The spacing of the initial momenta of these plane waves is $(T_{1/2}/T)\hbar G$, and these two different momentum periodicities are, in general, incommensurate. Only values of T close to, but not at, integer multiples of $T_{1/2}$ permit accelerator modes that involve large momentum transfers, so for accelerator modes with a significant momentum separation from the rest of the distribution these periodicities will not be too incommensurate. This means that the superposition is itself a momentum comb whose teeth are separated by a value close to $(T_{1/2}/T)\hbar G$, and have some finite width. This width will be smaller for values of T closer to integer multiples of $T_{1/2}$, for which the periodicities will be more commensurate.

The momentum distributions produced by the numerical simulation of the quantum system can be plotted using narrow momentum bins in order to allow the character of the distribution to be viewed at high resolution. Figure 4.16 shows the momentum distribution produced by the simulation after 50 pulses have been applied with a pulse period of 60.5μs. The width of each momentum bin is $0.1\hbar G$. The inset in the figure shows the accelerator mode on an expanded momentum scale. The comb-like structure of the momentum distribution in the accelerator mode is clear, in agreement with the previous discussion. Furthermore, the spacing between adjacent peaks in the comb is, to a good approximation, $(T_{1/2}/T)\hbar G$, as expected from the separation of the momenta that can give rise to the mode. The width of each element in the comb, and the very slight difference in the period from $(T_{1/2}/T)\hbar G$ (approximately 2%), reflect the incommensurate nature of the two periodicities that combine to produce this comb. The $(T_{1/2}/T)\hbar G$ periodicity is the 'dominant' one; each initial momentum that gives rise to an accelerator mode populates a distribution of momentum states separated by $\hbar G$, but the population

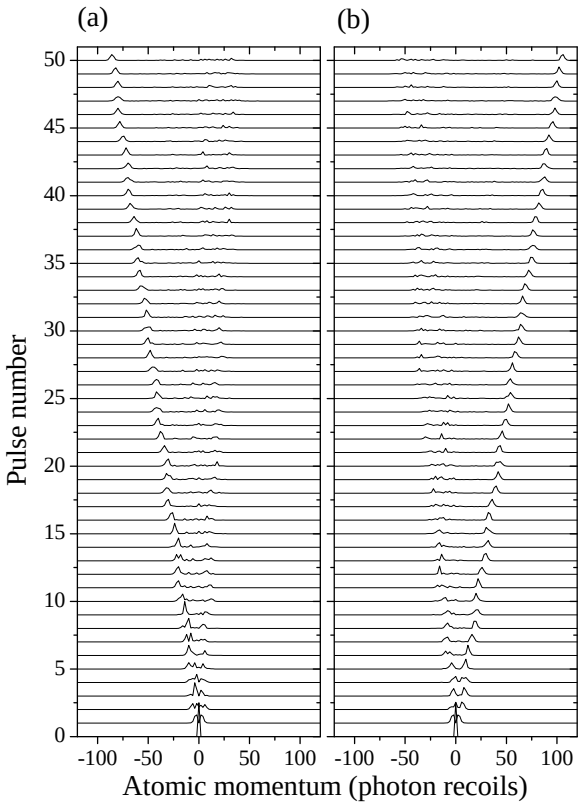

Figure 4.17: Momentum distributions after different pulse numbers ranging from 0 to 50, as generated by numerical simulation, resulting from one initial plane wave of momentum $\hbar k_1$ in the quantum δ-kicked accelerator system. The pulse period in (a) was 60.5μs, while that in (b) was 74.5μs; $\phi_d = 0.8\pi$. The bin size is $\hbar G$. Note that the population scale is linear, not logarithmic.

of one of these states is usually higher than that of the others. Figure 4.17 shows the variation with pulse number of the momentum distribution generated by one initial plane wave of momentum $\hbar k_1$, which gives rise to an accelerator mode, for pulse periods of (a) $T = 60.5\mu$s and (b) $T = 74.5\mu$s. The momentum bin size is $\hbar G$, which is all that is needed in this case since the momenta populated from an initial plane wave can only differ from the initial value by integer multiples of $\hbar G$. This figure confirms that one of the momentum states in the accelerator mode normally has a much larger population than those surrounding it. The superposition of such distributions from each initial plane wave yields a comb of the form shown in Fig. 4.16, in which the spacing between adjacent peaks is much closer to $(T_{1/2}/T)\hbar G$ than to $\hbar G$. It is also worth remarking that, as shown in Fig. 4.16, the momentum distribution of the atoms that have not entered the accelerator mode does not form a comb. The comb in the accelerator mode is a consequence of the selection of initial momenta that fulfil the rephasing criteria.

The existence of the momentum comb in the accelerator mode can be observed experimentally, as outlined schematically in Fig. 4.18. An accelerator mode can

be created in the usual way by application of a certain number of pulses n_1 of the standing wave in the presence of gravity, with a certain value of the pulse period T. These are labelled 'preparation pulses' in Fig. 2.9. The atoms can then be allowed to fall freely for a time $T_{\rm gap}$, over which time they are accelerated by gravity and hence translated linearly in momentum space by $mgT_{\rm gap}$. After this time, n_2 further pulses of the potential (which are labelled 'main pulses' in Fig. 2.9) are applied, also with pulse period T, and the momentum distribution is measured by the TOF system. The phase modulator is inactive while the main pulses are applied, so gravity's effect is present throughout the whole sequence. The rationale behind this method is that, for a given pulse to be successful in accelerating a group of atoms, the correct comb momenta have to be occupied. This condition is fulfilled in the course of a normal pulse sequence in which there is a constant interval between consecutive pulses. In the procedure now being discussed, the interval $T_{\rm gap}$ between the two sets of pulses means that the comb elements created by the first set of pulses may occupy momenta at the beginning of the second set of pulses that are different from those they would occupy if both sets of pulses formed a single pulse train with the given value of T. If the time $T_{\rm gap}$ is such that the momenta occupied by the comb elements at the beginning of the second set of pulses allow fulfilment of the rephasing condition and hence further acceleration, the accelerator mode will move out to the momentum that it would occupy if $(n_1 + n_2)$ pulses, with pulse period T, were applied continuously. If this condition is not fulfilled, further acceleration by the second set of pulses will not occur. If $T_{\rm gap}$ is scanned, acceleration of the atoms by both sets of pulses should occur at regular intervals, for values of $T_{\rm gap}$ that are separated in time by $T_{\rm comb}$. $T_{\rm comb}$ is the length of time that is needed to accelerate the atoms by gravity so that their momentum is shifted by the comb spacing $(T_{1/2}/T)\hbar G$. This indicates that the value of $T_{\rm comb}$ should be $(T_{1/2}/T)\hbar G/mg$.

Figure 4.19 shows the momentum distributions measured experimentally when two sets of 20 pulses were applied to the atoms with $T = 60.5\mu$s, separated by values of $T_{\rm gap}$ ranging from 0.2 ms to 2 ms. The detuning of the light forming the standing wave from the $(F = 4 \rightarrow F' = 3)$ transition was 30 GHz. A periodic variation in the population of atoms accelerated by both pulses out to a momentum in the region of $-60\hbar k_1$ is clear. The central momentum of an accelerator mode created by 40 consecutive pulses with $T = 60.5\mu$s was found experimentally (from the data shown in Fig. 4.6) to be $-64\hbar k_1$. A sinusoidal fit to the variation in the population at this momentum in Fig. 4.19 yields a period of $(763 \pm 4)\mu$s. Using the values $g = 9.80665\,{\rm m\,s^{-2}}$, $T = 60.5\mu$s, the standard values of m and $\hbar$ and the ideal value for G (assuming perfect retroreflection of the beam creating the standing wave) the formula for $T_{\rm comb}$ predicts a value of 753.7μs for this period, which is not too far from the experimentally determined value. If the latitude-corrected value $g = 9.8113\,{\rm m\,s^{-2}}$ were used [81], the value predicted for the period would be slightly altered to 753.4μs. Perfect agreement between theory and experiment could not be expected because, as discussed above, the finite duration of each pulse affects the experimental dynamics and reduces the inter-pulse free evolution time below 60.5μs. This effect would be expected to increase the comb spacing and

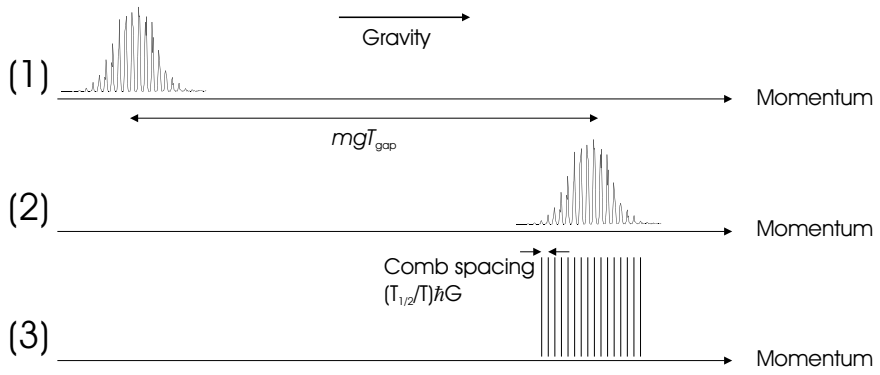

Figure 4.18: To allow experimental observation of the momentum comb structure of the accelerator mode (1) an accelerator mode is created with n_1 pulses, (2) the atoms fall freely under gravity for a time $T_{\rm gap}$, thus translating the momentum comb by $mgT_{\rm gap}$, and (3) n_2 further pulses, which define an ideal comb that will allow further acceleration, are applied. If $T_{\rm gap}$ is such that the existing comb of atoms matches the ideal comb, further acceleration of the atoms will occur.

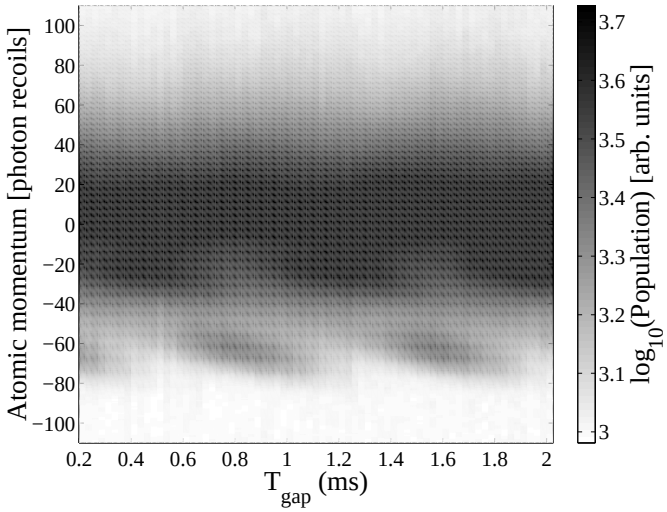

Figure 4.19: Experimentally measured momentum distributions following the application of two sets of 20 pulses of the standing wave, separated by a time $T_{\rm gap}$, to the ensemble of atoms. The pulse period used was 60.5μs, and the red-detuning of the light from the ($F = 4 \rightarrow F' = 3$) D1 transition was 30 GHz. In this figure, the density of shading is proportional to the logarithm of the population of atoms (in arbitrary units) at a certain momentum, for a certain pulse period. Hence each vertical slice in this figure is a momentum distribution analogous to that shown in Fig. 4.5(a). The periodic variation in the population of atoms accelerated by both sets of pulses demonstrates the existence of a momentum comb in the accelerator mode and hence the localisation in momentum space of the atomic wavefunctions.

hence the experimental value of T_{comb}. Furthermore, the non-parallel orientation of the standing wave relative to the gravitational acceleration would also increase the value of T_{gap} required to translate the momentum distribution by the spacing of the comb elements. A numerical simulation of this experiment, using $\phi_d = 0.8\pi$, gives good qualitative agreement with the form of the behaviour shown in Fig. 4.19. Therefore this figure shows the type of behaviour that would be expected to result from an accelerator mode consisting of a momentum comb as shown in Fig. 4.16. Since an accelerator mode consists of a comb of momenta, it may be said to be periodically localised in momentum space.

It is evident from Fig. 4.19 that the central momentum of the doubly accelerated group of atoms varies with T_{gap}. This is because the momentum distribution of the atoms in the accelerator mode is formed from a superposition of combs with two incommensurate periods, yielding a resultant comb whose spacing is about 98% of $(T_{1/2}/T)\hbar G$. Hence the spacing of the elements in this comb in not quite the same as that of the ideal comb defined by the second set of pulses, which is $(T_{1/2}/T)\hbar G$. This means that as T_{gap} is varied, so the position of the accelerator mode's comb in momentum space is scanned, there will be some values of T_{gap} for which the ideal comb defined by the second set of pulses (of spacing $(T_{1/2}/T)\hbar G$) has a good overlap only with elements in the wings of the accelerator mode (see Fig. 4.20). In this case the doubly accelerated population will be small, and the central momentum reached by it will differ from that which would be reached by an accelerator mode created by $n_1 + n_2$ consecutive pulses, since the atoms being accelerated by the second set of pulses either lead or lag in momentum the main bulk of atoms in the accelerator mode. Upon further acceleration, these atoms will reach a momentum centred on a higher or lower value than that which the main distribution would reach, depending on which wing of the accelerator mode has good overlap with the ideal comb. The maximal population of atoms to be accelerated by both sets of pulses occurs when there is the best overlap between the ideal comb and the central, highly populated elements of the accelerator mode comb, as shown in Fig. 4.20.

Figure 4.17, as stated, shows the momentum distributions that result, for $T = 60.5\mu$s and $T = 74.5\mu$s, from an initially plane wave that has the correct momentum to give rise to an accelerator mode. The fact that these distributions have some finite (indeed, considerable) extent in momentum space for any pulse number $n \geq 1$ means that they correspond to non-uniform distributions in position space. These spatial distributions, $|\psi(z)|^2$, may be obtained by performing a Fourier transform on the momentum distribution, the method of which is described in Sec. 3.3.2. The only difference in the case of the δ-kicked accelerator is that the wavevector of the momentum state $|u\rangle$ just before the nth pulse is given by $k_{u,n-1} = k_i + uG - (n-1)mgT/\hbar$, where k_i is the initial wavevector of the plane wave. The results for $|\psi(z)|^2$ obtained from using this transformation on the momentum distributions in Fig. 4.17, for pulse numbers from 0 to 30, are shown in Fig. 4.21. This figure shows that a wavefunction that supports an accelerator mode exhibits periodic localisation in position space. The precise region of localisation is also noteworthy. Figure 4.17(a) shows that the accelerator mode that exists when $T = 60.5\mu$s is

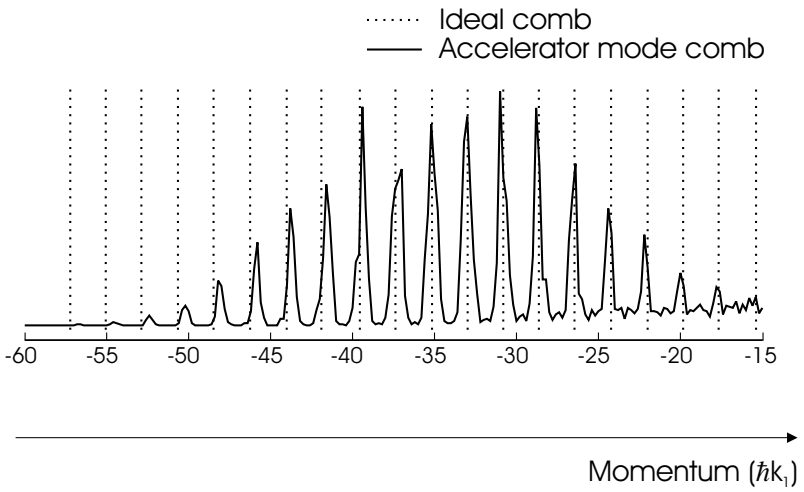

Figure 4.20: The overlap between the momentum comb created by 20 preparation pulses (as generated by numerical simulation) and the ideal comb defined by the main pulses at the instant when this overlap is approximately maximal. The scale is in units of the atomic momenta in the falling frame. The spacing of the elements in the accelerator mode comb is about 98% of that of the elements in the ideal comb. This means that for a slightly smaller value of $T_{\rm gap}$ there is greater overlap of the ideal comb with the elements on the side of the less-negative momenta. Conversely, for a slightly larger value of $T_{\rm gap}$ the overlap is greater with the elements on the more-negative momentum side. This accounts for the variation with $T_{\rm gap}$ of the central momentum of the doubly accelerated group of atoms, as well as the population of this group, as shown in Fig. 4.19 (see text).

in the negative momentum direction. From Fig. 4.21(a) it can be seen that as an increasing number of pulses is applied to the system the spatial localisation of the wavefunction is often at a position where the gradient of the potential is non-zero and positive. The classical force experienced by a particle at this position would be in the negative momentum direction, so the acceleration of atoms in this direction would be expected. For certain pulse numbers, *e.g.* the 17th, the localisation seems to be predominantly in the position of zero potential gradient, corresponding to zero classical force. In this case the momentum distribution changes little, as can be seen in Fig. 4.17(a), an intuitively reasonable result. Similarly, when $T = 74.5\mu$s, Fig. 4.17(b) shows that the accelerator mode is in the positive momentum direction. From Fig. 4.21(b) it can be seen that the corresponding spatial localisation is often at a position of non-zero and negative gradient, corresponding to a classical force in the positive momentum direction. As in the case of $T = 60.5\mu$s, for certain pulse numbers, *e.g.* the 13th, the localisation is predominantly in the position of zero classical force, yielding little change in the associated momentum distribution.

The spatial localisation of an accelerator mode can also be observed experimentally. The procedure is identical to that by which the momentum localisation (*i.e.* the momentum comb) is observed. A pulse train of n_1 preparation pulses, with pulse period T, is applied to the atoms to create an accelerator mode. The atoms are allowed to fall freely under gravity for a time T_{gap}, after which n_2 main pulses, with the same pulse period T, are applied and the resulting momentum distribution is measured. The phase modulator is inactive throughout, so gravity's effect is unmodified. The rationale is that for the atoms accelerated by the first set of pulses to be accelerated by the second set, their spatial distribution has to be localised on the correct part of the potential when the second pulse set commences. Following the first set of pulses, which results in the spatially localised distribution, the position of localisation is shifted because the accelerated atoms are moving with a certain velocity relative to the standing wave. This velocity is determined by the free-fall acceleration undergone by the atoms after molasses cooling, prior to application of the potential, plus the velocity acquired while the pulses are being applied, due to both the gravitational acceleration and the accelerator mode. If the value of T_{gap} is such that the shift in the position of the wavefunction's spatial localisation between the sets of pulses is an integer multiple of λ_{spat}, the localisation will then be in the correct position to allow further acceleration by the second set. Therefore, the population of doubly accelerated atoms should vary periodically with T_{gap} because the translation of the spatial localisation of the wavefunction is proportional to T_{gap}. If the atomic wavefunction is not periodically localised then the efficiency of double acceleration should not depend on T_{gap}, provided that the momentum comb condition is fulfilled.

Figure 4.22 shows the variation with T_{gap} in the population of atoms accelerated by two sets of 20 pulses, with $T = 60.5\mu$s, and a detuning of the standing wave light by 30 GHz from the $(F = 4 \rightarrow F' = 3)$ transition. The value of T_{gap} was scanned in the region of $2T$, from 114μs to 130μs, and the resulting behaviour is very similar to that which was observed when the scan was performed around T. A periodic variation in the population of atoms accelerated by both pulses

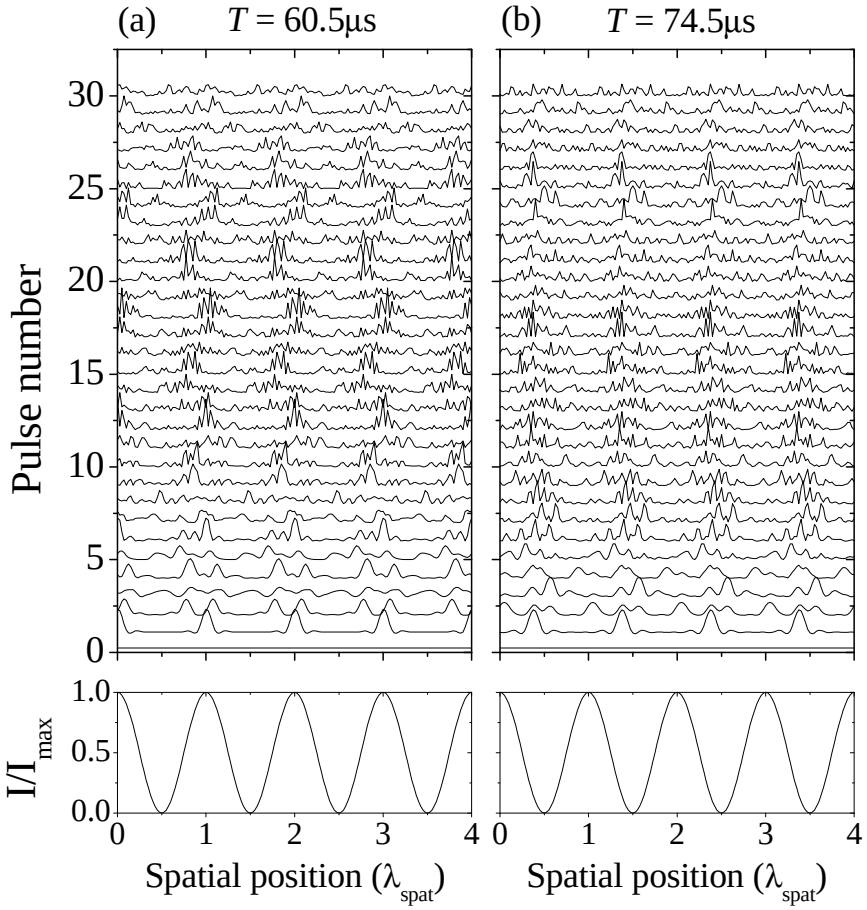

Figure 4.21: Variation of the spatial distribution with pulse number of an initially plane wave with momentum $\hbar k_1$, as calculated by numerical simulation. The phase modulation of the wave by the potential was $\phi_d = 0.8\pi$ and the pulse period T was (a) 60.5μs, (b) 74.5μs. The population scale is linear and the intensity profile $I/I_{\max}$ of the standing wave that forms the periodic potential is also shown. These spatial distributions are the Fourier transforms of the momentum distributions shown in Fig. 4.17.

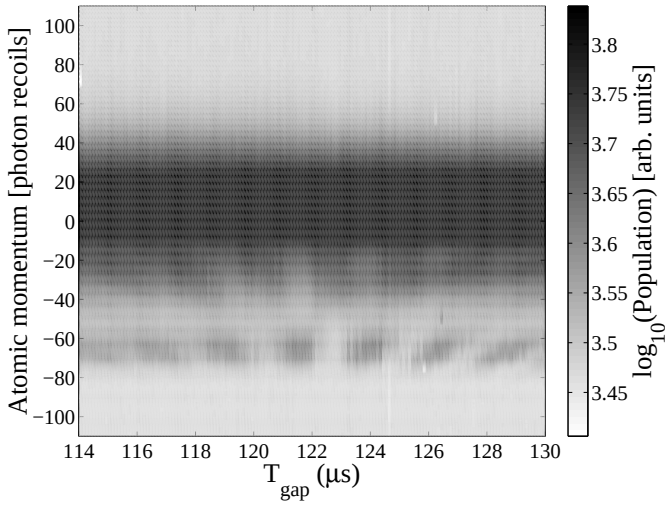

Figure 4.22: Experimentally measured momentum distributions following the application of two sets of 20 pulses of the standing wave, separated by a time T_{gap}, to the ensemble of atoms. The pulse period used was 60.5μs, and the red-detuning of the light from the ($F = 4 \rightarrow F' = 3$) D1 transition was 30 GHz. In this figure, the density of shading is proportional to the logarithm of the population of atoms (in arbitrary units) at a certain momentum, for a certain pulse period. Hence each vertical slice in this figure is a momentum distribution analogous to that shown in Fig. 4.5(a). The periodic variation in the population of atoms accelerated by both sets of pulses demonstrates the spatial localisation of the atomic wavefunctions.

out to around $-60\hbar k_1$ is clearly visible, and the visibility of this variation dies away as $T_{\rm gap}$ departs from values in the range 120μs to 125μs. A sinusoidal fit to the variation in the population at a momentum of $-64\hbar k_1$, the central momentum of an accelerator mode produced by 40 consecutive pulses, yields a period of $(2.56 \pm 0.03)\mu$s. This value can be accounted for as follows. Following the removal of the molasses cooling light, the atoms fell freely for 5.2 ms before being subjected to the first 20 pulses. Over this time they acquired a downwards velocity of $51\,{\rm mm\,s^{-1}}$. From the data shown in Fig. 4.6, the central momentum of an accelerator mode created by 20 pulses with $T = 60.5\mu$s is $-34\hbar k_1$, corresponding to a downwards velocity of $114\,{\rm mm\,s^{-1}}$. Acceleration due to gravity while the pulses were applied resulted in an additional $12\,{\rm mm\,s^{-1}}$ of downwards velocity. Hence the total downwards velocity of the atoms relative to the standing wave after the first 20 pulses was $177\,{\rm mm\,s^{-1}}$. A particle moving with this velocity takes 2.53μs to cover a distance of $\lambda_{\rm spat} = 447$nm (the change in velocity due to gravitational acceleration over such a small time may be neglected), which is in excellent agreement with the observed period of variation in the doubly accelerated population with $T_{\rm gap}$. These calculations assume that $g = 9.81\,{\rm m\,s^{-2}}$; given the accuracy of the measurements here, use of more than 3 significant figures in g is superfluous. When the time of free fall prior to application of the first preparation pulse was increased, so that the velocity of the atoms at the end of the preparation sequence was larger, the period of the variation in the doubly accelerated population was reduced, as expected. These results, therefore, constitute experimental evidence that the atomic wavefunction is spatially localised and that the position on the periodic potential of this localisation must be correct in order for an accelerator mode to be produced. The results of a numerical simulation of this experiment, using the value $\phi_d = 0.8\pi$, are qualitatively similar to those shown in Fig. 4.22, except that the period of variation is somewhat larger (around 3.2μs) because there is no free fall of the atoms prior to the application of the periodic potential. The use of such small values of $T_{\rm gap}$ in these experiments, and the small changes necessary to observe spatial localisation, meant that the momentum comb condition for acceleration by both sets of pulses was automatically fulfilled. The width of the momentum comb elements was sufficiently great that the momentum condition for double acceleration could be fulfilled by a large range of $T_{\rm gap}$. Figure 4.19 indicates that this condition could be satisfied over a $T_{\rm gap}$ range of more than 200μs. The experimental demonstration of spatial localisation, and of the existence of a momentum comb, means that an accelerator mode formed from an ensemble of atoms with a range of initial momenta comprises periodic localisation in both momentum and position space.

The difference between the experiment performed to observe the spatial localisation and that to observe the momentum localisation was in the time scale of $T_{\rm gap}$. Whereas $T_{\rm gap}$ was scanned by multiples of approximately 760μs (in the case of $T = 60.5\mu$s) to observe the momentum comb, it was varied by relatively small amounts around T or $2T$ to observe the spatial localisation. This time scale was set by the way in which the spatial localisation of a wave varies during the free evolution following a pulse of the potential, as shown in Fig. 3.14. From this figure

it is clear that in order to have strong, periodic spatial localisation at a particular potential gradient it is necessary for the wave to evolve after a pulse for times in the vicinity of, but not equal to, integer multiples of $T_{1/2}$, *i.e.* 66.7μs, 133.3μs, etc. This is why accelerator modes are only observed for values of T in these regions. They define the range of values of T_{gap} for which the spatial localisation can permit further acceleration by the main pulses and hence can be observed. For this acceleration to occur, not only must there be strong spatial localisation but it must also be in the correct position. An accelerator mode in the experiment is produced by, and consists of, a range of momenta. In the absence of gravity, the region of spatial localisation after a certain value of T_{gap} following diffraction of a plane wave with momentum p would differ by $(p/m)T_{\mathrm{gap}}$ from that which would be found for a plane wave with zero momentum. This spatial offsetting effect is the same as was discussed in Sec. 3.3.2. The presence of gravity, which causes the momenta to vary linearly with time following a pulse, will yield an additional shift in the localisation region. A value of T_{gap} close to T or $2T$ allows both the periodic spatial localisation to be strong and the position of that localisation due to all the momenta in the accelerator mode to be similar. This means that the spatial localisation of all the momenta can simultaneously be at the correct potential gradient for further acceleration by the main pulses. For larger values of T_{gap} that also yield the necessary degree of spatial localisation, the region of that localisation is so different for the momenta within the accelerator mode that the spatial distribution of the ensemble is smeared out. In this case, there will always be some momenta within the accelerator mode whose region of localisation after T_{gap} allows further acceleration by the main pulses, no matter what the position of the potential's profile. Altering this position, therefore, does not result in any modulation in the efficiency of acceleration by the main pulses. Only a fraction of the atoms that were accelerated by the preparation pulses are accelerated by the main pulses (subject to fulfilment of the momentum comb matching condition), whereas almost all of the prepared atoms can be accelerated by the main pulses for values of T_{gap} around T or $2T$.

Returning to Fig. 4.22, the fall-off in the visibility of the doubly accelerated population's variation away from values of T_{gap} in the range 120μs to 125μs can, therefore, be explained by these two requirements on the spatial localisation (*i.e.* that it is sufficiently strong, and that it is in the correct position). As the value of T_{gap} moves away from 122μs, the spatial localisation of the different momentum classes is more smeared out, reducing the dependence of the accelerated fraction on T_{gap}. Furthermore, the degree of this spatial localisation is smaller (see Fig. 3.14), so that even if only a very narrow momentum class were present the efficiency of acceleration by the main pulses would be reduced. The smearing out of the spatial localisation due to different momenta also explains why the central momentum of the doubly accelerated atoms varies with T_{gap}. Close to 122μs, all the momentum states are spatially localised in the same region and are accelerated simultaneously. Away from this time, different momenta have different regions of localisation and this difference grows as T_{gap} departs further from 122μs. As the position of the spatial localisation relative to the profile of the potential is varied by scanning T_{gap},

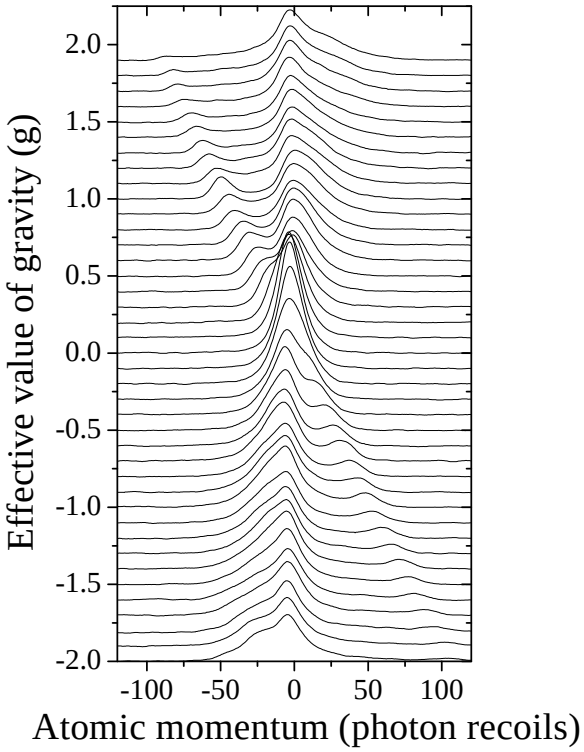

Figure 4.23: Experimentally measured momentum distributions in the case where 30 pulses of the periodic potential were applied to the atoms, with $T = 60.5\mu$s, for different effective values of gravity. The red-detuning of the light from the ($F = 4 \rightarrow F' = 3$) D1 transition was 20 GHz. Note that the population scale is linear, not logarithmic. The linear variation with the effective value of gravity in the momentum attained by the accelerator mode after 30 pulses is clear.

different momenta are at the correct position on the potential for acceleration by the main pulses so the central momentum of the resultant accelerator mode changes. It can also be seen from Fig. 4.22 that the variation with $T_{\rm gap}$ of the population at a specific momentum within the accelerator mode is more rapid for momenta of larger magnitude. This is expected, since the atoms with these momenta must move a larger distance over the periodic potential as $T_{\rm gap}$ increases.

Using the crystal phase modulator it was possible, as described in Sec. 2.4, to change the effective value of gravity experienced by the atoms in the system by varying the relative acceleration between the atoms and the standing wave. Figure 4.23 shows the experimentally measured momentum distributions that resulted from the application of 30 pulses with a pulse period $T = 60.5\mu$s for different values of the effective gravity. It is clear that the momentum of the accelerator mode after 30 pulses varies linearly with the effective value of gravity, and that it is in the negative direction when gravity acts downwards but in the positive direction when gravity acts upwards. This is expected, because a linear variation in the effective value of gravity from $-2g$ (*i.e. upwards*) to $+2g$ corresponds to a linear

variation in the value of B' from -1.0 to 1.0, while A' remains constant. Thus Eq. (4.27) predicts the observed variation in the momentum attained by the accelerator mode. The population of atoms in the accelerator mode after 30 pulses also varies with the effective gravity. There are three reasons for this. The first is that the use of the phase modulator varied the effective gravity imperfectly, because of uncertainty in the modulator's calibration and linearity of response to applied voltage. This caused a certain amount of 'noise' in the pulse-to-pulse position of the profile of the standing wave and hence a reduction in the population of the accelerator mode. Furthermore, there was a maximum voltage that could be applied to the modulator, so phase shifts were always applied *modulo* 2π. Imperfection in the calibration would lead to a greater accumulated error for larger phase shifts, such as would be needed to attain an effective gravity of $-2g$, and so a reduced efficiency of acceleration. Modulators of this type, when active, can also cause some deviation in the beam direction, and this would reduce the depth of the potential and hence the population of the accelerator mode. These modulator effects meant that the maximum population of the accelerator mode was found when the modulator was inactive, *i.e.* when gravity's effect was unmodified. The second reason for the reduced population when the effective gravity approaches $\pm 2g$ is that for these large values of the relative acceleration between standing wave and atoms the change in the preferentially occupied momentum state between consecutive pulses is twice as large as in the normal gravitational field. Thus a larger value of ϕ_d is required to attain the same population of these states. Since the value of ϕ_d applied to the atom in the experiment whose results are shown in Fig. 4.23 was kept constant, a reduced accelerator mode population for effective gravity in the region of $\pm 2g$ would be expected. The third reason for reduced population of the accelerator mode, when the effective gravity was in the region of $+2g$, is the violation of the Raman-Nath regime. Values of gravity in this region produce an accelerator mode with a large downwards velocity, which therefore reinforces the velocity attained by the atoms due to free-fall between molasses cooling and application of the pulses. Thus the distance moved by the atoms while a pulse was being applied was larger than when gravity had its usual value, and this meant that there was greater violation of the Raman-Nath condition. The result was a reduced accelerator mode population.

4.4 Summary

This chapter has discussed the characteristics of the quantum δ-kicked accelerator, as observed experimentally and through the use of numerical simulations, and has made a comparison with those of the corresponding classical system. The presence of an external unidirectional force acting on the particles in the system, which is the difference between the δ-kicked accelerator and δ-kicked rotor, dramatically alters the dynamics. The most remarkable phenomenon evident in the quantum δ-kicked accelerator system is the existence, for certain values of the pulse period, of quantum accelerator modes. These involve a large transfer of momentum to a

significant fraction of the atomic ensemble, and experimental momentum transfers in excess of $100\hbar k_1$ are quite feasible. Such behaviour is entirely absent in the classical system, and can be explained by consideration of the phase evolved between consecutive pulses by the different momentum states populated through the diffractive effect of the periodic potential. This model has allowed the expected momentum of an accelerator mode after a certain number of pulses to be predicted analytically, as well as the mode's dependence on pulse period and the magnitude and direction of the external force. The existence of the accelerator mode results in a large transfer of energy to the system, though for a continuous range of initial momenta the net momentum of the atomic system as a whole is conserved. The localisation of the accelerator mode in both momentum and position has been described and investigated experimentally. The presence of such localisation in both these conjugate quantities means that the accelerator mode isolates a particular region of phase space. Both the large momentum transfer associated with an accelerator mode, and the localisation of the mode in phase space, are properties of considerable potential utility. Further discussion on this subject will be found in Ch. 6.

Chapter 5

Decoherence in a δ-kicked system

The primary motivation for the original investigation of the quantum δ-kicked rotor (see Ref. [29], p. 334) was the fact that its classical analogue is a chaotic system that, though conceptually simple, can exhibit complex dynamics. As discussed in Ch. 3, the behaviour of the quantum system differs greatly from that of the classical. Phenomena such as dynamical localisation and quantum resonances are peculiar to the quantum system. They are manifested by the character of the evolution with time of the momentum distribution and mean energy of the particles. The differences in the behaviour of the quantum and classical versions of the δ-kicked accelerator, as discussed in Ch. 4, are no less dramatic. The most striking aspect of these differences is the quantum accelerator mode; again, this cannot be explained classically. The outcome of these investigations, therefore, leads to the conclusion that quantum mechanics radically alters the behaviour of these classically chaotic systems.

The fact that the quantum and classical types of behaviour are so different has led to conjecture that the present theory of quantum mechanics is incomplete because it does not fully embody quantum-classical correspondence [125]. Any successful quantum theory should be able to predict classical behaviour [126]. However, a considerable amount of theoretical work has been undertaken to seek to establish how quantum-classical correspondence can be reconciled with the present framework of quantum mechanics and these investigations have focused on the effect of *decoherence*. Decoherence is the 'monitoring' of the state of a system by its coupling to internal and external degrees of freedom that cannot be measured by an observer. This monitoring means that these degrees of freedom become entangled with the state of the system; there is transfer of information about the state of the system to the environment. Following the discussion by Joos and Zeh of the emergence of classical properties through interaction with the environment [127], the work of Zurek *et al.* has found that decoherence can produce a smooth quantum-to-classical transition in nonlinear dynamical systems [128, 129, 130, 131, 132] and thus provide a mechanism by which quantum-classical correspondence can be restored. The eigenstates of the observables monitored by the environment decohere

and behave like classical states. This is not a contrived escape from a failure of the theory. Every real quantum system does have interaction with its environment, so the effect of decoherence is an inescapable aspect of the Universe. Since the belief in quantum-classical correspondence arises from observation of a world in which decoherence is rife, it might be expected that any theory explaining its behaviour would crucially involve the effect of this decoherence [1].

Note the distinction between noise and decoherence. Noise describes a process in which the state of the environment becomes inscribed on the observable of interest. An example of this might be the vibrations that are present in an apparatus and which cause a random variation with time of the position of a standing wave relative to a particle. This randomisation cannot be interpreted as the making of a measurement on the system. With decoherence, on the other hand, information about the system is transferred to the environment. For example, if an atom undergoes spontaneous emission, the emitted photon carries information about the state of the atom that emitted it. If this photon is undetected, the information is lost but the system has still become entangled with its environment. Of course, noise (in the sense of disruption to the system) can accompany decoherence and a direct example of this would be the momentum recoil imparted to an atomic system when a photon is emitted.

The conclusion from the discussions in the work cited above was that decoherence can play a crucial role in reconciling the behavioural differences observed between classical and quantum systems. This means that its possible contribution to the genesis of classically chaotic behaviour in quantum systems should be investigated experimentally, in order to gain a greater understanding of both chaos and decoherence. This was undertaken using the δ-kicked rotor and accelerator systems described in Chs. 3 and 4. The decoherence was introduced through spontaneous emission of the atoms. Before the results of those studies are described, previous investigations of the effect of noise and decoherence on the quantum dynamics of classically chaotic systems will be outlined.

5.1 Previous investigations of noise and decoherence

Initially, the effect of perturbations to the evolution of a δ-kicked system was studied theoretically. The effect of noise on the momentum diffusion of the quantum δ-kicked rotor was first analysed by Ott *et al.* in 1984 [43]. The noise was introduced by including in the potential term of the Hamiltonian a random function of time that represented a noise component in the kicking. This consequently modified the momentum incrementation of the standard mapping for the classical

[1] An interesting point, beyond the scope of this thesis, is that this work has also allowed a definition of quantum chaos in terms of the rate of production of entropy in a decohering quantum system [130]. In the quantum analogue of a classically chaotic system, the entropy increases at a much faster rate than does that of the quantum analogue of a classically integrable system. This difference could be used as a diagnostic of the stability of a quantum system.

system, and the Floquet operator of the quantum system. The conclusion was that even a low level of noise, which would have little effect on the value of the classical diffusion parameter $D(K)$, would markedly alter the quantum dynamics. In particular, the momentum diffusion would no longer be zero after the quantum break time and dynamical localisation would not occur. Thus the signature of characteristically quantum behaviour would be degraded, and the observed dynamics of the quantum system would be more like those of its classical analogue. The investigation by Guarneri in Ref. [133] considered the case of a quantum rotor subjected to aperiodic δ-kicks. It showed that the expectation value of the kinetic energy was unbounded with time and dynamical localisation did not occur. Therefore the usual δ-kicked rotor would always exhibit normal diffusion if a level of noise in the form of random kicks, at a level comparable to the kick strength, were applied to the system. The random kicking would dominate the momentum diffusion of the corresponding classical system. Hence the more interesting case to study is that considered by Ott *et al.* [43], in which noise produces little modification to the dynamics of the classical system. In Refs. [120, 134], the momentum diffusion of numerous kicked quantum systems in the presence of specific types of noise was studied by Cohen. The consequent enhancement of the momentum diffusion was explained in terms of the destruction of dynamical correlations, and hence coherence, in the system. Dyrting [135] investigated theoretically the modifications in the chaotic dynamics of laser-cooled atoms caused by spontaneous emission. The atoms were subjected to periodic pulses of a standing wave, and the dynamics were parametrised by the momentum diffusion parameter $D(K)$. The cessation of momentum diffusion, characteristic of dynamical localisation, was destroyed by the spontaneous emission. The system considered in this paper was very similar to that discussed in this thesis; this emphasises that experiments on the quantum δ-kicked rotor, and also on the novel δ-kicked accelerator, can be a useful forum for investigating the effect of decoherence. In Ref. [136], Dyrting and Milburn showed how phase noise in the standing wave could be considered equivalent in its effect on the atoms to that of continuous measurement which, from the work of Zurek *et al.* may be expected to lead to the nature of the quantum system's behaviour becoming more classical.

A study by Kaulakys and Gontis [137] coined the term 'quantum anti-Zeno effect' for the role of measurement (which can, therefore, be linked to decoherence) in degrading dynamical localisation in the quantum δ-kicked rotor, enhancing the momentum diffusion and restoring chaotic dynamics. This is in contrast to the quantum Zeno effect [138], in which a system's evolution is prevented by repeated, frequent measurement of the system's state. It was subsequently shown by Facchi *et al.* [139] that repeated measurement of the momentum of a quantum δ-kicked system would result in normal diffusion of momentum, the characteristic of a classically chaotic system. This would occur even when the dynamics of the corresponding classical system were regular, as is the case in, for example, the region of small K where classical momentum diffusion is limited by the existence of the KAM tori. This result shows the sensitivity of the quantum system to decoherence. Further experimentally-informed numerical studies of the effect of decoherence on

quantum δ-kicked systems were performed by the Auckland group [140, 141, 142]. In the case where dynamical localisation is evident in the absence of decoherence, the momentum distributions [140] were found to evolve from exponential to Gaussian as the level of decoherence was increased. The growth in mean energy after the quantum break time was also found to be non-zero, and linear, in the presence of decoherence, and increased as the level of decoherence rose. Other investigations [141, 142] focused on the effect of structure in the classical phase space, such as KAM tori and cantori, in a quantum system in which decoherence was present. The classical boundaries were found to inhibit momentum diffusion in the quantum system, but the effect of decoherence was to increase the quantum momentum transport through the boundaries. Other theoretical studies undertaken in Auckland focused on the effect of decoherence on the behaviour of the δ-kicked rotor for different values of $\bar{k}$ [143]. This investigation made a connection between the enhancement of momentum diffusion due to decoherence and the diffusion rate prior to the onset of dynamical localisation. Its results, and the behaviour observed at the $\bar{k} = 2\pi$ quantum resonance, are directly relevant to some of the experimental investigations reported below, and will be discussed further in Sec. 5.6.

The experimental investigations of these phenomena have also been extensive, and have mainly been performed using atom optical systems. The first experiments in this context, however, studied the effect of noise on the microwave excitation and ionisation of Rydberg states of rubidium atoms [41, 144]. For this system, the quantity that took the role corresponding to that of 'momentum' in atom optics was the principal quantum number n of the atom, as discussed in Ch. 1. In the absence of noise, microwave excitation resulted in localisation of the values of this quantity attained by the atoms. Noise was introduced to the system by mixing electronic shot noise [41], or broadband noise [144], with the coherent microwave pulses in arbitrary ratios; the experimental scheme was otherwise similar to that shown in Fig. 1.1. The effect of the noise was to yield a more equal distribution of the atoms over the different values of n [41]. In Ref. [144] it was found that the noise reduced the strength of the microwave field required to ionise 10% of the atoms. In each experiment these results indicated that the introduction of noise had caused the destruction of the localisation. As shown in Ref. [144], the time dependence of the threshold for 10% ionisation in the cases where broadband noise was present and absent indicated that the quantum system exhibited diffusive growth in n when the noise was present. This behaviour, to be contrasted with the phenomenon of localisation, may be interpreted as a restoration of the classical limit.

Since the techniques of atom optics allow the realisation of a close approximation to the quantum δ-kicked rotor [47], most subsequent investigations of the effect of noise and decoherence have been performed in this experimental field by two experimental groups in Auckland and Austin. The Auckland group [42, 145] introduced decoherence to the system by the spontaneous emission of the caesium atoms subjected to the standing light wave that formed the periodic potential. The probability of emission, and hence the level of decoherence, was adjusted by varying the detuning of this light from the ($F = 4 \rightarrow F'' = 5$) D2 transition. The

presence of decoherence was observed to increase the rate of growth of the mean energy of the system with pulse number, in agreement with the theoretical work described above. The momentum distributions, however, still attained an exponential form, despite the destruction of dynamical localisation. This behaviour was found to be in good agreement with the results of numerical simulation [146]. The Austin group compared the effects of decoherence and amplitude noise on the evolution of atoms that were kicked by a pulsed standing wave of light [114, 147]. The decoherence was introduced by spontaneous emission of the atoms as they were exposed to low intensity molasses cooling light while the standing wave was being applied. The amplitude noise was realised through random variation in the intensity of the pulses of standing wave light. The effect of both these processes was similar, and resulted in an increased rate of growth in mean energy with kick number, indicating a breakdown in dynamical localisation, and broadened momentum distributions that were neither exponential nor Gaussian. This is compatible with the Auckland results because the level of spontaneous emission present in the Austin experiments was approximately three times larger. More recent work from the Austin group [116, 117] has focused on quantitative studies of the momentum diffusion of the quantum δ-kicked rotor and its classical analogue (as simulated numerically) in the presence of high levels of amplitude noise. These levels were sufficiently high as to destroy classical kick-to-kick correlations, thus removing the oscillatory nature of the variation with K of the diffusion parameter $D(K)$, which is shown in Fig. 3.4(a). The momentum distributions of the classical and quantum systems after kicking were found to be the same, and Gaussian in form, when the same high level of noise was present in each. The growth in the mean energy with kick number of both systems was greatly enhanced and remained similar in the two cases up to high pulse numbers (around 70). Therefore the quantum system did not exhibit dynamical localisation. The agreement between the behaviour of the two systems was not only qualitative but also quantitative; in each case the spontaneous emission dominated the energy growth. This, however, was not the regime in which the experiments to be discussed below were performed. The procedure used for those experiments, and the numerical simulations that accompanied them, will now be described.

5.2 Experimental and numerical techniques

Following the success of the experiments outlined above, and the indication from theoretical investigations that decoherence has a pronounced effect on the quantum analogue of a classically chaotic system, an experimental investigation of this effect was a logical progression from the studies of the quantum δ-kicked rotor and accelerator described in Ch. 3 and Ch. 4, respectively. In particular, the novel system constituted by the δ-kicked accelerator could provide an opportunity for verifying that the previously observed effects of decoherence on such classically chaotic systems also apply in this previously unexplored case. The experimental system under discussion was far from noise-free. The variation in the power

and frequency of the light in the standing wave forming the periodic potential has already been discussed in Ch. 3 and Ch. 4. Vibrations could, as mentioned in these chapters, have the effect of randomising the relative position of the atoms and the potential. Magnetic field fluctuations could also modify the response of the atoms to the applied potential. However, given that exponential momentum distributions and dynamical localisation were observed in the realisation of the quantum δ-kicked rotor, these sources of noise could not have radically affected the system's dynamics. They may have contributed, however, to the quantitative discrepancies between the results of numerical simulation and experiment in the δ-kicked rotor and accelerator. Due to the large detuning from the D1 transition, the mean number of spontaneous emissions per atom per pulse resulting from the application of the standing wave was less than 2×10^{-3}, and so completely negligible. In order to perform useful experiments, it was necessary to be able to introduce controllable levels of decoherence into the system, sufficiently high as to cause a qualitative change in the system's dynamics. This was achieved by pulsing on two of the beams of light used for trapping and molasses cooling while the train of kicking pulses was being applied. After each 500 ns pulse of the standing wave, these beams would be applied for 2μs. The detuning of the light from the $(F = 4 \rightarrow F'' = 5)$ caesium D2 transition was 60 MHz, resulting in an average of 0.2 spontaneous emissions per atom per period (kick + free evolution). Following the pulse sequence, the momentum distribution of the atoms was measured by the TOF system in the usual way.

Experiments in which spontaneous emission was induced in the atoms during the sequence of δ-like kicks were performed in both the case of the δ-kicked accelerator and, for comparison, the δ-kicked rotor. Just as for the (relatively) decoherence-free experiments described in Ch. 3 and Ch. 4, numerical simulations of the quantum and classical δ-kicked systems were constructed and run. The basis of these was the same as in the decoherence-free case; the only difference was that the effect of a spontaneous emission on an atom had to be incorporated. For this, a Monte Carlo technique was used, although the exact way in which this was implemented differed in the two cases. In the quantum simulation, the wavevectors of all the different momentum states $\rho_{u,n-1}$ resulting from a given initial plane wave (see Eq. (4.14)) just before the nth pulse would be modified by a certain amount if a spontaneous emission took place. The probability per iteration of the Floquet operator of this occurring was 0.2, and the decay photon was assumed to be equally likely to be emitted in any direction. The decay photon, in experimental units, had the wavevector k_2, corresponding to the D2 transition in caesium. Since the model assumed a one-dimensional system, the projection of the photon's momentum onto the z-axis would be taken and this was the amount by which the atomic wavevectors would be modified. This would, in turn, modify the value of ϕ_v (see Eq. (4.17)) and so the effect of spontaneous emission was to randomise the phase evolved by the atoms over the inter-kick free evolution. Each run of this simulation was repeated 10 times to take account of the stochastic nature of the decay process. In the classical simulation, there was a fixed probability per cycle of a spontaneous emission's taking place, and this corresponded to a certain

probability per unit time. The system of 10^5 particles with a range of initial values of χ and ρ was evolved and any particle that underwent a spontaneous emission would have its momentum modified by the projection of the photon's momentum, $\hbar k_2$, along the z-axis. Since so many trajectories were simultaneously propagated, it was not necessary to repeat runs of the simulation as the necessary degree of averaging was already present.

The results of such experiments will now be discussed. The aspects of the system's behaviour that will be considered are the same as previously, namely the momentum distribution, the variation in the mean energy with pulse number, and the variation in mean energy with pulse period. The aim was to investigate the role of coherence in the quantum δ-kicked systems, to what extent a quantum system could be regarded as being more classical if the coherence were perturbed, and whether there was a qualitative difference in the effect of decoherence on the δ-kicked accelerator as compared with the rotor.

5.3 Momentum distributions

To investigate the effect of decoherence on the evolution of the quantum δ-kicked rotor, 30 pulses of the standing wave were applied to the atoms and the phase modulator was used to nullify gravity's influence. The D2 light pulses that interleaved the standing wave pulses gave an average number of spontaneous emissions per atom per pulse period of 0.2. The pulse period of the standing wave was $T = 60.5\mu$s, a value that would yield dynamical localisation in the case where no additional decoherence were introduced. The resulting momentum distribution is shown in Fig. 5.1(a), along with that measured in the absence of this induced spontaneous emission. The behaviour of the corresponding classical system was modelled numerically, and the momentum distributions obtained both with and without the spontaneous emission are shown in Fig. 5.1(b). It is clear that decoherence has had some effect on the experimental, quantum system. The momentum distribution after 30 pulses is slightly broader than that which results in the absence of additional spontaneous emission (its FWHM has increased by $\sim 30\%$), but the shape is still predominantly exponential. This is in agreement with the results from the Auckland group described in Refs. [42, 145, 146], in which the exponential form proved to be more robust to the presence of spontaneous emission than did the cessation of momentum diffusion after the quantum break time. The slight bulging of the distribution in the presence of added spontaneous emission is of the sort observed by the Austin group in Refs. [114, 147] (though the latter experiments were performed with a pulse period of 20μs, yielding a larger localisation length than at 60.5μs, and a lower spontaneous emission probability per pulse period, 0.13). The results shown in Fig. 5.1(b) show that the randomisation of atomic momenta due to the presence of spontaneous emission in the classical system has had very little effect on the final momentum distribution. This final distribution is still Gaussian, and almost identical to that obtained in the absence of spontaneous emission. This confirms that the level of decoherence present in this system is of a

magnitude that corresponds to the case considered by Ott *et al.* which yielded a significant modification to the behaviour of the quantum system but little to that of the classical. Comparison of the results shown in Fig. 5.1(a) with those shown in Fig. 5.1(b) forces the conclusion that, in terms of the momentum distribution attained after 30 pulses, the behaviour of the experimental system is still far from classical. To be classical, the distribution would have to have become Gaussian in form. The results of the Austin group as reported in Refs. [116, 117] suggest that convergence in the form of the momentum distributions will only occur when the level of spontaneous emission is so large as to dominate the process of classical momentum diffusion.

In the quantum δ-kicked rotor, a quantum resonance exhibits qualitatively different behaviour from that which occurs for values of $\bar{k}$ not equal to rational multiples of 4π. Dynamical localisation is not observed, the momentum distribution is neither Gaussian nor exponential in form and exhibits no quantum break time, continuing to broaden with increasing pulse number. Hence it was natural to compare the effect of decoherence on the system when the value of T corresponded to a quantum resonance with that observed at $T = 60.5\mu$s, as just described. Therefore, 30 pulses of the standing wave, with the spontaneous emission-inducing D2 pulses present, were applied to the system with $T = 66.5\mu$s. This pulse period corresponded to the lowest second-order quantum resonance ($\bar{k} = 2\pi$). The resulting momentum distribution is shown in Fig. 5.2(a), along with that measured in the absence of this additional spontaneous emission. The momentum distributions obtained by numerical modelling of the corresponding classical system in both the presence and absence of spontaneous emission are shown in Fig. 5.2(b). It is clear from Fig. 5.2(a) that the spontaneous emission has broadened the momentum distribution. The degree of broadening is much larger than that at $T = 60.5\mu$s, as shown in Fig. 5.1(a). Thus the spontaneous emission has further increased the disparity between the $T = 60.5\mu$s and the $T = 66.5\mu$s cases in terms of the fraction of the population of atoms at high momenta. Comparison with the results of the numerical simulation of the classical system in Fig. 5.2(b) shows that the form of the experimental momentum distribution in the presence of significant spontaneous emission is still very different from that of the corresponding classical distribution. As at $T = 60.5\mu$s, the spontaneous emission has had very little effect on the momentum distribution of the classical system, which is still Gaussian (in fact, it has slightly broadened). Therefore the decoherence has produced a noteworthy effect in the quantum system, but cannot be said to have brought about a convergence in the quantum and classical behaviour.

In the quantum δ-kicked accelerator, the phenomenon of the accelerator mode, like the quantum resonance in the δ-kicked rotor, is accounted for in terms of the rephasing of different momentum states populated by diffraction. Given the clear effect of decoherence on the momentum distribution at the quantum resonance, as shown in Fig. 5.2(a), the effect on the momentum distribution of the δ-kicked accelerator at a value of T for which an accelerator mode can be created might also expected to be noticeable. Therefore 30 pulses of the standing wave with $T = 60.5\mu$s were applied to the atoms, along with the spontaneous-emission inducing

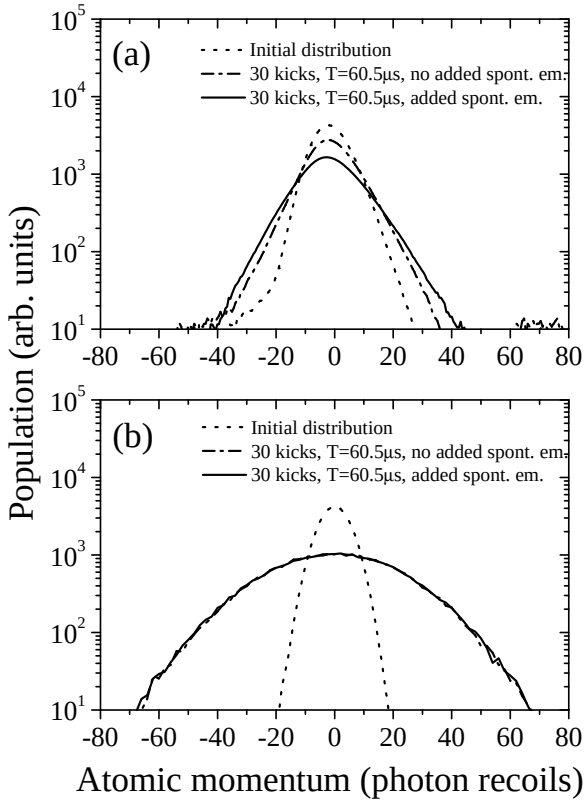

Figure 5.1: (a) Experimentally measured momentum distributions for the δ-kicked rotor system in the case where dynamical localisation is evident in the absence of induced decoherence. The dotted line is the distribution after cooling, prior to application of any pulses of the standing wave. The dash-dot line is the distribution after 30 pulses, for a pulse period of 60.5μs, with no added spontaneous emission (as in Fig. 3.10). The continuous line is the distribution after 30 pulses, for a pulse period of 60.5μs with 0.2 induced spontaneous emissions on average per pulse period. The light forming the standing wave was 30 GHz red-detuned from the ($F = 4 \rightarrow F' = 3$) D1 transition. (b) Momentum distributions produced by the numerical simulation of the classical δ-kicked rotor system. The dotted line is the initial distribution, prior to application of any kicks. The dash-dot line is the distribution after 30 kicks, for a pulse period $T = 60.5\mu$s, and $\phi_d = 0.8\pi$ ($\Rightarrow K = 14.3, \bar{k} = 1.81\pi$) and no spontaneous emission. The continuous line is the distribution after 30 kicks, with 0.2 induced spontaneous emissions on average per iteration of the standard map. Note that in both (a) and (b) the distributions are plotted on a logarithmic scale.

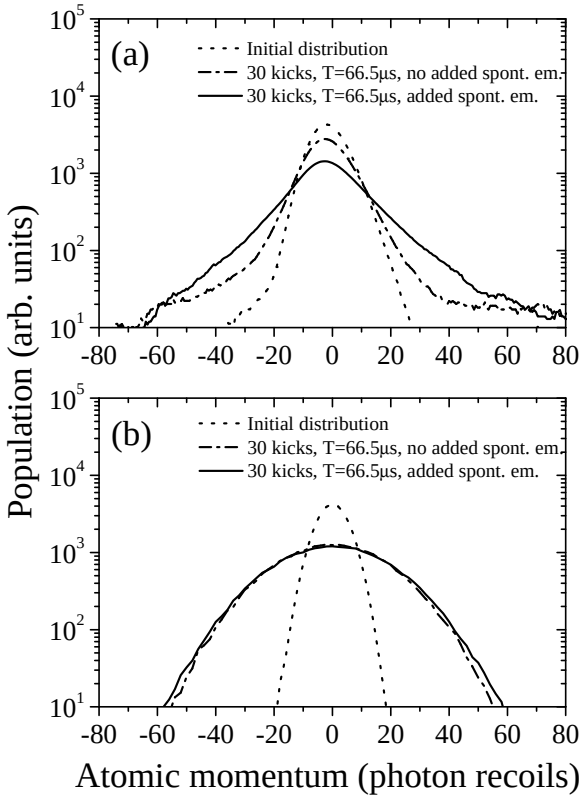

Figure 5.2: (a) Experimentally measured momentum distributions for the δ-kicked rotor system in the case where the broadening characteristic of a quantum resonance is evident in the absence of induced decoherence. The dotted line is the distribution after cooling, prior to application of any pulses of the standing wave. The dash-dot line is the distribution after 30 pulses, for a pulse period of 66.5μs, with no added spontaneous emission (as in Fig. 3.11). The continuous line is the distribution after 30 pulses, for a pulse period of 66.5μs with 0.2 induced spontaneous emissions on average per pulse period. The light forming the standing wave was 30 GHz red-detuned from the ($F = 4 \rightarrow F' = 3$) D1 transition. (b) Momentum distributions produced by the numerical simulation of the classical δ-kicked rotor system. The dotted line is the initial distribution, prior to application of any kicks. The dash-dot line is the distribution after 30 kicks, for a pulse period $T = 66.5\mu$s, and $\phi_d = 0.8\pi$ ($\Rightarrow K = 15.8, \bar{k} = 2\pi$) and no spontaneous emission. The continuous line is the distribution after 30 kicks, with 0.2 induced spontaneous emissions on average per iteration of the standard map. Note that in both (a) and (b) the distributions are plotted on a logarithmic scale.

pulses of D2 light. The phase modulator was inactive so that gravity's effect was unaltered. The resulting momentum distribution is shown in Fig. 5.3(a), along with that observed in the absence of induced spontaneous emission. For comparison, the results of the numerical simulation of the corresponding classical system are shown in Fig. 5.3(b). It is clear from Fig. 5.3(a) that the spontaneous emission has dramatically reduced the population of atoms in the quantum accelerator mode. The momentum distribution is still asymmetric, so gravity's effect is still evident. However, the degradation of the accelerator mode has rendered the momentum distribution much closer to that of the quantum δ-kicked rotor in the presence of spontaneous emission, as shown in Fig. 5.1(a), than was the case when the two systems were evolved in the absence of this decoherence. The decoherence has resulted in a certain degree of convergence in the two systems' behaviour. In Fig. 5.3(b), the effect of the spontaneous emission on the classical δ-kicked accelerator can be seen to be small. The distribution remains Gaussian and slightly asymmetric, but the results in the presence of the spontaneous emission are almost indistinguishable from those in its absence. This is in agreement with the behaviour observed in the case of the classical δ-kicked rotor. Dynamical localisation and quantum accelerator modes are both quantum effects, and both have been degraded by the application of induced spontaneous emission to the system. The same level of perturbation has made little difference to the momentum distribution of the corresponding classical systems. Hence the effect of decoherence on the δ-kicked rotor and the δ-kicked accelerator, both classically and quantum mechanically, is qualitatively similar. The only apparent exception to this statement is the effect of spontaneous emission in *enhancing* the resonant broadening of the momentum distribution at a quantum resonance in the δ-kicked rotor. This will, however, be discussed in more detail in Sec. 5.6.

5.4 Variation in mean energy with pulse number

The characterisation of the δ-kicked rotor in Ch. 3 and of the δ-kicked accelerator in Ch. 4, as well as the previous investigations into the effect of decoherence cited above, made use of the variation in the mean energy of the system with pulse number. This variation was also measured for both systems in the case where the spontaneous emission-inducing pulses of D2 light were applied with the standing wave pulses. The pulse period used was $T = 60.5\mu$s, so that the influence of decoherence on the dynamical localisation and accelerator mode processes could be examined, and the detuning of the light in the standing wave from the ($F = 4 \rightarrow F' = 3$) transition was 30 GHz. The number of pulses applied was varied up to 50. The corresponding variation of the mean energy as calculated from the resulting momentum distributions is shown in Fig. 5.4. Also shown are the results produced by numerical simulation of the quantum and classical systems in the case where the mean number of spontaneous emissions per pulse period was 0.2. To reduce the error in the calculated energies from signal noise in the wings of the experimentally measured distributions, a momentum boundary of $\pm 120\hbar k_1$

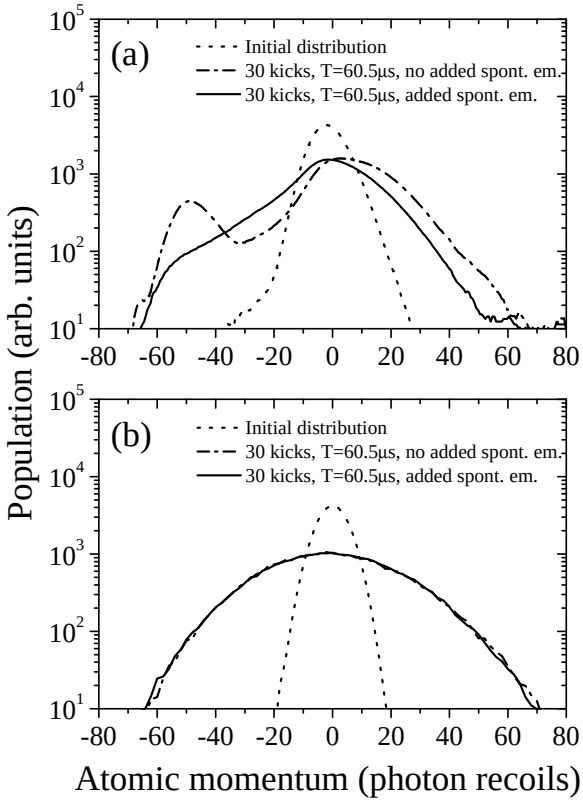

Figure 5.3: (a) Experimentally measured momentum distributions for the δ-kicked accelerator system (*i.e.* gravity present) in the case where a quantum accelerator mode is evident in the absence of induced decoherence. The dotted line is the distribution after cooling, prior to application of any pulses of the standing wave. The dash-dot line is the distribution after 30 pulses, for a pulse period of 60.5μs, with no added spontaneous emission (as in Fig. 4.5). The continuous line is the distribution after 30 pulses, for a pulse period of 60.5μs with 0.2 induced spontaneous emissions on average per pulse period. The light forming the standing wave was 30 GHz red-detuned from the ($F = 4 \rightarrow F' = 3$) D1 transition. (b) Momentum distributions produced by the numerical simulation of the classical δ-kicked accelerator system. The dotted line is the initial distribution, prior to application of any kicks. The dash-dot line is the distribution after 30 kicks, for a pulse period $T = 60.5\mu$s, and $\phi_d = 0.8\pi$ ($\Rightarrow K = 14.3, \bar{k} = 1.81\pi$) and no spontaneous emission. The continuous line is the distribution after 30 kicks, with 0.2 induced spontaneous emissions on average per iteration of the standard map. Note that in both (a) and (b) the distributions are plotted on a logarithmic scale.

was imposed on those distributions when calculating the mean energy, except for the case of the rotor in the absence of added decoherence. For this system the boundary was $\pm 80\hbar k_1$ as the resulting distributions were so narrow.

The experimental results in Fig. 5.4(a) show that this level of decoherence has a noticeable effect on the growth in mean energy of both the quantum δ-kicked accelerator and δ-kicked rotor systems, but that the effect is more dramatic in the case of the accelerator. This conclusion is supported by the results of the quantum simulation, shown in Fig. 5.4(b). The qualitative agreement between the results of the experiment, in Fig. 5.4(a), and the quantum simulation, in Fig. 5.4(b), is obvious but the quantitative agreement is not as good. This has already been explained in Ch. 3 and Ch. 4 by the range of values of ϕ_d experienced by the atoms in the experiment, the violation of the Raman-Nath regime, sources of noise in the experiment not taken into account in the simulation, and noise in the TOF signal.

In both the experimental data and the results of the quantum simulation, the energy growth of the δ-kicked accelerator system with pulse number is faster than linear in the absence of the added decoherence, but when this is present the growth becomes linear and the mean energy of the system after 50 pulses is much reduced. This linear behaviour is characteristic of normal momentum diffusion. From Fig. 5.4(c), two conclusions about the corresponding classical system can be made. Firstly, the energy growth is linear with pulse number. Secondly, the spontaneous emission has almost no effect on the rate of this growth. In fact, the energy attained by the classical δ-kicked accelerator system after 50 kicks is slightly reduced by the randomisation of the particle momenta. This is due to the destruction of certain kick-to-kick correlations that aid momentum diffusion. The fact that the quantum system in the presence of the added decoherence exhibits linear energy growth means that, in this respect, the behaviour of the system has become more classical *in appearance*. This conclusion is also valid for the quantum δ-kicked rotor in the presence of added decoherence. As is particularly clear from the inset figures in Fig. 5.4(a) and Fig. 5.4(b), in the absence of noise there is very little growth in mean energy with pulse number, but, on addition of decoherence, the growth is enhanced and is linear with pulse number. This enhancement is more dramatic for the simulation than the experiment because, even without added decoherence, the experiment is subject to numerous sources of noise that impede the process of dynamical localisation. This explains the non-zero growth in mean energy after the quantum break time. Nevertheless, the effect of the decoherence is clear. For this system, too, the resulting behaviour is closer to that of the corresponding classical system. As shown in Fig. 5.4(c), the growth in mean energy of the classical δ-kicked rotor is linear both with and without added decoherence, which makes almost no alteration to the mean energy attained after a given number of pulses. It slightly increases this number because it destroys some kick-to-kick correlations that inhibit momentum diffusion, and has a small 'heating' effect.

The addition of decoherence by inducing spontaneous emission causes the energy growth with pulse number of both the quantum δ-kicked accelerator and rotor

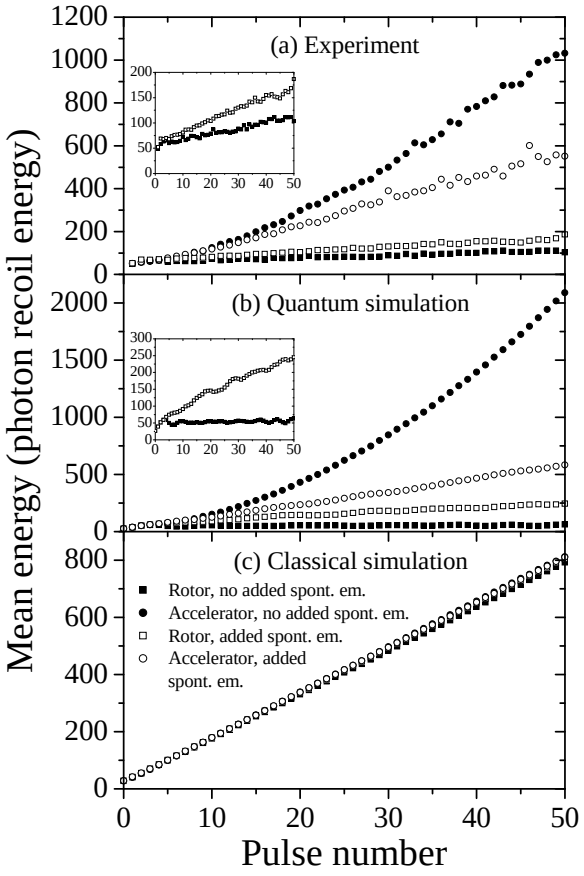

Figure 5.4: (a) Variation in the mean energy of the atomic ensemble with pulse number as calculated from the experimentally measured momentum distributions. The pulse period was $T = 60.5\mu$s; the light forming the potential was 30 GHz red-detuned from the ($F = 4 \rightarrow F' = 3$) D1 transition. (b) Variation in the mean energy of the atomic ensemble with pulse number as calculated from the momentum distributions generated by the quantum simulation. The pulse period was $T = 60.5\mu$s; the value of ϕ_d used was 0.8π. The inset figures in (a) and (b) show, on an expanded energy axis, the variation with pulse number of the mean energy of the δ-kicked rotor, with and without added spontaneous emission. (c) Variation in the mean energy of the atomic ensemble with pulse number as calculated from the momentum distributions generated by the classical simulation. The pulse period was $T = 60.5\mu$s and the value of ϕ_d used was 0.8π. In each case, where added decoherence was present the mean number of induced spontaneous emissions per atom per pulse period was 0.2. Note the differences between (a), (b) and (c) in the scales along the energy axis.

systems to become more classical in form. The pronounced quantum mechanical effects of quantum accelerator modes and dynamical localisation have been degraded because of the effect of decoherence in randomising the phases evolved between successive kicks by the populated momentum states. From Fig. 5.4(a) and Fig. 5.4(b) it can be seen that the two systems have become more similar to one another in terms of the variation of their mean energy with pulse number. Even so, the systems have not converged to the linear behaviour of their respective classical analogues (which differ little). The classical rate of energy growth is much larger than that of the two quantum systems in the presence of decoherence. The quantum systems have become qualitatively 'more classical', but great quantitative differences remain. In Ref. [42], the Auckland group referred to momentum diffusion that took place in the quantum δ-kicked rotor after the quantum break time as 'quantum diffusion'. The basis for this term was that this diffusion is not accounted for by classical behaviour of the system but by a modification of the quantum mechanical behaviour in the zero-diffusion case. This means that the quantum δ-kicked accelerator and δ-kicked rotor should not be expected to show the same energy growth as their corresponding classical systems when the level of spontaneous emission that each undergoes is at the level discussed in this thesis. In the Austin experiments [116, 117], true convergence in classical and quantum behaviour has previously been observed due to the very large level of noise in the amplitude of the kicking potential. In contrast, the energy growth of neither the quantum nor classical systems in the investigations discussed here is dominated by the heating effect of spontaneous emission.

5.5 Variation in mean energy with pulse period

It is also informative to study the effect of decoherence on the behaviour of the δ-kicked accelerator and δ-kicked rotor when the number of kicks applied to the system is fixed and the pulse period T is varied. Just as for the investigations into the effect of varying T described in Ch. 3 and Ch. 4, 30 pulses of the standing wave were applied to the atoms for values of T ranging from 6.5μs to 210.5μs, with a 30 GHz detuning of the light from the $(F = 4 \rightarrow F' = 3)$ transition. The pulses of D2 light that induced decoherence in the atoms were applied amidst the pulses of the periodic potential in the usual way so that the mean number of spontaneous emissions per atom per pulse period was 0.2. These experiments were performed in the cases of both the δ-kicked rotor and the δ-kicked accelerator, and the resulting variation with T in the mean energy of the atoms, as calculated from the measured momentum distributions in the two cases, is shown in Fig. 5.5 and Fig. 5.6, respectively. The variation in energy in the absence of induced spontaneous emission, which has been discussed in Ch. 3 and Ch. 4 is also shown. To reduce the effect of noise in the wings of the TOF signal in artificially increasing the calculated values of the mean energy, momentum boundaries of $\pm 120\hbar k_1$ were imposed on the data used to calculate the energy. Also shown in these figures are the results of the corresponding numerical simulations of the quantum system,

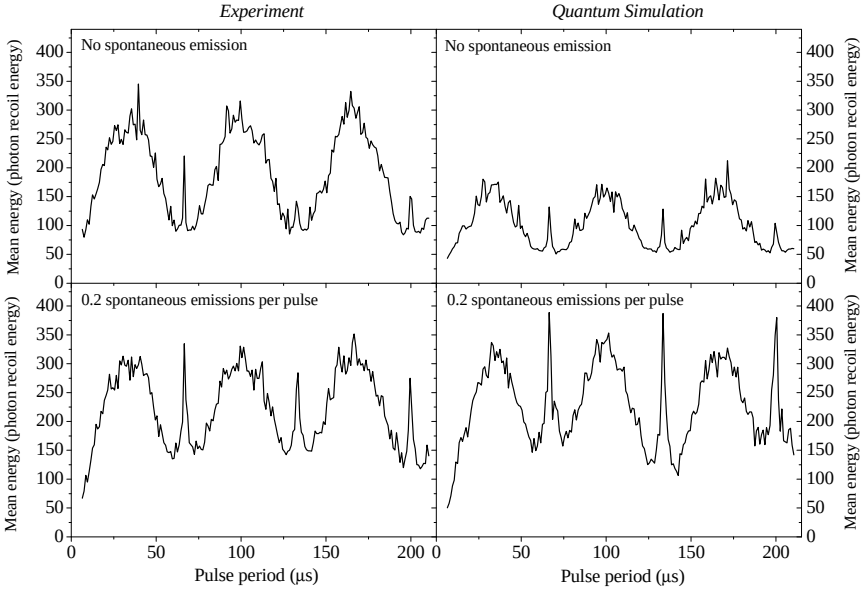

Figure 5.5: Variation with pulse period of the mean energy of the atomic ensemble in the δ-kicked rotor system after 30 potential pulses. These values of energy were calculated from the experimentally measured momentum distributions and those produced by the quantum simulation. The pulse period ranged from $T = 6.5\mu$s to 210.5μs; the red-detuning from the ($F = 4 \rightarrow F' = 3$) D1 transition of the light forming the potential was 30 GHz, while the value of ϕ_d used in the simulation was 0.8π. Where non-zero, the mean number of induced spontaneous emissions per atom per pulse period was 0.2.

both in the absence and presence of added decoherence.

The response of the experimental quantum δ-kicked rotor system to the applied decoherence, as shown in Fig. 5.5, is to exhibit for all values of T an increase in the mean energy attained after 30 pulses compared with the case of zero applied decoherence. However, qualitatively different behaviour can be identified for different values of T. For values of T that yield a large localisation length in the absence of decoherence, such as $T \sim 30\mu$s, 100μs, and 170μs, the fractional increase in the mean energy is less than that for values where the localisation length is very small, *i.e.* close to, but not at, the first- and second-order quantum resonances. The regions where the quantum feature of dynamical localisation is most pronounced are the regions where the system is most sensitive to the addition of decoherence, apart from at the quantum resonances. As discussed in Sec. 5.3 in the context of the momentum distributions, and in Sec. 5.4 in the context of the growth in mean energy with pulse number, the presence of a high level of decoherence has degraded a characteristically quantum aspect of the system's behaviour. The exception to this conclusion is the response of the system at the first- and second-order quantum resonances, $T = 66.7\mu$s, 133.3μs and 200.0μs ($\hbar = 2\pi, 4\pi, 6\pi$, respectively). In the absence of the induced spontaneous emission, there is a pronounced peak in the mean energy. This is due to a symmetric spreading of the momentum distribution with pulse number and was explained in Sec. 3.2 by consideration of the

phase differences evolved between different occupied momentum states resulting from the diffraction of particular initial plane waves. Since this explanation is in terms of rephasing, the enhancement of momentum diffusion is a quantum feature that one would expect to be degraded by decoherence. However, far from being degraded, the local maximum in mean energy is *enhanced* by decoherence, and the fractional increase in the mean energy is larger than that at the neighbouring values of T where dynamical localisation in the absence of decoherence is strong. This effect is observed both in the experimental system and in the simulation, and is quite contrary to what one would expect to be the effect of decoherence. It will be considered in more detail in Sec. 5.6.

The qualitative agreement between the results of the experiment and the numerical simulation is obvious, and the same differences in response to decoherence for different values of T are observable. Quantitative agreement is less good; the addition of decoherence yields a larger fractional increase in the mean energy attained by the system in the simulation than in the experiment. As already discussed, this can be explained by the fact that, in the absence of induced spontaneous emission, the system in the simulation was a perfectly noise-free scenario while that in the experiment was not. Thus induced decoherence yields a greater alteration to the dynamics in the simulation. The quantitative agreement between simulation and experiment in the case where induced spontaneous emissions take place is good, as the extent of perturbation to the dynamics of an ideal system is then comparable in the two cases. The enhanced peaks in the mean energy at the quantum resonances in the presence of added decoherence are higher in the simulation than in the experiment. This can be accounted for by the fact that the signal-noise ratio in the wings of the experimental momentum distributions is small. The peaks in the mean energy are due to the atomic population in the wings, so a small signal-noise ratio will mean that the signal threshold imposed to limit the error due to noise may actually exclude some of the true signal and hence artificially lower the mean energy of the ensemble. Additionally, all the atoms in the simulation were subjected to the same value of ϕ_d, whereas the atoms in the experiment experienced a range of ϕ_d. This made quantitative agreement between the two systems difficult to achieve.

Figure 5.6 shows that applied decoherence also has a pronounced effect on the behaviour of the quantum δ-kicked accelerator as observed both experimentally and by numerical simulation. As discussed in Sec. 4.2.3, the large peaks in the mean energy after 30 pulses for values of T in the vicinity of, but not at, the quantum resonances are due to the existence of quantum accelerator modes. The presence of added spontaneous emission results in a drastic reduction in the height of these peaks. The randomisation that it causes in the momentum of the states diffracted by the periodic potential has prevented the correct rephasing that allows constructive interference and hence the existence of quantum accelerator modes. The outstanding quantum mechanical feature of this system has been degraded by decoherence, and the qualitative agreement in this respect between experiment and simulation is excellent. As in the case of the quantum δ-kicked rotor, the quantitative differences between the experiment and simulation in the absence

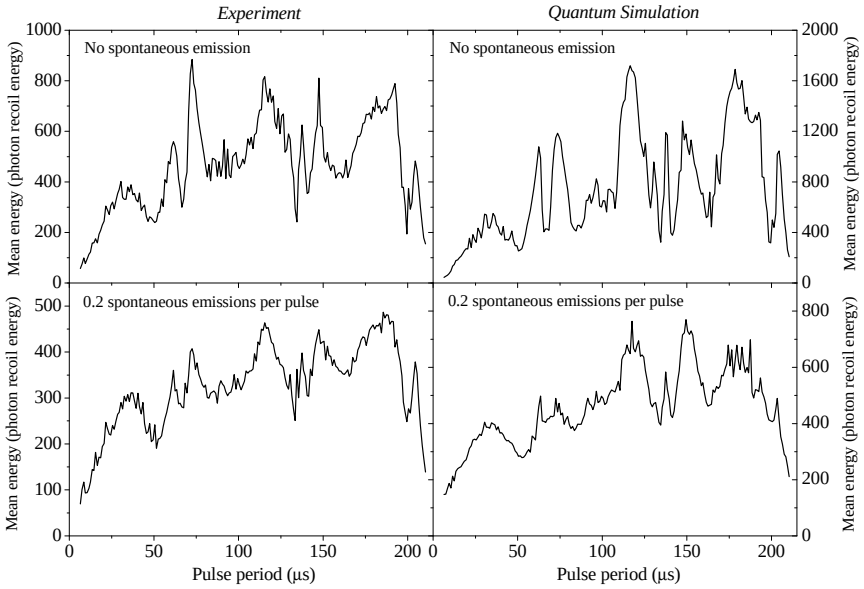

Figure 5.6: Variation with pulse period of the mean energy of the atomic ensemble in the δ-kicked accelerator system after 30 potential pulses. These values of energy were calculated from the experimentally measured momentum distributions and those produced by the quantum simulation. The pulse period ranged from $T = 6.5\mu$s to 210.5μs; the red-detuning from the ($F = 4 \rightarrow F' = 3$) D1 transition of the light forming the potential was 30 GHz, while the value of ϕ_d used in the simulation was 0.8π. Where non-zero, the mean number of induced spontaneous emissions per atom per pulse period was 0.2. Note that the vertical scales for the experimental data are different from those of the simulation.

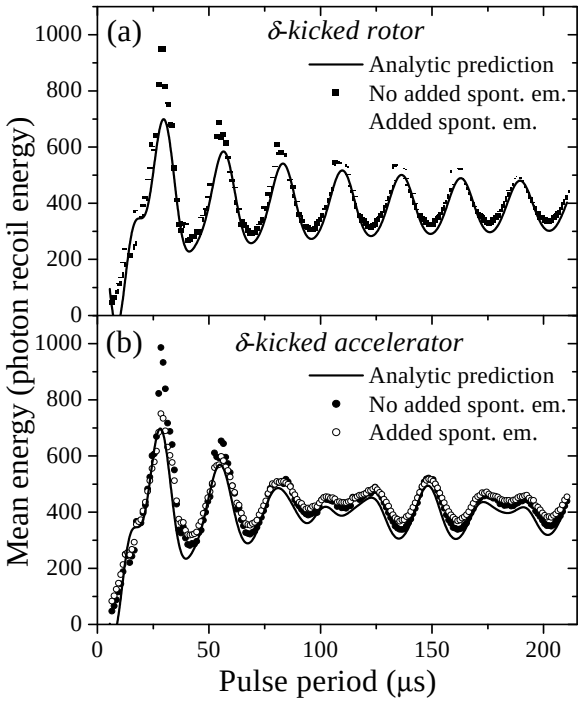

Figure 5.7: Variation with pulse period in the mean energy after 30 kicks of the atomic ensemble in (a) the classical δ-kicked rotor system and (b) the classical δ-kicked accelerator system. This was calculated from the momentum distributions generated by the classical simulations, in which the value of ϕ_d used was 0.8π. The results in both the absence and presence of added spontaneous emission are shown. Where present, the mean number of spontaneous emissions per atom per pulse period was 0.2. Also shown is the mean energy that each system is predicted to attain after 30 kicks in the absence of spontaneous emission, using the analytical expression for $D(K)$ in (a) Eq. (3.9) and (b) Eq. (4.6).

of induced decoherence, which have been accounted for in Sec. 4.2.2, are much reduced in the case where added decoherence is present. In the presence of this level of decoherence, the variation in mean energy after 30 pulses with T is rather featureless.

How does the effect of the decoherence on the quantum δ-kicked rotor and δ-kicked accelerator compare with that on their corresponding classical systems? Figure 5.7 shows that the randomisation in the momentum of the classical particles caused by spontaneous emission makes little difference to the energy growth of either system. The variation in the mean energy with T for the δ-kicked rotor, shown in Fig. 5.7(a), continues to resemble closely that predicted analytically by using the expression in Eq. (3.9) for $D(K)$. Likewise, the variation for the δ-kicked accelerator, shown in Fig. 5.7(b), continues be similar to that predicted analytically using Eq. (4.6), which gives $D(K)$ in the presence of gravity. Indeed, in both cases the differences between the numerical results and the analytical predictions at the mean energy peaks are smaller in the presence of spontaneous emission than in

its absence. This is because the momentum randomisation does have the effect of destroying kick-to-kick correlations in the particles' motion. These are responsible for the existence of anomalous diffusion and are most significant at the peaks of the variation in the mean energy with T. They therefore account for the quantitative disagreement between the results of the classical numerical simulations, which can model classical accelerator modes, and the analytical prediction, which does not take high-order correlations into account. When these high-order correlations are destroyed by the momentum jitter due to spontaneous emission, the discrepancy between simulation and analytical prediction is reduced. At the minima in the mean energy, the momentum randomisation due to the addition of spontaneous emission acts as a source of heating and therefore leads to a small rise in the mean energy attained after 30 pulses.

The limited effect of the spontaneous emission confirms that the decoherence regime being considered in these investigations is one that produces little modification to the dynamics of the classical system, as assumed in the initial theoretical investigation by Ott *et al.* [43]. This makes its profound effect on the quantum systems all the more noteworthy. However, comparison of the form of the experimental momentum distributions in the presence of added decoherence, shown in Figs. 5.1, 5.2 and 5.3, with those of the corresponding classical systems emphasises that the quantum and classical systems still behave very differently. This conclusion is reinforced by a comparison of the variation in the presence of induced spontaneous emission of the mean energy with T for the quantum δ-kicked rotor, shown in Fig. 5.5, the quantum δ-kicked accelerator, shown in Fig. 5.6, and their classical analogues, shown in Fig. 5.7. Although particular signatures of quantum behaviour have been degraded, the quantum systems continue to behave quite differently from the classical. In truth, it might be expected that application of decoherence alone would not be sufficient to make the behaviour of the quantum systems truly more classical in nature. The limit $\hbar \to 0$ (by which, more carefully, is meant the tending to zero of a dimensionless combination of physical quantities with $\hbar$ in the numerator, such as $\bar{k}$), which is a necessary condition for a system to reach the classical limit, has not been approached in these experiments. It has been argued [148] that, though necessary, the $\hbar \to 0$ condition is not sufficient to yield the classical limit, and that the long-time limit, $t \to \infty$ must also be applied. Such questions, though profound and interesting, will not addressed here.

5.6 Quantum enhancement of resonant momentum growth

As stated in Sec. 5.5, the effect of added decoherence on the behaviour of the quantum δ-kicked rotor system at the first- and second-order quantum resonances is surprising. The local maxima in the mean energy after 30 pulses of the periodic potential, which have the form of spikes when the variation of this mean energy with T is plotted (see Fig. 5.5), are increased by the presence of substantial spontaneous emission. This occurs despite the fact that the ballistic increase in the width

of the momentum distribution that occurs at a quantum resonance is a peculiarly quantum mechanical effect. It is explained by the fulfilment of a rephasing condition on the momentum states populated by diffraction from certain initial plane waves, as discussed in Sec. 3.3. Being such a quantum feature, it might naively be expected to be degraded by decoherence. This does not appear to be the case.

The addition of decoherence was found to degrade the strong dynamical localisation that is evident for values of T close to, but not at, the first- and second-order quantum resonances. On the other hand it had a relatively small effect at values of T where localisation was relatively weak and thus the localisation length large. The fractional increase in the mean energy for the level of spontaneous emission (0.2 emissions per atom per pulse period, on average) shown in Fig. 5.5 is significantly larger at the quantum resonances than at neighbouring values of T, where, in turn, the response is larger than at values of T mid-way between the resonances. This difference in response can be clearly illustrated by showing how the mean energy after a fixed number of pulses at values of T in the three different regimes increases with an increasing level of spontaneous emission. In order to investigate this variation in the mean energy, experiments were performed in which 30 pulses of the standing wave, red-detuned by 30 GHz from the ($F = 4 \rightarrow F' = 3$) D1 transition, were applied to the atoms for different intensities of interleaved D2 pulses. The phase modulator was active, so as to compensate for gravity and hence realise the quantum δ-kicked rotor system. The intensity of D2 light was varied so that the mean number of spontaneous emissions undergone by each atom per pulse period varied between 0 and 0.5. The final momentum distribution was measured, allowing the mean energy of the atoms to be calculated. These experiments were performed with three different values of T. The first value, $T = 20.5\mu$s, is one where the localisation length is large; the second, $T = 61.5\mu$s, is one where the localisation is strong and the localisation length small. The third, $T = 66.5\mu$s, is the lowest second-order quantum resonance. The results are shown in Fig. 5.8.

Figure 5.8 demonstrates that the response of the system to decoherence is quite distinct in the three regimes of behaviour. At the quantum resonance, $T = 66.5\mu$s, even low levels of spontaneous emission result in a large fractional increase in the mean energy attained after 30 pulses. When the mean number of spontaneous emissions per pulse is 0.1, the mean energy after 30 pulses at this value of T has doubled. On the other hand, for this level of spontaneous emission there has been negligible increase in the mean energy of the system for either $T = 20.5\mu$s or $T = 61.5\mu$s. The system at the quantum resonance is far more sensitive to the effect of decoherence than in the regimes where dynamical localisation, whether with a large or small localisation length, can take place. As the level of spontaneous emission is increased further, the mean energy after 30 pulses at $T = 66.5\mu$s continues to increase. The mean energy at $T = 61.5\mu$s, where the localisation length is small, also increases, though the rate of increase with spontaneous emission does not match that at $T = 66.5\mu$s until the mean number of spontaneous emissions per pulse is about 0.25. Up until this level of decoherence has been attained the increase in the mean energy at $T = 20.5\mu$s is slight. For higher levels of spontaneous emission, the system displays an increase in the mean energy after 30

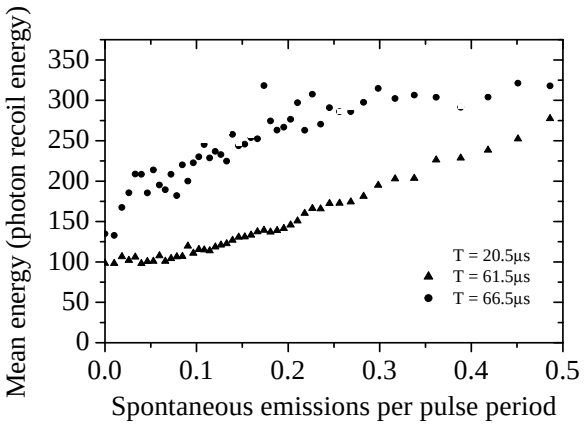

Figure 5.8: Variation with level of decoherence (as expressed by the mean number of induced spontaneous emissions per atom per pulse period) of the experimentally measured mean energy of the atomic ensemble in the δ-kicked rotor system after 30 pulses of the periodic potential. Three different values of the pulse period, $T = 20.5\mu$s, $T = 61.5\mu$s and $T = 66.5\mu$s were used; the red-detuning from the ($F = 4 \rightarrow F' = 3$) D1 transition of the light forming the potential was 30 GHz. The mean number of induced spontaneous emissions per atom per pulse period was varied from 0 to 0.5.

pulses for all three values of T, such that when the mean number of spontaneous emissions per atom per pulse is 0.5 the mean energy of the system after 30 pulses is approximately the same in each case. In this regime the momentum diffusion due to the random kicks associated with spontaneous emission has begun to dominate the energy growth of the system, and so it is to be expected that the value of T with which the pulses of the standing wave are applied matters less.

Why is the response of the system to decoherence at $T = 66.5\mu$s so much more dramatic than that at the other pulse periods studied? The nature of this response can be clarified by using numerical simulations to examine the behaviour of different initial plane waves when subjected to pulses of the potential with different pulse periods (as was done in Fig. 3.13 and Fig. 3.16), and how this behaviour is altered by the presence of decoherence. Figure 5.9 shows the variation with pulse number of the mean energy of the quantum δ-kicked rotor system, for different initial plane waves with the momentum values shown, as modelled by numerical simulation. The pulse period is $T = 60.5\mu$s, for which dynamical localisation occurs after a small number of pulses, and the value of ϕ_d is 0.8π. The dotted lines show the values of the mean energy in the case where there is no spontaneous emission, given in Fig. 3.13. The solid lines show the values when the mean number of spontaneous emissions per pulse is 0.2. For all the values of the initial momentum, in the absence of decoherence the mean energy exhibits the short-lived initial rise followed by a cessation of growth that is characteristic of dynamical localisation. The randomisation of the phase evolved by the different populated momentum states between consecutive pulses caused by the spontaneous emission means that momentum diffusion is no longer inhibited and there is a

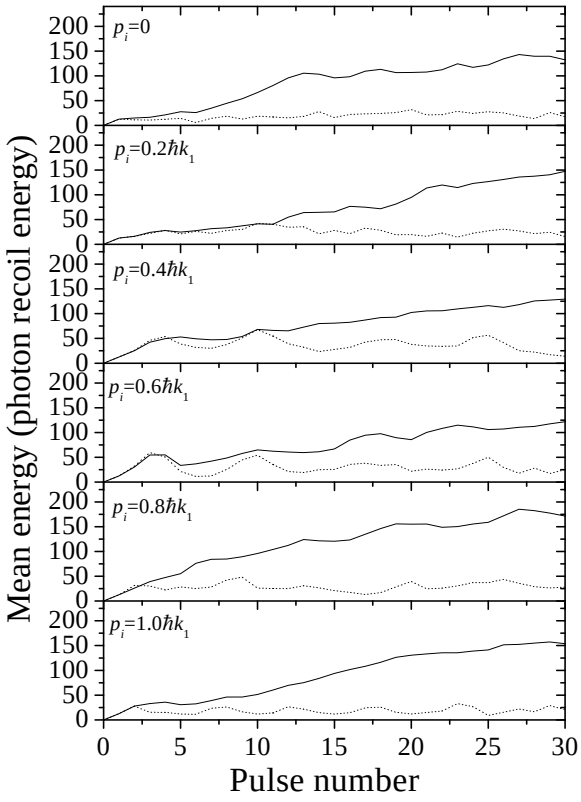

Figure 5.9: Variation in the mean energy with pulse number of different initial plane waves, as calculated from the momentum distributions generated by the quantum simulation. The pulse period was 60.5μs and the value of ϕ_d used was 0.8π. The plane waves had initial momenta p_i equal to 0, $0.2\hbar k_1$, $0.4\hbar k_1$, $0.6\hbar k_1$, $0.8\hbar k_1$ and $1.0\hbar k_1$, as labelled on the figure. The dotted lines show the values obtained in the absence of induced spontaneous emission; the continuous lines show the values obtained when the mean number of spontaneous emissions per pulse period was 0.2.

general trend of linear growth in mean energy with pulse number. In each case the mean energy attained after 30 pulses is in the region of 150 times the photon recoil energy.

The behaviour for $T = 60.5\mu$s should be contrasted with that shown in Fig. 5.10, for which the pulse period is equal to the half-Talbot time $T_{1/2}$, the lowest second-order quantum resonance. The behaviour in the absence of spontaneous emission is that depicted by the dotted line in Fig. 3.16. When the initial momentum does not equal a value that allows fulfilment of the $F_{v,v-1,\rho_i} = 2Z\pi$ condition for a quantum resonance, as discussed in Sec. 3.3.1 and where F is defined by Eq. (3.29), the mean energy varies periodically with pulse number. The existence of these oscillations was explained in Sec. 3.3.2. The amplitude of the oscillations increases as the initial momentum p_i of the plane wave approaches a resonant value. When $T = T_{1/2}$, such a value is $p_i = \hbar k_1$ and in this case the mean energy of the system increases quadratically with n, without bound. For all the values of p_i in

Fig. 5.10 the presence of decoherence significantly modifies the behaviour. The phase randomisation prevents the $p_i = \hbar k_1$ system from continually satisfying the rephasing condition that allows ballistic growth in the momentum width, and quadratic growth in the mean energy, to continue. Therefore the growth in mean energy is substantially reduced for this value of p_i. This is in accordance with the degrading effect of decoherence on the other quantum phenomena of dynamical localisation and accelerator modes. However, the growth in the mean energy for all other, non-resonant, values of p_i is greatly increased, and by a much larger fraction than in the $T = 60.5\mu$s case. The reason for this is that the randomly directed momentum impulses due to spontaneous emission can modify the momenta of the momentum states so that the quantum resonance condition on the momentum can be fulfilled (the quantum resonance condition on the pulse period has already been fulfilled). That is, the value of p_i can effectively be altered by the emission so that ballistic increase in the momentum width can occur. Of course, this can only take place for a limited number of pulses until a subsequent emission alters the momenta again and stops any further growth. Examination of Fig. 5.10 shows that the growth in mean energy with pulse number is far from uniform, and the system undergoes phases of rapid growth interspersed with phases of little growth, or even decline (corresponding to a narrowing of the momentum distribution, by fulfilment of the appropriate rephasing conditions). For the experimental system, which comprises a continuous range of momenta, the increase in the mean energy attained by the non-resonant initial plane waves (which form the majority of initial momenta present in the system) due to decoherence outweighs the decrease in that of the resonant momenta. Therefore the mean energy at a quantum resonance of the system as a whole *increases* with decoherence, leading to an enhancement of the mean energy growth that is characteristic of a quantum resonance.

The decoherence-induced enhancement in mean energy growth at the quantum resonance is not due to an increased level of growth amongst the momentum classes that normally participate in resonant growth (this growth is degraded by the decoherence) but is due to the fact that decoherence allows non-resonant initial momenta classes to participate for limited times in the ballistic momentum growth. This participation means that the enhancement in energy growth is greater than that at neighbouring values of T, such as 60.5μs, where dynamical localisation occurs in the absence of decoherence. As shown in Fig. 3.13, there is no value of p_i for which an incident plane wave experiences ballistic increase in the width of the momentum distribution when $T = 60.5\mu$s. Therefore the randomisation in the value of p_i associated with spontaneous emission does not lead to a large increase in energy transfer to the system. After evolving freely for 60.5μs after a pulse, an initially plane wave is strongly (and periodically) localised in space, as shown in Fig. 3.14, and experiences a particular potential gradient. This is true no matter what the initial momentum of the plane wave, which only affects the region of localisation. If subjected to a further pulse at this instant the wave may be expected to behave quite differently from the case where it has evolved for $T_{1/2}$ and has no spatial localisation at all, and hence experiences all potential gradients equally. The randomly directed momentum impulses due to spontaneous emission

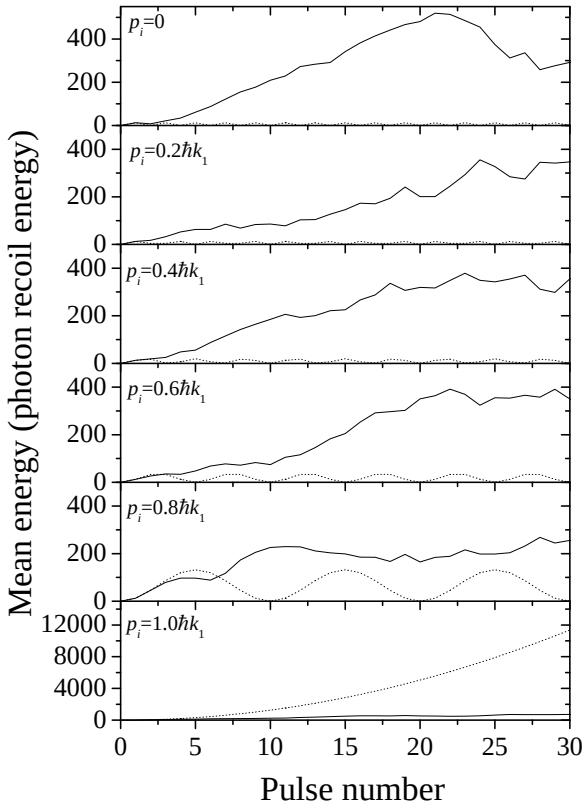

Figure 5.10: Variation in the mean energy with pulse number of different initial plane waves, as calculated from the momentum distributions generated by the quantum simulation. The pulse period was $T_{1/2}$ and the value of ϕ_d used was 0.8π. The plane waves had initial momenta p_i equal to 0, $0.2\hbar k_1$, $0.4\hbar k_1$, $0.6\hbar k_1$, $0.8\hbar k_1$ and $1.0\hbar k_1$, as labelled on the figure. The dotted lines show the values obtained in the absence of induced spontaneous emission; the continuous lines show the values obtained when the mean number of spontaneous emissions per pulse period was 0.2.

may alter the position of the localisation, and the momentum of the wave as a whole, relative to the profile of the potential. This randomises the momentum impulse that the next application of the potential will impart, but does not alter the degree of spatial localisation, nor its periodic nature. The spontaneous emission does, however, stop dynamical localisation by constantly 'resetting' the phases of the populated momentum states, and changing the effective values of p_i so that normal, classical-like momentum diffusion can occur to arbitrarily high n. The rate of this growth is determined by the initial rate of quantum growth prior to dynamical localisation in the absence of decoherence [143]. For non-resonant values of T this rate is lower than for the ballistic growth possible at resonant values. Therefore as T is varied the enhancement in the mean energy due to spontaneous emission is greater at the quantum resonances than at other values of T.

In the theoretical investigation by Daley *et al.* in Ref. [143], the probability per pulse period of spontaneous emission in a quantum kicked rotor was varied up to 0.1 (which was lower than in the investigations described in this thesis), for different values of k. It was concluded that the late-time rate of energy growth in the decoherence-affected quantum system is larger than that of the corresponding classical system. This does not agree with the results shown in Fig. 5.4. According to Ref. [143] the initial quantum rate of growth, prior to the onset of dynamical localisation, is higher than that of the classical system. Since decoherence allows this growth rate to be maintained by preventing localisation, it causes the mean energy of the quantum system to grow more quickly than that of the classical. However, Fig. 3.12 shows the growth with pulse number of the mean energy of the decoherence-free quantum and classical δ-kicked rotor systems discussed in this thesis, at $T = 60.5\mu$s. The initial growth rate of the quantum system is, in fact, not larger than that of the classical. Using the rationale in Ref. [143], therefore, the energy growth of the quantum δ-kicked rotor discussed in this thesis would not be expected to be larger in the presence of a moderate level of spontaneous emission than that of the corresponding classical system for this value of T. It would also be expected to be smaller than the growth at the quantum resonance in the presence of the same level of spontaneous emission, as observed experimentally and in the numerical simulations. In Ref. [143], the enhancement in the momentum diffusion rate at the $k = 2\pi$ quantum resonance was found to be greater than that for other, non-resonant, values of k. In this respect the behaviour was in agreement with that discussed earlier in this section.

5.7 Summary

This chapter has examined the effect of decoherence on the experimental quantum δ-kicked rotor and δ-kicked accelerator systems. The decoherence, introduced by causing spontaneous emission in the atomic ensemble, was found to degrade the characteristically quantum mechanical features of the systems' behaviour. These features are dynamical localisation, in the case of the rotor, and accelerator modes, in the case of the accelerator. The variation with pulse number of the mean energy

of the system was found, in each case, to become more classical in form, though significant quantitative differences remained. The spontaneous emission modified considerably the variation of each system's mean energy with pulse period, but in each case this was still very different from that of the corresponding classical system. The effect of the same level of spontaneous emission on an ideal classical system was small, showing the higher sensitivity of quantum behaviour to decoherence. The enhancement by decoherence of the energy growth at the first- and second-order quantum resonances in the δ-kicked rotor was not due to a failure of decoherence to degrade the rephasing-dependent response of an individual plane wave. Rather, it was accounted for by the randomisation in atomic momenta caused by spontaneous emission. This allowed many momentum classes of atom to participate for limited periods in ballistic momentum increase. Decoherence can be said to have made the behaviour of the system more classical in certain respects, and the effect of decoherence in the quantum δ-kicked accelerator is qualitatively similar to that in the kicked rotor. However, many differences between the resulting behaviour and that of a truly classical system remain, differences that are attributable to quantum mechanics.

Chapter 6

Applications of quantum accelerator modes

The new and surprising phenomenon of the quantum accelerator mode, discovered in the experimental realisation of the quantum δ-kicked accelerator system, holds out the prospect of a number of potential applications.

- An accelerator mode is characterised by the efficient transfer of momentum to a substantial fraction of the atomic ensemble. This fact, coupled with the coherent nature of the momentum transfer process and the way in which it can be controlled, means that the quantum accelerator mode is a potential tool for use in atom optics.
- The fact that its existence depends on the presence of a unidirectional external force in the system means that the details of the atoms' behaviour could be used as a means of measuring this force. Hence accelerator modes in the experimental system under discussion could be used to measure gravity.
- As discussed in Ch. 4, an accelerator mode consists of a comb of momenta, and is periodically localised in space on a certain gradient of the potential, thus isolating a certain region of phase space. Therefore the response of an accelerator mode to further pulses could be interpreted in such a way as to characterise the dynamics of that region of quantum phase space. This in turn could be linked to the behaviour of the corresponding classical system and thus make a link between classical and quantum chaos.

These different types of application, and the features of the quantum accelerator mode that make it appropriate for each, will be discussed in this chapter.

6.1 Coherent control of atomic momenta

Manipulation of the momentum state of atoms is crucial to the field of atom optics. This has been carried out through the use of nanofabricated matter gratings [149],

static magnetic fields [150] and light. The latter category comprises the widest range of techniques, and since this is also the class into which quantum accelerator modes fall the performance of some of the other techniques will now be summarised. Four characteristics are key: the amount of momentum that can be transferred, the spread in the magnitude of this transfer, its efficiency, and whether the momentum is imparted coherently. This last criterion must be fulfilled if the technique is to be available for atom interferometry [61, 63].

6.1.1 Momentum transfer to atoms using light

The following techniques have been used to control and manipulate the momenta of atoms found in a beam or optical molasses:

1. In diffraction from a standing light wave, as in the experiments described in this thesis, the light behaves as a phase grating for the atoms. In the case of a thin grating, the population in the different diffraction orders is determined by the values of the Bessel functions given in Fig. 3.7. As ϕ_d is increased, a greater number of orders is populated; this means that, as the maximum momentum imparted to the atoms by a single interaction is increased, so is the spread of momentum. This was observed in Ref. [103], in which up to 8 photon recoils were transferred by a standing wave of laser light to a beam of sodium atoms. The fact that atom interferometry has been performed using diffraction gratings composed of standing waves of light [151] shows that this technique of momentum transfer is coherent.

   To attain larger momentum transfers (> 20 photon recoils), repeated diffraction is required. The most feasible way of achieving this is in the time-domain rather than in the spatial-domain. However, in the δ-kicked rotor, for example, the largest transfer of momentum occurs at the quantum resonances but the efficiency is poor. As shown in Fig. 3.11, only 4% of the atoms have been accelerated beyond ± 40 photon recoils. Furthermore, a continuous range of momenta up to the maxima are populated so no class of atoms is spatially separated from the rest. This would preclude realisation of a separated-path interferometer in this system.

2. Bragg scattering from a standing wave of light has been used to change the momentum of incoming atoms by multiples of 2 photon recoils. In Ref. [109], over 40% of the sodium atoms in a beam could experience a momentum change of 2 photon recoils due to interaction with the standing wave, though this fraction fell with increasing momentum transfer. For example, only around 20% of the atoms could be made to receive a momentum impulse of 4 photon recoils. The momentum spread of the diffracted beam was mainly determined by that of the incident beam (which, in these experiments, was around 1 photon recoil) and increased with the momentum transfer. More recent experiments with a Bose-Einstein condensate [152] have succeeded

in transferring 12 photon recoils with an efficiency of 15%. The momentum spread of the diffracted atoms was approximately 0.16 photon recoils, less than half that of the initial condensate. Bragg diffraction is a coherent process, and has allowed the observation of matter wave interference [153]. However, this technique is not promising as a means of imparting large momentum changes (> 50 photon recoils, say) to atoms with high efficiency.

3. Another method of momentum transfer involves the use of Raman transitions. Although early experiments with molasses-cooled sodium atoms [154] imparted only two photon recoils to part of the atomic wavefunction, this work demonstrated that the momentum was imparted coherently. Interference was observed upon recombination of this part of the wavefunction with that which had not been accelerated. In later work [155, 156], repeated application of Raman π pulses to caesium atoms that had already been Raman-cooled (*i.e.* velocity selected, giving a momentum width of < 0.2 photon recoils) yielded a 64 photon recoil momentum splitting in an interferometer. Half the momentum splitting was imparted to each of two hyperfine states, in opposite directions. The efficiency of momentum transfer for a π pulse was 85%, meaning that less than 10% of the velocity-selected sample (which was itself a fraction of the total number of trapped atoms) could be split in momentum by the maximum amount. A study of the experimental system described in this thesis [157] implies that if Raman pulses were to be used on an atomic ensemble with a comparable momentum spread then only 20% of the atoms would undergo a momentum transfer of 2 photon recoils.

4. Adiabatic transfer pulses [158, 159] were used to achieve a transfer of over 140 photon recoils to laser-cooled caesium atoms. The efficiency of this momentum transfer was over 95% per exchanged photon pair, meaning that less than 5% of the accelerated atoms experienced the maximum momentum transfer. Furthermore, due to the necessity of velocity selection (to yield a momentum spread of ~ 0.7 photon recoils) only 18% of the initial atomic ensemble participated in this acceleration, so the signal at the highest momenta was small. This technique was shown to be coherent by the observation of interference fringes upon overlap of the previously spatially separated parts of the wavefunction.

5. The optical Stern-Gerlach effect [160] was used to split in momentum space different superpositions of the magnetic substates of excited helium atoms in an atomic beam. The superpositions experienced potentials in the standing wave that were equal in magnitude but opposite in sign, and hence received an oppositely directed momentum impulse. Theory predicts that the two beams produced should be completely coherent, though this has not been experimentally demonstrated. Since the atomic beam only interacted with a fraction of one period of the wave, the momentum imparted was not quantised in units of the photon recoil but was continuously variable. Although the efficiency of momentum transfer was good (approximately 30% of the

atoms were deflected into each of the positive and negative directions), only around 4 photon recoils were imparted by this method, and the spread in the momentum transferred was approximately 2 photon recoils.

6. The magneto-optic beamsplitter [161] acts on magnetically sensitive states. This could be a disadvantage for interferometric applications, as it would make the system susceptible to unwanted phase shifts due to stray magnetic fields. In Ref. [161], passage of a beam of excited helium atoms through a standing light wave in the presence of a magnetic field resulted in a triangular spatial modulation of phase shift, not sinusoidal as in a standing light wave alone. This phase modulation was caused by a combination of the light shift in the standing wave and the $\mu \cdot \mathbf{B}$ energy level shift of an atom in a magnetic field, and constituted a blazed diffraction grating. This technique resulted in a momentum splitting of 42 photon recoils, and transferred this momentum approximately 50% more efficiently than would be achieved using only a standing wave. The resultant momentum distribution exhibited two peaks, between which there was a continuous range of momenta; hence there was a considerable spread in the magnitude of the momentum transfer. The magneto-optic beamsplitter should be a coherent technique, relying as it does on diffraction, but this has not been explicitly verified through experiment.

7. Reflection of atoms that is complete [162] or partial [163] (thereby splitting the probability amplitude), can be effected using an evanescent light wave. However, reflection does not grant complete flexibility in manipulating the atoms' momenta, so this technique is of somewhat limited utility. It also results in some heating of the atoms [162]. Furthermore, the efficiency of partial reflection is only large (greater than 0.1) for low incident atomic momenta, *i.e.* less than 1 photon recoil. The partial reflection should constitute a coherent splitting of the wavefunction as it is due to classically forbidden reflection of the atoms' probability amplitude from a potential gradient.

8. A technique that is very similar in concept to the techniques discussed in this thesis is to use an amplitude-modulated standing wave of light to subject an ensemble of molasses-cooled atoms to a spatially periodic potential whose strength varies sinusoidally in time [164]. The potential causes a fraction of the initial atomic momentum distribution to be accelerated. This acceleration, unlike the quantum accelerator mode, is symmetric (the symmetry-breaking effect of gravity is not present), and the final distribution shows two narrow momentum peaks at large positive and negative momenta. In Ref. [164], the momentum width of each peak was approximately 5 photon recoils (while that of the atomic ensemble from which they were generated was 13 photon recoils), and momenta of ± 70 photon recoils were attained. When the number of modulation periods was 1.75, so that the accelerated peaks attained momenta of ± 33 photon recoils, each accelerated peak contained 30% of the atomic ensemble [165]. Hence this technique is a promising means of accelerating atoms efficiently to high momenta. It has not yet been

shown, however, to maintain coherence between the two accelerated groups, though its basis in diffraction implies that this is the case.

The capabilities of the quantum accelerator mode in terms of the extent and efficiency of momentum transfer, and the coherence of the process, will now be discussed.

6.1.2 Momentum transfer by quantum accelerator modes

As described in Sec. 4.2, in the experiments on the quantum δ-kicked accelerator that used a pulse period $T = 60.5\mu$s, approximately 10% of the atomic ensemble was to be found in an accelerator mode after 50 pulses. At this point the momentum that had been imparted by the light to the atoms was over 75 photon recoils. The momentum width of the accelerator mode was 15 photon recoils, largely determined by the width of the initial distribution from which the mode was created. The fraction of atoms in the accelerator mode fell linearly with increasing pulse number (see Fig. 4.7(a)), and the population in the accelerator mode after 50 pulses was 68% of that after 30 pulses. The results from the simulation, in which there was no violation of the Raman-Nath condition, show that 20% of the atoms were in the accelerator mode after 50 pulses and that the pulse-to-pulse efficiency of momentum transfer was over 98%. There was an exponential decrease with pulse number of the fraction of atoms in the accelerator mode (see Fig. 4.7(b)). Experimentally, it would be possible to come closer to this ideal regime by increasing the intensity of light in the standing wave and reducing the duration of each pulse, thus increasing the already high efficiency of momentum transfer. As shown in Fig. 4.6, momenta in excess of 100 photon recoils have been imparted to atoms in an accelerator mode by the pulsed standing wave. The size of the momentum transfers attainable, and the corresponding levels of efficiency, mean that, purely as a means of accelerating atoms, the accelerator mode is competitive with the techniques described above.

Quantum accelerator modes in the δ-kicked accelerator result from diffraction in the time-domain, but the efficiency of momentum transfer is much larger than for diffraction in the δ-kicked rotor. Furthermore, a group of atoms is separated in momentum space from the rest of the ensemble, unlike in the δ-kicked rotor. This is a useful outcome as, provided the momentum splitting that results is coherent, the momentum transfer technique could be applied to atom interferometry. The splitting produced by quantum accelerator modes is an external state splitting, such as that which is produced by diffraction of an atomic beam from diffraction gratings of light [151]. To be useful as an interferometric technique, however, the pulsed application of a periodic potential must be capable of bringing accelerated atoms to a halt, or of maintaining their location in momentum space. The dependence of the accelerator mode on the value of the effective value of gravity, as shown in Fig. 4.23, leads to the expectation that a change in the effective value of gravity at some point during a pulse sequence might be successful in modifying the variation with pulse number of the momentum of an accelerator mode. The

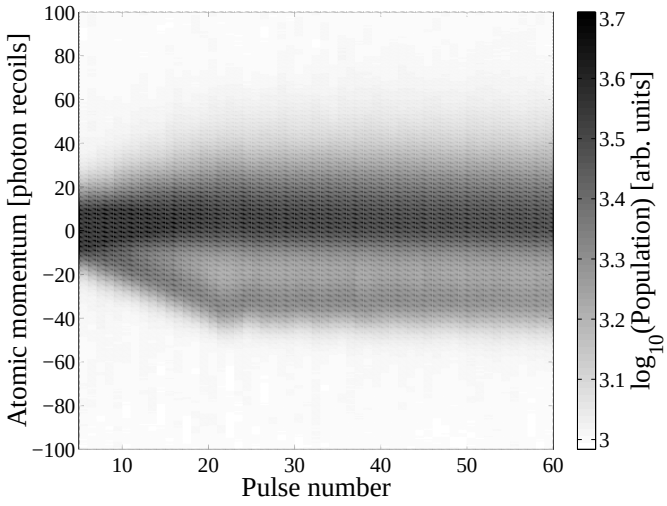

Figure 6.1: Experimentally measured momentum distributions following the application of a range of pulse numbers, from 5 to 60. The pulse period used was 60.5μs, and the detuning of the standing wave light from the ($F = 4 \rightarrow F' = 3$) transition was 30 GHz. For pulse trains in which the total number of pulses was larger than 20, the effective value of gravity was set to zero by the phase modulator after the 20th pulse. In this figure, the density of shading is proportional to the logarithm of the population of atoms (in arbitrary units).

data shown in Fig. 6.1 and Fig. 6.2 confirm that this expectation is experimentally met.

Figure 6.1 shows the experimentally measured momentum distributions when the number of pulses applied to the atoms, with a period $T = 60.5\mu$s, was varied from 5 to 60. For pulse trains of more than 20 pulses, the phase modulator was activated after the 20th pulse so as to cancel the effect of gravity. It is clear that no further transfer of momentum to the atoms in the accelerator mode occurs after the 20th pulse and the atoms are held in a fixed location in momentum space. This means, of course, that they continue to move away in position space from the unaccelerated group of atoms with a constant relative velocity. Although no momentum is transferred to the accelerator mode as a whole after the 20th pulse, the mode is not entirely unaffected by the subsequent pulses. In fact, the width of the distribution of atoms in the accelerator mode is broadened by the pulses in which gravity's effect is counteracted, from $15\hbar k_1$ to $20\hbar k_1$. This effect is not unexpected; after all, pulses in the absence of gravity do lead to momentum diffusion in the quantum δ-kicked rotor before dynamical localisation occurs. Nevertheless, this is a useful method of holding the atoms in momentum space, as the population of atoms in the accelerator mode after 60 pulses is over 93% of that after 20 pulses.

To have complete control of atomic momenta, it would be necessary to be able to reverse the direction of the momentum transfer. This capability would be required in, for example, interferometry to permit the re-overlap of portions of the wavefunction that had been spatially separated by the initial burst of accelerating

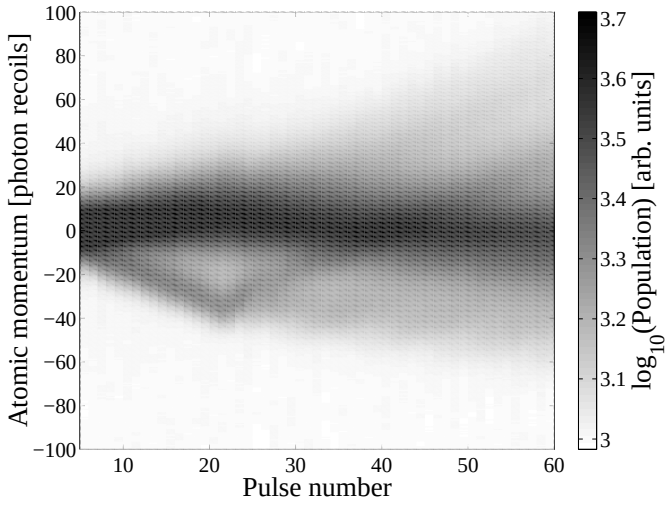

Figure 6.2: Experimentally measured momentum distributions following the application of a range of pulse numbers, from 5 to 60. The pulse period used was 60.5μs, and the detuning of the standing wave light from the ($F = 4 \rightarrow F' = 3$) transition was 30 GHz. For pulse trains in which the total number of pulses was larger than 20, the effective value of gravity was reversed by the phase modulator after the 20th pulse. In this figure, the density of shading is proportional to the logarithm of the population of atoms (in arbitrary units).

pulses. Figure 6.2 shows the experimentally measured momentum distributions that resulted when pulse trains consisting of between 5 and 60 pulses, with period $T = 60.5\mu$s, were applied to the atoms. For trains in which the total number of pulses was greater than 20, the phase modulator was activated after the 20th pulse so as to reverse the effective direction of gravity as experienced by the atoms, while keeping its magnitude the same. Figure 6.2 shows that, upon reversal of the effective direction of gravity, the direction of the impulse imparted to atoms in the existing accelerator mode (the 'primary' accelerator mode) by the light pulses is also reversed. Hence when the total number of pulses applied is 40, the atoms in the accelerator mode have returned to their original momentum state. In position space they would, therefore, be spatially separated from the group of unaccelerated atoms but the two groups would have no relative velocity. In Fig. 6.2, a 'secondary' accelerator mode, consisting of atoms that move out from the main unaccelerated group in the positive momentum direction from the 21st pulse onwards, is just visible. It can also be seen from Fig. 6.2 that further pulses beyond the 40th actually lead to the primary accelerator mode being found in the opposite momentum direction to its initial one. This would allow the accelerated atoms to be brought back in position space towards the unaccelerated group, thus permitting the two groups to be re-overlapped.

The major drawback in this technique is that the experimental efficiency of momentum reversal is not high; many atoms fail to remain in the primary accelerator mode upon reversal of the effective direction of gravity. The atoms that

leave the accelerator mode are diffracted in both positive and negative momentum directions by subsequent pulses. Therefore, in Fig. 6.2, by the stage that 40 pulses have been applied there is a spread of population over quite a wide range of negative momenta. For the pulse numbers used in these experiments it is difficult to quantify from the measured distributions the fraction of atoms that are lost in the reversal of acceleration direction. This loss only becomes evident several pulses after the reversal, after which the primary accelerator mode is no longer well separated from the peak of unaccelerated atoms. After 60 pulses the reversed primary accelerator mode should have reached close to the same magnitude of momentum in the positive direction as it reached in the negative momentum due to the 20 pulses applied before gravity's reversal. From Fig. 6.2 it is clear that the height of the primary accelerator mode after 60 pulses is much lower than that after 20 pulses. The primary mode has been broadened by the pulses that were applied after gravity's reversal and is not well separated from other atoms in both the broad, unaccelerated peak and the secondary accelerator mode. The atoms in the secondary mode form a broad, low peak at momenta in excess of $50\hbar k_1$.

The failure of atoms to remain in the primary accelerator mode after gravity's reversal can only partly be accounted for by experimental imperfections, such as the error in calibrating the phase modulator. The loss of atoms also occurs in the numerical simulations because not all atoms in the accelerator mode after 20 pulses (*i.e.* not all the momentum states that they occupy) fulfil the conditions for acceleration in the positive momentum direction after reversal of the effective value of gravity. The location in momentum space of the accelerator mode after n pulses, prior to any reversal of gravity, is given by Eq. (4.27); the accelerator mode, of course, consists of a comb of momenta. When the effective value of gravity is reversed, there is a condition on the values of the 'initial' momenta (the momenta after the first 20 pulses) that can undergo acceleration in the opposite direction. This condition is a modification of Eq. (4.32), in which the sign of g is reversed. Hence the momentum classes that enter an accelerator mode when gravity is in the positive direction are not the same as those that enter when it is in the negative direction. The proportion of atoms that do change accelerator mode direction will depend on the momentum of the accelerator mode at the time of gravity's reversal, since this will determine the degree of overlap with the elements of the ideal momentum comb that can enter the reversed mode. The pulse period T is the same all the way through the pulse train, so the spacing of the momentum comb in the existing primary accelerator mode after 20 pulses is the same as that in the ideal comb that can undergo further acceleration after reversal of gravity's direction. The overlap between the elements of the two combs may be large or small, depending on exactly how many pulses were applied prior to gravity's reversal, and so the efficiency of reversal of the mode's direction may also be large or small. Furthermore, some atoms in the group that was not accelerated by the pulses before gravity's reversal succeed in fulfilling the initial condition for acceleration by those that are applied after reversal. This explains the existence of the secondary accelerator mode.

The results of the numerical simulation corresponding to the experimental data

in Fig. 6.2 do not allow the fraction of atoms remaining in the primary accelerator mode after gravity's reversal to be established. This is because of the extent of the overlap, after 60 pulses, of the primary mode with the unaccelerated peak. However, by performing simulations where up to 80 pulses were applied following gravity's reversal, it has been possible to see that less than 20% of the atoms that are in the primary accelerator mode after 20 pulses are still in it after 60 further pulses have been applied with gravity reversed. Furthermore, a simulation in which 50 pulses were applied with gravity in the usual direction, so that the primary accelerator mode was well separated from the unaccelerated peak, followed by 50 further pulses with gravity reversed has shown that approximately 62% of the atoms in the primary accelerator mode after 50 pulses fail to reverse their momentum space trajectory when gravity is changed. If only 49 pulses are applied prior to gravity's reversal, 57% of the atoms in the primary mode fail to reverse their momentum trajectory. This demonstrates that this fraction is dependent on the momentum of the accelerator mode immediately prior to the reversal.

It is also useful to examine the behaviour of an individual plane wave. The simulated variation with pulse number of the momentum distribution resulting from application of the potential to a plane wave with initial momentum $\hbar k_1$, with $T = 60.5\mu$s, was shown in Fig. 4.17(a). This data indicates that 43% of the distribution is to be found in the accelerator mode after 50 pulses. If further pulses are applied, with gravity's direction reversed, simulation results indicate that after 20 of these pulses only 8% of the distribution is still to be found in the primary accelerator mode. That is, less than 20% of the population of the primary mode after 50 pulses has remained in it following gravity's reversal. The efficiency of primary mode reversal is poor. However, if gravity is reversed after 49 pulses, rather than 50, the efficiency is much higher. After the first 49 pulses, 44% of the distribution is to be found in the primary accelerator mode. After 21 further pulses following gravity's reversal, 36% of the distribution is still in the primary mode. Thus over 80% of the population of the primary mode has survived gravity's reversal. These results can be accounted for by the different momentum of the accelerator mode after 49 and 50 pulses. They show that efficient momentum reversal is possible provided that the overlap between the momentum comb of the primary mode and the ideal comb defined by the pulses after gravity's reversal is large. Experimentally, this overlap could be varied so as to optimise the reversal efficiency by using the crystal phase modulator to impose an additional relative velocity between the atoms in the primary accelerator mode and the periodic potential. Experimental imperfections such as noise and the violation of the Raman-Nath condition would serve to make the efficiency obtained somewhat less than could be achieved in this ideal situation. Nevertheless, both the experiment and the simulation indicate that a useful fraction of the primary accelerator mode can be made to reverse its momentum trajectory. This degree of momentum control might find an application in lithography [108], particularly when the spatial localisation of atoms in the accelerator mode is taken into account, as it would facilitate etching of structures on the scale of λ_{spat} over large areas.

It would be possible, if desired, to reverse the direction of momentum transfer

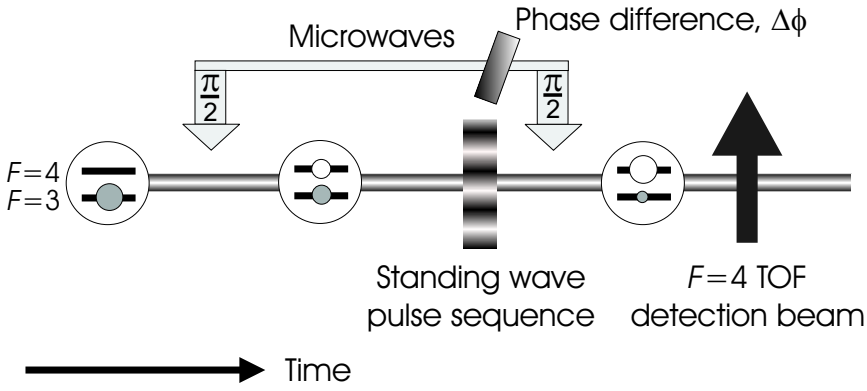

Figure 6.3: Scheme for testing the coherence of the accelerator mode process.

to the primary accelerator mode again after the 60 pulses shown in Fig. 6.2 and accelerate the atoms under the unmodified effect of gravity for 20 further pulses. They would then overlap, in both position and momentum, with the atoms that had not participated in any acceleration. Thus it would be possible to spatially separate and then recombine parts of an atomic wavepacket, as would be necessary for interferometry. The question is whether this process would manipulate the atoms coherently.

6.1.3 Coherence of the accelerator mode

The technique used to investigate the coherence of the quantum accelerator mode was interferometric in nature, and based on the Ramsey configuration of separated oscillatory fields [83, 84]. This technique consists of the application, in two bursts, of oscillating electromagnetic fields to the system under examination. The bursts are separated in time and/or space, and between them the system evolves under a constant or zero field. In the system under discussion in this thesis, the oscillating fields were provided by pulses of microwaves whose frequency was resonant with the $(F = 3 \rightarrow F = 4)$ magnetic dipole transition between the ground state hyperfine levels in the caesium atom. These microwaves were discussed in some detail in Sec. 2.5. In order to perform these investigations, pulses of both microwaves and light had to be used. A schematic diagram of the sequence of pulses is shown in Fig. 6.3, while the timing and duration of the pulses are shown in Fig. 2.9.

Following trapping and cooling in the usual way, and immediately after the shut-off of the repumper light, all the atoms in the MOT were in the $F = 4$ hyperfine level, though spread over all the m_F magnetic sub-states. A π pulse of microwaves, labelled '$F = 3$ pump pulse' in Fig. 2.9, was then applied to the atoms. This was polarised so as to induce only $\Delta m_F = 0$ transitions, and had a frequency such that atoms initially in the $F = 4, m_F = 0$ state could make the transition to the $F = 3, m_F = 0$ state. The energies of the magnetically sensitive $m_F \neq 0$ states were shifted out of resonance by the local magnetic field so that these did not participate significantly in any transitions. Following this pump pulse, a

'blow-away' pulse of light 15 MHz red-detuned from the ($F = 4 \rightarrow F'' = 5$) D2 transition was applied to the atoms in order to push away those that were still in the $F = 4$ level. All the atoms remaining were in the $F = 3, m_F = 0$ state. Then the experimental scheme shown in Fig. 6.3 commenced. The first $\pi/2$ pulse of microwaves was applied, creating in the atoms an equal superposition of the $F = 3, m_F = 0$ and $F = 4, m_F = 0$ states. The atoms then evolved freely for a short time. If another $\pi/2$ pulse, with some variable phase difference $\Delta\phi$ relative to the first, had now been applied to the atoms, this would amount to a realisation of the Ramsey interferometer. In this case, scanning $\Delta\phi$ would have resulted in $\cos^2$ fringes in the final population of the $F = 4$ state, and these would have a visibility of over 90% [166].

In these investigations, however, the first $\pi/2$ pulse was followed by a sequence of 20 pulses of the standing wave of light, with $T = 60.5\mu$s and gravity's effect unmodified. The red-detuning of the light from the ($F = 4 \rightarrow F' = 3$) D1 transition was 22 GHz, and therefore the red-detuning from the ($F = 3 \rightarrow F' = 4$) D1 transition was 32 GHz (see Fig. 2.3). As the size of the light shift is proportional to $1/\delta_L$, as given in Eq. (3.24), this meant that the depths of the potential to which the two hyperfine states in the atomic superposition were exposed were different, *i.e.* there was a different value of ϕ_d for each state. The value of the power in the standing light wave for these experiments was around 60% of its value in the experiments described in Ch. 3 and Ch. 4, and since the detuning of the light from the ($F = 4 \rightarrow F' = 3$) D1 transition was 22 GHz rather than 30 GHz, the value of ϕ_d experienced by the $F = 4$ state was around 80% of that in the previously discussed experiments. The value of the detunings meant that the potential experienced by the $F = 3, m_F = 0$ state was approximately 70% of that experienced by the $F = 4, m_F = 0$ state. Nevertheless, for each of these states the potential was sufficiently large that an accelerator mode of significant population could be produced. The population of the mode created in the $F = 3$ state was between a third and a half of that in the $F = 4$ state. From the analysis in Sec. 4.3, the momentum of an accelerator mode after a given number of pulses depends on T and g, but not on ϕ_d. This meant that the parts of the atomic superposition that were in each of the hyperfine states were accelerated by the light pulses to the same region in momentum and position space, and hence continued to overlap spatially after the pulse train had finished. Following the application of the periodic potential and a short period of free evolution under gravity, a second $\pi/2$ pulse, with phase $\Delta\phi$ relative to the first, was applied to the atomic ensemble. The value of $\Delta\phi$ was controlled by varying the phase of the first $\pi/2$ pulse. Finally, the momentum distribution of atoms in the $F = 4$ state was measured by the TOF system. For each value of $\Delta\phi$, the result was averaged over 10 repetitions in order to improve the signal-noise ratio. Over the course of the experiment the value of $\Delta\phi$ was varied from 0 to 4π in steps of $\pi/5$. The signature of coherence in the accelerator mode would be a periodic variation in the population of accelerated atoms in the $F = 4$ state. This observation of interference between the accelerated populations in the two hyperfine states would confirm that the acceleration process had preserved the phase relationship between

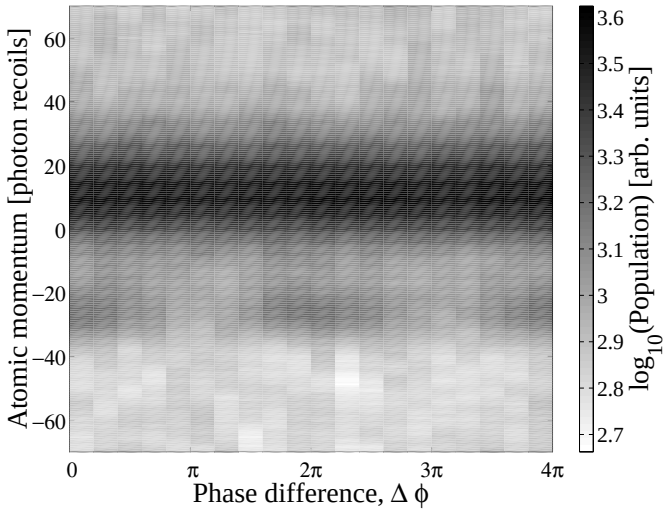

Figure 6.4: Variation with the phase difference $\Delta\phi$ between the two $\pi/2$ microwave pulses, as defined in Fig. 6.3, of the measured momentum distribution of atoms in the $F = 4$ hyperfine state after the atoms had been subjected to the light and microwave pulse sequence shown in Fig. 6.3 and described in the text. The detuning of the light in the standing wave from the ($F = 4 \rightarrow F' = 3$) transition was 22 GHz, $T = 60.5\mu$s and the measurements were averaged over 10 repetitions. In this figure, the density of shading is proportional to the logarithm of the population of atoms (in arbitrary units).

the two parts of the atomic superposition.

Figure 6.4 shows the experimentally measured momentum distributions as $\Delta\phi$ was varied. It is clear that the population of accelerated atoms in the $F = 4$ state, at a momentum of around $-30\hbar k_1$, varies periodically as $\Delta\phi$ is changed. The period of this variation is 2π and the visibility is $(42\pm4)\%$. The visibility V is defined by the relationship $P = A(1 + V\cos[\Delta\phi + \tau])$, where P is the population, A is the amplitude of the variation and τ is a phase offset dependent on ϕ_d. This periodic variation proves that there is a well-defined phase relationship between the $F = 3$ and $F = 4$ components of the atomic wavefunction after acceleration, and hence that the accelerator mode process has maintained phase coherence between these components. The values of $\Delta\phi$ for which the maxima and minima in population occur are partially determined by the value of ϕ_d experienced by the atoms. Since the atoms in the experiment experience a range of values of ϕ_d, due to the Gaussian beam profile and finite size of the MOT, different atoms will yield the maximum $F = 4$ population at different values of $\Delta\phi$; this is responsible for a considerable reduction in the visibility compared to that which would be observed for a unique value of ϕ_d. There is also a low-contrast periodic variation (4% visibility) in the $F = 4$ population of atoms that do not participate in the accelerator mode, though the low visibility means that this is not clear from Fig. 6.4. Recent simulations [167] that include the hitherto neglected global phase ϕ_d, seen in Eq. (3.16), indicate that the positions of the maxima and minima in this unaccelerated peak are more dependent on the value of ϕ_d than are those of the accelerated atoms.

Thus there is greater washing out of the fringes and much lower visibility. If the accelerator mode is created using pulses with a period of 74.5μs rather than 60.5μs, the fringes in the accelerator mode are almost unobservable. Again, simulations including the global phase indicate that the positions of the maxima in the accelerated $F = 4$ population are much more sensitive to the value of ϕ_d than when the accelerating pulse period is 60.5μs [167]. Similarly, in the accelerator modes that occur for values of T to either side of the quantum resonance at $3T_{1/2}$, the accelerator mode at $T = 189.5\mu$s exhibits $F = 4$ fringes with much higher visibility than those of the mode at $T = 206.5\mu$s. These visibility differences are interesting, and are an indicator as to where future investigations should be directed.

The non-zero, and indeed rather large, visibility of the variation with $\Delta\phi$ in the accelerated $F = 4$ population demonstrates that the quantum accelerator mode preserves coherence. It is therefore, in this respect, suitable for use as an atom optical technique with which to perform interferometry. Since the accelerator mode produces external state splitting, it offers the possibility of interferometry in which the mechanism that forms the internal state superposition (the microwave pulses) is separate from that which spatially splits the atomic wave packets. This is along the same lines as the separated path Ramsey atom interferometer [166]. Challenges to be overcome include the relatively inefficient reversal of the momentum of an accelerator mode, which would be necessary in order to re-overlap the spatially separated parts of the wavefunction, and the fact that when re-overlap has occurred it does so at the location in momentum and position space where the atoms that were never accelerated are to be found. Since there are many such atoms, detecting on top of them a signal that is due to interference between relatively small coherent populations will be difficult. Nevertheless, the large magnitude of momentum that can be imparted to atoms in a quantum accelerator mode means that a separated path interferometer using this as a beam splitting method would have a high sensitivity to gravitational forces and could attain a large separation between the arms. This would increase the interferometer's sensitivity to rotations because it would result in a large enclosed area. It would also allow an electric field, for example, to act on one arm but not the other, thus permitting properties of the atom such as polarisability to be investigated. Such an interferometer could be very useful as an instrument for precision measurement.

6.2 Measurement of gravity

Since relative acceleration between a δ-kicked quantum system and the periodic potential to which it is being subjected is necessary for the existence of a quantum accelerator mode, the characteristics of that mode offer a possible means of measuring the relative acceleration. In the experiments discussed in this thesis, the relative acceleration was provided by the unidirectional external force of gravity, unless the crystal phase modulator was active in shifting the standing wave profile between successive pulses. There are a number of features of the accelerator mode and its behaviour that are determined by the value of the local gravitational

acceleration. The first is the variation with pulse number of the momentum of the mode, as given in Eq. (4.27). The width of the accelerator mode, generally greater than 15% of the momentum reached by the mode as a whole, means that the experimental uncertainty in the central momentum is rather large and does not lend itself to yielding a precise value of the local gravitational acceleration.

The other means by which an effect of gravity can be detected is the experimental procedure that was used to observe the momentum comb and spatial localisation of the accelerator mode in Sec. 4.3. The accelerator mode was created by the application of 20 preparation pulses to the δ-kicked accelerator system, then the system was allowed to evolve freely under gravity for a time T_{gap} before a further set of 20 main pulses was applied to the atoms. For the results shown in Fig. 4.19 and Fig. 4.22, the pulse period for both the preparation pulse sequence and the main pulse sequence was 60.5μs. In the analysis in Sec. 4.3 that accompanies these figures, it was shown that the local value of the gravitational acceleration determines the period in T_{gap} of the variation in the population of atoms accelerated by both sets of pulses. In the observation of the momentum comb, this period was equal to the time taken for gravity to impart to the atoms an amount of momentum equal to the spacing between the elements of the momentum comb in the accelerator mode. In the case of the spatial localisation, this period was equal to the time taken for atoms to travel a distance equal to λ_{spat}. This time was determined by their velocity due to free-fall following release from the molasses cooling, plus the momentum imparted to them in the accelerator mode created by the preparation pulses. Due to the free-fall, the period of variation was dependent on the local value of g. The measured values of the period in the two cases were shown to be consistent with a physically reasonable value of g.

Since the period of the variation with T_{gap}, whether due to the momentum comb or spatial localisation, is dependent on the value of g, an assumption that the theory of the accelerator mode were well understood would, in principle, allow the measured values of this period to be used to calculate a value for g. In practice, various aspects of the experimental arrangement described in this thesis make any great precision in the value thus calculated unfeasible. When comparing the experimentally measured trajectory of the accelerator mode with pulse number, as shown in Fig. 4.6, with that produced by numerical simulation, as shown in Fig. 4.8, there was found to be a discrepancy between the momentum attained in the two cases after 50 pulses. This was explained in Sec. 4.3 as being due to the effect on the dynamics of the finite duration of each experimental pulse, the imperfect retroreflection of the beam forming the standing wave and the non-parallel alignment of the standing wave with the local gravitational acceleration. Since the spacing of the momentum comb in an accelerator mode is given by $(T_{1/2}/T)\hbar G$, use of the consequent periodic variation in the doubly accelerated population with T_{gap} in order to measure g would depend on accurate knowledge of G. It would also be necessary to take account of the finite duration of each kick, and the fact that the inter-kick free evolution time is less than the pulse period. With care, it should certainly be possible to retroreflect the beam forming the standing wave sufficiently well as to obtain a value of G that differed from

the ideal by less than 1 part in 10^6. It would be more difficult to quantify the effect of the finite duration of each pulse. The correct approach would probably be to perform a numerical simulation that modelled the behaviour of the system in the case where pulses had a finite duration, and work out the effect of gravity on the system under these circumstances. This could then be compared with the experimental data, and conclusions drawn as to the value of g experienced by the atoms. Even then, the uncertainty in the measured period of the variation with T_{gap} of the doubly accelerated population would be a limiting factor on the precision, as it would be difficult to reduce this uncertainty much below 0.5%.

When the doubly accelerated population varies with T_{gap} due to the spatial localisation, this population is an indicator of the atoms' position. The standing wave is effectively used as a 'ruler' to measure the movement of the atoms, and the period of the variation is determined by the momentum of the atoms at the end of the preparation pulse sequence. To measure the value of g, the contribution of the gravitational acceleration to this momentum would have to be ascertained. The accelerator mode's contribution could be measured by applying only the preparation pulses and reading out from the TOF system. This could then be subtracted from the total momentum at the end of the preparation pulses. By knowing the time for which the atoms had been falling under gravity after release from the molasses cooling, it would then be possible to obtain a value for g. In this method, the finite duration of each pulse or the duration of the inter-kick free evolution would not need to be analysed explicitly. The precision in the value of g would depend on the precision with which several different quantities were known. The first is the time of free-fall, which could be measured without difficulty to better than 1 part in 10^4. The second is the value of λ_{spat}, which equals $2\pi/G$. As discussed, it should be quite possible to achieve a precision in G better than 1 part in 10^6. The third is the contribution to the atomic velocity due to the quantum accelerator mode. Due to the momentum spread in the mode itself, this cannot be determined to better than 1%. The fourth is the period of the variation with T_{gap} of the doubly accelerated population of atoms, which cannot be determined to much better than 0.5%. Taking all the uncertainties into account, therefore, this technique seems unlikely to yield a measurement precision better than 1%.

Attempts to find a precise value of g would also have to overcome the experimental difficulties that face any gravitational measurement, such as the detrimental effects of vibrations, local mass distributions, atmospheric pressure, and noise in the signals. A more fundamental shortcoming of this technique is that the doubly accelerated population varies with gT_{gap}, whether due to the fulfilment of the momentum comb or spatial localisation conditions. On the other hand, the phase shift between two arms of an appropriately oriented atom interferometer is proportional to $g\tau^2$, where τ is the time over which the two arms of the interferometer are allowed to evolve in the gravitational field with different momenta [61, 168]. The greater sensitivity to time means that the interferometric technique is capable of much greater measurement precision, the best so far being $\Delta g/g = 1 \times 10^{-10}$ [168]. It seems impossible that the accelerator mode technique could be used to attain a measurement precision in any way comparable with this.

6.3 Characterisation of phase space

When gravity's effect is compensated for, the system whose experimental investigation is described in this thesis is the quantum mechanical analogue of a classically chaotic system, the δ-kicked rotor. One of the defining features of a classically chaotic system is the exponential divergence of phase space trajectories that are initially in close proximity. It might be thought that the quantum mechanical analogue of this phenomenon would be an exponential decay with time of the overlap integral between two initially similar wavefunctions. However, this is not the case. Consider two states $|\psi_1(t)\rangle$ and $|\psi_2(t)\rangle$. The time derivative of their overlap integral $A_{21} = \langle\psi_2|\psi_1\rangle$ is given by

$$\begin{aligned}
\frac{\partial A_{21}}{\partial t} &= \int \left(\psi_2^* \frac{\partial \psi_1}{\partial t} + \frac{\partial \psi_2^*}{\partial t} \psi_1 \right) dz && (6.1)\\
&= \frac{1}{i\hbar} \int \left(\psi_2^* \hat{H} \psi_1 - \left(\hat{H} \psi_2 \right)^* \psi_1 \right) dz && (6.2)\\
&= \frac{1}{i\hbar} \langle \psi_2 | \hat{H} | \psi_1 \rangle - \frac{1}{i\hbar} \langle \psi_2 | \hat{H}^\dagger | \psi_1 \rangle && (6.3)\\
&= 0 && (6.4)
\end{aligned}$$

The Hermitian nature of the Hamiltonian, embodying the unitarity of quantum dynamics, means that the overlap between two states remains constant as they evolve in time, irrespective of the stability or otherwise of the phase space occupied by the states. Therefore a definition of quantum chaos based on the variation of A_{21} in response to a given Hamiltonian is not possible. However, classically chaotic systems are also characterised by extreme sensitivity to slight changes of the dynamics. This has led to a proposal by Peres [32, 33] that the evolution of an initial state $|\psi_0\rangle$ under two slightly different, classically chaotic, Hamiltonians $\hat{H}_1$ and $\hat{H}_2$ could be examined. The behaviour of the overlap integral B_{21} between the resulting states $|\psi_1(t)\rangle$ and $|\psi_2(t)\rangle$, where $|\psi_1(t)\rangle = \exp(-i\hat{H}_1 t/\hbar)|\psi_0\rangle$ and $|\psi_2(t)\rangle = \exp(-i\hat{H}_2 t/\hbar)|\psi_0\rangle$, is predicted to be quite different depending on the character of the region of phase space initially occupied by $|\psi_0\rangle$. There are semi-quantitative arguments [169] that lead to the conclusion that perturbation theory does not converge for quantum systems whose classical analogue is chaotic. Two arbitrarily similar Hamiltonians corresponding to such systems have, in general, completely different sets of eigenvectors. This means that if the phase space initially occupied by $|\psi_0\rangle$ is chaotic in nature then $|\psi_1(t)\rangle$ and $|\psi_2(t)\rangle$ will quickly become very different as evolution under the two Hamiltonians takes place. Thus there will be a rapid decay in the magnitude of B_{21} with time and, once small, its value may vary erratically with time [32]. On the other hand, if $|\psi_0\rangle$ is found in a stable region of phase space then perturbation theory does converge and the magnitude of B_{21} will only decline slowly, and vary regularly, as the system develops. Therefore the variation of B_{21} with time allows the region of phase space occupied by $|\psi_0\rangle$ to be characterised.

An experimental investigation of this behaviour, using a trapped ion to realise a version of the quantum δ-kicked harmonic oscillator, has been proposed [170, 171]

but the system under investigation in this thesis also has the potential to facilitate such experiments. As discussed in Sec. 4.3, the quantum accelerator mode consists of a comb of momenta, adjacent elements of which are separated by 98% of $(T_{1/2}/T)\hbar G$. It was noted in Sec. 3.2 that scaled momenta ρ separated by integer multiples of 2π are equivalent in terms of their response to the potential, a result that holds both classically and quantum mechanically. Their phase space trajectories are, therefore, the same and so the periodicity in momentum of phase space is $(T_{1/2}/T)\hbar G$ (in experimental units). Since the spacing of the accelerator mode's momentum comb is so close to this value, and the experimental number of highly occupied comb elements is sufficiently small that the tiny difference between the two periodicities is insignificant (see Fig. 4.20), every momentum comb element in the experiment occupies essentially the same region of phase space. Scaled positions χ that are separated by integer multiples of 2π, which is λ_{spat} in experimental units, are also equivalent in the dynamics of a classical particle. This equivalence also holds quantum mechanically, and is a consequence of the spatially periodic potential (and hence force) to which particles are subjected. Therefore λ_{spat} is the period in position of phase space, both classical and quantum mechanical. The 'reduced phase space' has extent λ_{spat} in the z-direction and $(T_{1/2}/T)\hbar G$ in the p-direction and, due to the periodicity of phase space, contains all information about the dynamics of the system.

The momentum comb generated by the numerical simulation of the quantum system when $T = 60.5\mu$s (in which case $T_{1/2}/T = 1.10$), and shown in Fig. 4.20, indicates that the width of each comb element for this value of T is around $0.4\hbar G$. Therefore each element, and hence the accelerator mode as a whole, singles out a certain limited range of momentum within the reduced phase space. Furthermore, due to the periodic spatial localisation of the wavefunction of an atom that gives rise to an accelerator mode, as shown in Fig. 4.21, an accelerator mode also isolates a particular region of position within the reduced phase space. This region is generally in the vicinity of non-zero potential gradient, corresponding to a classical force in the direction of momentum transfer to the mode. Numerical simulation indicates that the localisation is generally around $0.3\lambda_{\text{spat}}$ in extent. The accelerator mode occupies a restricted region in both momentum and position space, thus isolating a certain zone of the reduced phase space. Hence it could be used as a means of phase space preparation.

To perform investigations of this kind, it is necessary to subject the same initial state $|\psi_0\rangle$ to two different Hamiltonians. This, too, is possible using the system described here. When a caesium atom is subjected to the standing wave of linearly polarised light that has a certain red-detuning from the $(F = 4 \rightarrow F' = 3)$ D1 transition, the red-detuning from the $(F = 3 \rightarrow F' = 4)$ transition is 10.4 GHz greater. As a result, the potential experienced by an atom in the $F = 3, m_F = 0$ state is smaller than that experienced by an atom in the $F = 4, m_F = 0$ state, and the Hamiltonians experienced by the two states are different. If an accelerator mode were used to prepare the atoms in some region of phase space, and the atoms were then placed in a superposition of the $F = 3, m_F = 0$ and $F = 4, m_F = 0$ states, both states would have the same distribution $|\psi_0\rangle$ in

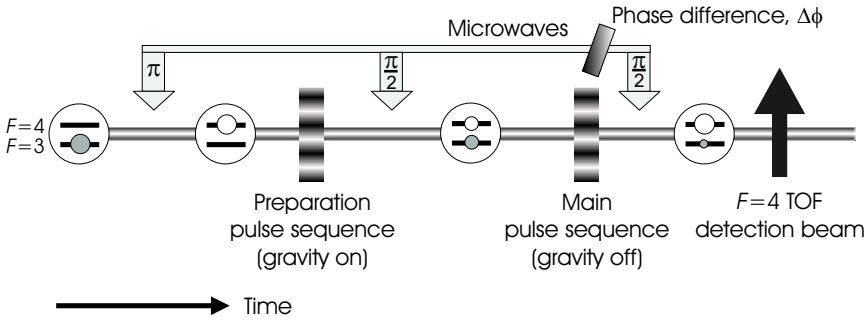

Figure 6.5: Scheme for investigating the stability of quantum phase space.

position and momentum. Further pulses, the 'main' pulses, of the standing wave would apply two different Hamiltonians to $|\psi_0\rangle$. If gravity's effect were removed by using the crystal phase modulator while these main pulses were applied, $|\psi_0\rangle$ would initially occupy a certain part of the phase space of the quantum δ-kicked rotor. The prepared atoms' subsequent behaviour would allow a characterisation of this region. Figure 6.5 shows a scheme that could be used to implement the experiment outlined above; the precise timings for this sequence are given in Fig. 2.9. After release from the optical molasses, atoms would be subjected to the $F = 3$ pump pulse, which is a π pulse of microwaves, followed by the blow-away pulse of D2 light. This procedure was described for the case of the coherence experiment in Sec. 6.1.3, and would leave all remaining atoms in the $F = 3, m_F = 0$ state. Following this, the sequence shown in Fig. 6.5 would begin.

Since the potential experienced by the $F = 4$ state, and therefore the efficiency of populating an accelerator mode, would be larger than for the $F = 3$ state, it would be advantageous to have all the atoms in the $F = 4$ state while applying the preparation pulses. Therefore another π pulse of microwaves, the '$F = 4$ repump pulse', would be used to place all the atoms in the $F = 4, m_F = 0$ state. The preparation pulses of the standing wave, with the phase modulator inactive, would be applied next in order to accelerate part of the atomic ensemble and isolate a region of phase space. After, say, 40 such pulses, the atoms would be subjected to a $\pi/2$ pulse of microwaves that would place them in a 50:50 superposition of the $F = 3, m_F = 0$ and $F = 4, m_F = 0$ states. They would now be ready for the application of the two Hamiltonians by the main pulse sequence. Each part of the superposition would evolve under the effect of its own Hamiltonian. Following these pulses, a final $\pi/2$ microwave pulse, with a variable phase $\Delta\phi$ relative to the first, would be applied. Depending on the phase of each part of the superposition, and on $\Delta\phi$, this would leave a certain population in the $F = 4$ state, which would then be detected by the TOF system. As in the experiment used to investigate the coherence of the accelerator mode, this procedure would be repeated while the value of $\Delta\phi$ was scanned from 0 to 4π, and the corresponding variation in the final population in the $F = 4$ state would be plotted. This would show a sinusoidal variation, but the visibility would depend on the overlap in position and momentum

between the parts of the wave that had been subjected to the two Hamiltonians. Therefore a measurement of the visibility would allow B_{12} to be determined. This, in turn, would yield information on the stability of the initially occupied region of phase space. If the visibility were high, because B_{12} had remained large, this would indicate that the phase space region occupied by $|\psi_0\rangle$ was stable. On the other hand, if the visibility were low, the phase space could be described as unstable or 'chaotic', in the quantum sense of the word.

There is no doubt that this system seems well suited to use in making a characterisation of quantum phase space, because it affords the possibility of selecting a region of phase space, applying two different Hamiltonians to the same initial distribution $|\psi_0\rangle$, and measuring the variation of the overlap integral B_{21}. However, there are a number of aspects of both the ideal quantum accelerator mode and the experimental system as it exists in practice that make this application complicated, though hopefully not unfeasible. Firstly, the precise region of phase space that is isolated by the accelerator mode depends on the number of preparation pulses used to create it. The momentum imparted to an accelerator mode by each pulse is given by Eq. (4.27) as $(B'/A')\hbar G$. In general, this is not equal to an integer multiple of $(T_{1/2}/T)\hbar G$, meaning that the region of reduced phase space on which the accelerator mode is centred is shifted in momentum by each pulse. Furthermore, from Fig. 4.21 it can be seen that the exact position of the maximum spatial localisation of a wavefunction in which an accelerator mode exists also varies from pulse to pulse. Therefore the region of reduced phase space occupied is also shifted in position by each pulse. In fact, this movement of the region of occupation could be useful as it would mean that the accelerator mode could select and be used to characterise different regions simply by applying a different number of preparation pulses.

It will be important to be able to establish exactly which region is being occupied by the mode after a certain number of pulses. A straightforward way to establish the region occupied in momentum space would be to increase the resolution of the TOF system so that the momentum comb could be observed directly. This would require a smaller initial trap size and a TOF beam that was narrower in the z-direction. In the experimental setup described in Ch. 2, the spatial separation of atoms whose momenta after interaction with the standing light wave differed by $\hbar k_1$ was approximately 1 mm by the time they reached the TOF system. This meant that, as discussed in Sec. 2.6, the initial trap diameter of around 1 mm and the 1.5 mm thickness of the TOF beam both limited the resolution of momentum measurement to $\hbar k_1$. Therefore the momentum comb could not be observed directly. Since the numerical simulation indicates that the width of each comb element is around $0.8\hbar k_1$, if the resolution of the TOF system could be increased by a factor of 5 then the comb should be observable directly. This would necessitate a 10-fold decrease in both the diameter of the MOT and the z-width of the TOF beam, both of which would have implications for the signal-noise ratio. An alternative method of high-resolution momentum detection would be the use of Raman-beams to pump a selected, narrow momentum class into a state that would then be detected by a probe beam [172]. The selected momentum class would be

varied by altering the relative detuning of the counter-propagating Raman beams. Provided that the spectral width of the detuning was sufficiently small ($< 1\,\mathrm{kHz}$ for Raman beams detuned from the caesium D2 transition), a momentum resolution of $0.1\hbar k_1$ could be attained. The spatial variation of the frequency of the atomic transition due to local magnetic field inhomogeneities would also affect the momentum selectivity. This variation, however, should be small as the experiment would be carried out with the magnetically insensitive $m_F = 0$ atomic states, and further screening of stray fields using the Helmholtz coils and a μ-metal box could be carried out. The Raman pulses would need to act on the atoms for a sufficient length of time (around 1 ms) in order to attain the level of momentum resolution that would permit direct observation of the momentum comb.

Unfortunately, direct detection of the momentum comb could not be used to establish the region of spatial localisation. This is because the detected momentum distribution would contain none of the phase information that must exist in the momentum-space wavefunction and which would be necessary in order to use a Fourier transform technique to generate the spatial distribution (as was done in order to generate Fig. 4.21 using the data in Fig. 4.17). However, it might be possible to use a numerical simulation of the system, which took into account the finite duration of each pulse of the standing wave, to help in identifying the region of spatial localisation. Given that the momentum comb could be detected directly, this could be compared with that produced by the simulation. When the two combs matched, one might be justified in claiming that the region of spatial localisation indicated by the simulation was the same as that in the experiment. The similarity in the momentum distributions measured experimentally and produced by the numerical simulations in the cases where T_{gap} was scanned (see Fig. 4.19, Fig. 4.22 and the discussion in Sec. 4.3) already implies that the simulations can be useful in this regard. Once the experimental imperfections are taken into account they may well produce quantitative results that are trustworthy. An alternative, experimentally-based technique would be to apply a standing wave of on-resonant light to the atoms following preparation, parallel to the kicking potential. Only those atoms at the intensity minima of the standing wave would be detected by the subsequent TOF measurement as all others would be blown away by the force of the resonant light. The detected number would, therefore, be a maximum when the region of strong spatial localisation coincided with the intensity minimum of the standing wave. By varying the relative positions of the profile of this standing wave and of that which applied the kicking potential, the detected fraction of atoms could be used to determine the region of spatial localisation.

Once the exact region in phase space occupied by an accelerator mode had been established for a certain number of preparation pulses, it would, in fact, not be necessary to apply a different number of pulses to change the selected region. If this were done then the potentially laborious procedure by which the phase space region had been identified would have to be repeated for this different number of pulses. An alternative method of varying this region would be to use the phase modulator to shift the standing wave after the preparation pulses. To vary the region in the momentum direction, a pulse-to-pulse shift, during the main pulses,

in the position of the standing wave profile that mimicked the effect of a relative velocity between atoms and standing wave could be used. To vary the region in the position direction, the spatial profile of the standing wave could be shifted once, following the preparation pulses. Use of this technique would mean that only the region of spatial localisation would be shifted, but its form would not be changed. Likewise the extent of each momentum comb element would be unmodified by the velocity offset in the standing wave, only its location in momentum space. This lack of variation might simplify the interpretation of experimental data. Since phase space is periodic in both p and z, one would expect to see a periodicity in the variation of B_{21}, and hence the visibility in the variation with $\Delta\phi$ of the final state $F = 4$ population, as the initially selected region of phase space were altered.

The fractional difference in the values of the potential experienced by the $F = 3$ and $F = 4$ states in the proposed experiment would be rather large. For example, if the detuning of the light in the standing wave from the $(F = 4 \rightarrow F' = 3)$ D1 transition were 30 GHz, this would mean that the potential experienced by the $F = 3, m_F = 0$ state would be 0.74 times that experienced by the $F = 4, m_F = 0$, due to the greater detuning of this light from the $(F = 3 \rightarrow F' = 3)$ transition. In the proposal by Gardiner *et al.* [170, 171], the size of the kicks delivered to the two states differed by 12.5%, approximately half that in the present discussion. In the original discussion by Peres [32], the parameter determining the dynamics only differed for the two initially identical states under test by 1 part in 10^4! The use of numerical simulations that modelled the experimental arrangement as accurately as possible would be required in order to establish a magnitude scale for B_{21} and how it would vary with pulse number in the different types (stable or chaotic) of phase space region. A chaotic region should lead to a much more rapid decay of B_{21} than a stable region, for which an oscillatory type of behaviour would be expected [32, 170, 171]. The initial experimental approach might, therefore, be to look for qualitative, and periodic, differences in the variation of B_{21} with the number of main pulses as the selected region of phase space were varied. However, if the difference in the Hamiltonians were too great then B_{21} might decay so rapidly even in stable regions that it would not be possible to discriminate between this type of behaviour and that due to chaotic regions. Simulations would help to clarify whether this was a problem. An increase in the detuning of the light in the standing wave from the $(F = 4 \rightarrow F' = 3)$ D1 transition would reduce the fractional difference in the potentials experienced by the two hyperfine states. However, as this would also reduce ϕ_d and hence the efficiency of population of the accelerator mode, there is not much room for manoeuvre in this direction.

Another drawback in the proposed experiment is that the atoms would experience a range of values of ϕ_d. Hence there would a corresponding range of values in the classical stochasticity parameter, K. From Fig. 3.3 it is evident that as K increases the chaotic regions of phase space increase in area at the expense of the stable regions. Therefore in the experiment the phase space being characterised might effectively be a superposition of phase spaces of quite different character. Atoms subject to smaller ϕ_d would be in a phase space containing more, and larger, stable regions than those subject to a larger ϕ_d. Therefore the observed visibility

in the variation with $\Delta\phi$ of the $F = 4$ population could not be said to characterise the value of B_{21} resulting from a particular region of a well-defined phase space. A solution to this problem might be to expand the beam, and reduce the diameter of the MOT, so that atoms would experience a more uniform value of ϕ_d.

Even allowing for the foregoing difficulties, this experimental technique holds out the promise of an exciting and unprecedented method of characterising the stability of quantum phase space, and hence attaching a clear signature to quantum chaos. It was mentioned in Sec. 6.1.3 that, when performing the experiment to show that the accelerator mode preserves the phase relationship between different hyperfine states, the fringes in the $F = 4$ population were of larger visibility for $T = 60.5\mu$s and $T = 189.5\mu$s than for $T = 74.5\mu$s and $T = 206.5\mu$s. It may be that these visibilities reflect some difference in the character of the phase space of the system (in this case, the δ-kicked accelerator, rather than rotor), because different values of T yield different values of K. This is speculation, but further investigation should be able to resolve this question. Over the course of the experiments to verify the coherence of the accelerator mode, it was also found that, for a given value of T, the visibility of the fringes grew with increasing detuning of the light in the standing wave. Could this be due to a reduced fractional difference in the potentials experienced by the two hyperfine states while being accelerated? We do not yet know. If different regions of phase space could be selected and their stability characterised, this would allow a comparison with the stability of the phase space of the corresponding classical system to be made. This would cast new light on the operation of the correspondence principle and hence on a fundamental tenet of quantum mechanics. Such a goal makes this proposal worth pursuing further.

6.4 Summary

This chapter has discussed aspects of the quantum accelerator mode that make it suitable for various different applications. The fact that it results in the coherent transfer of a large momentum to part of the atomic ensemble with high efficiency means that it could be used as a tool in atom optics to achieve, for example, a large area interferometer. The process of momentum transfer can be controlled in a straightforward manner, and with reasonable precision, by shifting the spatial profile of the periodic potential. This might allow the accelerator mode to be used for lithography. The accelerator mode could potentially be used to measure gravity, on which its existence depends. However, a number of considerations, both experimental and intrinsic to the accelerator mode, make the attainment of high precision in such measurements unlikely. Since the accelerator mode selects a region in both momentum and position space, it could be used as a method of preparation to allow characterisation of quantum phase space. Notwithstanding some difficulties that will have to be overcome in order to carry out this type of experiment, this could be the most important application of all, yielding a new manifestation of quantum chaos and permitting further investigation of quantum-classical correspondence.

Chapter 7

Conclusions and Outlook

This thesis has described experimental and numerical investigations of two quantum systems whose classical analogues are chaotic: the δ-kicked rotor and the δ-kicked accelerator. The δ-function-like kicks to laser-cooled atoms were provided by pulses of a standing wave of light. In each case, the behaviour of the quantum system was found to be quite different from that of its classical counterpart. The quantum behaviour could be accounted for by consideration of the diffractive effect of the periodic potential on the atoms' de Broglie waves, and the phase accumulated between consecutive applications of the potential by the momentum states thus populated. The results of numerical simulations based on such a picture were found to be in excellent qualitative agreement; quantitative disagreements were accounted for in terms of the non-ideal aspects of the experimental realisation.

The phenomena associated with the quantum suppression of the classical diffusion of the action variable in the δ-kicked rotor (the process of dynamical localisation) were observed and the results were consistent with the findings of previous investigations conducted by groups in Austin and Auckland. The behaviour of this system at the quantum resonances was also studied. It was found to be characterised by an absence of dynamical localisation, a non-exponential momentum distribution and a higher rate of growth in the mean energy with pulse number than for neighbouring, non-resonant values of the pulse period. The introduction of controllable levels of decoherence into the system, by inducing spontaneous emission in the atoms, was found to degrade the quantum phenomenon of dynamical localisation, and to restore a classical-like diffusion of momentum. However, the extent of this momentum diffusion, and the form of the momentum distribution, remained quite different from those of the corresponding classical system. True convergence between the two systems was not achieved and decoherence was only partially successful in causing the system to approach classicality. Surprisingly, the decoherence was found to enhance, rather than degrade, the growth in mean energy with pulse number at the quantum resonances. This, however, was explained by consideration of the effect of the recoils from spontaneous emission on initially non-resonant values of atomic momenta. By allowing these to participate temporarily

in resonant growth, the overall energy growth of the system was increased, despite the detrimental effect of the decoherence on the growth of the initially resonant momenta. Thus the effect of decoherence at a quantum resonance was not, in fact, different in kind from that at non-resonant values of the pulse period.

The δ-kicked accelerator, in which a constant external acceleration is applied to the δ-kicked rotor, had never been investigated prior to the work of the group in Oxford. In the studies reported in this thesis, the external acceleration was provided by gravity, sometimes modified by controlled shifts in the position of the standing wave's profile. The most dramatic effect revealed in the investigations of the δ-kicked accelerator's behaviour was the existence of quantum accelerator modes, in which there was large momentum transfer to around 20% of the atomic ensemble. As the accelerator mode is a quantum effect due to diffraction, decoherence would be expected to degrade it and this was, indeed, found to be the case. Diffusive behaviour in the atomic momentum was restored and the quantum and classical systems became more similar in behaviour, though significant differences remained. The direction and magnitude of the momentum transfer per pulse to atoms in the accelerator mode could be controlled by shifting the spatial profile of the periodic potential constituted by the standing wave. Coupled with the periodic spatial localisation that an accelerator mode was experimentally shown to exhibit, this meant that the accelerator mode could be a possible tool for use in atom lithography. It was also shown to be a coherent process, and could, therefore, have an application as a beam-splitter for atom interferometry. An analytical expression for the variation of the accelerator mode's momentum with pulse number was obtained. This made clear the way in which the mode depended on the relative acceleration between the kicked system and the kicking potential, so the observed behaviour could, in principle, be used to measure this relative acceleration. High precision in this measurement would, however, be difficult to achieve. The analysis also indicated that an accelerator mode consists of a comb of momenta, and this was confirmed experimentally. The momentum comb and the periodic spatial localisation mean that a quantum accelerator mode could be used to prepare atoms in a specific region of phase space, allowing this to be characterised. This would enable investigation of the correspondence between the stability of classical and quantum phase space, offering more insight into quantum signatures of chaos.

In the immediate future, the next step will be to perform the phase space characterisation experiment proposed in Sec. 6.3. This will allow the first experimental determination of the stability of different regions of quantum phase space and allow comparison with the behaviour of the system's classical analogue. Hopefully, this will also provide an explanation for the different visibilities of the fringes in the $F = 4$ accelerator mode population that were observed for pulse periods of 60.5μs and 74.5μs, around $T_{1/2}$, and for pulse periods of 189.5μs and 206.5μs, around $3T_{1/2}$.

Subsequent work will be carried out with two different emphases. The first will be on further investigation of chaotic behaviour. Recent experimental studies [173, 174] have observed 'dynamical tunnelling' of cold atoms between different regions of phase space. This tunnelling involves the crossing of KAM boundaries

between these different regions of phase space and hence is classically forbidden. In each of these studies, the system used consisted of cold atoms (which were Bose-condensed in the experiment described in Ref. [173]) subjected to a horizontal standing wave of light whose amplitude was modulated sinusoidally in time. Observation of this tunnelling provides further information regarding the modifications that quantum mechanics makes to the behaviour of a classically chaotic system. Furthermore, evidence was presented in Ref. [174] that the rate of this tunnelling is enhanced by the chaotic nature of the system's classical analogue. This chaos-assisted tunnelling would provide a clear link between classical chaos and quantum behaviour. Investigations of this nature would also be possible in the quantum δ-kicked rotor. Use of a BEC is helpful, though not obligatory, for preparation of the atoms in a well-defined region of phase space due to its narrow momentum and spatial distributions [173]. The considerable expertise that exists in Oxford in this field would make BEC an option for this investigation, if necessary.

Use of a minimum-uncertainty BEC would also allow a specific region of phase space to be selected in order to carry out the type of investigation described in Sec. 6.3, in which two different Hamiltonians would be applied to the same initial state. A rubidium BEC could be placed in a superposition of hyperfine states by microwaves, each of which would experience a different potential, just as readily as thermal caesium atoms. Measurement of the overlap of the states after exposure to δ-function kicks would characterise the stability of the selected phase space and would be a complementary, or even superior, experiment to that described in Sec. 6.3. It would also be interesting to see how a BEC as a whole responded to kicks of the spatially periodic potential. Would it retain the appearance of a localised, classical particle? If so, would its dynamics be classical, and therefore chaotic, in appearance? Would this be a different manifestation of 'quantum chaos'? Alternatively, would the BEC break up? How would the response of the atoms differ from that of a non-condensed, thermal ensemble, as used so far? It would be very interesting to answer these questions. In a different approach to the question of classicality, investigations into the behaviour of an experimental δ-kicked rotor realised with nanoparticles, rather than cold atoms, would allow an investigation of the transition to classical behaviour. Nanoparticles are more macroscopic than atoms, and hence would be expected to behave in a more classical manner. Comparison of the behaviour of this system with that of existing quantum realisations, and of an ideal classical system, could be made. Hopefully, this would allow the operation of quantum mechanics, and the way in which classically chaotic effects emerge from the quantum regime, to be better understood.

The second emphasis of future work will be on further investigation of the quantum accelerator mode, and attempts to apply it to interferometry. Numerical studies [175] indicate that a realisation of the δ-kicked accelerator using a BEC instead of thermal atoms would still permit the creation of a quantum accelerator mode. The small size of a BEC compared with a thermal cloud would allow a much more uniform potential to be applied to the atoms. This would result in a higher efficiency of population of the accelerator mode and less spread in the

value of ϕ_d, and hence the phase imprint on the de Broglie wave, as a result of the diffraction process. Both these improvements would facilitate the use of an accelerator mode to perform interferometry. The small momentum spread of a minimum uncertainty BEC would also increase the acceleration efficiency. This increase would be obtained because the fraction of atoms with a momentum close to the ideal value that satisfied the condition for acceleration could be made to be greater than in the case of molasses-cooled atoms, with their large momentum spread. For example, a condensate confined to a region $\lambda_{\mathrm{spat}}/\pi$ in extent would have a momentum spread equal to $\hbar G/4$. Simulations indicate that the range of initial momenta (around an ideal value) that can enter an accelerator mode is also approximately $\hbar G/4$ in extent, though this depends on T. Moreover, the fact that the BEC was localised at a particular potential gradient might further increase the efficiency of populating an accelerator mode. The numerical simulations described in Ch. 4 indicated that only 43% of the momentum distribution was in the accelerator mode after 50 pulses when the initial state was a plane wave suitable for production of this mode (see Sec. 6.1.2). The fact that this initial state was a plane wave, whereas an accelerator mode involves a high degree of spatial localisation, may mean that a spatially localised initial state with the correct momentum could populate the accelerator mode more efficiently. This could be provided by use of a BEC.

The large, efficient, coherent momentum transfer possible in a quantum accelerator mode will, hopefully, be applied to the realisation of a large-area interferometer. The sensitivity of an interferometer to rotations scales linearly with the enclosed area [63], and large momentum transfer would aid in increasing this area. For a given enclosed area, the sensitivity of an atom interferometer to rotations is, in principle, around 10^{11} times that of a light interferometer. The use of this sensitivity to attain high precision would be dependent on overcoming experimental limitations such as vibrations and particle flux, but this would seem to be feasible. The ultra-high sensitivity could find gyroscopic applications, and may permit measurement of 'frame-dragging' by a rotating massive body, the Lense-Thirring effect [176]. The rotation of the Earth, for example, would cause an additional rotation of 6×10^{-15}rad s^{-1} to be measured by a gyroscope orbiting the Earth at an altitude of about 650 km [177]. This small effect might be detectable using an atom interferometer. A large momentum splitting would also permit greater precision in the measurement of phase shifts due to a gravitational field. When applied to the measurement of g, and the gradient of g, this would yield improved mapping of the Earth's gravitational field. This capability would be of benefit to geophysical surveying, oil exploration and covert navigation.

The ability to measure precisely the gravitational force experienced by atoms would allow tests of Newton's Law of Gravitation. There are numerous theoretical reasons for undertaking such tests. Firstly, the gravitational constant G is rather poorly known compared with the other fundamental constants, and the methods used in its determination are mainly mechanical laboratory experiments [178]. Atom interferometry could provide a complementary method, and potentially greater precision than has previously been attained. Secondly, certain the-

ories that seek to unify the gravitational force with the other fundamental interactions postulate the existence of extra dimensions [179]. The existence of such dimensions could lead to a departure of gravity's behaviour from a $1/r^2$ force law for distances between the interacting bodies of less than 1 mm. The behaviour of gravity has recently been tested down to a range of 218μm [180], and no deviations from Newtonian physics have been observed. A large splitting between the arms of a matter wave interferometer could allow one arm but not the other to experience the gravitational attraction of a nearby mass. The resulting phase shift could allow the variation of this attraction with distance between the interacting particles to be measured and hence a study of the behaviour of gravity at even shorter ranges. Theoretical work has also suggested that the existence of extra dimensions might manifest itself by small extra forces in nature [181]. Measurement of the short range force between atoms in one arm of an interferometer and a mass in close proximity might allow such forces to be detected. Fluctuations in the fabric of space-time may mean that different phase shifts occur in the arms of an interferometer in which the spatial splitting is sufficiently large [182]. The use of quantum accelerator modes to perform the splitting may render such exotic phenomena observable for the first time. The use of a BEC for the interferometric applications just described may allow a longer interaction time and a greater signal-noise ratio, thus yielding even greater measurement precision. By virtue of its narrow momentum distribution, a BEC could also permit new techniques in nanofabrication and lithography that make use of the quantum accelerator mode.

The investigation of the conceptually simple δ-kicked rotor and δ-kicked accelerator systems has resulted in the observation of phenomena that have been surprising, but also have contributed to a deeper understanding of the quantum analogue of a classically chaotic system. The exciting field of atom optics has provided, and will continue to provide, opportunities for the experimental investigation of deep questions involving chaotic dynamics and the nature of quantum mechanics, as well as allowing the development of interferometric tools to probe the nature of our Universe. The study of quantum chaos in atom optics involves the fusion of two of the most rapidly developing areas of physics; it is the study of simplicity and complexity, turbulence and beauty. There is much still to be learned, but the progress made thus far provides the assurance that this challenge will be met over the years to come.

Appendix A

The kicking potential

A clear exposition of some of the theory contained in this Appendix can be found in the '*Atomic, Molecular and Optical Physics Handbook*' [102].

Consider a two-level atom consisting of an upper state $|e\rangle$ and a lower state $|g\rangle$ separated in energy by $\hbar\omega_0$, and with a dipole moment $\mathbf{d}$ (see Fig. A.1). Suppose that the atom is in a single classical travelling wave light field of frequency ω_L and wavevector k_L that is propagating along the z-axis

$$\mathbf{E}(z,t) = \mathbf{e}_y E_0 \cos(k_L z - \omega_L t) \tag{A.1}$$

This electric field can be expressed as $\mathbf{E} = \mathbf{E}^+ + \mathbf{E}^-$, where the positive frequency part of the field is

$$\mathbf{E}^+ = \frac{1}{2}\mathbf{e}_y E_0 \exp[i(k_L z - \omega_L t)] \tag{A.2}$$

Hence the field can be written

$$\mathbf{E} = \frac{1}{2}\mathbf{e}_y\{E_0 \exp[i(k_L z - \omega_L t)] + c.c.\} \tag{A.3}$$

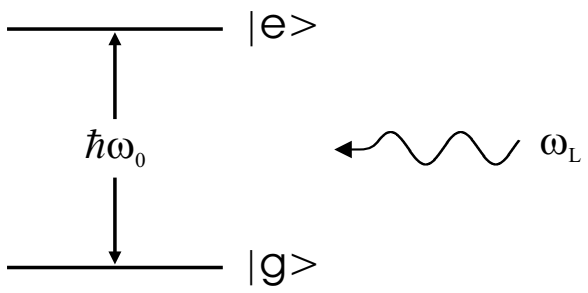

Figure A.1: A two-level atom consisting of an upper state $|e\rangle$ and lower state $|g\rangle$. These are separated in energy by $\hbar\omega_0$ and are subjected to incident light of frequency ω_L.

We will make the semiclassical approximation in which the electric field is described classically. In the absence of dissipation mechanisms, the Hamiltonian of a two-level atom in which there is a dipole interaction between a quasi-monochromatic classical field and the atom is

$$H = \frac{p^2}{2m} + \hbar\omega_e|e\rangle\langle e| + \hbar\omega_g|g\rangle\langle g| - \mathbf{d}.\mathbf{E} \tag{A.4}$$

where p is the momentum and m the mass of the atoms. The upper and lower atomic levels have frequencies ω_e and ω_g, respectively, and $\omega_0 = \omega_e - \omega_g$. The electric dipole operator couples the excited and ground levels and may be expressed as

$$\mathbf{d} = \epsilon_{\mathbf{d}} d(|e\rangle\langle g| + |g\rangle\langle e|) \tag{A.5}$$

where $\epsilon_{\mathbf{d}}$ is a unit vector in the direction of the dipole and d is the matrix element between the ground and excited states which, for simplicity, we take to be real. This allows the Hamiltonian to be expressed as

$$H = \frac{p^2}{2m} + \hbar\omega_e|e\rangle\langle e| + \hbar\omega_g|g\rangle\langle g| - d(|e\rangle\langle g| + |g\rangle\langle e|)[E^+ + E^-] \tag{A.6}$$

We can now introduce the pseudo-spin operators

$$s_z = \frac{1}{2}(|e\rangle\langle e| - |g\rangle\langle g|) \tag{A.7}$$

$$s_+ = |e\rangle\langle g| \tag{A.8}$$

$$s_- = s_+^\dagger \tag{A.9}$$

If we also redefine the zero of energy so that it is $(\hbar\omega_g + \hbar\omega_e)/2$, the part of the Hamiltonian describing the interaction of the atom with the E-field can be written

$$H_i = \hbar\omega_0 s_z - d(s_+ + s_-)[E^+ + E^-] \tag{A.10}$$

Under the influence of the E-field at frequency ω_L, the atom undergoes transitions between its lower and upper states by interacting with either the positive or negative frequency part of the field. The corresponding contributions to the atomic dynamics oscillate at frequencies $\omega_0 - \omega_L$ and $\omega_0 + \omega_L$, respectively, and their contributions to the probability amplitudes contain this same frequency dependence. For near-resonant atom-field interactions, the rapidly oscillating contributions lead to small corrections and these are neglected in the *rotating wave approximation* (RWA). In this approximation, the atomic system is described by the interaction Hamiltonian

$$H_i = \hbar\omega_0 s_z - d[s_+ E^+ + s_- E^-] \tag{A.11}$$

or, in a frame rotating at the frequency ω_L of the field

$$H_i = \hbar\delta_L s_z - \frac{1}{2} dE_0[s_+ + s_-] \tag{A.12}$$

where $\delta_L = \omega_0 - \omega_L$ is the atom-light detuning. At this point the Rabi frequency can be introduced, defined by

$$\Omega_1 = \frac{dE_0}{\hbar} \tag{A.13}$$

This is the frequency at which an atom will make stimulated transitions between the lower and upper levels when subjected to on-resonant light, *i.e.* light for which $\delta_L = 0$. For a general light frequency ω_L, the atom makes transitions between these levels at the modified Rabi frequency, Ω, given by

$$\Omega = (\Omega_1^2 + \delta_L^2)^{1/2} \tag{A.14}$$

If the atom is initially in the lower state then the probability that it is in the excited state at some subsequent time t is given by Rabi's formula

$$P_e(t) = \left(\frac{\Omega_1}{\Omega}\right)^2 \sin^2\left(\frac{\Omega t}{2}\right) \tag{A.15}$$

The atomic dynamics can alternatively be described in terms of a dressed states basis instead of the bare states $|e\rangle$ and $|g\rangle$. The dressed states approach finds eigenstates of the (atom + field) system instead of examining the states $|e\rangle$ and $|g\rangle$, which are eigenstates of the Hamiltonian of the isolated atom. The dressed states are the eigenstates of H_i (see Eq. (A.12)). These dressed states are labelled $|1\rangle$ and $|2\rangle$ and, by convention, $|1\rangle$ is the state with greater energy. The interaction Hamiltonian can be written

$$H_i = \frac{\hbar\delta_L}{2}(|e\rangle\langle e| - |g\rangle\langle g|) - \frac{\hbar\Omega_1}{2}(|e\rangle\langle g| + |g\rangle\langle e|) \tag{A.16}$$

If we move to a matrix representation in which the components of the column vector $\begin{pmatrix} \alpha \\ \beta \end{pmatrix}$ give the coefficients of $|e\rangle$ and $|g\rangle$ so that the total state is $|\psi\rangle = \alpha|e\rangle + \beta|g\rangle$,

$$H_i = \begin{pmatrix} \hbar\delta_L/2 & -\hbar\Omega_1/2 \\ -\hbar\Omega_1/2 & -\hbar\delta_L/2 \end{pmatrix} \tag{A.17}$$

$$= \frac{\hbar}{2}\begin{pmatrix} \delta_L & -\Omega_1 \\ -\Omega_1 & -\delta_L \end{pmatrix} \tag{A.18}$$

The eigenvalues of this matrix are $E_1 = +\hbar\Omega/2$ and $E_2 = -\hbar\Omega/2$; the corresponding eigenstates can be written

$$|1\rangle = \sin\theta|g\rangle + \cos\theta|e\rangle \tag{A.19}$$

$$|2\rangle = \cos\theta|g\rangle - \sin\theta|e\rangle \tag{A.20}$$

respectively, where θ is the Stückelberg angle, given by

$$\sin 2\theta = -\frac{\Omega_1}{\Omega} \tag{A.21}$$

$$\cos 2\theta = \frac{\delta_L}{\Omega} \tag{A.22}$$

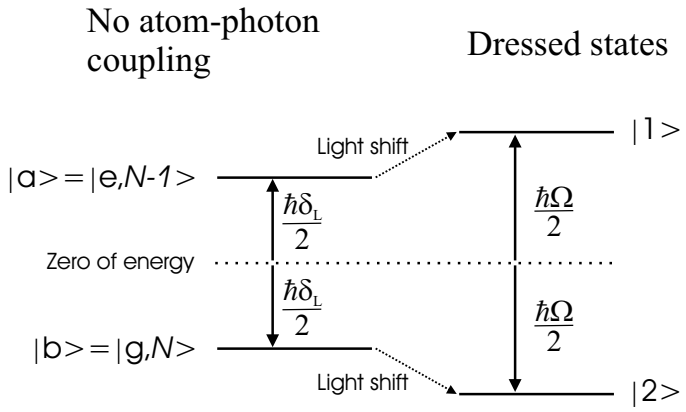

Figure A.2: The light shift experienced by the two-level atom of Fig. A.1 in a light field for which $\delta_L > 0$ (see text).

The asymptotic values to which E_1 and E_2 tend as δ_L becomes very large are $+\hbar\delta_L/2$ and $-\hbar\delta_L/2$, respectively. When δ_L is very large and positive, $|1\rangle$ consists almost entirely of $|e\rangle$, whereas when δ_L is very large and negative, $|1\rangle$ consists almost entirely of $|g\rangle$. When $\delta_L = 0$, both the bare states $|e\rangle$ and $|g\rangle$ contribute with equal amplitude to $|1\rangle$ and $|2\rangle$. The atom-photon interaction has resulted in a shift in the energies of the bare atomic levels. This is called the *light shift* or *ac Stark shift*.

One way of understanding this effect is by comparing the energies of a system in which there is no atom-field coupling and one where this coupling has been taken into account by finding the eigenstates of H_i. If there is no coupling, we can have either a situation where the atom is in its excited state $|e\rangle$ and there are $(N-1)$ photons in the light field (we call this state of the system $|a\rangle$), or the atom is in its ground state $|g\rangle$, and there are N photons in the light field (we call this state of the system $|b\rangle$, see Fig. A.2). The energy of $|e\rangle$ exceeds that of $|g\rangle$ by $\hbar\omega_0$, while the energy of a light field containing N photons exceeds that of one containing $(N-1)$ photons by $\hbar\omega_L$. Hence the energy of state (a) exceeds that of (b) by $(\hbar\omega_0 - \hbar\omega_L)$, which is just $\hbar\delta_L$. By a suitable choice of the zero of energy, the energies of states (a) and (b) can be written as $+\hbar\delta_L/2$ and $-\hbar\delta_L/2$, respectively, as shown in Fig. A.2. Now taking into account the atom-field coupling and finding the dressed states as above, the energies of the upper and lower states are $+\hbar\Omega/2$ and $-\hbar\Omega/2$, respectively. The energy of the upper state $|1\rangle$ has been raised relative to that of $|a\rangle$, while the energy of the lower state $|2\rangle$ has been lowered relative to that of $|b\rangle$. These energy shifts are the light or ac Stark shifts. The treatment here, in which the photon number in the light field is taken into account, is discussed more fully in Ref. [56]. Thus the upwards light shift of the upper level is $\hbar(\Omega-\delta_L)/2$, as is the downwards shift of the lower level. Put another way, for a given value of δ_L, the energy differences between E_1 and its asymptote for $|\delta_L| \gg \Omega_1$, *i.e.* $+\hbar\delta_L/2$, and between E_2 and its asymptote of $-\hbar\delta_L/2$, are the energy shifts of the bare atomic levels by virtue of their interaction with the laser

field.

Since when $\delta_L > 0$, $|1\rangle$ contains a greater proportion of $|e\rangle$ than of $|g\rangle$, we can say that the light shift of $|e\rangle$ in these circumstances is positive, because the energy E_1 is greater than $\hbar\delta_L/2$. Similarly, since $|2\rangle$ contains a greater proportion of $|g\rangle$ than of $|e\rangle$ when $\delta_L > 0$, we can say that the light shift of $|g\rangle$ is negative because $E_2 < -\hbar\delta_L/2$. The situations are reversed for $\delta_L < 0$. $E_1 > -\hbar\delta_L/2$, so the light shift of $|g\rangle$ is positive, while $E_2 < +\hbar\delta_L/2$, so the light shift of $|e\rangle$ is negative. To calculate the light shift of a state, we need to find the difference between E_1 or E_2 and its corresponding asymptote in the limit $|\delta_L| \gg \Omega_1$. For E_1 and $\delta_L > 0$, the light shift is

$$\begin{aligned}
\Delta E_1 &= \frac{\hbar\Omega}{2} - \frac{\hbar\delta_L}{2} && \text{(A.23)}\\
&= \frac{\hbar(\Omega_1^2 + \delta_L^2)^{1/2}}{2} - \frac{\hbar\delta_L}{2} && \text{(A.24)}\\
&= \frac{\hbar\delta_L}{2}\left[\left(1 + \frac{\Omega_1^2}{\delta_L^2}\right)^{1/2} - 1\right] && \text{(A.25)}\\
&\simeq \frac{\hbar\delta_L}{2}\left[1 + \frac{\Omega_1^2}{2\delta_L^2} - 1\right] && \text{(A.26)}\\
\Rightarrow \Delta E_1 &= \frac{\hbar\Omega_1^2}{4\delta_L} && \text{(A.27)}
\end{aligned}$$

assuming that $\delta_L \gg \Omega_1$. An analogous calculation can be performed to find the light shift for E_2, and the result is

$$\Delta E_2 = -\frac{\hbar\Omega_1^2}{4\delta_L} \tag{A.28}$$

In order to calculate the value of the Rabi frequency, Ω_1, and hence allow the light shift to be quantified, use is made of the fact that quantum electrodynamics gives the spontaneous emission rate, Γ, of the upper level $|e\rangle$ to the lower level $|g\rangle$ as

$$\Gamma = \frac{1}{4\pi\epsilon_0}\frac{4d^2\omega_0^3}{3\hbar c^3} \tag{A.29}$$

d can be expressed in terms of Γ, a measurable quantity, and this can be used in the expression $\Omega_1 = dE_0/\hbar$. E_0 determines the intensity of the light field of the travelling wave in which the atom is located. The intensity is given by $I_0 = c\epsilon_0 E_0^2/2$ and thus Ω_1 is defined by the relationship

$$\frac{\Omega_1^2}{\Gamma^2} = \frac{I}{I_{\text{sat}}} \tag{A.30}$$

where the saturation intensity, I_{sat}, of the transition is that intensity for which $\Omega_1 = \Gamma$. It is given by

$$I_{\text{sat}} = \frac{\hbar\omega_0^3}{6\pi c^2}\Gamma \tag{A.31}$$

The use of Eq. (A.30) assumes that the Clebsch-Gordan coefficient for the transition being considered is 1 so that the matrix element, d, of the dipole operator is linked to the total spontaneous emission rate from $|e\rangle$ by Eq. (A.29). If this is not the case, Eq. (A.30) must be modified to read

$$\frac{\Omega_1^2}{\Gamma^2} = (\text{C-G})^2 \frac{I}{I_{\text{sat}}} \tag{A.32}$$

where $(\text{C-G})^2$ is the square of the Clebsch-Gordan coefficient appropriate to the transition in question.

As discussed in Ch. 2, the potential that the cold caesium atoms experienced in the system used to carry out the experiments described in this thesis was created by a standing wave of light that was $\sim 30\,\text{GHz}$ red-detuned ($\delta_L > 0$) from the $(6^2S_{1/2} \rightarrow 6^2P_{1/2})$ $(F = 4 \rightarrow F' = 3)$ D1 transition. The finite duration of each pulse, t_p, was 500 ns so that the product $\delta_L t_p$ was approximately 1×10^5. For the regime $\delta_L t_p \gg 1$, the two-level particle model described in this Appendix so far can be simplified because real transitions do not occur in such a strongly detuned two-level system; only virtual transitions can occur. For atoms in the lower state $|g\rangle$ prior to the application of any light, the upper state $|e\rangle$ can be neglected when considering the dynamics of the system. One way[1] of viewing this approximation is that in the limit of such a large detuning, the lower-energy dressed state $|2\rangle$, an eigenstate of the (atom+field) Hamiltonian, consists almost entirely of the bare state $|g\rangle$ if $\delta_L > 0$ and $|1\rangle$ consists almost entirely of $|e\rangle$. Thus $|e\rangle$ and $|g\rangle$ may be uncoupled and their energies are E_1 and E_2, respectively. The energy shift of $|g\rangle$ due to the presence of the light field is the light shift

$$\Delta E_2 = -\frac{\hbar\Omega_1^2}{4\delta_L} \tag{A.33}$$

Since $\delta_L > 0$ in our experimental system, $|g\rangle$ was lowered in energy by the application of the light. As $|g\rangle$ can be considered uncoupled from $|e\rangle$, the time-evolution of the amplitude of $|g\rangle$, ψ_g, was described by

$$i\hbar\frac{\partial\psi_g}{\partial t} = \hat{H}\psi_g \tag{A.34}$$

where p is the CM momentum of the atom and

$$\hat{H} = \frac{\hat{p}^2}{2m} + \hat{V}_g(z,t) \tag{A.35}$$

$V_g(z,t)$ was the potential, *i.e.* the light shift, experienced by the atom. It was dependent on both the position in the standing wave, since the light intensity in a standing wave is sinusoidally dependent on position, and the time, because the

[1]Note that another way of viewing the procedure by which the effect of the state $|e\rangle$ on the atom's dynamics is eliminated is that of *adiabatic elimination*. This is discussed in Refs. [74] and [183].

pulses of the standing wave were applied as a regularly-spaced sequence. If the electric fields of the counter-propagating travelling waves that created the standing wave were $E_a(z,t) = E_0\cos(k_L z - \omega_L t)$ and $E_b(z,t) = E_0\cos(k_L z + \omega_L t)$ (so that the intensity of each was $I_0 = c\epsilon_0 E_0^2/2$) then the electric field of the standing wave was $E_{\rm tot}(z,t) = 2E_0\cos(k_L z)\cos(\omega_L t)$. Thus the intensity in the standing wave as a function of z was

$$\begin{aligned} I(z) &= \frac{c\epsilon_0}{2} 4E_0^2\cos^2(k_L z) && \text{(A.36)} \\ &= I_{\rm max}\cos^2(k_L z) && \text{(A.37)} \\ &= \frac{1}{2} I_{\rm max}[1+\cos(Gz)] && \text{(A.38)} \end{aligned}$$

where $I_{\rm max} = 4I_0$ was the maximum intensity and $G = 2k_L$.

The time interval between successive pulses of the standing wave was T. For sufficiently small momenta, the atoms could be considered to be in the Raman-Nath regime. In this regime, the kinetic energy of an atom is neglected over the time t_p and, physically, this corresponds to the case where the distance travelled by an atom over the duration of a pulse is small compared to the spatial period of the standing wave potential, $\lambda_{\rm spat} = 2\pi/G$. Though the definition of how far an atom must travel in the time t_p for the Raman-Nath approximation to substantially break down is somewhat arbitrary, a useful estimate might be $\sim \lambda_{\rm spat}/10$. In the Raman-Nath regime, the pulses can be considered to be equivalent, in terms of their effect on the atoms, to δ-functions. The maximum impulse, $X_{\rm max}$, that the periodic potential could deliver classically over a time t_p is given by

$$X_{\rm max} = \frac{1}{2}\left(\frac{\hbar\Omega_{1,\rm max}^2}{4\delta_L}\right) t_p G \qquad \text{(A.39)}$$

where $\Omega_{1,\rm max}$ is the Rabi frequency for a light intensity of $I_{\rm max}$. If the effect of the pulses of finite duration t_p in our system is described by the application of instantaneous δ-functions (this approximation is valid in the Raman-Nath regime) then the potential experienced by the atoms can be written

$$V_g(z,t) = -\frac{X_{\rm max}}{G}[1+\cos(Gz)]\sum_{n=0}^{\infty}\delta(t-nT) \qquad \text{(A.40)}$$

Therefore the Hamiltonian that, in our regime of $\delta_L t_p \gg 1$, determines the evolution of the atom in the standing wave potential is

$$\hat{H} = \frac{\hat{p}^2}{2m} - \frac{X_{\rm max}}{G}[1+\cos(G\hat{z})]\sum_{n=0}^{\infty}\delta(t-nT) \qquad \text{(A.41)}$$

Since the detuning of the light field from the transition is so great, any momentum transfer of $\pm\hbar k_L$ that the potential can impart to the atom due to the absorption of a photon must be accompanied by another momentum transfer of $\pm\hbar k_L$ due to the coherent de-excitation [183] that must follow within a short time $\delta_L^{-1} \ll t_p$ after

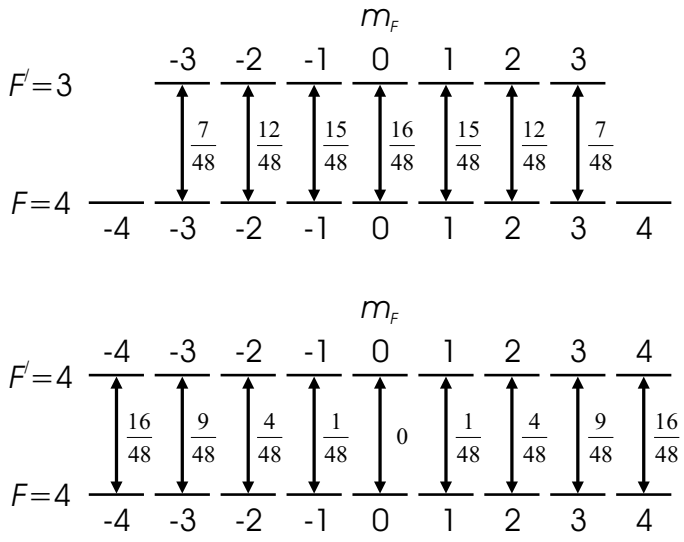

Figure A.3: The squared values of the D1 Clebsch-Gordan coefficients for the $\Delta m_F = 0$ transitions that π-polarised light can induce from the $F = 4$ hyperfine level of the ground state in caesium.

the excitation so that the atom remains in the ground state. Thus only momenta that are integer multiples of $2\hbar k_L$, *i.e.* $\hbar G$, can be imparted to the atom.

In order to estimate the potential experienced by the cold caesium atoms in the experiment, use must be made of Eqs. (A.32), (A.39) and (A.40). As stated, the light forming the standing wave was $\sim 30\,\mathrm{GHz}$ red-detuned from the $(6^2S_{1/2} \rightarrow 6^2P_{1/2})$ $(F = 4 \rightarrow F' = 3)$ D1 transition. This means that this light was $\sim 31\,\mathrm{GHz}$ red-detuned from the $(6^2S_{1/2} \rightarrow 6^2P_{1/2})$ $(F = 4 \rightarrow F' = 4)$ transition (see Fig. 2.3). Since the detunings from these transitions were close in magnitude and of the same sign (namely red) then both transitions would contribute additively to the light shift experienced by the state $|g\rangle$ and hence the potential in the Hamiltonian of Eq. (A.41). We call the detuning of the light from the $(F = 4 \rightarrow F' = 3)$ transition $\delta_1 = 2\pi \times 30 \times 10^9\,\mathrm{rad\,s^{-1}}$ and the detuning from the $(F = 4 \rightarrow F' = 4)$ transition $\delta_2 = 2\pi \times 31 \times 10^9\,\mathrm{rad\,s^{-1}}$. The light applied to the atoms was linearly polarised, so only transitions for which $\Delta m_F = 0$ need be considered in evaluating the light shift. The squares of the Clebsch-Gordan coefficients for these transitions are shown in Fig. A.3. Thus, from Eqs. (A.32) and (A.33), the total light shift of the $F = 4$, $m_F = \pm 4$ states was

$$\Delta E_4 = -\frac{\hbar}{4}\frac{I}{I_{\mathrm{sat}}}\Gamma^2\left(\frac{16}{48}\frac{1}{\delta_2}\right) \tag{A.42}$$

The total light shift of the $F = 4$, $m_F = \pm 3$ states was

$$\Delta E_3 = -\frac{\hbar}{4}\frac{I}{I_{\mathrm{sat}}}\Gamma^2\left(\frac{7}{48}\frac{1}{\delta_1} + \frac{9}{48}\frac{1}{\delta_2}\right) \tag{A.43}$$

The total light shift of the $F = 4$, $m_F = \pm 2$ states was

$$\Delta E_2 = -\frac{\hbar}{4}\frac{I}{I_{\mathrm{sat}}}\Gamma^2\left(\frac{12}{48}\frac{1}{\delta_1} + \frac{4}{48}\frac{1}{\delta_2}\right) \tag{A.44}$$

The total light shift of the $F = 4$, $m_F = \pm 1$ states was

$$\Delta E_1 = -\frac{\hbar}{4}\frac{I}{I_{\rm sat}}\Gamma^2\left(\frac{15}{48}\frac{1}{\delta_1} + \frac{1}{48}\frac{1}{\delta_2}\right) \tag{A.45}$$

The total light shift of the $F = 4$, $m_F = 0$ state was

$$\Delta E_0 = -\frac{\hbar}{4}\frac{I}{I_{\rm sat}}\Gamma^2\left(\frac{16}{48}\frac{1}{\delta_1}\right) \tag{A.46}$$

Hence the mean light shift undergone by a magnetic sublevel of the $F = 4$ manifold was

$$\Delta E_{\rm mean} = -\frac{\hbar}{144}\frac{I}{I_{\rm sat}}\Gamma^2\left(\frac{7}{\delta_1} + \frac{5}{\delta_2}\right) \tag{A.47}$$

We shall regard the light shift to the $F = 4$ hyperfine level as being $\Delta E_{\rm mean}$. For the D1 transition in caesium, $I_{\rm sat} = 1.66\,{\rm mW/cm^2}$ and $\Gamma = 2\pi \times 4.55\,{\rm MHz}$ (*i.e.* $28.6 \times 10^6\,{\rm rad\ s^{-1}}$) [184]. As described in Ch. 2, the standing wave was created by two counter-propagating beams with a Gaussian intensity profile (FWHM $\simeq 1\,{\rm mm}$) and a total power in each of approximately 120 mW. This means that the peak intensity in each beam was $I_0 = 1.1 \times 10^4\,{\rm mW/cm^2}$ and the peak intensity in the standing wave was $I_{\rm max} = 4I_0 = 4.2 \times 10^4\,{\rm mW/cm^2}$. If the value of $\Delta E_{\rm mean}$ for a light intensity of $I_{\rm max}$ is called $V_{\rm max}$, as in Ch. 3, then $V_{\rm max} = 9.6 \times 10^{-28}\,{\rm J}$. The maximum classical impulse that could be delivered by a potential whose strength was equal to the maximum value of the light shift in the standing wave is

$$X_{\rm max} = \frac{V_{\rm max} t_p G}{2} \tag{A.48}$$

The wavelength of the counter-propagating light beams forming the standing wave was 894.347 nm [102] so that $k_L = 7.025 \times 10^6\,{\rm m^{-1}}$ and $G = 1.405 \times 10^7\,{\rm m^{-1}}$. Therefore $X_{\rm max} = 3.4 \times 10^{-27}\,{\rm kg\,m\,s^{-1}}$. As defined in Ch. 3, the quantity ϕ_d is the maximum classical impulse that can be received by a particle, expressed in units of momentum recoil from the phase grating, *i.e.* $\phi_d = X_{\rm max}/\hbar G$. Therefore the maximum value of ϕ_d experienced by the atoms in the experiment was 2.3. Since ϕ_d is the amplitude of the phase modulation produced in the de Broglie waves by the application of the potential, a natural unit in which it can be expressed is π. From these calculations the maximum value of ϕ_d experienced by the atoms in the experiment was 0.7π. If the FWHM of the intensity distribution in the travelling waves was w and the FWHM of the Gaussian density distribution of atoms in the MOT was ℓ, then the mean value of ϕ_d experienced by atoms in the MOT, $\bar{\phi}_d$, is related to the maximum value of ϕ_d, that is $\phi_{d,\rm max}$, by

$$\bar{\phi}_d = \frac{w^2}{w^2 + \ell^2}\phi_{d,\rm max} \tag{A.49}$$

Since in the experiment $w = \ell = 1\,{\rm mm}$, $\bar{\phi}_d = (\phi_{d,\rm max}/2) = 0.35\pi$.

As discussed in Sec. 2.3, there was some uncertainty in the value of the light intensity experienced by the atoms in the standing wave. The results of the numerical simulations described in Chs. 3 and 4 gave the best qualitative agreement

with the experimental behaviour when a value $\phi_d = 0.8\pi$ was used. Since the experimental response of the atoms to the standing wave was dominated by those which experienced the strongest potential, the mean value of ϕ_d may not have been as large as the value of ϕ_d required to produce the best agreement in the simulation (for which all particles were assumed to experience the same potential). Nevertheless, the experimental value of $\phi_{d,\max}$ must have been larger than 0.8π. It seems likely that the value of $\phi_{d,\max}$ deduced from the calculations above was a factor of up to 1.5 too small. This is quite consistent with the experimental uncertainties.

Appendix B

The method of Fourier paths

To obtain the expression for the classical diffusion parameter in the presence of gravity, as given in Eq. (4.6), the derivation essentially follows that for the δ-kicked rotor diffusion parameter in Chapter 5 of Lichtenberg and Lieberman [86]. The same method of Fourier paths is used, with appropriate modifications to incorporate the effect of γ. Thus the recursion relation for the Fourier coefficients takes the form

$$\begin{aligned} a_n(m,q) &= \frac{1}{(2\pi)^2}\int d\chi d\rho \exp[-i(m\chi+q\rho)] \\ &\times \int d\chi' d\rho' \delta[\rho-\rho'-K\sin(\chi')+\gamma]\delta[\chi-\chi'-\rho'-K\sin(\chi')+\gamma/2] \\ &\times \int dq' \sum_{m'} \exp[i(m'\chi'+q'\rho')]a_{n-1}(m',q'), \end{aligned} \tag{B.1}$$

which, after integration, becomes

$$a_n(m,q) = \sum_{l=-\infty}^{\infty} J_l(|q+m|K)a_{n-1}[m+l\,\mathrm{sgn}(q+m), q+m]\exp[i(q+m/2)\gamma]. \tag{B.2}$$

Through repeated substitution of this recursion relation we arrive at

$$a_n(m_n,q_n) = \sum_{l_n,\cdots,l_1} J_{l_n}(|q_{n-1}|K)\cdots J_{l_1}(|q_0|K)a_0(m_0,q_0)\exp\left[i\gamma\left(\sum_{k=1}^{n} q_{n-k} - \frac{m_{n-k}}{2}\right)\right]. \tag{B.3}$$

In the case of a path of n steps remaining at the origin in Fourier space, this simplifies to

$$a_n(0,q) = [J_0(Kq)]^n a_0(m_0,q)\exp\left[i\gamma\sum_{l=1}^{n} q\left(q_{n-l} - \frac{m_{n-l}}{2}\right)\right]. \tag{B.4}$$

Including the standard low-order corrections by consideration of paths which briefly leave the origin, we determine the following K- and γ-dependent diffusion parameter

$$\tilde{D}_n(K,\gamma) = \frac{K^2}{2}\left[\frac{1}{2} - J_2(K)\cos(\gamma) - J_1^2\cos(2\gamma) + J_3^2(K) + J_2^2(K)\right] - \gamma\bar{\rho}_i + \frac{n\gamma^2}{2}, \tag{B.5}$$

where $\bar{\rho}_i$ is the mean initial scaled momentum. This is the expression used in Eq. (4.5) of Ch. 4. The series of Bessel functions is a truncated series that is correct to order K^{-1}. To take account of higher-order kick-to-kick correlations it would have to include further terms.

The free-fall effect of gravity on the centre-of-mass motion of the atomic ensemble is not of interest in the context of this thesis, so the last term on the RHS of this equation will be neglected, as discussed in Sec. 4.1.1. Many thanks to Dr. Simon Gardiner for the derivation of this result.

Appendix C

The inter-pulse free evolution

The operator $\hat{U}_{\text{free}}$, defined in Eq. (4.11), expresses the free evolution of a wave between kicks from the potential and has the following form:

$$\hat{U}_{\text{free}} = \exp\left(-\frac{i}{\hbar}\left[\frac{\hat{p}^2}{2m} + mg\hat{z}\right]T\right) \tag{C.1}$$

The argument of this operator contains a sum of terms involving position and momentum operators. For the purposes of analysis, it would be simpler to have a free evolution operator that was a product of operators that each acted only on position or momentum. The following unitary evolution operator, which is a function of the dummy variable ξ, has the desired form.

$$\hat{B}(\xi) = \exp([a\hat{p}^2 + b\hat{p}]\xi)\exp(c\hat{z}\xi) \tag{C.2}$$

where $\hat{z}$ and $\hat{p}$ are the unscaled position and momentum operators, respectively. The derivative of this operator with respect to ξ can be written

$$\frac{\partial\hat{B}(\xi)}{\partial\xi} = \{[a\hat{p}^2 + b\hat{p}] + \exp([a\hat{p}^2 + b\hat{p}]\xi)c\hat{z}\exp(-[a\hat{p}^2 + b\hat{p}]\xi)\}\hat{B} \tag{C.3}$$

The following relation can be used to simplify the RHS of the equation.

$$\begin{aligned}\exp([a\hat{p}^2 + b\hat{p}]\xi)c\hat{z}(-[a\hat{p}^2 + b\hat{p}]\xi) \equiv& \\ c\hat{z} + \xi[(a\hat{p}^2 + b\hat{p}), c\hat{z}] + \frac{\xi^2}{2!}[(a\hat{p}^2 + b\hat{p}), [(a\hat{p}^2 + b\hat{p}), c\hat{z}]] + \cdots& \quad \text{(C.4)}\\ \equiv\ c\hat{z} + \xi(-2iac\hbar\hat{p} - ibc\hbar)& \quad \text{(C.5)}\end{aligned}$$

Therefore the derivative of the operator can now be written

$$\frac{\partial\hat{B}(\xi)}{\partial\xi} = ([a\hat{p}^2 + b\hat{p}] + c\hat{z} + \xi[-2iac\hbar\hat{p} - ibc\hbar])\hat{B} \tag{C.6}$$

This means that $\hat{B}$ itself has the following form

$$\hat{B}(\xi) = C \exp\left([a\hat{p}^2 + b\hat{p} + c\hat{z}]\xi - iac\hbar\hat{p}\xi^2 - \frac{ibc\hbar}{2}\xi^2\right) \tag{C.7}$$

where C is a scalar quantity corresponding to a global phase. Since the evolution represented by the operator is unitary, $C = 1$. If the value of ξ is now set to 1,

$$\begin{aligned} \hat{B}(\xi) &= \exp([a\hat{p}^2 + b\hat{p}])\exp(c\hat{z}) & \text{(C.8)} \\ &\equiv \exp\left([a\hat{p}^2 + b\hat{p} + c\hat{z}] - iac\hbar\hat{p} - \frac{ibc\hbar}{2}\right) & \text{(C.9)} \end{aligned}$$

This is somewhat similar in form to the free evolution operator given in Eq. (C.1), but there is no $\hat{p}$-dependent term in Eq. (C.1). This means that the coefficients of $\hat{p}$ must cancel and hence $b = iac\hbar$. Therefore $\hat{B}$ can be written

$$\hat{B} = \exp(a\hat{p}^2 + c\hat{z})\exp\left(\frac{ac^2\hbar^2}{2}\right) \tag{C.10}$$

Finally we may equate this to the expression in Eq. (C.2) and, using the relation $b = iac\hbar$, write

$$\exp(a\hat{p}^2 + c\hat{z}) = \exp([a\hat{p}^2 + iac\hbar\hat{p}])\exp(c\hat{z})\exp\left(-\frac{ac^2\hbar^2}{2}\right) \tag{C.11}$$

Thus we have succeeded in separating the free evolution operator into a product of operators that each act only on position or momentum. By comparison of the LHS of this equation with the RHS of Eq. (C.1), $a = -iT/2m\hbar$ and $c = -imgT/\hbar$. Therefore we may write

$$\begin{aligned} \hat{U}_{\text{free}} &= \exp\left(-\frac{i}{2\hbar}\left[\frac{\hat{p}^2T}{m} + \hat{p}gT^2\right]\right)\exp\left(-\frac{i}{\hbar}mgT\hat{z}\right) \\ &\quad \times \exp\left(-\frac{i}{\hbar}\frac{mg^2T^3}{4}\right) & \text{(C.12)} \\ &= \exp\left(-\frac{i}{2\hbar}[\hat{\rho}^2 + \gamma\hat{\rho}]\right)\exp\left(-\frac{i}{\hbar}\gamma\hat{\chi}\right)\exp\left(-\frac{i}{4\hbar}\gamma^2\right) & \text{(C.13)} \end{aligned}$$

where scaled units have now been introduced. This accounts for the expression given in Eq. (4.13). As discussed in Sec. 4.1.2, the term $\exp(-i[\hat{\rho}^2 + \gamma\hat{\rho}]/2\hbar)$ represents a phase shift to the de Broglie wave during its free evolution in the gravitational field, while $\exp(-i\gamma\hat{\chi}/\hbar)$ is a momentum displacement operator and $\exp(-i\gamma^2/4\hbar)$ represents a global phase applied to the system as a whole, which may be neglected. For the state that has received v units of momentum in the diffractive process, the free evolution phase shift over the interval between the nth and $(n+1)$th kicks is given by $\phi_v = (\rho_{v,n}^2 + \gamma\rho_{v,n})/2\hbar$, where $\rho_{v,n}$ is the scaled laboratory momentum of this state immediately prior to the $(n+1)$th pulse of the

potential, an expression for which is given by use of Eq. (4.14). Expansion of this expression yields the result

$$\phi_v = \frac{1}{2k}[\rho_i^2 + (vk)^2 + n(n-1)\gamma^2 - \gamma(2n-1)(\rho_i + vk) + 2vk\rho_i] \tag{C.14}$$

as given in Eq. (4.17). Many thanks to Dr. Simon Gardiner for this derivation.

Appendix D

Publications

The investigations described in this thesis have led to the following publications:

'Approaching Classicality in Quantum Accelerator Modes Through Decoherence'
M.B. d'Arcy, R.M. Godun, M.K. Oberthaler, G.S. Summy, K. Burnett, S.A. Gardiner
Phys. Rev. E **64**, 056233 (2001)

'Quantum Enhancement of Momentum Diffusion in the Delta-Kicked Rotor'
M.B. d'Arcy, R.M. Godun, M.K. Oberthaler, D. Cassettari, and G.S. Summy
Phys. Rev. Lett. **87**, 074102 (2001)

'Quantum Accelerator Modes: A Tool for Atom Optics'
R.M. Godun, M.B. d'Arcy, M.K. Oberthaler, G.S. Summy, and K. Burnett
Phys. Rev. A **62**, 013411 (2000)

'Observation of Quantum Accelerator Modes'
M.K. Oberthaler, R.M. Godun, M.B. d'Arcy, G.S. Summy, and K. Burnett
Phys. Rev. Lett. **83**, 4447 (1999)

Bibliography

[1] Aristotle (translated by J. Barnes), *The Complete Works of Aristotle: Revised Oxford Translation*, Princeton University Press, Princeton, New Jersey, 1983.

[2] Ptolemy (translated by G.J. Toomer), *Ptolemy's Amalgest*, Duckworth, London, 1984.

[3] I. Newton, *Philosophiae Naturalis Principia Mathematica*, Smith, London, 1687.

[4] H. Poincaré, Acta Math. **13**, 1 (1890).

[5] H. Poincaré, *Les Methodes Nouvelles de la Mécanique Celeste*, Gauthier-Villars, Paris, 1899.

[6] E.N. Lorenz, J. Atmos. Sci. **20**, 130 (1963).

[7] S.H. Strogatz, *Nonlinear Dynamics and Chaos*, Addison-Wesley, Reading, Massachusetts, 1994.

[8] B. Pascal (translated by A.J. Krailsheimer), *Pensées*, Penguin, London, 1995.

[9] H.L. Swinney, Physica D **7**, 3 (1983).

[10] R. Buizza, Nuovo Cimento Soc. Ital. Fis. C **24**, 273 (2001).

[11] B. LeBaron, Phil. Trans. R. Soc. Lond. A **348**, 397 (1994).

[12] M.J. Keeling, P. Rohani and B.T. Grenfell, Physica D **148**, 317 (2001).

[13] A. Einstein, Ann. Phys. (Leipzig) **17**, 132 (1905).

[14] A.H. Compton, Phys. Rev. **21**, 715 (1923).

[15] A.H. Compton, Phys. Rev. **22**, 409 (1923).

[16] L. de Broglie, Nature **112**, 540 (1923).

[17] L. de Broglie, Phil. Mag. **47**, 446 (1924).

[18] L. de Broglie, Ann. Phys. (Paris) **3**, 22 (1925).

[19] C. Davisson and L.H. Germer, Phys. Rev. **30**, 705 (1927).

[20] G.P. Thomson, Proc. R. Soc. Lond. A **117**, 600 (1928).

[21] I. Estermann and O. Stern, Z. Phys. **61**, 95 (1930).

[22] W. Heisenberg, Z. Phys. **33**, 879 (1925).

[23] E. Schrödinger, Ann. Phys. (Leipzig) **79**, 361 (1925).

[24] E. Schrödinger, Ann. Phys. (Leipzig) **79**, 489 (1925).

[25] E. Schrödinger, Ann. Phys. (Leipzig) **80**, 437 (1926).

[26] E. Schrödinger, Ann. Phys. (Leipzig) **81**, 109 (1926).

[27] E. Schrödinger, Ann. Phys. (Leipzig) **79**, 734 (1926).

[28] P.A.M. Dirac, *The Principles of Quantum Mechanics (4th ed., rev.)*, Clarendon Press, Oxford, 1981.

[29] G. Casati and J. Ford (eds.), *Stochastic Behavior in Classical and Quantum Hamiltonian Systems*, Springer-Verlag, New York, 1979.

[30] M.C. Gutzwiller, *Chaos in Classical and Quantum Mechanics*, Springer-Verlag, New York, 1990.

[31] L.E. Reichl, *The Transition to Chaos*, Springer-Verlag, New York, 1992.

[32] A. Peres, *Quantum Theory: Concepts and Methods*, Kluwer Academic, Dordrecht, 1993.

[33] F. Haake, *Quantum Signatures of Chaos (2nd ed.)*, Springer-Verlag, Berlin, 2001.

[34] B.V. Chirikov, Phys. Rep. **52**, 264 (1979).

[35] S. Fishman, D.R. Grempel, and R.E. Prange, Phys. Rev. Lett. **49**, 509 (1982).

[36] D.R. Grempel, R.E. Prange, and S. Fishman, Phys. Rev. A **29**, 1639 (1984).

[37] J.E. Bayfield and D.W. Sokol, Phys. Rev. Lett. **61**, 2007 (1988).

[38] E.J. Galvez, B.E. Sauer, L. Moorman, P.M. Koch and D. Richards, Phys. Rev. Lett. **61**, 2011 (1988).

[39] J.E. Bayfield, G. Casati, I. Guarneri, and D.W. Sokol, Phys. Rev. Lett. **63**, 364 (1989).

[40] F.L. Moore, J.C. Robinson, C. Bharucha, P.E. Williams, and M.G. Raizen, Phys. Rev. Lett. **73**, 2974 (1994).

[41] R. Blümel, R. Graham, L. Sirko, U. Smilansky, H. Walther, and K. Yamada, Phys. Rev. Lett. **62**, 341 (1989).

[42] H. Ammann, R. Gray, I. Shvarchuck, and N. Christensen, Phys. Rev. Lett. **80**, 4111 (1998).

[43] E. Ott, T.M. Antonsen, Jr., and J.D. Hanson, Phys. Rev. Lett. **53**, 2187 (1984).

[44] J.E. Bayfield and P.M. Koch, Phys. Rev. Lett. **33**, 258 (1974).

[45] G. Casati, I. Guarneri, and D.L. Shepelyansky, IEEE J. Quantum Electron. **24**, 1420 (1988).

[46] J.D. Meiss, Phys. Rev. Lett. **62**, 1576 (1989).

[47] F.L. Moore, J.C. Robinson, C.F. Bharucha, B. Sundaram, and M.G. Raizen, Phys. Rev. Lett. **75**, 4598 (1995).

[48] H. Rauch, Science **262**, 1384 (1993).

[49] C.S. Adams, M. Sigel, and J. Mlynek, Phys. Rep. **240**, 143 (1994).

[50] O.R. Frisch, Z. Phys. **86**, 42 (1933).

[51] S. Chu, L. Hollberg, J.E. Bjorkholm, A. Cable, and A. Ashkin, Phys. Rev. Lett. **55**, 48 (1985).

[52] S. Chu, Science **253**, 861 (1991).

[53] E.L. Raab, M. Prentiss, A. Cable, S. Chu, and D.E. Pritchard, Phys. Rev. Lett. **59**, 2631 (1987).

[54] C.J. Foot, Contemp. Phys. **32**, 369 (1991).

[55] H.J. Metcalf and P. van der Straten, *Laser Cooling and Trapping*, Springer-Verlag, New York, 1999.

[56] C. Cohen-Tannoudji, J. Dupont-Roc, G. Grynberg, *Atom-photon interactions: basic processes and applications*, Wiley, Chichester, 1992.

[57] J.E. Bjorkholm, R.R. Freeman, A. Ashkin, and D.B. Pearson, Phys. Rev. Lett. **41**, 1361 (1978).

[58] S. Chu, J.E. Bjorkholm, A. Ashkin, and A. Cable, Phys. Rev. Lett. **57**, 314 (1986).

[59] V.I. Balykin, V.S. Letokhov, Yu.B. Ovchinnikov, and A.I. Sidorov, Phys. Rev. Lett. **60**, 2137 (1988).

[60] T. Sleator, T. Pfau, V. Balykin, and J. Mlynek, Appl. Phys. B **54**, 375 (1992).

[61] P. Berman (ed.), *Atom Interferometry*, Academic Press, San Diego, 1997.

[62] J. Baudon, R. Mathevet, and J. Robert, J. Phys. B: At. Mol. Opt. Phys. **32**, R173 (1999).

[63] R.M. Godun, M.B. d'Arcy, G.S. Summy, and K. Burnett, Contemp. Phys. **42**, 77 (2001).

[64] E.W. Hagley, L. Deng, M. Kozuma, J. Wen, K. Helmerson, S.L. Rolston, and W.D. Phillips, Science **283**, 1706 (1999).

[65] M. Key, I.G. Hughes, W. Rooijakkers, B.E. Sauer, E.A. Hinds, D.J. Richardson and P.G. Kazansky, Phys. Rev. Lett. **84**, 1371 (2000).

[66] N.H. Dekker, C.S. Lee, V. Lorent, J.H. Thywissen, S.P. Smith, M. Drndić, R.M. Westervelt, and M. Prentiss, Phys. Rev. Lett. **84**, 1124 (2000).

[67] D. Cassettari, B. Hessmo, R. Folman, T. Maier, and J. Schmiedmayer, Phys. Rev. Lett. **85**, 5483 (2000).

[68] M.J. Renn, E.A. Donley, E.A. Cornell, C.E. Wieman, and D.A. Anderson, Phys. Rev. A **53**, R648 (1996).

[69] M.H. Anderson, J.R. Ensher, M.R. Matthews, C.E. Wieman and E.A. Cornell, Science **269**, 1989 (1995).

[70] K.B. Davis, M.-O. Mewes, M.R. Andrews, N.J. van Druten, D.S. Durfee, D.M. Kurn and W. Ketterle, Phys. Rev. Lett. **75**, 3969 (1995).

[71] M. Inguscio, S. Stringari, and C.E. Wieman (eds.), *Bose-Einstein Condensation in Atomic Gases*, Proceedings of the International School of Physics "Enrico Fermi", IOS Press, Amsterdam, 1999.

[72] A. Aspect and J. Dalibard (eds.), C. R. Acad. Sci. Paris, Série IV **2**, (3,4) (2001).

[73] Nature Insight *Ultracold Matter*, Nature **416**, 205 (2002).

[74] R. Graham, M. Schlautmann, and P. Zoller, Phys. Rev. A **45**, R19 (1992).

[75] C. Monroe, W. Swann, H. Robinson, and C. Wieman, Phys. Rev. Lett. **65**, 1571 (1990).

[76] IAGA Division V, Working group 8, *International Geomagnetic Reference Field, 2000 revision*, http://www.ngdc.noaa.gov/IAGA/wg8/, released Nov. 1999.

[77] G.D. Rovera, G. Santarelli, and A. Clairon, Rev. Sci. Instrum. **65**, 1502 (1994).

[78] P.D. Featonby, *Atom Interferometry*, DPhil thesis, Clarendon Laboratory, University of Oxford, 1998.

[79] C.L. Webb, *Experiments with a Caesium Atom Interferometer*, DPhil thesis, Clarendon Laboratory, University of Oxford, 1999.

[80] P.J. Mohr and B.N. Taylor, Rev. Mod. Phys. **72**, 351 (2000).

[81] International Association of Geodesy, *Geodetic Reference System 1967*, Publi. Spéc. no. 3 du Bulletin Géodésique, Paris, 1971.

[82] J. Vanier and C. Audoin, *The Quantum Physics of Atomic Frequency Standards*, Adam Hilger, Bristol and Philadelphia, 1989, Vol. 2.

[83] N.F. Ramsey, Phys. Rev. **78**, 695 (1950).

[84] N.F. Ramsey, *Molecular Beams*, Oxford University Press, Oxford, 1986.

[85] A.C. Corney, *Atomic and Laser Spectroscopy*, Oxford University Press, Oxford, 1977.

[86] A.J. Lichtenberg and M.A. Lieberman, *Regular and Chaotic Dynamics*, Springer-Verlag, New York, 1992.

[87] M.K. Oberthaler, R.M. Godun, M.B. d'Arcy, G.S. Summy, and K. Burnett, Phys. Rev. Lett. **83**, 4447 (1999).

[88] A. N. Kolmogorov, Dokl. Akad. Nauk. SSSR **98**, 527 (1954).

[89] J. Moser, Nachr. Akad. Wiss. Göttingen II Math.-Phys. Kl. **1**, 1 (1962).

[90] V.I. Arnold, Sov. Math. Dokl. **3**, 136 (1963).

[91] K. Vant, G. Ball, H. Ammann, and N. Christensen, Phys. Rev. E **59**, 2846 (1999).

[92] J. Klafter, M.F. Shlesinger, G. Zumofen, Phys. Today **49**, (2) 33 (Feb. 1996).

[93] F.M. Izrailev and D.L. Shepelyanskii, Sov. Phys. Dokl. **24**, 996 (1979).

[94] F.M. Izrailev and D.L. Shepelyanskii, Theor. Math. Phys. **43**, 553 (1980).

[95] V. Mangulis, *Handbook of Series for Scientists and Engineers*, Academic Press, New York and London, 1965.

[96] N.W. Ashcroft and N.D. Mermin, *Solid State Physics*, Saunders College Publishing, Orlando, 1976.

[97] S.R. Elliott, *The Physics and Chemistry of Solids*, Wiley, Chichester, 2000.

[98] H.F. Talbot, Phil. Mag. **9**, 401 (1836).

[99] M.S. Chapman, C.R. Ekstrom, T.D. Hammond, J. Schmiedmayer, B.E. Tannian, S. Wehinger, and D.E. Pritchard, Phys. Rev. A **51**, R14 (1995).

[100] P.L. Kapitza and P.A.M. Dirac, Proc. Camb. Phil. Soc. **29**, 297 (1933).

[101] L. Deng, E.W. Hagley, J. Denschlag, J.E. Simsarian, M. Edwards, C.W. Clark, K. Helmerson, S.L. Rolston, and W.D. Phillips, Phys. Rev. Lett. **83**, 5407 (1999).

[102] G.W.F. Drake, ed., *Atomic, Molecular and Optical Physics Handbook*, AIP Press, Woodbury, New York, 1996.

[103] P.L. Gould, G.A. Ruff, and D.E. Pritchard, Phys. Rev. Lett. **56**, 827 (1986).

[104] H. Batelaan, Contemp. Phys. **41**, 369 (2000).

[105] S. Gupta, A.E. Leanhardt, A.D. Cronin, and D.E. Pritchard, C. R. Acad. Sci. Paris, Série IV **2**, 479 (2001).

[106] D.L. Freimund, K. Aflatooni and H. Batelaan, Nature **413**, 142 (2001).

[107] C. Salomon, J. Dalibard, A. Aspect, H. Metcalf and C. Cohen-Tannoudji, Phys. Rev. Lett. **59**, 1659 (1987).

[108] G. Timp, R.E. Behringer, D.M. Tennant, J.E. Cunningham, M. Prentiss, and K.K. Berggren, Phys. Rev. Lett. **69**, 1636 (1992).

[109] P.J. Martin, B.G. Oldaker, A.H. Miklich, and D.E. Pritchard, Phys. Rev. Lett. **60**, 515 (1988).

[110] S. Kunze, S. Dürr, and G. Rempe, Europhys. Lett. **34**, 343 (1996).

[111] S. Fishman, R.E. Prange, and M. Griniasty, Phys. Rev. A **39**, 1628 (1989).

[112] D.L. Shepelyansky, Phys. Rev. Lett. **56**, 677 (1986).

[113] D.L. Shepelyansky, Physica D **28**, 103 (1987).

[114] B.G. Klappauf, W.H. Oskay, D.A. Steck, and M.G. Raizen, Phys. Rev. Lett. **81**, 1203 (1998).

[115] W.H. Oskay, D.A. Steck, V. Milner, B.G. Klappauf, M.G. Raizen, Opt. Comm. **179**, 137 (2000).

[116] V. Milner, D.A. Steck, W.H. Oskay, and M.G. Raizen, Phys. Rev. E **61**, 7223 (2000).

[117] D.A. Steck, V. Milner, W.H. Oskay, and M.G. Raizen, Phys. Rev. E **62**, 3461 (2000).

[118] T. Hogg and B.A. Huberman, Phys. Rev. Lett. **48**, 711 (1982).

[119] T. Hogg and B.A. Huberman, Phys. Rev. A **28**, 22 (1983).

[120] D. Cohen, Phys. Rev. A **44**, 2292 (1991).

[121] S. Fishman, I. Guarneri, and L. Rebuzzini, to be published in J. Stat. Phys., e-print nlin.CD/0202047 (2002).

[122] S. Fishman, I. Guarneri, and L. Rebuzzini, to be published in Phys. Rev. Lett., e-print nlin.CD/0205006 (2002).

[123] I. Guarneri (private communication) (2000).

[124] A.V. Oppenheim, A.S. Willsky with S.H. Nawab, *Signals and Systems (2nd ed.)*, Prentice-Hall, London, 1997.

[125] J. Ford and G. Mantica, Am. J. Phys. **60**, 1086 (1992).

[126] D. Kleppner, Phys. Today **44**, (8) 9 (1991).

[127] E. Joos and H.D. Zeh, Z. Phys. B: Condens. Matter **59**, 223 (1985).

[128] W.H. Zurek, Phys. Today **44**, (10) 36 (1991).

[129] W.H. Zurek and J.P. Paz, Phys. Rev. Lett. **72**, 2508 (1994).

[130] W.H. Zurek and J.P. Paz, Physica D **83**, 300 (1995).

[131] S. Habib, K. Shizume, and W.H. Zurek, Phys. Rev. Lett. **80**, 4361 (1998).

[132] W.H. Zurek, Physica Scripta **T76**, 186 (1998).

[133] I. Guarneri, Lett. Nuovo Cimento Soc. Ital. Fis. **40**, 171 (1984).

[134] D. Cohen, Phys. Rev. A **43**, 639 (1991).

[135] S. Dyrting, Phys. Rev. A **53**, 2522 (1996).

[136] S. Dyrting and G.J. Milburn, Quantum Semiclassic. Opt. **8**, 541 (1996).

[137] B. Kaulakys and V. Gontis, Phys. Rev. A **56**, 1131 (1997).

[138] P. Knight, Nature **344**, 493 (1990).

[139] P. Facchi, S. Pascazio, and A. Scardicchio, Phys. Rev. Lett. **83**, 61 (1999).

[140] A.C. Doherty, K.M.D. Vant, G.H. Ball, N. Christensen and R. Leonhardt, J. Opt. B: Quantum Semiclassic. Opt. **2**, 605 (2000).

[141] G.H. Ball, K.M.D. Vant, H. Ammann and N.L. Christensen, J. Opt. B: Quantum Semiclassic. Opt. **1**, 357 (1999).

[142] G. Ball, K. Vant, and N. Christensen, Phys. Rev. E **61**, 1299 (2000).

[143] A.J. Daley, A.S. Parkins, R. Leonhardt, and S.M. Tan, Phys. Rev. E **65**, 035201 (2002).

[144] M. Arndt, A. Buchleitner, R.N. Mantegna, and H. Walther, Phys. Rev. Lett. **67**, 2435 (1991).

[145] H. Ammann, R. Gray, I. Shvarchuck, and N. Christensen, J. Phys. B: At. Mol. Opt. Phys. **31**, 2449 (1998).

[146] K. Vant, G. Ball, and N. Christensen, Phys. Rev. E **61**, 5994 (2000).

[147] B.G. Klappauf, W.H. Oskay, D.A. Steck, and M.G. Raizen, Phys. Rev. Lett. **82**, 241 (1999).

[148] M.V. Berry, in *Chaos et Physique Quantique, Proceedings of the Les Houches Summer School Session LII*, edited by M.-J. Giannoni, A. Voros, and J. Zinn-Justin, p. 251, Elsevier, Amsterdam, 1991.

[149] D.W. Keith, C.R. Ekstrom, Q.A. Turchette, and D.E. Pritchard, Phys. Rev. Lett. **66**, 2693 (1991).

[150] T.M. Roach, H. Abele, M.G. Boshier, H.L. Grossman, K.P. Zetie, and E.A. Hinds, Phys. Rev. Lett. **75**, 629 (1995).

[151] E.M. Rasel, M.K. Oberthaler, H. Batelaan, J. Schmiedmayer, and A. Zeilinger, Phys. Rev. Lett. **75**, 2633 (1995).

[152] M. Kozuma, L. Deng, E.W. Hagley, J. Wen, R. Lutwak, K. Helmerson, S.L. Rolston, and W.D. Phillips, Phys. Rev. Lett. **82**, 871 (1999).

[153] D.M. Giltner, R.W. McGowan, and S.A. Lee, Phys. Rev. Lett. **75**, 2638 (1995).

[154] M. Kasevich and S. Chu, Phys. Rev. Lett. **67**, 181 (1991).

[155] D.S. Weiss, B.C. Young, and S. Chu, Phys. Rev. Lett. **70**, 2706 (1993).

[156] D.S. Weiss, B.C. Young, and S. Chu, Appl. Phys. B: Lasers Opt. **59**, 217 (1994).

[157] R.M. Godun, *Beam Splitting Mechanisms for a Caesium Atom Interferometer*, DPhil thesis, Clarendon Laboratory, University of Oxford, 2000.

[158] M. Weitz, B.C. Young, and S. Chu, Phys. Rev. A **50**, 2438 (1994).

[159] M. Weitz, B.C. Young, and S. Chu, Phys. Rev. Lett. **73**, 2563 (1994).

[160] T. Sleator, T. Pfau, V. Balykin, O. Carnal, and J. Mlynek, Phys. Rev. Lett. **68**, 1996 (1992).

[161] T. Pfau, Ch. Kurtsiefer, C.S. Adams, M. Sigel, and J. Mlynek, Phys. Rev. Lett. **71**, 3427 (1993).

[162] M.A. Kasevich, D.S. Weiss, and S. Chu, Opt. Lett. **15**, 607 (1990).

[163] C. Henkel, C.I. Westbrook and A. Aspect, J. Opt. Soc. Am. B **13**, 233 (1996).

[164] A.G. Truscott, M.E.J. Friese, W.K. Hensinger, H.M. Wiseman, H. Rubinsztein-Dunlop, and N.R. Heckenberg, Phys. Rev. Lett. **84**, 4023 (2000).

[165] W.K. Hensinger, A.G. Truscott, B. Upcroft, N.R. Heckenberg, and H. Rubinsztein-Dunlop, J. Opt. B: Quantum Semiclass. Opt. **2**, 659 (2000).

[166] P.D. Featonby, G.S. Summy, C.L. Webb, R.M. Godun, M.K. Oberthaler, A.C. Wilson, C.J. Foot, and K. Burnett, Phys. Rev. Lett. **81**, 495 (1998).

[167] S. Schlunk, M.B. d'Arcy, S.A. Gardiner, D. Cassettari, R.M. Godun, and G.S. Summy, Phys. Rev. Lett. (submitted) (2002).

[168] A. Peters, K.Y. Chung, and S. Chu, Metrologia **38**, 25 (2001).

[169] M. Feingold and A. Peres, Phys. Rev. A **34**, 591 (1986).

[170] S.A. Gardiner, J.I. Cirac, and P. Zoller, Phys. Rev. Lett. **79**, 4790 (1997).

[171] S.A. Gardiner, J.I. Cirac, and P. Zoller, Phys. Rev. Lett. **80**, 2968 (1998).

[172] J. Ringot, P. Szriftgiser, J.C. Garreau, and D. Delande, Phys. Rev. Lett. **85**, 2741 (2000).

[173] W.K. Hensinger, H. Häffner, A. Browaeys, N.R. Heckenberg, K. Helmerson, C. McKenzie, G.J. Milburn, W.D. Phillips, S.L. Rolston, H. Rubinsztein-Dunlop, and B. Upcroft, Nature **412**, 52 (2001).

[174] D.A. Steck, W.H. Oskay, and M.G. Raizen, Science **293**, 274 (2001).

[175] S. Hennigan, S. Choi, M.B. d'Arcy, and K. Burnett (in preparation) (2002).

[176] I. Ciufolini, E. Pavlis, F. Chieppa, E. Fernandes-Vieira and J. Pérez-Mercader, Science **279**, 2100 (1998).

[177] I. Ciufolini and J.A. Wheeler, *Gravitation and Inertia*, Princeton University Press, Princeton, New Jersey, 1995.

[178] C.C. Speake and T.J. Quinn (conference organizers), Meas. Sci. Technol. **10**, 421 (1999).

[179] N. Arkani-Hamed, S. Dimopoulos, G. Dvali, and N. Kaloper, Phys. Rev. Lett. **84**, 586 (2000).

[180] C.D. Hoyle, U. Schmidt, B.R. Heckel, E.G. Adelberger, J.H. Gundlach, D.J. Kapner, and H.E. Swanson, Phys. Rev. Lett. **86**, 1418 (2000).

[181] P.S. Wesson, B. Mashhoon, H. Liu, and W.N. Sajko, Phys. Lett. B **456**, 34 (1999).

[182] I.C. Percival and W.T. Strunz, Proc. R. Soc. Lond. A **453**, 431 (1997).

[183] R. Graham and S. Miyazaki, Phys. Rev. A **53**, 2683 (1996).

[184] O.S. Heavens, J. Opt. Soc. Am. **51**, 1058 (1961).